TABLE OF CONTENTS

Section Title Page No.

1.0 SUMMARY 1 1/B4

2.0 INTRODUCTION 3 1/B6
2.1 Background 3 1/B6
2.2 Program Description 4 1/B7

3.0 APPARATUS 6 1/B9
3.1 Acoustic Wind Tunnel 6 1/B9
3.1.1 Adapter Section 8 1/B11
3.1.2 Instrumentation Section 9 1/B12
3.1.3 Exit Plane Traverse Instrumentation 10 1/B13
3.1.4 Acoustic Instrumentation 11 1/B14
3.2 Aerodynamic Wind Tunnel 12 1/C1
3.3 Nozzle Configurations 14 1/C3
3.3.1 Reference Convergent Nozzle 14 1/C3
3.3.2 Coannular Nozzles 15 1/C4
3.3.3 Ejector 17 1/C6

4.0 DATA 18 1/C7
4.1 Aerodynamic Data Reduction 20 1/C9
4.1.1 Thrust Coefficients and Flow Coefficients 26 1/D1
4.1.2 Surface Static Pressure 27 1/D2
4.1.3 Exit Profiles and Ejector Inlet Total Pressures 28 1/D3
4.2 Acoustic Data Reduction 31 1/D6
4.3 Comparison With Outdoor Results 46 1/E12
4.4 Coannular Noise Synthesis 51 1/F3

5.0 RESULTS AND DISCUSSION 53 1/F5
5.1 Discussion of Acoustic Results 53 1/F5
5.1.1 Acoustic Results 53 1/F5
5.1.2 Correlation of OASPL Noise Reduction with Relative Velocity Exponents 82 2/A8
5.1.3 Velocity Profile Correlation 109 2/C7
5.2 Application of Acoustic Results 113 2/C11
5.2.1 Comparison of Results with Synthesis 114 2/C12
5.2.2 Results Scaled to Full Size 120 2/D4
5.2.3 Application of Results to SCAR Noise Predictions 123 2/D7
5.3 Aerodynamic Performance 131 2/E1
5.3.1 Convergent Nozzle 131 2/E1
5.3.2 Coannular Nozzles 132 2/E2
5.3.3 Flow Coefficients 136 2/E6

6.0 SUMMARY OF RESULTS 140 2/E10
6.1 Acoustic Results 140 2/E10
6.2 Aerodynamic Performance Results 141 2/E11

TABLE OF CONTENTS (Cont'd.)

Section	Title	Page No.
REFERENCES		143 2/E13
APPENDIX A		145 2/F1
Part 1	Model Scale Overall Sound Power Level and Overall Sound Pressure Level Directivity on Theoretical Day	145 2/F1
Part 2	Relative Velocity and Convective Exponents	153 2/G3
APPENDIX B	Supersonic Screech Elimination	155 2/G5
APPENDIX C	Theoretical Day Atmospheric Absorption Correction	163 2/G13
APPENDIX D	Shear Layer Refraction Correction	170 3/A8
LIST OF ABBREVIATIONS		180 3/B4

Item 830-

NAS 1.26:3018

OCT 10 1978

COMPLETED
ORIGINAL

NASA Contractor Report 3018

Flight Effects on the Aerodynamic and Acoustic Characteristics of Inverted Profile Coannular Nozzles

Hilary Kozlowski and Allan B. Packman

CONTRACT NAS3-17866
AUGUST 1978

NASA

199

Item 830 H-14 NAS 1.26:3018

NASA Contractor Report 3018

Flight Effects on the Aerodynamic and Acoustic Characteristics of Inverted Profile Coannular Nozzles

Hilary Kozlowski and Allan B. Packman
United Technologies Corporation
East Hartford, Connecticut

Prepared for
Lewis Research Center
under Contract NAS3-17866

National Aeronautics
and Space Administration

Scientific and Technical
Information Office

1978

Blank

Page

FOREWORD

The authors wish to acknowledge Kam Wing Ng and Douglas P. Nelson, both of Pratt & Whitney Aircraft Group, and C. Y. Chen, United Technologies Research Center, for their significant contributions to the total program and to this report.

Blank

Page

LIST OF ILLUSTRATIONS

Figure	Title	Page
3.1-1	Schematic of Acoustic Research Tunnel, United Technologies Research Center	6
3.1-2	Schematic of Coannular Nozzle Installation in Acoustic Research Tunnel	7
3.1-3	Details of Adapter and Instrumentation Section Shown With a Coannular Nozzle and Ejector Mounted	8
3.1-4	Details of Instrumentation Section	9
3.1-5	Traverse System Deployed With Coannular Nozzle and Ejector	10
3.1-6	Details of Traverse Probe	11
3.2-1a	Overall Wind Tunnel Arrangement	12
3.2-1b	Test Section of Large Subsonic Wind Tunnel	12
3.2-1	Aerodynamic Test Facilities, United Technologies Research Center	12
3.2-2	Large Subsonic Wind Tunnel Three-Flow Exhaust Nozzle Force Balance	13
3.3-1	Details of Reference Convergent Nozzle	15
3.3-2	Details of 0.75 Area Ratio Coannular Nozzle	16
3.3-3	Details of 1.2 Area Ratio Coannular Nozzle	16
3.3-4	Details of 0.75 Area Ratio Coannular Nozzle With Ejector	17
4.1-1	Sample of the Aerodynamic Data Contained in the Comprehensive Data Report NASA CR-135189	29
4.2-1	Acoustic Data Reduction Procedure For Static Conditions	31
4.2-2	Acoustic Data Reduction Procedure For Flight Simulated Conditions	32
4.2-3	Schematic of Simulated Flight Data	35
4.2-4	Schematic of Shear Layer and Moving Medium Corrections	36

LIST OF ILLUSTRATIONS (Cont'd)

Figure	Title	Page
4.3-1A	Comparison of Wind Tunnel (UTRC) and Outdoor Stand (Ref. 1) Static Data for Convergent Nozzle Model Data at Subsonic Jet Velocity, Nozzle Exit Area, $A_T = 0.0025$ in^2 (3.89 in^2)	47
4.3-1B	Comparison of Wind Tunnel (UTRC) and Outdoor Stand (Ref. 1) Static Data for Convergent Nozzle Model Data at Supersonic Jet Velocity, Nozzle Exit Area $A_T = 0.0025$ in^2 (3.89 in^2)	48
4.3-2A	Comparison of Wind Tunnel (UTRC) and Outdoor Stand (Ref. 1) Static Data for 0.75 Area Ratio Coannular Nozzle Model Data at Subsonic Fan Jet Velocity Nozzle Exit Area, $A_T = 0.0025$ in^2 (3.89 in^2)	49
4.3-2B	Comparison of Wind Tunnel (UTRC) and Outdoor Stand (Ref. 1) Static Data for 0.75 Area Ratio Coannular Nozzle Model Data at Supersonic Jet Velocity Nozzle Exit Area, $A_T = 0.0025$ in^2 (3.89 in^2)	50
4.4-1	Coannular Jet Noise Synthesis Procedure	51
4.4-2	Comparison of Measured and Synthesized OASPL Directivity for 0.75 Area Ratio Coannular Nozzle Model	52
5.1.1-1	Effect of Relative Velocity on Spectra of Convergent Nozzle Model At Subsonic Jet Velocity	54
5.1.1-2	Effect of Relative Velocity on Directivity of Convergent Nozzle Model At Subsonic Jet Velocity	55
5.1.1-3	Effect of Relative Velocity on Spectra of Convergent Nozzle Model At Supersonic Jet Velocity	56
5.1.1-4	Effect of Relative Velocity on Directivity of Convergent Nozzle Model at Supersonic Jet Velocity	57
5.1.1-5	Comparison of Convergent Nozzle Model Data With Broadband Shock Noise Prediction From Reference 13, at Static Conditions	58
5.1.1-6	Effect of Relative Velocity on Spectra of 0.75 Area Ratio Coannular Nozzle Model at Subsonic Fan Jet Velocity	59
5.1.1-7	Effect of Relative Velocity on Directivity of 0.75 Area Ratio Coannular Nozzle Model at Subsonic Fan Jet Velocity	60

LIST OF ILLUSTRATIONS (Cont'd)

Figure	Title	Page
5.1.1-8	Effect of Relative Velocity on Spectra of 0.75 Area Ratio Coannular Nozzle Model at Supersonic Fan Jet Velocity	61
5.1.1-9	Effect of Relative Velocity on Directivity of 0.75 Area Ratio Coannular Nozzle Model at Supersonic Fan Jet Velocity	62
5.1.1-10	Effect of Ejector on SPL and PNL Spectra of 0.75 Area Ratio Coannular Nozzle Model at Static Condition	63
5.1.1-11	Effect of Relative Velocity on Spectra of 0.75 Area Ratio Coannular Nozzle Model With Ejector at Subsonic Fan Jet Velocity	66
5.1.1-12	Effect of Relative Velocity on Directivity of 0.75 Area Ratio Coannular Nozzle Model With Ejector at Subsonic Fan Jet Velocity	67
5.1.1-13	Effect of Relative Velocity on Spectra of 0.75 Area Ratio Coannular Nozzle Model With Ejector at Supersonic Fan Jet Velocity	68
5.1.1-14	Effect of Relative Velocity on Directivity of 0.75 Area Ratio Coannular Nozzle Model With Ejector at Supersonic Fan Jet Velocity	69
5.1.1-15	Effect of Ejector on Directivity of 0.75 Area Ratio Coannular Nozzle Model at Two Supersonic Fan Jet Velocities	70
5.1.1-16	Effect of Relative Velocity on Spectra of 1.2 Area Ratio Coannular Nozzle Model at Subsonic Fan Jet Velocity	72
5.1.1-17	Effect of Relative Velocity on Directivity of 1.2 Area Ratio Coannular Nozzle Model at Subsonic Fan Jet Velocity	73
5.1.1-18	Effect of Relative Velocity on Spectra of 1.2 Area Ratio Coannular Nozzle Model at Supersonic Fan Jet Velocity	74
5.1.1-19	Effect of Relative Velocity on Directivity of 1.2 Area Ratio Coannular Nozzle Model at Supersonic Fan Jet Velocity	75
5.1.1-20	Effect of Area Ratio on Spectra of Coannular Nozzle Model at Subsonic Fan Jet Velocity	75
5.1.1-21	Effect of Area Ratio on Directivity of Coannular Nozzle Model at Subsonic Fan Jet Velocity	76

LIST OF ILLUSTRATIONS (Cont'd)

Figure	Title	Page
5.1.1-22	Effect of Area Ratio on Spectra of Coannular Nozzle Model at Supersonic Fan Jet Velocity	76
5.1.1-23	Effect of Area Ratio on Directivity of Coannular Nozzle Model at Supersonic Fan Jet Velocity	77
5.1.1-24	Effect of Primary Stream on Directivity of 0.75 Area Ratio Coannular Nozzle Model at Subsonic Fan Jet Velocity	78
5.1.1-25	Effect of Primary on Spectra of 0.75 Area Ratio Coannular Nozzle Model at Subsonic Fan Jet Velocity	78
5.1.1-26	Effect of Primary Stream on Directivity of 0.75 Area Ratio Coannular Nozzle Model at Supersonic Fan Jet Velocity	79
5.1.1-27	Effect of Primary Stream on Spectra of 0.75 Area Ratio Coannular Nozzle Model At Supersonic Fan Jet Velocity	80
5.1.1-28	Spectral Comparison of Coannular, Annular and Convergent Nozzle Model at Supersonic Jet Velocity	80
5.1.1-29	Effect of Relative Velocity on Exit Velocity Profiles of 0.75 Area Ratio Coannular Nozzle Model	81
5.1.1-30	Effect of Relative Velocity on Exit Velocity Profiles with Annular Flow Only Nozzle Model	81
5.1.2-1	Correlation of Relative Velocity Effect on OASPL for Convergent Nozzle Model	86
5.1.2-2	Relative Velocity Exponents n_1 for Convergent Nozzle at Diffuser Nozzle Pressure Ratio and Temperatures	87
5.1.2-3	Convection Exponents n_6 for Convergent Nozzle at Different Nozzle Pressure Ratios	89
5.1.2-4	Correlations of Relative Velocity Effect on OASPL Using Fan Jet Velocity for 0.75 Area Ratio Coannular Nozzle	91
5.1.2-5	Correlations of Relative Velocity Effect on OASPL Using Mixed Jet Velocity of 0.75 Area Ratio Coannular Nozzle Model	92

LIST OF ILLUSTRATIONS (Cont'd)

Figure	Title	Page
5.1.2-6	Correlations of Relative Velocity Effect on OASPL Using Primary Jet Velocity of 0.75 Area Ratio Coannular Nozzle Model	93
5.1.2-7	Correlations of Relative Velocity Effect on OASPL Using Fan Jet Velocity of 0.75 Area Ratio Coannular Nozzle Model With Ejector	95
5.1.2-8	Correlations of Relative Velocity Effect on OASPL Using Mixed Jet Velocity of 0.75 Area Ratio Coannular Nozzle Model With Ejector	96
5.1.2-9	Correlations of Relative Velocity Effect on OASPL Using Primary Jet Velocity of 0.75 Area Ratio Coannular Nozzle Model With Ejector	97
5.1.2-10	Correlation of Relative Velocity Effect on OASPL Using Fan Jet Velocity of 1.2 Area Ratio Coannular Nozzle Model	98
5.1.2-11	Correlations of Relative Velocity Effect on OASPL Using Mixed Jet Velocity of 1.2 Area Ratio Coannular Nozzle Model	99
5.1.2-12	Correlations of Relative Velocity Effect on OASPL Using Primary Jet Velocity of 1.2 Area Ratio Coannular Nozzle Model	100
5.1.2-13	Relative Velocity Exponents as Function of Angular Position for 0.75 Area Ratio Coannular Nozzle; n_1 Based on Fan Jet Velocity	101
5.1.2-14	Relative Velocity Exponents as Function of Angular Position for 0.75 Area Ratio Coannular Nozzle With Ejector; n_1 Based on Fan Jet Velocity	101
5.1.2-15	Relative Velocity Exponents as Function of Angular Position for 1.2 Area Ratio Coannular Nozzle; n_1 Based on Fan Jet Velocity	102
5.1.2-16	Convection Exponents as Function of Angular Position for 0.75 Area Ratio Coannular Nozzle	103
5.1.2-17	Convection Exponents as Function of Angular Position for 0.75 Area Ratio Coannular Nozzle With Ejector	103
5.1.2-18	Convection Exponents as Function of Angular Position for 1.2 Area Ratio Coannular Nozzle	104

LIST OF ILLUSTRATIONS (Cont'd)

Figure	Title	Page
5.1.2-19	Effect of Nozzle Configuration on Relative Velocity Exponents at Subsonic Jet Velocity; n_1 Based on Fan Jet Velocity	105
5.1.2-20	Effect of Nozzle Configuration on Relative Velocity Exponents at Supersonic Jet Velocity; n_1 Based on Fan Jet Velocity	105
5.1.2-21	Effect of Jet Temperature on Relative Velocity Exponents for Convergent Nozzle at a Pressure Ratio of 1.8	107
5.1.2-22	Effect of Jet Temperature in Relative Velocity Exponents for Convergent Nozzle at a Pressure Ratio of 2.5	107
5.1.2-23	Effect of Jet Temperature on Relative Velocity Exponents for 0.75 Area Ratio Coannular Nozzle at a Fan Pressure Ratio of 1.8; n_1 Based on Fan Jet Velocity	108
5.1.2-24	Effect of Jet Temperature on Relative Velocity Exponents for 0.75 Area Ratio Coannular Nozzle at a Fan Pressure Ratio of 2.5; n_1 Based on Fan Jet Velocity	108
5.1.3-1	Velocity Profiles Measured Two Nozzle Diameters Downstream of Nozzle Exit for Various Nozzle Configurations at Static Condition	110
5.1.3-2	Velocity Profiles Measured Two Nozzle Diameters Downstream of Nozzle Exit for Various Nozzle Configurations at a Simulated Flight Speed of 104 mps (340 fps)	110
5.1.3-3	Correlation of OAPWL and Velocity Profile Parameter for Non-Ejector Nozzle Model Configurations	111
5.1.3-4	Correlation of OAPWL and Velocity Profile Parameter for 0.75 Area Ratio Coannular Nozzle Model With Ejector	111
5.1.3-5	Effect of Ejector on PNL Spectra of 0.75 Area Ratio Coannular Nozzle at Subsonic Fan Jet Velocity	112
5.1.3-6	Effect of Ejector on PNL Spectra of 0.75 Area Ratio Coannular Nozzle Model at Supersonic Fan Jet Velocity	113
5.2.1-1	Comparison of Measured and Synthesized OASPL Directivity for 0.75 Area Ratio Coannular Nozzle Model at Subsonic Fan Jet Velocity	115

LIST OF ILLUSTRATIONS (Cont'd)

Figure	Title	Page
5.2.1-2	Effect of Relative Velocity on OASPL Benefit of 0.75 Area Ratio Coannular Nozzle Model at Supersonic Fan Jet Velocity	116
5.2.1-3	Effect of Relative Velocity on OASPL Benefit of 0.75 Coannular Nozzle Model With Ejector at Subsonic Fan Jet Velocity	117
5.2.1-4	Effect of Relative Velocity on OASPL Benefit of 0.75 Coannular Nozzle Model With Ejector at Supersonic Fan Jet Velocity	118
5.2.1-5	Effect of Relative Velocity on OASPL Benefit of 1.2 Area Ratio Nozzle Model at Subsonic Fan Jet Velocity	119
5.2.1-6	Effect of Relative Velocity on OASPL Benefit of 1.2 Area Ratio Nozzle Model at Supersonic Fan Jet Velocity	119
5.2.2-1	Comparison of Measured and Synthesized PNL Directivity for 0.75 Area Ratio Coannular Nozzle Scaled to 1.27 m (50 in) Equivalent Diameter at Subsonic Fan Jet Velocity	121
5.2.2-2	Effect of Relative Velocity on PNL Benefit of 0.75 Area Ratio Coannular Nozzle Scaled to 1.27 m (50 in) Equivalent Diameter at Subsonic Fan Jet Velocity	121
5.2.2-3	Comparison of Measured and Synthesized PNL Directivity For 0.75 Area Ratio Coannular Nozzle Scaled to 1.27 m (50 in) Equivalent Diameter at Supersonic Fan Jet Velocity	122
5.2.2-4	Effect of Relative Velocity on PNL Benefit of 0.75 Area Ratio Coannular Nozzle Scaled to 1.27 m (50 in) Equivalent Diameter at Supersonic Fan Jet Velocity	122
5.2.3-1	Relative Velocity Exponents as Function of Angular Position for Various Nozzle Configurations	124
5.2.3-2	In-Flight Noise Prediction Procedure Based on ΔOASPL Relative Velocity Exponent Method	125
5.2.3-3	Model Based Separation of Jet Noise Components for ΔSPL Relative Velocity Exponents Method	126
5.2.3-4	In-Flight Noise Prediction Procedure Based on ΔSPL Relative Velocity Exponents Method	127

LIST OF ILLUSTRATIONS (Cont'd)

Figure	Title	Page
5.2.3-5	In-Flight Noise Spectra Prediction Based on ΔSPL Relative Velocity Exponent Method for VSCE-502 at Fuel to Air Ratio of 0.005	129
5.2.3-6	Comparison of In-Flight Noise Prediction Methods for VSCE-502 at Fuel to Air Ratio of 0.005	129
5.2.3-7	Comparison of In-Flight Noise Prediction Method for VSCE-502 at Fuel to Air Ratio of 0.030	130
5.2.3-8	Peak PNL Predictions Based on ΔSPL Relative Velocity Exponents Method for VSCE-502 and LBE-430 Engines	130
5.3-1	Aerodynamic Performance of Reference Convergent Nozzle	132
5.3-2	Aerodynamic Performance of 0.75 Area Ratio Coannular Nozzle at a Primary Pressure Ratio of 1.53	132
5.3-3	Aerodynamic Performance of 0.75 Area Ratio Coannular Nozzle With Ejector at Primary Pressure Ratio of 1.53	133
5.3-4	Aerodynamic Performance of 1.2 Area Ratio Coannular Nozzle at a Primary Pressure Ratio of 1.53	134
5.3-5	Internal Performance Losses for Reference Convergent Nozzle and Coannular Nozzles	135
5.3-6	Comparison of Measured and Adjusted Aerodynamic Performance of 0.75 Area Ratio Coannular Nozzle at a Primary Pressure Ratio of 1.53	135
5.3-7	Correlation of Aerodynamic Performance and External Velocity for 0.75 Area Ratio Coannular Nozzle	135
5.3-8	Correlation of Aerodynamic Performance and Nozzle Area Ratio of Coannular Nozzles	136
5.3-9	Flow Coefficients for Reference Convergent Nozzle	136
5.3-10	Flow Coefficients for 0.75 Area Ratio Coannular Nozzle at a Primary Pressure Ratio of 1.53	137
5.3-11	Flow Coefficients for 0.75 Area Ratio Coannular Nozzle With Ejector at a Primary Pressure Ratio of 1.53	138

LIST OF ILLUSTRATIONS (Cont'd)

Figure	Title	Page
5.3-12	Typical Static Pressure Distribution for 0.75 Area Ratio Coannular Nozzle With Ejector	138
5.3-13	Flow Coefficients for 1.2 Area Ratio Coannular Nozzle at a Primary Pressure Ratio of 1.53	139

LIST OF TABLES

Table	Title	Page
3-I	Pertinent Geometric Variables of Nozzle Configurations	14
4-I	Acoustic Test Matrix	21
4-II	Aerodynamic Performance Test Matrix	25
4-III	Atmospheric Absorption Estimates for a Typical Data Point	34
4-IV	Shear Layer Correction	37
4-V	Angle Correction for Moving Medium	37
4-VI	Sample Simulated Flight Data	38
4-VII	Sample Simulated Flight Data	39
4-VIII	Sample Simulated Flight Data	40
4-IX	Sample Model Scale Acoustic Data	41
4-X	Sample Full Scale Engine Acoustic Data	42
5.2-I	VSCE-502 Operating Line	124

1.0 SUMMARY

The effect of simulated flight speed on the acoustic and aerodynamic characteristics of coannular nozzles suitable for advanced supersonic engines was established in this program through wind tunnel experiments. Scale models representing exhaust systems without mechanical jet noise suppressors were tested over a range of exhaust conditions, and at aircraft flight speeds up to 130 mps.

The test configurations consisted of a 0.75 area ratio coannular nozzle with and without an ejector, a 1.2 area ratio coannular nozzle and a reference convergent nozzle. The total jet area of all the models was equivalent to a 0.057m (2.23 in) diameter convergent nozzle, or approximately one twenty-second (1/22) of the anticipated full size system.

The jet noise levels of the coannular nozzles were reduced due to the simulated flight speed by approximately the same amount as has been found for single stream nozzles. Thus, the coannular noise benefits found during the earlier static test program were essentially retained in the simulated flight environment. The noise reduction due to the flight effect was a function of the nozzle stream velocities and the simulated flight speed.

At supersonic jet velocities ($M_j > 1.0$), broadband shock noise was present in the noise spectra, especially at the side and forward angles. For both the coannular and single stream reference nozzles, the shock noise was essentially unchanged due to flight at the side angles, and slightly increased at the forward angles.

The impact of fan to primary nozzle area ratio and the presence of an ejector on flight effects were investigated and found to be relatively unimportant. The overall sound pressure level noise reductions were correlated in terms of relative velocity exponents. An additional correlation of the data showed that the noise was related to the measured velocity profile existing in the jet plume downstream of the nozzle.

The impact of flight speed on the individual components of coannular jet noise was ascertained. The noise components considered independently were: a) pre-merged mixing noise generated by the annular fan stream close to the nozzle exit prior to merging with the primary exhaust, b) post-merged noise generated by the merged jet arising from the fully mixed fan and primary streams, and c) the broadband shock noise generated by the interaction of turbulence and shock waves in the annular fan exhaust under supercritical operation (i.e., $Mi > 1.0$). The prediction of total jet noise for actual supersonic cruise vehicle cycles can be reconstructed by adding the contributions of the individual components.

The force data indicated that the efficiency of the exhaust system observed statically, decayed only slightly (< 1%) at take-off airspeed. Addition of the ejector increased this performance loss somewhat, indicating the need for refinement of the ejector.

Acoustic measurements were taken at 230 test conditions with the external velocity ranging from 0 to 130 mps. The fan stream pressure ratios were varied from 1.3 to 3.2, while the fan stream temperature ranged from 394°K (250° F) to 700°K (800°F). The primary stream conditions were maintained constant. The primary pressure ratio was 1.53 and the primary temperature was 394°K (250°F).

The force data were taken in a separate facility using an unheated air supply. A total of 80 data points was obtained. The external velocity range was the same as covered in the acoustic tests, as were the pressure ratios of each stream.

All the detail acoustic and performance data taken are presented in the companion Comprehensive Data Report NASA CR-135189.

2.0 INTRODUCTION

2.1 BACKGROUND

Prior to this program, extensive analytical and experimental propulsion system studies, conducted as part of the NASA sponsored Supersonic Cruise Airplane Research (SCAR) effort, identified the Variable Stream Control Engine (VSCE) as a promising cycle in terms of both system performance and low noise generation. The VSCE cycle can be matched to provide a high velocity duct (fan) stream surrounding a low velocity core (primary) stream resulting in an exit velocity profile which has inherent jet noise benefits without the use of mechanical suppressors.

The results (Ref. 1, 2, 3) of noise experiments conducted during Task IV of NASA Contract NAS 3-17866 showed that the jet noise produced by a coannular nozzle exhaust having an inverted velocity profile" (i.e., $V_f > V_p$), was significantly less than the predictions based on existing coaxial jet prediction methods. The reduced noise of this type of coannular exhaust has been shown to be related to the enhanced aerodynamic mixing and rapid decay of the peak velocity in the jet due to the annular nature of the fan exhaust and its ability to mix with the low velocity primary stream in addition to mixing with the ambient air. The impact of these results on a supersonic cruise aircraft are significant in terms of cycle definition and mission economics.

The noise reductions of the coannular nozzle exhaust described above were measured in a static environment. Complete jet noise characteristics, however, must be established for the aircraft in the take-off mode, having a forward speed of approximately 0.3 Mach number. The effect of forward speed on jet noise has been investigated in a number of wind tunnel and flyover experiments. These experiments, although restricted to conventional turbojet and turbofan exhausts, have resulted in some confusion as to the effects of flight on jet noise. Independent wind tunnel simulations of the forward speed effect on jet noise, conducted by Packman, Ng and Paterson (Ref. 4) and by Cocking and Bryce (Ref. 5) have indicated that for subsonic single jet exhausts, the jet noise is reduced in flight at all angles by an amount that can be expressed as:

$$\Delta OASPL = 10 \log (V_j/V_{rel})^n$$

where the exponent n is a function of angle and absolute jet velocity, V_j and V_{rel} are the jet absolute and relative velocity, respectively. Flyover measurements conducted by The Boeing Company (Ref. 6) and the Douglas Aircraft Company (Ref. 7) have shown good agreement with the wind tunnel results, indicating that the simulation of in-flight effects by an acoustic wind tunnel is a valid technique. Prior to the current program, there had been no experiments to define the effects of flight on the jet noise produced by a coannular jet having an inverted velocity profile (IVP). Because of the significant difference in the static noise characteristics of the IVP coannular jet relative to conventional jet exhausts, it would have been speculative to assume that the in-flight effects would be similar. Thus, the current investigation was conducted to determine the effect of flight velocity on the noise of IVP coannular jets, and in particular, to determine if the noise reductions relative to the predictions for the IVP coannular jet observed under static conditions would be retained in flight.

2.2 PROGRAM DESCRIPTION

The major objectives of this program were to determine the effects of flight on the noise and aerodynamic performance of coannular nozzle exhaust systems over a large range of operating conditions, in particular at conditions where the fan-to-primary velocity ratio was greater than one.

A total of four (4) model nozzle configurations was designed and fabricated in a scale approximately 1/22 the size of a full size VSCE exhaust system. These models had essentially the same aerodynamic lines as the model nozzles tested in the earlier static test program (Ref. 1). The nozzle exit lip geometry of each configuration was modified to eliminate shock screech discrete tones in order to more realistically simulate the jet noise of a full scale engine. The model configurations were:

1) Reference convergent nozzle
2) 0.75 area ratio (fan-to-primary area ratio) coannular nozzle
3) 0.75 area ratio coannular nozzle with hardwall ejector
4) 1.2 area ratio coannular nozzle

The models were tested under static and simulated take-off conditions in both acoustic and aerodynamic test facilities located at the United Technologies Research Center in East Hartford, Connecticut.

Noise tests were conducted in the Acoustics Research Tunnel, a low turbulence open jet wind tunnel where noise measurements are taken in a large anechoic chamber with microphones situated outside the tunnel flow. One-third octave band sound pressure levels and overall sound pressure levels were obtained.

A total of 230 test points was run on the four nozzle configurations. For the coannular nozzles, the pressure ratio in the fan stream was varied from 1.3 to 3.2 while primary stream pressure ratio was held at a constant value of 1.53. Fan stream temperature was varied from 394°K to 700°K (250° to 800°F) while primary stream temperature was 394°K (250°F) for all test points. These temperatures were the maximum obtainable in the test facility. The fan-to-primary velocity ratio resulting from these operating conditions varied from 0.8 to 2.1. Cycles currently envisioned for use in the SCAR program have primary stream temperatures up to 978°K (1300°F) and velocities up to 608 mps (2000 fps), and have fan stream temperatures up to 1866°K (1900°F) and velocities up to 881 mps (2900 fps). Thus, the practical range of velocity ratio for supersonic cruise aircraft propulsion cycles was covered, although the individual stream conditions were not attained.

The acoustic data obtained from the test, however, are extremely valuable in assessing the effects of forward flight on the jet noise of supersonic cruise aircraft propulsion cycles. In particular, the impact of flight speeds on the individual components of coannular nozzle noise comprising the total exhaust noise was ascertained. The prediction of noise for actual supersonic cruise vehicle cycles can be reconstructed by adding the noise of the individual components.

The tunnel speed was varied from zero to 129.5 mps (425 fps), simulating the full range of speeds that would be encountered by a supersonic cruise airplane during take-off and landing operations. Far-field jet noise signals were measured every 10 degrees from 70° to 150° relative to the upstream jet axis. The effects of acoustic signal refraction caused by the tunnel shear layer were analytically corrected by the method of Amiet (Ref. 8) allowing the noise results to be presented in a frame of reference corresponding to airplane flyover measurements corrected to the angle of noise emission.

Nozzle charging station pressure, temperature and weight flow for each stream were measured for all test points. Exit pressure and temperature profiles as well as ejector inlet and surface pressures were measured for selected test points.

The aerodynamic performance tests were conducted in the Large Subsonic Wind Tunnel at the United Technologies Research Center. The same nozzle models used in the acoustic tests were evaluated over the same range of pressure ratios and forward speeds establishing the thrust and flow coefficients of the exhaust systems. Since the facility employs an unheated air supply, the stream temperatures were constant. All data obtained during the testing are contained in the Comprehensive Data Report (Ref. 9), while the major results are contained in this report.

3.0 APPARATUS

The experimental apparatus used in this program is described herein. This includes the acoustic test facility, the force measurement facility, supplementary hardware and instrumentation, as well as the model nozzle configurations evaluated in the program.

3.1 ACOUSTIC WIND TUNNEL

This facility, shown in Figure 3.1-1, is a controlled turbulence level, open circuit, open jet wind tunnel specifically designed for noise research. It is located at the United Technologies Research Center. The open jet test section in this facility is enclosed in a 4.88 m (16 ft) high by 5.49 m (18 ft) long by 6.71 m (22 ft) wide anechoic chamber lined with 0.3 m (1 ft) acoustic wedges. Use of turbulence supression screens in conjunction with a contraction ratio of 11.5 at the contraction outlet produces both a low turbulence level and a spatial mean velocity distribution in the test section measured to be uniform within 0.25 percent. Also, to obtain a low turbulence level and high signal-to-noise ratio, the tunnel is operated in a suction mode as opposed to the blowing mode of operation of conventional free jet facilities to simulate a flight environment. The test chamber is anechoic at all frequencies above 250 Hz to eliminate the sound reflection problems that are associated with facilities that require outdoor measurements (and their accompanying ground reflection problems) or indoor measurements in a hardwall tunnel.

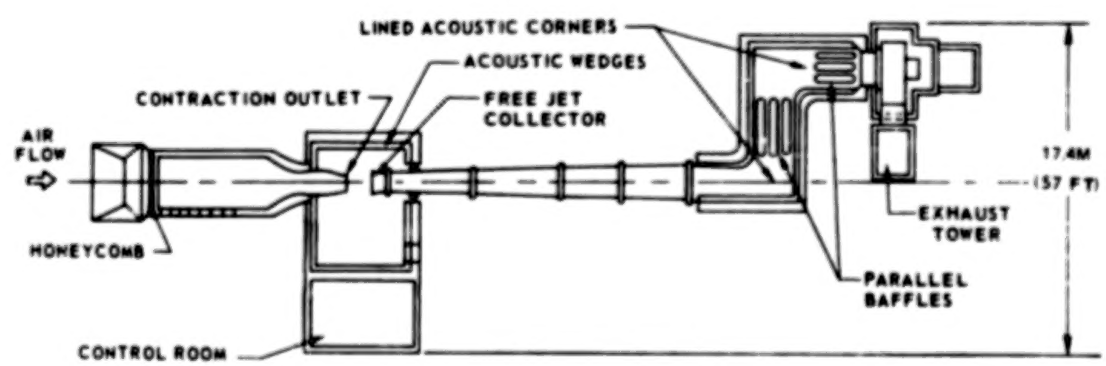

TOP VIEW

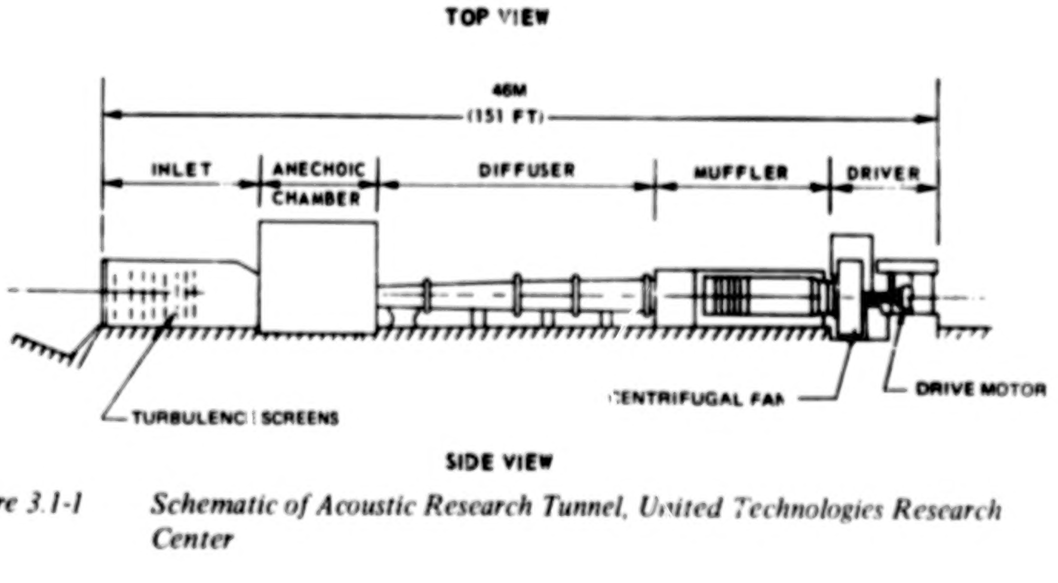

SIDE VIEW

Figure 3.1-1 *Schematic of Acoustic Research Tunnel, United Technologies Research Center*

A two stream air supply for the testing of coannular nozzles is located on the tunnel centerline as illustrated in Figure 3.1-2. The airflow to the test facility is provided at 2.8 X 10^6 N/m^2 (400 psia) and 394°K (250°F) in two separate streams. Throttling valves and venturies are installed in each line to provide individual flow control and flow measurement of the fan and primary streams. An electrical heater is located in the fan stream air line to provide temperatures up to 700°K (800°F) at the model. The streams are muffled to attenuate air-supply noise generated by the throttling valves. The muffled flows then feed into the transition section which produces a coannular flow arrangement, which is then continued into the tunnel inlet chamber. An adapter section location in the tunnel contraction provides attachment of the nozzle models to the coannular ducting.

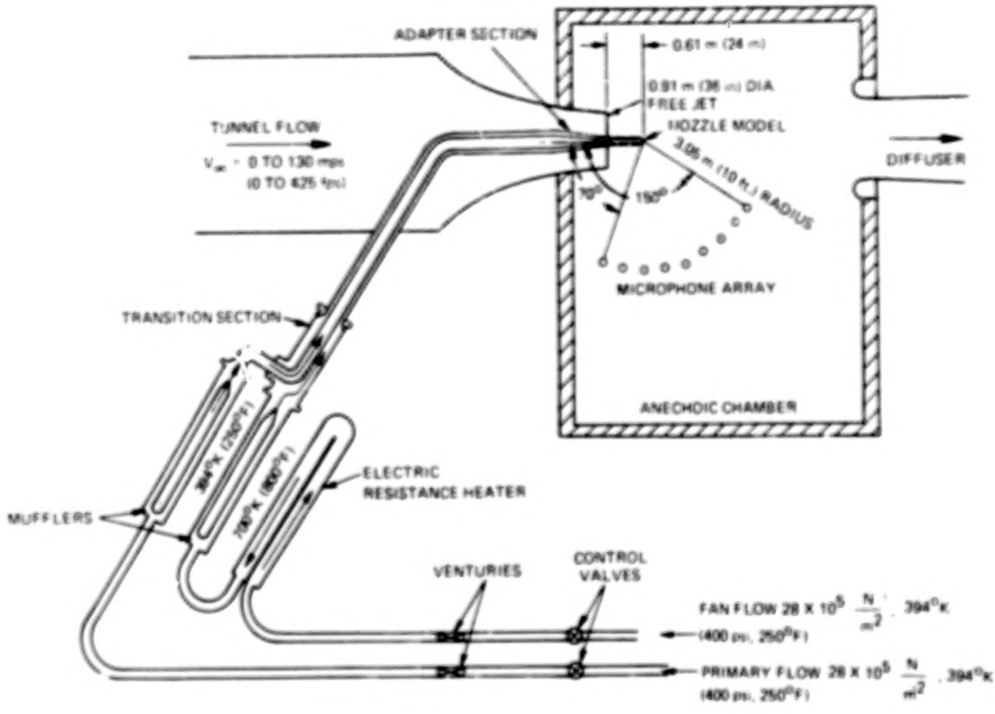

Figure 3.1-2 *Schematic of Coannular Nozzle Installation in Acoustic Research Tunnel*

The transition section is designed to direct the two separate streams into a coannular arrangement such that the heated flow is directed through the annular fan passage and the lower temperature flow is directed through the primary duct as required for testing the variable stream control nozzle models. To allow testing of the convergent reference nozzle at elevated temperatures, the elbow inside the transition section is removed, allowing the heated fan stream supply to mix with the colder primary air supply in order to provide a uniform air supply to the model.

The model exhaust plane is located 0.61 m (24 in) downstream of the 0.91 m (36 in) diameter free jet exit as indicated in the sketch. The large ratio of test section area to nozzle area (262) precluded flow interference between the tunnel turbulent shear layer and jet exhaust for the significant noise producing region of the jet. An array of microphones is positioned at a 3.05 m (10 ft) radial distance from the nozzle exit, at the centerline height of the test nozzles.

The tunnel flow discharges through a diffuser that has an entrance diameter of 1.07 m (42 inches). Downstream of the diffuser an absorptive and reactive Z-shaped section consisting of two sections of treated baffles and two 90° lined bends provides acoustic muffling of the tunnel drive fan. This centrifugal fan exhausts to the atmosphere through an exhaust tower.

The components of the testing assembly are shown in detail in Figure 3.1-3 and described in the following sections. The relative position of the various components are indicated by station numbers which equal the distance (in inches) from the reference mounting flange (STA 0).

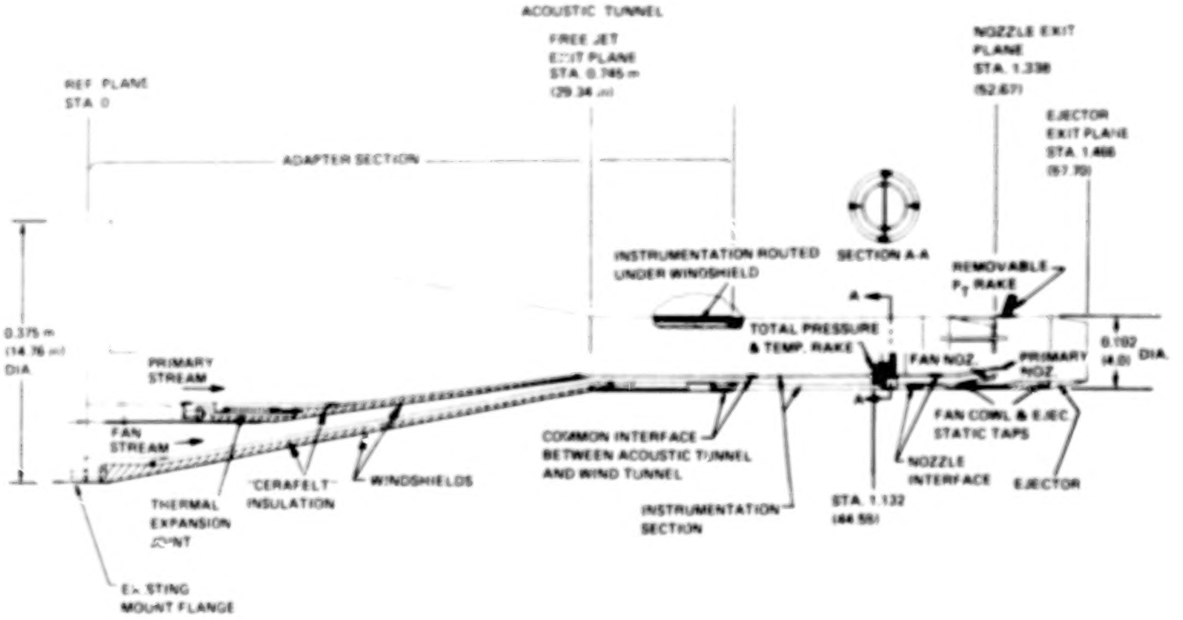

Figure 3.1-3 *Details of Adapter and Instrumentation Section Shown With a Coannular Nozzle and Ejector Mounted*

3.1.1 Adapter Section

The adapter section mates the instrumentation section and nozzle model assembly to the acoustic tunnel coannular air supply piping flange. It consists of a set of conical approach ducts covered by windshields to eliminate excessive airflow turbulence. The internal space between the windshield and conical approach ducts is insulated with "Cerafelt" to minimize heat transfer between the fan flow and primary flow, and between the fan flow and tunnel airflow. The pressure and thermocouple lines from the instrumentation section and nozzle are routed under the outer windshield to avoid disturbing the external flow.

An expansion joint is provided in the primary section to accommodate the thermal growth of the hot fan pipe relative to the cooler primary section. The joint consist of a high temperature graphite yarn winding that is wrapped at both ends by carbon rings. A threaded gland nut exerts pressure on the carbon rings pressing the self lubricating yarn against the inner and outer walls, providing a sliding seal. The adapter section is fabricated from cold rolled low carbon steel with welded construction.

3.1.2 Instrumentation Section

The instrumentation section serves a dual purpose. In addition to containing the pressure and temperature instrumentation necessary to define the flow properties of both nozzle streams, it serves the purpose of maintaining the concentricity of the coannular nozzles.

The major portion of the instrumentation section is shown in Figure 3.1-4. A pair of airfoil shaped struts, containing the pressure and temperature instrumentation are located at 90° to each other. The vertical full span strut contains the primary stream total pressure and temperature rakes, and the fan stream total pressure rakes. The vertical strut also anchors the inner and outer pipes together. The fan stream total temperature rakes are located in the horizontal part span struts. Electron beam welding was employed in assembling the struted section to avoid damage to the instrumentation and minimize warpage.

PRESSURE PROBE RADIUS ~ "R"

	PROBE NO.	"R" ~ m	"R" ~ (in)
PRIMARY RAKE	P_1 P_2 P_3 P_4 P_5 P_6 P_7	0 0.014 0.018 0.021 0.024 0.026 0.029	0 (0.540) (0.700) (0.830) (0.940) (1.040) (1.130)
FAN RAKES	$P_{8,12}$ $P_{9,13}$ $P_{10,14}$ $P_{11,15}$	0.034 0.037 0.040 0.042	(1.350) (1.460) (1.567) (1.662)

TEMPERATURE PROBE RADIUS ~ "R"

	PROBE NO.	"R" ~ m	"R" ~ (in)
PRIMARY RAKE	T_1 T_2 T_3 T_4 T_5 T_6	0.014 0.018 0.021 0.024 0.026 0.029	(0.540) (0.700) (0.830) (0.940) (1.040) (1.140)
FAN RAKES	$T_{7,11}$ T_8 T_9 $T_{10,12}$	0.034 0.037 0.040 0.042	(1.350) (1.460) (1.567) (1.662)

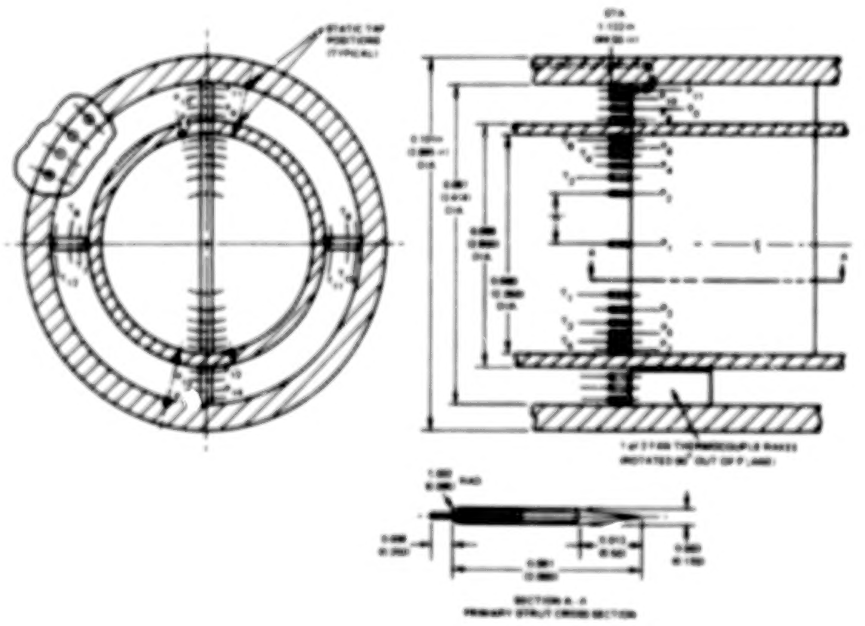

Figure 3.1-4 Details of Instrumentation Section

The primary stream instrumentation consists of seven total pressure (P_t) probes, six total temperature (T_t) probes and two wall static pressure (P_s) taps. The fan stream instrumentation consists of eight total pressure probes, six total temperature probes and four wall static pressure taps. The total pressure probes are fabricated from 0.0012 m (0.049 in) stainless steel tubing. The total temperature probes are fabricated from chromel-alumel thermocouple wire sheathed in 0.0012 m (0.049 in) tubing. All of the instrumentation leads exit from the ends of the struts and are routed within the outer wall to avoid any disturbance of the external air flow. Provisions are also made in the instrumentation section to route the model instrumentation lines through the outer wall coming out under the windshield upstream. The instrumentation section was fabricated from AMS 5613 stainless steel. The adapter section/instrumentation section interface and the model interface joints are sealed with high temperature silicone "O" rings to avoid leakage.

3.1.3 Exit Plane Traverse Instrumentation

The mechanism used to traverse the exhaust plume of the test nozzles, shown in Figure 3.1-5, consists of a wedge type probe mounted on a remotely controlled linear actuator. The purpose of the traverse is to acquire static and total pressure and total temperature data required to establish the velocity and temperature distribution along a radial line in the flow field. The traverse was conducted at station 57.90, which is slightly downstream of the ejector exit plane. The probe and supporting hardware were removed from the tunnel when acoustic data was taken to eliminate the possibility of any extraneous noise.

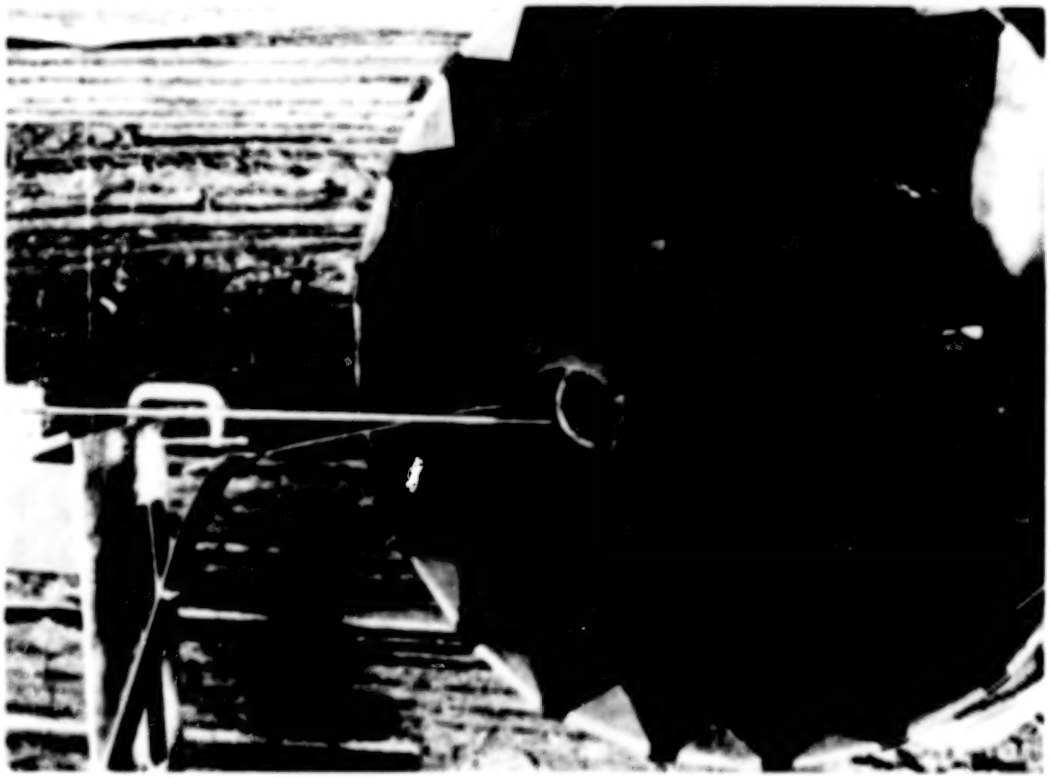

Figure 3.1.5 Traverse System Deployed With Coannular Nozzle and Ejector

The details of the probe are shown in Figure 3.1-6. The static pressures were measured with two orifices (a and b); one on each side of the 20° wedge. The total pressure was measured at point c, at the front edge of the wedge. The total temperature was determined by means of a thermocouple that is exposed to flow through ports at the rear of the wedge, at points d and e. The flow exits at the base of the wedge through port f, which controls the flow past the thermocouple head. This port was sized to establish the best balance between conductive and convective heat transfer. The probe was calibrated for pressure and temperature measurement over the range of flow parameters in the ejector/nozzle flow.

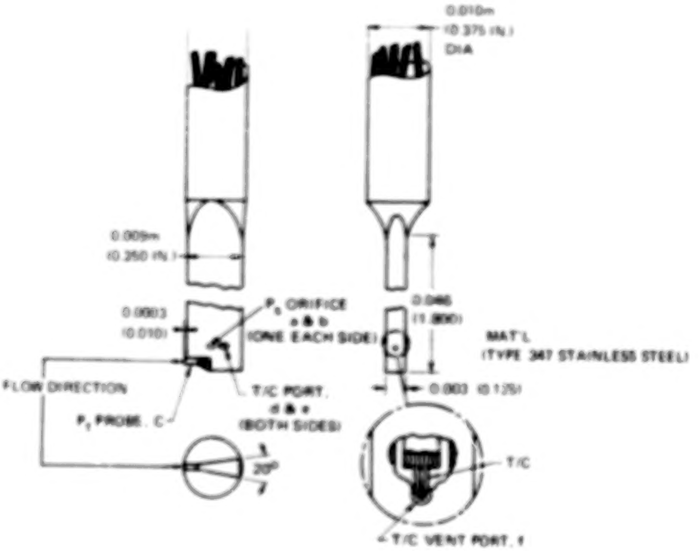

Figure 3.1-6 Details of Traverse Probe

3.1.4 Accustic Instrumentation

Laboratory calibrated Bruell and Kjaer #4135 0.006 m (1/4 in.) microphones were employed without protective grids or wind screens. They were positioned at normal incidence in a polar array containing nine microphones at 10 degree increments from 70 to 150 degree relative to the upstream jet axis at a distance of 3.05 m (10 ft) from the exit of the nozzle. Microphone signals were recorded on magnetic tape by a Honeywell System 96 wide band Group 2 recorder operating at 0.762 mps (30 ips). The dynamic range of this recorder was 32 dB. The frequency response of the microphones and tape system were flat up to a frequency of 80K Hz. On-line data were acquired during testing using a Spectral Dynamic SD-310C-302C-305A third-octave analyzer to assist in the conduct of the test program.

In order to apply analytical atmospheric air attenuation corrections to the measured data, temperature and relative humidity inside the anechoic chamber were measured for each test point. The temperature was measured by a thermocouple located at the 130° microphone support and the relative humidity was recorded by a Texas Electronics relative humidity measuring system located approximately 3.66 m (12 ft.) from the nozzle centerline on the nozzle exit plane.

3.2 AERODYNAMIC WIND TUNNEL

The nozzle aerodynamic performance tests were conducted in the United Technologies Research Center Large Subsonic Wind Tunnel (LSWT). The wind tunnel, depicted in Figure 3.2-1a, is a single-return, closed throat facility driven by a 6710 kw (9000 hp) synchronous motor. An eight foot octagonal test section was employed for this program. Tunnel stagnation pressure is equal to atmospheric pressure, and stagnation temperature of the airstream is held in the range of 289°K - 339°K (60 - 150°F) by means of air exchanger valves.

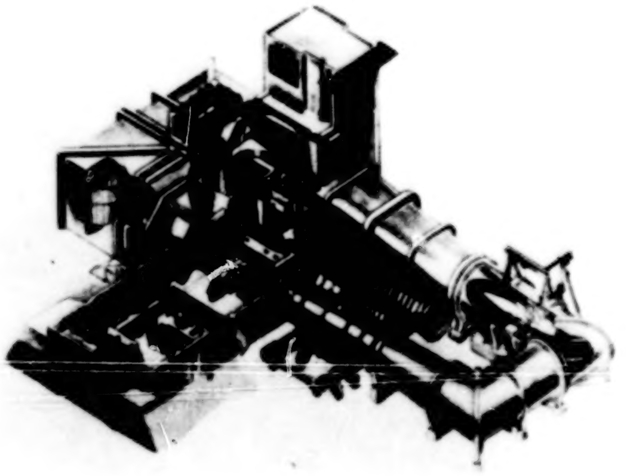

Figure 3.2-1a Overall Wind Tunnel Arrangement

An exhaust nozzle thrust balance is mounted within the test section and supports the shafting and model assembly as shown in Figure 3.2-1b. The balance and support shafting as illustrated in Figure 3.2.2 supplies fan and primary air to the test model through two separate flow metering systems within the balance. Bellmouths designed according to the ASME Power Test Codes provide flow measurement. Ball valves installed downstream of the meters provide flow control. The balance measures nozzle net thrust by applying a controlled pressure to a known base area on the flexured assembly. The applied force is matched to the nozzle net thrust by maintaining a null position of the flexure assembly relative to the housing.

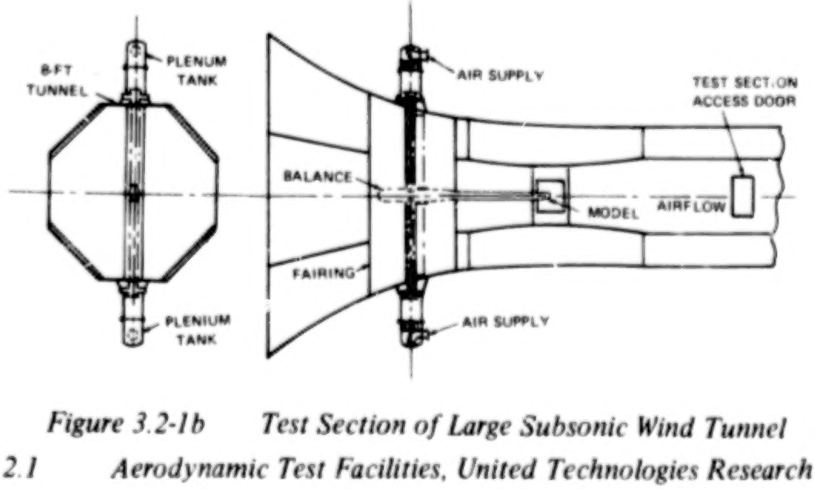

Figure 3.2-1b Test Section of Large Subsonic Wind Tunnel

Figure 3.2.1 Aerodynamic Test Facilities, United Technologies Research Center

To test the nozzle models, the instrumentation section described in Section 3.1.2 was connected directly to the support shafting illustrated in Figure 3.2-2. Therefore the flow properties of each stream for both the acoustic and the aerodynamic tests were obtained with the same instrumentation array. The same test models were also evaluated in each portion of the test program.

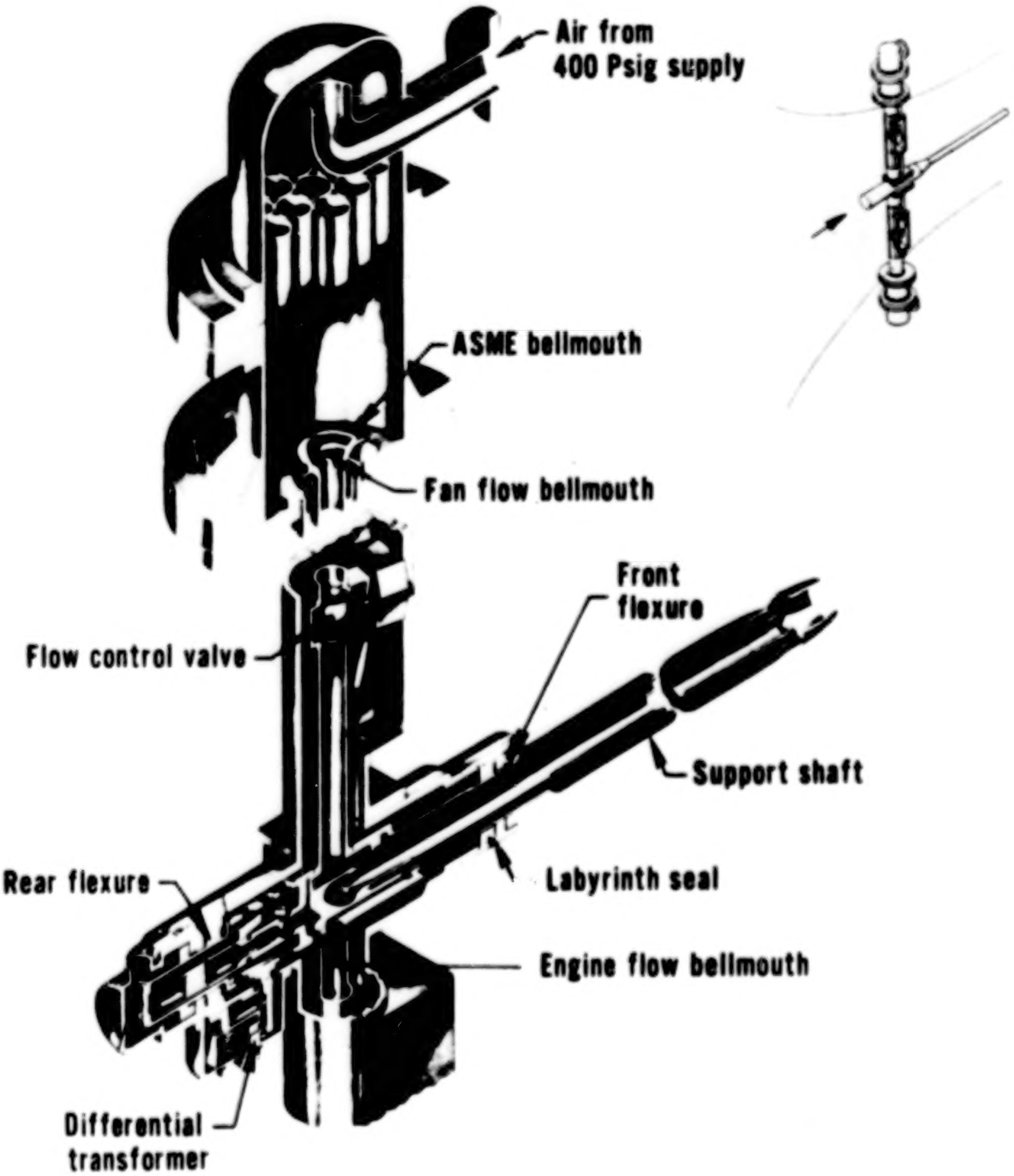

Figure 3.2-2 Large Subsonic Wind Tunnel Three-Flow Exhaust Nozzle Force Balance

3.3 NOZZLE CONFIGURATIONS

Three basic nozzle models, a reference convergent and two coannular configurations, were evaluated in this program. One of the coannular models was tested with an ejector. The pertinent geometric variables of the basic configurations are presented in Table 3-I. The variables include fan stream exit area (A_f), primary stream exit area (A_p), total exit area (A_t), equivalent diameter (D_{eq}) based on total exit area, and the diameter encompassing the fan and primary nozzle assembly (D_{per}), which represents the outer perimeter of the total basic nozzle unit.

TABLE 3-I

PERTINENT GEOMETRIC VARIABLES OF NOZZLE CONFIGURATIONS

	Configuration	A_f m^2 (in^2)	A_p m^2 (in^2)	A_f/A_p	A_t m^2 (in^2)	D_{eq} m (in)	D_{per} m (in)
1.	Reference Convergent Nozzle	–	–	–	.00251 (3.89)	.0566 (2.23)	.0566 (2.23)
2.	Coannular Nozzle	.00108 (1.67)	.00143 (2.22)	0.75	.00251 (3.89)	.0566 (2.23)	.0599 (2.36)
3.	Coannular Nozzle with Ejector	.00108 (1.67)	.00143 (2.22)	0.75	.00251 (3.89)	.0566 (2.23)	.0599 (2.36)
4.	Coannular Nozzle	.00137 (2.12)	.00114 (1.77)	1.2	.00251 (3.89)	.0566 (2.23)	.0599 (2.36)

Detailed descriptions of all the test models are presented in the following sections.

3.3.1 Reference Convergent Nozzle

The single stream reference nozzle is a low angle conical convergent nozzle, shown in Figure 3.3-1. In order to adapt this nozzle to the coannular ducting of the test rig, a primary duct fairing was designed to merge the two streams. The fairing is tapered, maintaining a constant fan-to-primary area ratio to provide uniform nozzle exit flow. To monitor external flow effects, six static taps are located on the nozzle boattail as indicated in the sketch. To eliminate supersonic nozzle screech, eight tabs were placed symetrically around the nozzle lip. The tabs are illustrated in Figure 3.3-1.

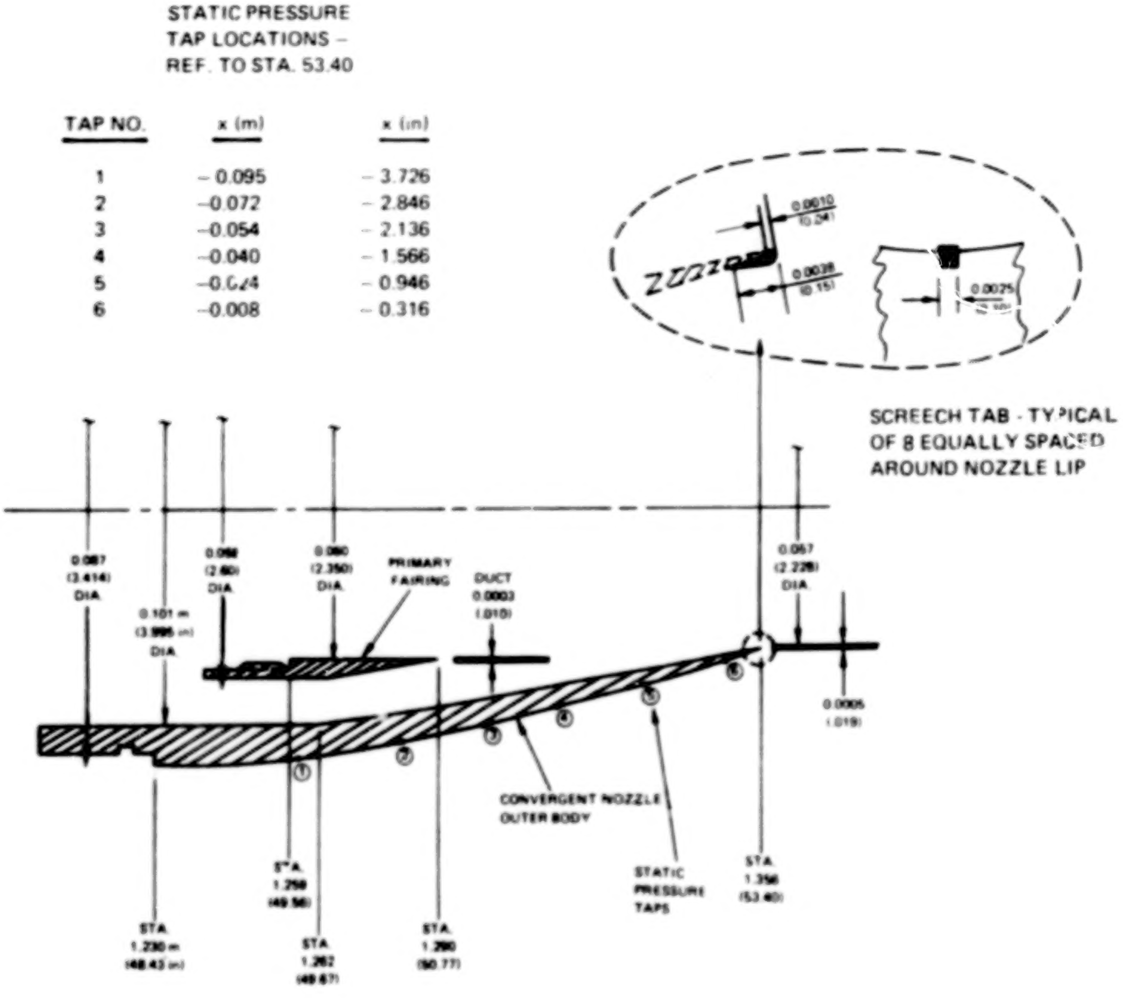

STATIC PRESSURE TAP LOCATIONS – REF. TO STA. 53.40

TAP NO.	x (m)	x (in)
1	– 0.095	– 3.726
2	–0.072	– 2.846
3	–0.054	– 2.136
4	–0.040	– 1.566
5	–0.024	– 0.946
6	–0.008	– 0.316

SCREECH TAB - TYPICAL OF 8 EQUALLY SPACED AROUND NOZZLE LIP

Figure 3.3-1 Details of Reference Convergent Nozzle

3.3.2 Coannular Nozzles

The two coannular nozzle models are configured from a common fan cowl and two interchangeable primary nozzles. The first model with a fan-to-primary area ratio of 0.75 is illustrated in Figure 3.3-2, and the second model with a 1.2 fan-to-primary area ratio is shown in Figure 3.3-3. The primary nozzles are convergent-divergent with an exit to throat area ratio of 1.1. The geometry of the fan stream nozzle and the axial spacing between the fan and primary nozzle exit planes are representative of the coannular nozzles being considered in the AST/SCAR design studies. To monitor external flow effects, six static pressure taps are located on the fan cowl as indicated in the sketch. The tabs for all the coannular models are located relative to station 52.54 which is the position of the leading edge of the ejector, whether an ejector is used or not. This allows convenient comparison of axial pressure distributions. Eight screech suppression tabs were also placed on the fan nozzle lip. The detail of the tabs used in both coannular nozzles are illustrated in Figure 3.3-3.

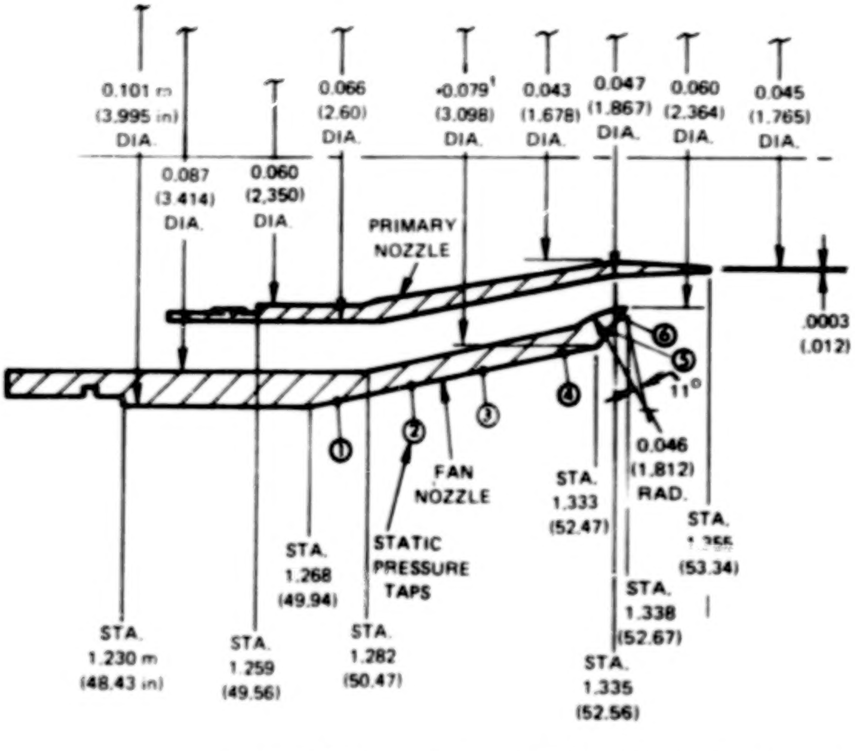

STATIC PRESSURE TAP LOCATIONS – REF. TO STA. 52.54

TAP. NO.	x (m)	x (in)
1	−0.058	−2.297
2	−0.043	−1.687
3	−0.026	−1.037
4	−0.009	−0.357
5	−0.001	−0.027
6	0.002	0.073

Figure 3.3-2 *Details of 0.75 Area Ratio Coannular Nozzle*

STATIC PRESSURE TAP LOCATIONS – REF. TO STA. 52.54

TAP. NO.	x (m)	x (in)
1	−0.058	−2.297
2	−0.043	−1.687
3	−0.026	−1.037
4	−0.009	−0.357
5	−0.001	−0.027
6	0.002	0.073

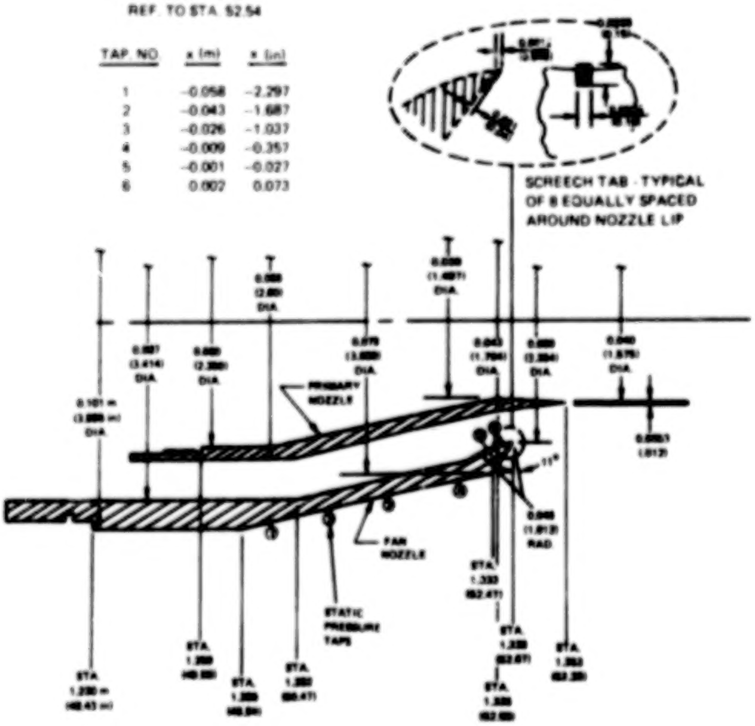

Figure 3.3-3 *Details of 1.2 Area Ratio Coannular Nozzle*

3.3.3 Ejector

The ejector geometry is based on preliminary nozzle design configurations used for AST/SCAR engine studies. The configuration is representative of the vehicle requirements in the take-off flight mode with the 0.75 area ratio coannular nozzle as illustrated in Figure 3.3-4. The ejector contains six pressure taps located along the axis of the ejector. A six probe total pressure rake is also installed in the ejector inlet to monitor the external flow effects on the ejector inlet.

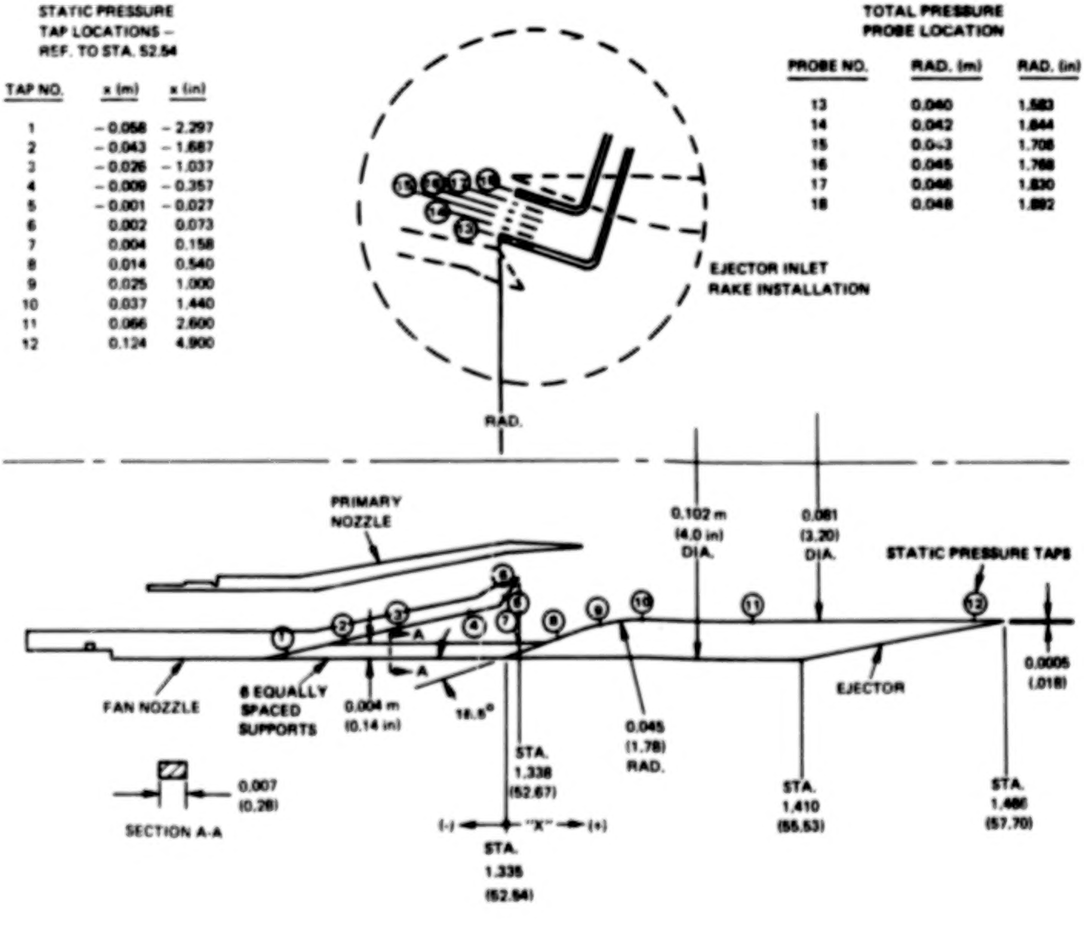

STATIC PRESSURE
TAP LOCATIONS –
REF. TO STA. 52.54

TAP NO.	x (m)	x (in)
1	– 0.058	– 2.297
2	– 0.043	– 1.687
3	– 0.026	– 1.037
4	– 0.009	– 0.357
5	– 0.001	– 0.027
6	0.002	0.073
7	0.004	0.158
8	0.014	0.540
9	0.025	1.000
10	0.037	1.440
11	0.066	2.600
12	0.124	4.900

TOTAL PRESSURE
PROBE LOCATION

PROBE NO.	RAD. (m)	RAD. (in)
13	0.040	1.583
14	0.042	1.644
15	0.043	1.708
16	0.045	1.768
17	0.046	1.830
18	0.048	1.892

Figure 3.3-4 Details of 0.75 Area Ratio Coannular Nozzle with Ejector

4.0 DATA

The types of data produced during the experimental testing are described in this section, along with the test procedure and a matrix showing the conditions at which each of the model configurations was tested. Various acoustic and aerodynamic parameters were obtained from the testing of the 4 different configurations over a matrix of pressure ratios and temperatures. Acoustic data and nozzle exit survey data acquired in the Acoustic Test Facility covered a total of 230 operating points. Aerodynamic performance data taken in the large Subsonic Wind Tunnel (LSWT) include a total of 80 operating conditions. Acoustic data from this program are documented in model size and in addition, for selected operating conditions, the model test data were scaled to represent a full size AST powerplant. The acoustic data contained in this report are presented as "simulated flight data." That is, the data were transformed analytically to account for the tunnel shear layer refraction and moving medium effects, as described in detail in Section 4.2. The data are thus in the same form as would be obtained from airplane flyover data referred to noise emission angle, and where the frequencies are corrected by the Doppler effect. The data are also available in the as-measured form (without shear layer and moving medium corrections) in the Comprehensive Data Report, NASA CR- 135189.

The model scale data are based on the 0.057 m (2.23 in) equivalent diameter size models tested. The acoustic parameters are:

- One-third octave band sound pressure level spectra at 3.05 m (10 ft) radius from 70° to 150° relative to the upstream jet axis, corrected to theoretical day conditions. "Theoretical day" is a hypothetical day with atmospheric conditions producing zero atmospheric attenuation of noise. The noise levels thus were corrected for the full amount of atmospheric absorption occurring during each test point.

- Overall sound pressure level at 3.05 m (10 ft) for the same angles as the above spectra.

- One-third octave band power spectra for the 0.057 m (2.23 in) equivalent diameter models.

- Overall sound power level.

The following acoustic parameters are scaled 22.5 times to a 1.27 m (50 in) size to represent a full size AST powerplant.

- One-third octave band sound pressure level spectra corrected to FAA day, 298°K (77°F) and 70% relative humidity at 45.7 m (150 ft) radius from 70° to 150° relative to the upstream jet axis.

- Overall sound pressure level at 45.7 m (150 ft) radius from 70° to 150° relative to the upstream jet axis.

- One-third octave band power spectra.

- Perceived noise levels calculated at various sideline distances (61 m (200 ft), 113 m (370 ft), 244 m (800 ft) and 649 m (2128 ft)) from 70° to 150° relative to the upstream jet axis.

The aerodynamic parameters are:

- Nozzle thrust coefficient.
- Nozzle flow coefficient for each stream.
- Static pressure distribution along the external surface of the fan nozzle and the internal surface of the ejector.
- Velocity profiles in the plane of the ejector exit (whether or not the ejector was in place) and total pressures at the ejector inlet when the ejector was in place.

The actual test procedure used to obtain the acoustic data in the Acoustic Test Facility was as follows:

1. The heater in the air supply system was started and allowed to run for sufficient time to provide the desired test stand air supply temperature of 394°K (250°F).
2. The acoustic and pressure measuring systems were checked and calibrated.
3. Wind tunnel velocity was set and allowed to stabilize.
4. Pressure and temperature were set in each stream and allowed to stabilize.
5. Pressure and temperature were read under steady state operating conditions and entered on computer coding sheets for subsequent computerized data reduction.
6. Acoustic data were tape recorded simultaneously on 9 channels for subsequent processing.
7. On-line one-third octave band analysis was performed on signals from selected microphones (i.e., 90° and 150°) to ensure satisfactory operation.

The above test procedure was followed in the testing of all configurations ensuring consistency in the results obtained during the program.

The test procedure used to obtain the aerodynamic data in the LSWT was as follows:

1. The tunnel motor was started and the tunnel and nozzle balance temperature allowed to stabilize.
2. Pressure measuring transducers were calibrated.
3. The required tunnel velocity was established.
4. The nozzle balance fan and primary flow valves were set to a given nozzle pressure ratio.
5. The balance base cavity pressure was adjusted to return the balance to the null position.
6. All pressure and temperature data were recorded on magnetic tape for subsequent data reduction.

The major acoustic and aerodynamic findings of the program are presented in this report for each configuration. In addition, a tabulation of acoustic power level, peak perceived noise level and overall sound pressure levels at all measurement angles, for all test points, is included in Appendix A.

Due to the large amount of data involved, the complete results of the testing have been compiled separately in the Comprehensive Data Report (CDR), NASA CR-135189. This report includes the model scale data as measured and transformed to "Simulated Flight" as well as selected full size data.

Table 4-I lists the nozzle operating conditions for each acoustic test point. In this table, nominal values of the stream temperatures and pressures are listed.

The matrix of conditions simulated in the aerodynamic performance tests is presented in Table 4-II. An unheated air supply system was employed, therefore only pressure ratios are identified.

The detailed data reduction procedures and sample data outputs are presented in Section 4.1 and 4.2. A discussion of the acoustic data validity based on a comparison of static data with previous results is presented in Section 4.3. The method used to synthesize the jet noise of a coannular nozzle is presented in Section 4.4 for reference purposes.

4.1 AERODYNAMIC DATA REDUCTION

The measured aerodynamic properties are divided into three categories:

(a) Thrust Coefficients and Flow Coefficients

(b) Surface Static Pressures

(c) Nozzle Exit Profiles and Ejector Inlet Total Pressures

The basic aerodynamic performance characteristics are presented in category (a) along with the flow properties in each stream. The static pressures (b) provide the axial pressure distributions useful in diagnosing the performance of the nozzles. The exit profiles (c) include the temperature and velocity surveys measured in the nozzle plume. The ejector inlet pressures complement the exit surveys. The thrust coefficients and flow coefficient were measured in the LSWT. The surface static pressures were measured in both the LSWT and the Acoustic Test Facility. The nozzle exit profile and ejector inlet pressures were measured in the Acoustic Test Facility.

These data are based on pressure, temperature and thrust measurements made while maintaining steady-state model flow conditions during each test point. The pressure data were established by means of a pressure transducer system. The temperatures were measured with the use of digital thermocouple indicators. The thrust measurements were based on the output of the force balance. The reduction of the basic data to the final aerodynamic parameters is described in detail in the following sections.

TABLE 4-I

ACOUSTIC TEST MATRIX

Configuration 1 – Convergent Reference Nozzle

P_t/P_a	T_t (°K)	Static	Tunnel Speed V_∞ (mps)		
			30	61	104
1.3	394	X	X	X	X
1.53		X	X	X	X
1.8		X	X	X	X
2.0		X	X	X	X
2.5		X	X	X	X
3.2		X	X	X	X
1.3	589	X	X	X	X
1.8		X	X	X	X
2.5		X	X	X	X
3.2		X	X	X	X
1.3	700	X	X	X	X
1.8		X	X	X	X
2.5		*X	*X	*X	*X
3.2		X	X	X	X

*Ejector exit plane traverse

TABLE 4-I (Cont'd)

Configuration 2 – 0.75 Area Ratio Coannular Nozzle

				Tunnel Speed V_∞ (mps)				
P_{tp}/P_a	T_{tp} (°K)	P_{tf}/P_a	T_{tf} (°K)	Static	30	61	104	130
1.53	394	1.3	394	X	X	X	X	
		1.53		X	X	X	X	
		1.8		X	X	X	X	
		2.5		X	X	X	X	
		3.2		X	X	X	X	
		1.3	589	X	X	X	X	
		1.8		X	X	X	X	
		2.5		X	X	X	X	
		3.2		X	X	X	X	
No primary flow		1.3	700	X	X	X	X	
		1.8		X	X	X	X	
		2.5		*X	X	*X	*X	*X
		3.2		X	X	X	X	X
		1.3	700	X		X	X	
		1.8		X		X	X	
		2.5		*X		*X	*X	
		3.2		X		X	X	

* Ejector exit plane traverse

TABLE 4-I (Cont'd)

Configuration 3 – 0.75 Area Ratio Coannular Nozzle With Ejector

				Tunnel Speed V_∞ (mps)				
P_{tp}/P_a	T_{tp} (°K)	P_{tf}/P_a	T_{tf} (°K)	Static	30	61	104	130
1.53	394	1.3	394	X	X	X	X	
		1.53		X	X	X	X	
		1.8		X	X	X	X	
		2.5		X	X	X	X	
		3.2		X	X	X	X	
		1.3	589	X	X	X	X	
		1.8		X	X	X	X	
		2.5		X	X	X	X	
		3.2		X	X	X	X	
		1.3	700	*X	X	*X	*X	
		1.8		*X	X	*X	*X	
		2.5		*X	X	*X	*X	*X
		3.2		*X	X	*X	*X	*X

* Ejector inlet and exit traverse

TABLE 4-I (Cont'd)

Configuration 4 – 1.2 Area Ratio Coannular Nozzle

P_{tp}/P_a	T_{tp} (°K)	P_{tf}/P_a	T_{tf} (°K)	Tunnel Speed V_∞ (mps) Static	30	61	104	130
1.53	394	1.3	394	X	X	X	X	
		1.53		X	X	X	X	
		1.8		X	X	X	X	
		2.5		X	X	X	X	
		3.2		X	X	X	X	
		1.3	589	X	X	X	X	
		1.8		X	X	X	X	
		2.5		X	X	X	X	
		3.2		X	X	X	X	
		1.3	700	X	X	X	X	
		1.8		X	X	X	X	
		2.5		•X	X	•X	•X	•X
		3.2		X	X	X	X	X

• Ejector exit plane traverse

TABLE 4-II

AERODYNAMIC PERFORMANCE TEST MATRIX

Configuration 1 – Convergent Reference Nozzle

		Tunnel Speed – V_∞ (mps)		
P_{tp}/P_a	Static	61	104	130
1.3	X	X	X	X
1.53	X	X	X	X
1.8	X	X	X	X
2.5	X	X	X	X
3.2	X	X	X	X

Configuration 2 – 0.75 Area Ratio Coannular Nozzle
Configuration 3 – 0.75 Area Ratio Coannular Nozzle With Ejector
Configuration 4 – 1.20 Area Ratio Coannular Nozzle

			Tunnel Speed – V_∞ (mps)		
P_{tp}/P_a	P_{tf}/P_a	Static	61	104	130
1.53	1.3	X	X	X	X
1.53	1.53	X	X	X	X
1.53	1.8	X	X	X	X
1.53	2.5	X	X	X	X
1.53	3.2	X	X	X	X

For all tests nozzle flow temperatures were ambient (i.e. 289°K - 300°K (60°F - 80°F)

4.1.1 Thrust Coefficients and Flow Coefficients

The thrust coefficient of a nozzle is a function of the thrust produced by the nozzle (F) and the ideal thrust which is available (F_i) based on the properties of the flow entering the nozzle. When external flow tests are conducted the nozzle force (F) is a combination of internal and external (i.e., drag) forces. The nozzle thrust coefficient, C_F, is defined as:

$$C_F = \frac{F}{F_{i_t}}$$

where:

$F = F_b + \Delta F$ (N, lbs)

and F_b = balance force

ΔF = external friction on nozzle support shaft

The total ideal thrust (F_{it}) is defined as:

$$F_{i_t} = F_{i_{Primary}} + F_{i_{Fan}} \qquad \text{(N, lbf)}$$

The ideal thrust (F_i) of each stream is calculated by the equation:

$$F_i = P_t A^* \sqrt{\frac{2\gamma^2}{\gamma-1}\left(\frac{2}{\gamma+1}\right)^{\frac{\gamma+1}{\gamma-1}}\left[1-\left(\frac{P_a}{P_t}\right)^{\frac{\gamma-1}{\gamma}}\right]}$$

where:

P_t = Total pressure at instrumentation station (N/m^2, psia)

P_a = ambient pressure (N/m^2, psia)

$$A^* = \frac{W_t}{P_t}\sqrt{\frac{T_t \mathscr{R}}{g_c \gamma}}\left(1+\frac{\gamma-1}{2}\right)^{\frac{\gamma+1}{2(\gamma-1)}}$$

and W_t = Air flow rate, measured at the upstream bellmouth (kg/sec, lbm/sec)
T_t = Total temperature at instrumentation station (°K, °R)
γ = Specific heat ratio
$\mathscr{R}$ = Gas constant = (88.51 Nm/kg °K, 53.3 lbf ft/lbm °R)
g_c = Conversion factor = (1.0 kg m/N sec^2, 32.174 lbm ft/lbf sec^2)

The nozzle flow coefficient for each stream is calculated by the equation:

$$C_D = \frac{W_t}{W_i}$$

where: $$W_i = \frac{P_t A}{\sqrt{T_t}} \, M \sqrt{\frac{\gamma g_c}{\mathscr{R}}} \left(1 + \frac{\gamma - 1}{2} M^2\right)^{-\frac{(\gamma + 1)}{2(\gamma - 1)}} \; ; M \leqslant 1.0$$

(kg/sec, lbm/sec)

for $M > 1$ use $M = 1$

A = Nozzle exit area in each stream (m^2, in^2)

$$M = \text{Fully Expanded Mach Number} = \sqrt{\frac{2}{\gamma - 1}\left((P_t/P_a)^{\frac{\gamma - 1}{\gamma}} - 1\right)}$$

The thrust coefficients and flow coefficients for all the test configurations are included in Volume III of the CDR. A sample of the data available in the CDR is presented in Figure 4.1-1A for Configuration (3), the 0.75 area ratio coannular nozzle with ejector. The thrust and flow coefficients are tabulated with the pressure ratios of each stream (P_t/P_a) and the external velocity (V_o), in feet per second.

4.1.2 Surface Static Pressure

Static pressures (P) were measured along the external surface of the nozzle and along the internal surface of the ejector. The pressures are ratioed to tunnel ambient pressure (P_a) and tabulated in the CDR where they are identified by pressure orifice number (TAP) and axial location, X/L, where:

X = position of pressure orifice relative to station 52.54 (which corresponds to leading edge of the ejector)

L = Ejector length = 0.131 m (5.17 in)

All pressure data are presented relative to ejector length regardless of whether ejector was used or not. All of the static pressure data are presented in Volume III of the CDR. A sample of the data is presented in Figure 4.1-1B for Configuration (3), the 0.75 area ratio coannular nozzle with the ejector.

4.1.3 Exit Profiles and Ejector Inlet Total Pressures

Temperature and velocity profiles were obtained in the plane of the ejector exit. All configurations (with or without an ejector) were traversed along a radial line in the same plane. When the ejector was installed, it was oriented circumferentially such that the traverse probe was midway between the support struts. The probe readings therefore reflect an average of the circumferential distribution.

The probe simultaneously measured a static pressure (P_s), a total pressure (P_t) and a total temperature (T_t) at a given radial position (R). The velocity (V) was then calculated by the following equation:

$$V = \sqrt{\left(\frac{\gamma g_c \mathcal{R} T_t M^2}{1 + \frac{\gamma - 1}{2} M^2}\right)} \qquad \text{(m/sec, ft/sec)}$$

where:

$$M = \sqrt{\frac{2}{\gamma - 1}\left((P_t/P_s)^{\frac{\gamma - 1}{\gamma}} - 1\right)}$$

The ejector inlet total pressures (P_t) were measured radially between the ejector lip and nozzle wall. The pressures are non-dimentionalized by the tunnel total pressure (P_{to}).

A sample of the traverse data is illustrated in Figure 4.1-1c. It is tabulated at each radial position (R), non-dimensionalized to the exit radius of the ejector (R_{exit}). A sample of the ejector inlet data is illustrated in Figure 4.1-1d. It is tabulated at each radial position (R), non-dimensionalized to the radius of the leading edge of the ejector ($R_{L.E.}$).

All the resultant traverse and ejector inlet total pressure data are included in Volume III of the CDR.

(A) Sample Thrust and Flow Coefficient Data

CONFIG NO.	RUN/PT	PTP/PA	PTF/PA	CF	CDP	CDF	VO
3	49/04	1.54	1.30	.932	1.019	.934	342.8
3	49/05	1.53	1.30	.924	1.021	.923	425.0
3	49/06	1.53	1.53	.928	1.019	.950	426.2
3	50/02	1.53	1.51	.960	1.020	.970	.0

(B) Sample Static Pressure Data

CONFIG		3, 0.75	AF/AP	COANNULAR EJECTOR NOZZLE					RUN/PT	49/04		
TAP	1	2	3	4	5	6	7	8	9	10	11	12
X/L	-.444	-.326	-.201	-.069	-.005	.014	.031	.104	.193	.279	.503	.948
P/PA	.991	.997	1.066	1.005	1.003	1.000	1.009	1.005	1.000	.998	1.004	1.009
CONFIG		3, 0.75	AF/AP	COANNULAR EJECTOR NOZZLE					RUN/PT	49/05		
TAP	1	2	3	4	5	6	7	8	9	10	11	12
X/L	-.444	-.326	-.201	-.069	-.005	.014	.031	.104	.193	.279	.503	.948
P/PA	.987	.996	1.103	1.013	1.013	1.009	1.022	1.014	1.007	1.004	1.012	1.015
CONFIG		3, 0.75	AF/AP	COANNULAR EJECTOR NOZZLE					RUN/PT	49/06		
TAP	1	2	3	4	5	6	7	8	9	10	11	12
X/L	-.444	-.326	-.201	-.069	-.005	.014	.031	.104	.193	.279	.503	.948
P/PA	.986	.995	1.104	1.007	1.002	1.000	1.014	1.006	.998	.994	1.006	1.014
CONFIG		3, 0.75	AF/AP	COANNULAR EJECTOR NOZZLE					RUN/PT	50/02		
TAP	1	2	3	4	5	6	7	8	9	10	11	12
X/L	-.444	-.326	-.201	-.069	-.005	.014	.031	.104	.193	.279	.503	.948
P/PA	1.000	.999	1.000	.991	.959	.956	.943	.959	.965	.964	.969	.995

Figure 4.1-1 *Sample of the Aerodynamic Data Contained in the Comprehensive Data Report NASA CR-135189*

(C) Sample Traverse Data
Configuration 3 0.75 AR Coannular Nozzle with Ejector

Run 3534

R/R Exit	0	.188	.375	.500	.563	.625	.750	.875	.938	1.0
T_T Exit (°F)	224	270	452	559	564	522	380	248	193	120
V Exit (fps)	915	948	1117	1462	1634	1626	1211	658	499	63

Run 3536

R/R Exit	0	.188	.375	.500	.563	.625	.750	.875	1.0	1.125
T_T Exit (°F)	192	220	414	524	534	494	436	361	75	.60
V Exit (fps)	846	907	1102	1415	1557	1554	1415	1172	133	188

(D) Sample Ejector Inlet Total Pressures - Pt/Pto
Configuration 3, 0.75 AR Coannular Nozzle with Ejector

	Probe #	13	14	15	16	17	18
Run #	R/R L.E.	.792	.823	.854	.885	.916	.947
3534		.998	1.001	1.0016	1.0016	.9996	.8965
3536		1.0112	1.0148	1.0176	1.0189	1.0197	1.0204
3537		1.0098	1.0134	1.0155	1.0169	1.0183	1.0189
3539		.9993	.9986	.9979	.9979	.9966	.9066

Figure 4.1-1 Sample Aerodynamic Data (Continued)

4.2 ACOUSTIC DATA REDUCTION

The measured acoustic signals recorded by the microphone array at 3.05 m (10 ft) radius were analyzed, corrected and converted to full size engine data (22.5X model size) by the procedure illustrated in Figures 4.2-1 and 2 for data without and with tunnel flow (static and in-flight conditions), respectively. These figures also indicate the data output available for both the 0.0566m (2.23 in) equivalent diameter model size and the 1.27 m (50 in) full size scaled engine data. The corrections used are described in more detail in the following paragraphs. All of the model data are available in the companion Comprehensive Data Report (CDR) NASA CR-135189 (Ref. 9).

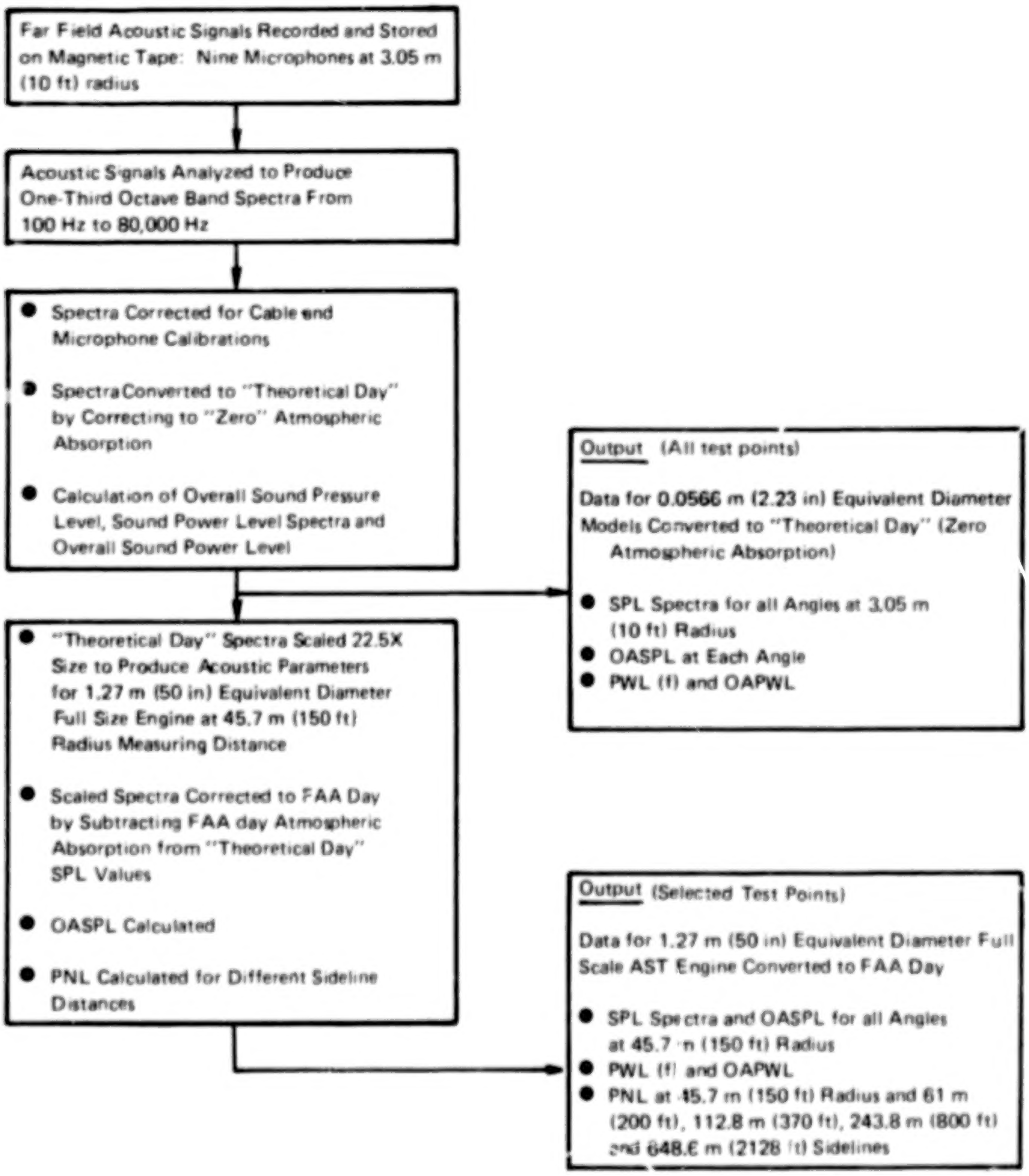
Far Field Acoustic Signals Recorded and Stored on Magnetic Tape: Nine Microphones at 3.05 m (10 ft) radius
Acoustic Signals Analyzed to Produce One-Third Octave Band Spectra From 100 Hz to 80,000 Hz
● Spectra Corrected for Cable and Microphone Calibrations
● Spectra Converted to "Theoretical Day" by Correcting to "Zero" Atmospheric Absorption
● Calculation of Overall Sound Pressure Level, Sound Power Level Spectra and Overall Sound Power Level
Output (All test points)
Data for 0.0566 m (2.23 in) Equivalent Diameter Models Converted to "Theoretical Day" (Zero Atmospheric Absorption)
● SPL Spectra for all Angles at 3.05 m (10 ft) Radius
● OASPL at Each Angle
● PWL (f) and OAPWL
● "Theoretical Day" Spectra Scaled 22.5X Size to Produce Acoustic Parameters for 1.27 m (50 in) Equivalent Diameter Full Size Engine at 45.7 m (150 ft) Radius Measuring Distance
● Scaled Spectra Corrected to FAA Day by Subtracting FAA day Atmospheric Absorption from "Theoretical Day" SPL Values
● OASPL Calculated
● PNL Calculated for Different Sideline Distances
Output (Selected Test Points)
Data for 1.27 m (50 in) Equivalent Diameter Full Scale AST Engine Converted to FAA Day
● SPL Spectra and OASPL for all Angles at 45.7 m (150 ft) Radius
● PWL (f) and OAPWL
● PNL at 45.7 m (150 ft) Radius and 61 m (200 ft), 112.8 m (370 ft), 243.8 m (800 ft) and 648.6 m (2128 ft) Sidelines

Figure 4.2-1 Acoustic Data Reduction Procedure For Static Conditions

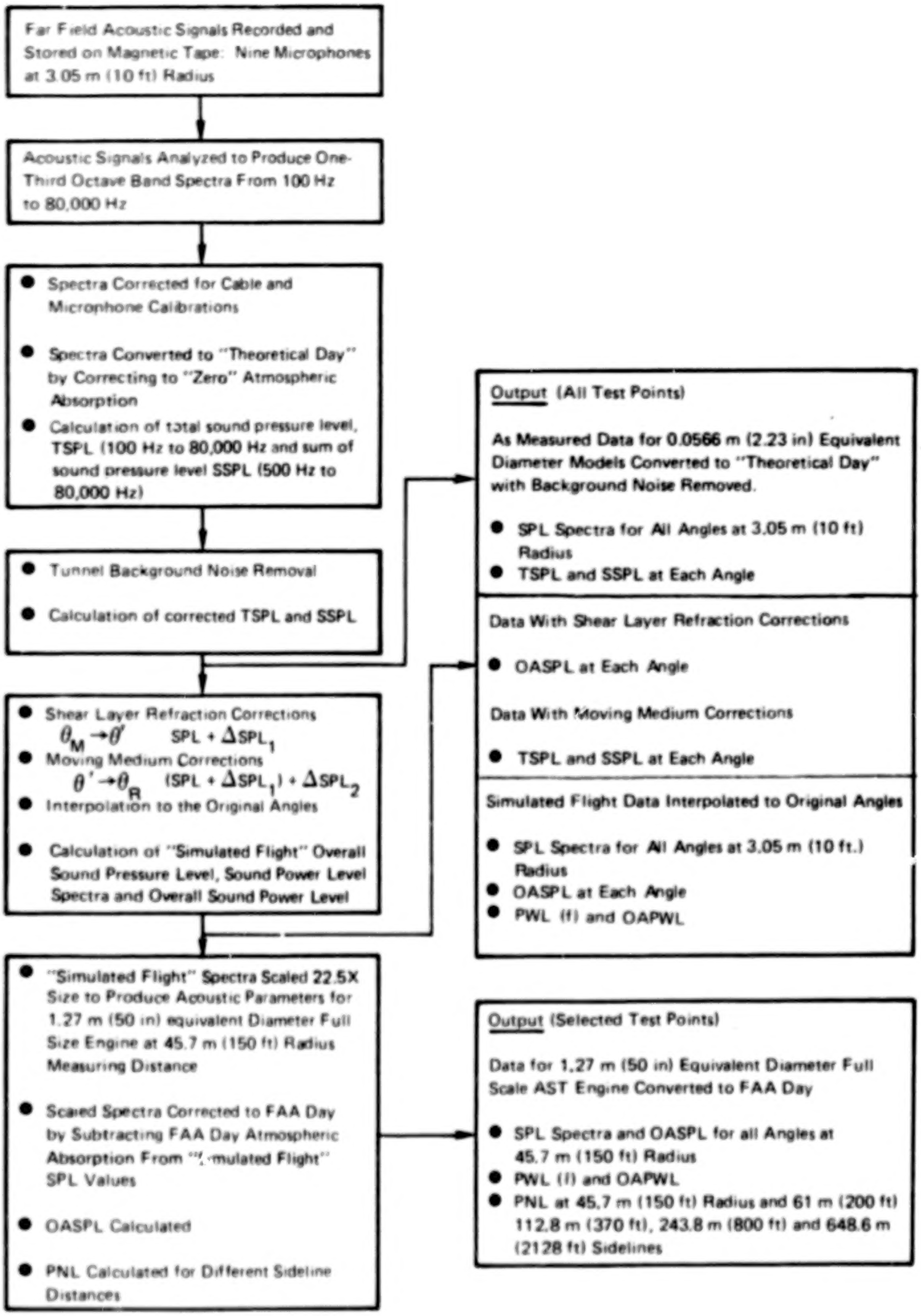
Far Field Acoustic Signals Recorded and Stored on Magnetic Tape: Nine Microphones at 3.05 m (10 ft) Radius
Acoustic Signals Analyzed to Produce One-Third Octave Band Spectra From 100 Hz to 80,000 Hz
● Spectra Corrected for Cable and Microphone Calibrations
● Spectra Converted to "Theoretical Day" by Correcting to "Zero" Atmospheric Absorption
● Calculation of total sound pressure level, TSPL (100 Hz to 80,000 Hz and sum of sound pressure level SSPL (500 Hz to 80,000 Hz)
● Tunnel Background Noise Removal
● Calculation of corrected TSPL and SSPL
● Shear Layer Refraction Corrections
$\theta_M \rightarrow \theta'$ SPL + ΔSPL$_1$
● Moving Medium Corrections
$\theta' \rightarrow \theta_R$ (SPL + ΔSPL$_1$) + ΔSPL$_2$
● Interpolation to the Original Angles
● Calculation of "Simulated Flight" Overall Sound Pressure Level, Sound Power Level Spectra and Overall Sound Power Level
● "Simulated Flight" Spectra Scaled 22.5X Size to Produce Acoustic Parameters for 1.27 m (50 in) equivalent Diameter Full Size Engine at 45.7 m (150 ft) Radius Measuring Distance
● Scaled Spectra Corrected to FAA Day by Subtracting FAA Day Atmospheric Absorption From "Simulated Flight" SPL Values
● OASPL Calculated
● PNL Calculated for Different Sideline Distances
Output (All Test Points)
As Measured Data for 0.0566 m (2.23 in) Equivalent Diameter Models Converted to "Theoretical Day" with Background Noise Removed.
● SPL Spectra for All Angles at 3.05 m (10 ft) Radius
● TSPL and SSPL at Each Angle
Data With Shear Layer Refraction Corrections
● OASPL at Each Angle
Data With Moving Medium Corrections
● TSPL and SSPL at Each Angle
Simulated Flight Data Interpolated to Original Angles
● SPL Spectra for All Angles at 3.05 m (10 ft.) Radius
● OASPL at Each Angle
● PWL (f) and OAPWL
Output (Selected Test Points)
Data for 1.27 m (50 in) Equivalent Diameter Full Scale AST Engine Converted to FAA Day
● SPL Spectra and OASPL for all Angles at 45.7 m (150 ft) Radius
● PWL (f) and OAPWL
● PNL at 45.7 m (150 ft) Radius and 61 m (200 ft) 112.8 m (370 ft), 243.8 m (800 ft) and 648.6 m (2128 ft) Sidelines

Figure 4.2-2 Acoustic Data Reduction Procedure For Flight Simulated Conditions

The tape recorded far-field signals from the nine microphones were reduced to one-third octave band sound pressure levels (SPLs) by analog/digital analysis equipment. This analysis was performed on a General Radio No. 1921 analyzer.

The one-third octave band as-measured model size sound pressure levels, analyzed from 100 Hz to 80,000 Hz, were corrected for calibrated cable and microphone frequency response. The frequency response of the installed cathode follower and microphone extension cable from the microphone to the recording console was obtained by a point-to-point sine wave insertion covering the range of measurement frequencies. The microphones were calibrated in the laboratory utilizing a variable frequency, electro-static actuator to obtain the open circuit sensitivity and frequency response. The calibration data were processed by a computer program which provided a printout of one-third octave band corrections. To establish the complete system sensitivity, a B&K type 4220 piston phone was used. Immediately prior to each series of test recordings, an acoustic calibration was performed by applying the B&K piston phone to each microphone, providing a known sinusoidal sound pressure level at 250 Hz to the microphone diaphragm, thereby establishing an acoustic reference level.

The measured data were transformed into "theoretical day" data by applying the values of atmospheric absorption defined in Reference 11. This procedure entails adding algebraically ΔSPL as a function of frequency, relative humidity, and ambient temperature to the measured SPL. The ΔSPL corrections represent an estimate of the absolute sound absorption in each of the one-third octave bands. The resulting "theoretical day" data represents the noise that would be measured at the microphone if no noise was lost through atmospheric absorption. Data in this form can thus be scaled to represent the noise of a full scale engine. Typical values of atmospheric absorption, calculated by the method of Reference 11 for the 3.05 m (10 ft) measuring distance, used in this program are illustrated in Table 4-III.

The corrections at the very high frequencies, i.e., above 40K Hz, become quite large. At 80K Hz, the correction of 6.4 dB for the case shown in Table 4-III represents a loss of nearly 77% of the sound energy that would have been radiated to the microphone if no atmospheric absorption were present. The atmospheric absorption values resulting from the formula used in reference 11 have been found to be in acceptable agreement to recent NASA sponsored experimental results for frequencies up to 100K Hz (see Appendix C). The application of these corrections to the noise data resulted in an "uplift" in noise levels at the very high frequencies for much of the data compared to "ideal" jet noise behavior. However, since the University of Mississippi procedure is considered to be the "state-of-the-art," the formula of Reference 11 were used directly to calculate the values of atmospheric absorption for frequencies up to 80,000 Hz. The "theoretical day" SPLs were integrated over the measured frequency range to obtain overall sound pressure levels (OASPLs). A detailed discussion on the "theoretical day" data are contained in Appendix C.

TABLE 4-III
ATMOSPHERIC ABSORPTION ESTIMATES FOR A TYPICAL DATA POINT

3.05 m (10 ft) Radius
Temperature – 286°K (55°F)
Relative Humidity – 50%

Freq. (K Hz)	Δ SPL (dB)
< 2.0	0.0
2.5	0.1
3.2	0.1
4.0	0.1
5.0	0.1
6.3	0.2
8.0	0.3
10.0	0.4
12.5	0.6
16.0	0.8
20.0	1.2
25.0	1.6
31.5	2.2
40.0	2.9
50.0	3.7
63.0	4.8
80.0	6.4
100.0	8.1

When the tunnel flow was on, simulating the in-flight operation, three corrections were applied to the data in order to account for; (a) the tunnel background noise, (b) the tunnel shear layer refraction and (c) the moving medium (tunnel flow) effect. The tunnel background noise was removed by logarithmic subtraction of the background noise spectra from the data. The shear layer refraction correction accounts for sound wave refraction by the tunnel shear layer. Sound propagating through the shear layer is refracted and changed in amplitude. A detailed theoretical discussion on the shear layer refraction correction is contained in Appendix D. The theory of Amiet (Ref. 8) provides correction equations for amplitude and angle which when applied, result in directivity patterns that are consistent with moving the shear layer to infinity. (See Fig. 4.2-3a) Data corrected by this method correspond to a frame of reference in which source and observer are fixed relative to each other in an airstream extending to infinity and would be equivalent to measurements taken by a microphone moving with the aircraft. In this frame of reference, the airstream that extends to infinity convects the sound wave fronts during propagation from source to microphone. Rather than use this coordinate frame of reference, it is desirable to convert to a nozzle fixed coordinate system with zero mean velocity. To do this, the shear layer corrected angle, θ' must be corrected to the retarded angle (or angle of noise emission), θ_R. As shown in Figure 4.2-3b, correction of the angle, θ', to angle of noise emission, θ_R, at stream Mach number, M_∞, is given by the relation:

$$\tan \theta' = \frac{\sin \theta_R}{\cos \theta_R - M_\infty} \qquad \text{Eq. 4-1}$$

where the angles are measured relative to the upstream jet axis. Corrections based on Equation 4.1 are referred to as moving medium corrections. The combined shear layer and moving medium correction procedure is illustrated in Figure 4.2-4. Application of the moving medium and shear layer correlations provides data that can be compared directly with static test noise spectra and directivity for purposes of determining flight effects. The angle and amplitude corrections are tabulated in Tables 4-IV and 4-V for the shear layer refraction and moving medium correction. The first table, 4-IV, lists the 9 microphone measurement angles, θ_M. The shear layer corrected angle, θ', and the amplitude correction, **ΔSPL**, are listed for each θ_M at each tunnel speed V_∞. The second table, 4-V, also lists the shear layer corrected angles shown in Table 4-IV and the noise emission angles, θ_R, corresponding to each microphone measurement angle θ_M to θ_R changes the ray path distance by the factor $\sin \theta'/\sin \theta_R$. The SPL level is thus corrected for spherical divergency by the factor $\Delta SPL_2 = 20 \log \sin \theta'/\sin \theta_R$.

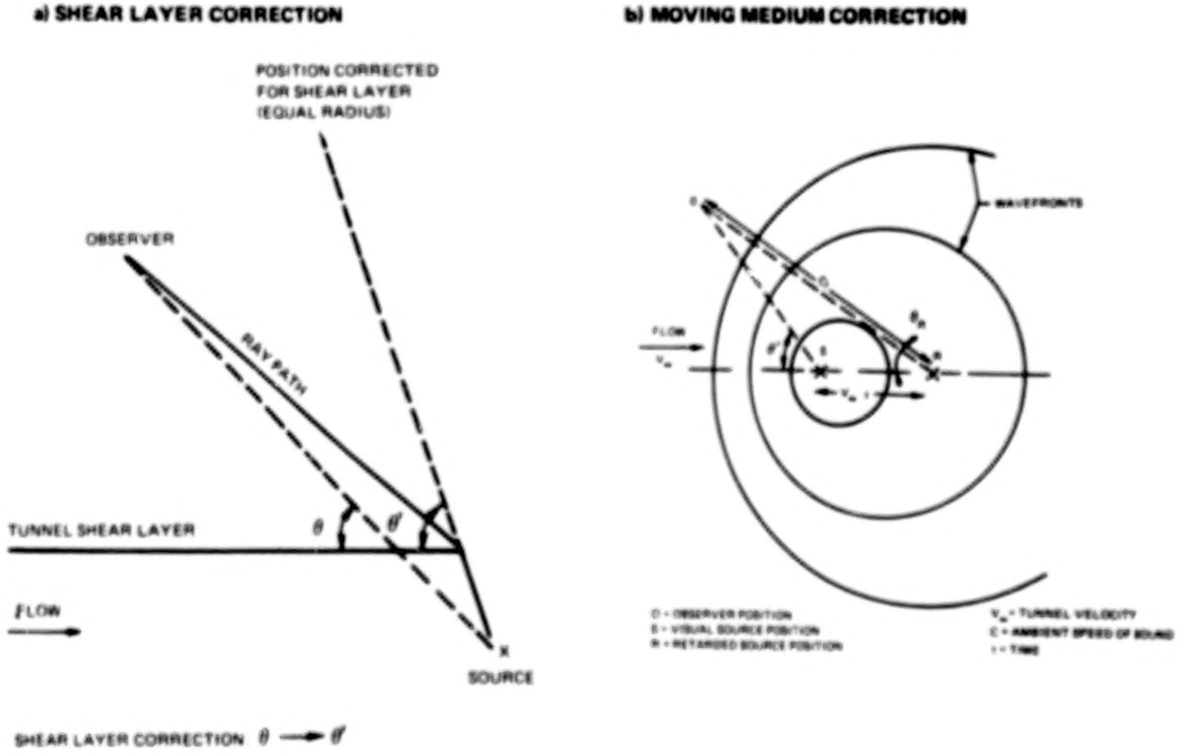
a) SHEAR LAYER CORRECTION
POSITION CORRECTED FOR SHEAR LAYER (EQUAL RADIUS)
OBSERVER
RAY PATH
TUNNEL SHEAR LAYER
θ
θ'
FLOW
SOURCE
SHEAR LAYER CORRECTION θ → θ'
b) MOVING MEDIUM CORRECTION
WAVEFRONTS
O
S
R
θ'
θ_R
FLOW
V_∞
$V_\infty t$
O = OBSERVER POSITION
S = VISUAL SOURCE POSITION
R = RETARDED SOURCE POSITION
V_∞ = TUNNEL VELOCITY
C = AMBIENT SPEED OF SOUND
t = TIME

Figure 4.2-3 Schematic of Simulated Flight Data Corrections

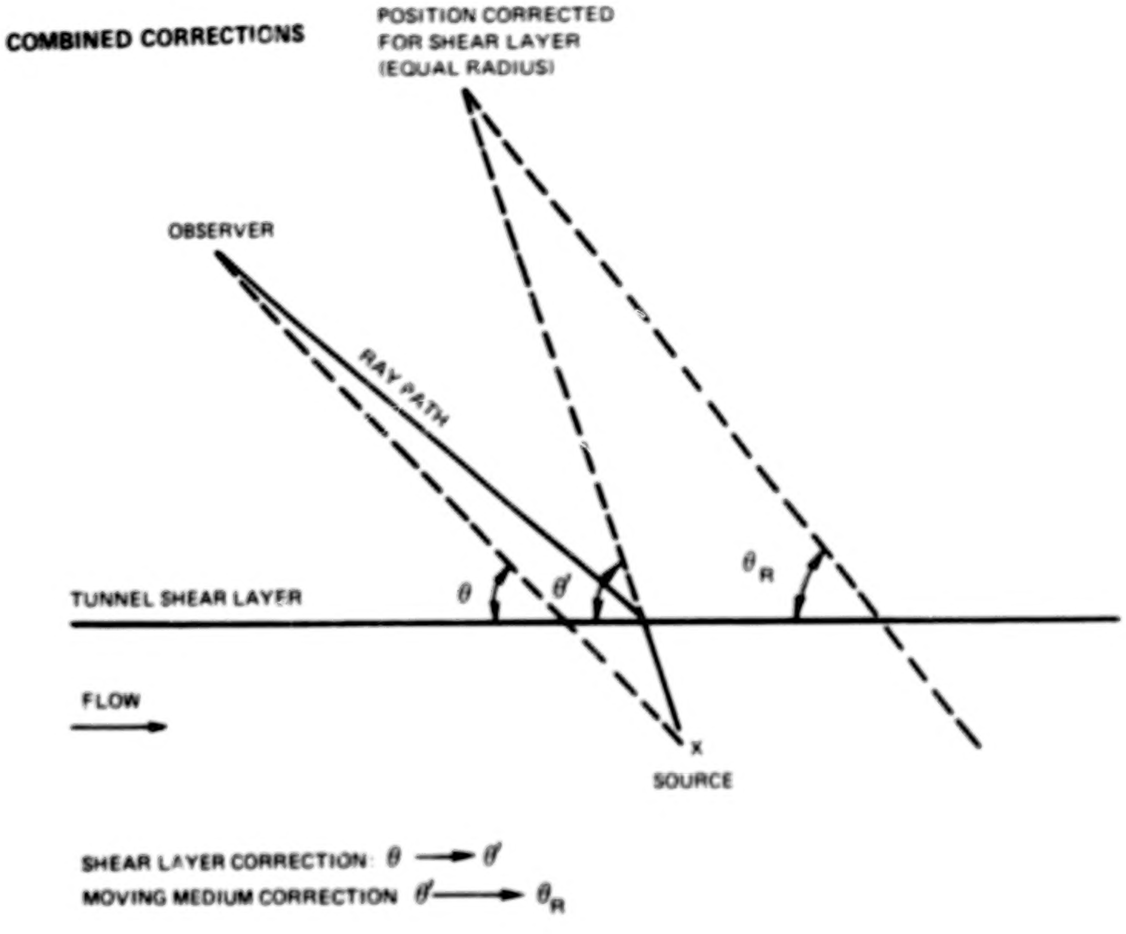
COMBINED CORRECTIONS
POSITION CORRECTED FOR SHEAR LAYER (EQUAL RADIUS)
OBSERVER
RAY PATH
θ
θ'
θ_R
TUNNEL SHEAR LAYER
FLOW
SOURCE
SHEAR LAYER CORRECTION: θ → θ'
MOVING MEDIUM CORRECTION θ' → θ_R

Figure 4.2-4 Schematic of Shear Layer and Moving Medium Corrections

The complete results of the testing have been compiled separately in the Comprehensive Data Report, NASA CR-135189 (Ref. 9), which includes both the model scale and selected full size data. All the model data is presented for a "theoretical day," while the full size data is presented for an FAA day (RH = 70%, Temp. = 298°K). Typical sample data pages for the flight data in the as measured condition with background noise removed, and with shear layer and moving medium corrections incorporated (simulated flight) are shown in Tables 4-VI to 4-VIII. Table 4-IX is a sample model data page for both static and simulated light condition with the pertinent nozzle operating parameters. At selected test points for both static and flight condition, the theoretical day noise data were scaled 22.5X model size to represent a full size engine jet exhaust. A sample of scaled engine data is shown in Table 4-X.

Table 4-VI is a sample data page of the "as measured" model data on a theoretical day with the tunnel background noise removed. The title lists the computer program (DECK) where the data are stored, the length of data (LD), the test date (DATE) and the test stand (STND). The test run number is listed under (OBS) and (CORR).

TABLE 4-IV

SHEAR LAYER CORRECTION

Tunnel Velocity, V_∞

$\theta_{Measured}$	30 mps (100 fps)		61 mps (200 fps)		104 mps (340 fps)		130 mps (425 fps)	
	θ'	ΔSPL_1	θ'	ΔSPL_1	θ'	ΔSPL_1	θ'	ΔSPL_1
70°	75.0	.42	79.5	.92	87.5	1.84	92.0	2.48
80°	84.5	.24	89.0	.55	96.0	1.20	100.0	1.66
90°	94.5	.05	98.5	.18	104.5	.55	108.0	.82
100°	104.0	-.13	108.5	-.20	113.5	-.12	117.0	-.02
110°	114.0	-.32	118.5	-.57	123.5	-.82	126.5	-.88
120°	124.5	-.52	129.0	-.96	133.5	-1.43	136.5	-1.70
130°	135.0	-.70	139.5	-1.30	144.0	-1.98	146.5	-2.32
140°	145.5	-.85	150.0	-1.48	155.0	-1.80	157.0	-1.96
150°	156.0	-.76	160.0	-.70	163.5	-.24	164.5	-.10

NOTE: 1) For 3.05 m (10 ft) polar array microphones,
0.91 m (36 in) dia. test nozzle.

2) θ' and ΔSPL_1 determined from equations
1 through 3 of Appendix D.

TABLE 4-V

ANGLE CORRECTION FOR MOVING MEDIUM

Tunnel Velocity, V_∞

$\theta_{Measured}$	30 mps (100 fps)		61 mps (200 fps)		104 mps (340 fps)		130 mps (425 fps)	
	θ'	θ_R	θ'	θ_R	θ'	θ_R	θ'	θ_R
70°	75.0	70.0	79.5	70.0	87.5	70.0	92.0	70.0
80°	84.5	79.5	89.0	79.0	96.0	78.5	100.0	78.0
90°	94.5	89.5	98.5	88.5	104.5	87.5	108.0	87.0
100°	104.0	99.5	108.5	99.0	113.5	97.5	117.0	97.5
110°	114.0	109.5	118.5	109.5	123.5	109.5	126.5	109.0
120°	124.5	120.5	129.0	121.0	133.5	121.5	136.5	121.5
130°	135.0	131.5	139.5	133.0	144.0	134.0	146.5	135.0
140°	145.5	143.0	150.0	145.5	155.0	148.0	157.0	148.5
150°	156.0	154.0	160.0	156.0	163.5	158.5	164.5	158.5

$$M_\infty = \frac{V_\infty}{a_0} \qquad \operatorname{Tan}\theta' = \frac{\operatorname{Sin}\theta_R}{\cos\theta_R - M_\infty} \qquad \Delta SPL_2 = 20\ \operatorname{Log}\frac{\operatorname{Sin}\theta'}{\operatorname{Sin}\theta_R}$$

TABLE 4-VI

SAMPLE SIMULATED - FLIGHT DATA

```
DECK  LD  DATE       ENG  MOD ENG NO STAD C  C85 CCMM
WA31  315 05/21/76        -00 000000 XAFF 0 3644 3644
                                                                  GBTF JET NOISE TEST CONF. 1  2.2" DIA
                                                                   . NOZ.  TAPE 4914              10.2049
```

JET NOISE SPECTRA WITH BACKGROUND NOISE REMOVED

BAND CENTER FREQ (HZ)	MICROPHONE ANGLES IN DEGREES								
	70.0	80.0	90.0	100.0	110.0	120.0	130.0	140.0	150.0
100	78.1	78.3	76.4	77.5	72.3	70.9	75.3	81.5	89.9
125	74.7	76.8	74.9	74.7	70.6	73.2	74.8	79.7	90.0
160	72.5	75.6	73.7	74.6	72.6	73.1	74.2	79.7	82.0
200	73.4	75.9	73.7	76.5	73.8	75.7	79.6	80.8	78.8
250	74.0	65.3	75.8	76.9	78.9	78.8	79.7	84.6	75.0
315	75.1	78.2	79.1	79.3	79.0	79.5	80.8	86.0	94.9
400	78.1	78.2	78.6	79.7	79.4	80.4	84.7	87.4	95.3
500	77.4	77.0	78.6	79.6	80.6	83.3	86.6	91.6	95.2
630	78.9	79.4	80.2	81.5	82.5	84.6	87.5	92.4	98.3
800	84.1	81.7	82.8	84.6	84.5	85.8	89.7	95.3	100.2
1000	81.8	84.1	85.0	86.7	86.4	87.3	90.2	96.3	100.4
1250	83.1	84.1	84.2	86.8	88.3	89.2	91.9	97.0	100.4
1600	83.7	84.4	85.5	87.8	89.5	90.5	93.0	97.1	100.2
2000	84.2	85.8	87.8	89.5	90.0	91.6	94.5	97.3	99.2
2500	84.9	85.6	86.2	89.0	90.5	92.6	94.3	97.2	97.3
3150	85.0	85.9	87.2	89.2	90.6	92.2	94.7	96.6	95.7
4000	85.2	86.0	86.6	89.0	91.0	92.8	94.5	96.4	94.0
5000	85.6	86.6	87.0	89.6	91.3	93.1	94.8	95.6	92.8
6300	85.3	86.2	87.2	89.5	91.1	92.8	94.4	94.3	91.3
8000	85.9	85.9	86.9	89.3	91.3	93.2	93.8	93.7	89.6
10000	85.4	86.1	86.9	88.8	90.7	92.2	93.2	92.6	88.1
12500	84.9	85.6	86.3	88.7	90.3	91.7	92.3	90.9	86.8
16000	84.8	85.4	86.0	88.2	89.8	91.1	91.4	89.4	85.4
20000	83.8	84.5	85.2	87.1	88.9	89.9	90.6	87.8	83.5
25000	83.3	84.4	84.9	86.7	88.8	89.2	89.6	87.0	82.6
31500	82.7	83.5	84.2	86.0	87.7	88.6	87.7	85.6	81.4
40000	82.4	83.2	84.1	85.5	86.9	87.7	86.7	84.3	80.6
50000	82.0	82.7	83.8	85.7	86.5	87.1	86.1	83.7	80.0
63000	82.0	83.0	84.1	85.4	86.7	87.0	85.7	83.7	80.0
80000	82.5	83.0	84.2	85.6	86.5	86.7	85.5	83.3	80.4
TSPL	97.6	98.4	99.2	101.3	102.7	104.0	105.5	107.6	109.5
SSPL	97.4	98.2	99.1	101.1	102.6	104.0	105.5	107.5	109.0

V_∞ = 199 fps
T_a = 55°F
RH_a = 71%
P_a = 14.27 psia

TABLE 4-VII

SAMPLE SIMULATED - FLIGHT DATA

```
DECK  LD  DATE       ENG  MOD ENG NO STNU C  OBS CORR
W631  315 05/21/76        -00 C00000 XARF 0 3644 3644
                                                                      DBTF JET NOISE TEST CONF. 1  2.2" DIA
                                                                       - NOZ.  TAPE 4914                10.2049

                              ANGLES AND TOTAL SPL RESULTING FROM SHEAR LAYER REFRACTION CORRECTIONS


                                                   ANGLES IN DEGREES

               80.    89.    99.   109.   119.   129.   140.   150.   160.

       TSPL    98.6   98.9   99.4  101.1  102.1  103.1  104.2  106.1  108.8

       SSPL    98.4   98.7   99.2  100.9  102.0  103.0  104.2  106.0  108.3


                                   ANGLES AND TOTAL SPL AFTER MOVING MEDIUM CORRECTIONS


                                             ANGLES IN DEGREES (NOISE EMISSION ANGLES)

               70.    79.    89.    99.   110.   121.   133.   146.   156.

       TSPL    99.0   99.1   99.3  100.7  101.5  102.2  103.2  105.0  107.3

       SSPL    98.8   98.9   99.1  100.6  101.4  102.2  103.1  104.9  106.8

                              ORIGINAL   MICROPHONE ANGLES

              70.0   80.0   90.0  100.0  110.0  120.0  130.0  140.0  150.0
```

TABLE 4-VIII

SAMPLE SIMULATED - FLIGHT DATA

```
DECK  LD  DATE       ENG  MOD ENG NU STND C  CLS CORR                DBTF JET NOISE TEST COMP. 1  2.2" DIA
W631  315 05/21/76        -00 000000 AAHF 0 3144 3444                . NOZ.  TAPE 4914              10.2049
```

SPL SPECTRA CORRECTED FOR SHEAR LAYER REFRACTION AND MOVING MEDIUM EFFECTS
(INTERPOLATED TO THE ORIGINAL ANGLES)

BAND CENTER FREQ (HZ)	NOISE EMISSION ANGLES IN DEGREES 70	80	90	100	110	120	130	140	150
100	79.4	78.8	76.4	76.7	71.0	69.1	71.8	75.8	82.3
125	76.0	77.4	74.7	73.8	69.4	71.2	71.9	74.2	81.0
160	73.8	76.3	73.6	73.9	71.4	71.3	71.4	74.8	78.5
200	74.7	76.5	73.8	75.8	72.6	73.7	76.6	78.2	77.8
250	75.3	66.2	76.5	76.4	77.7	77.0	76.9	81.0	79.5
315	76.4	79.1	79.2	78.7	77.6	77.6	78.0	80.6	86.8
400	79.4	78.9	78.7	79.2	78.2	78.4	81.5	83.2	87.7
500	78.8	77.8	78.8	79.1	79.4	81.3	83.4	86.8	90.7
630	80.2	80.1	80.4	81.0	81.4	82.6	84.4	87.4	92.2
800	85.4	82.3	83.1	84.0	83.3	83.8	86.3	90.2	94.9
1000	83.1	84.9	85.2	86.1	85.2	85.4	87.0	91.0	95.7
1250	84.4	84.8	84.4	86.4	87.2	87.3	88.8	92.2	96.1
1600	85.0	85.2	85.8	87.4	88.4	88.6	90.0	92.7	96.0
2000	85.6	86.6	88.1	89.0	88.9	89.7	91.6	93.6	95.7
2500	86.2	86.3	86.5	88.6	89.4	90.1	91.5	93.6	95.1
3150	86.3	86.7	87.5	88.7	89.4	90.2	91.6	93.5	94.0
4000	86.6	86.7	86.8	88.6	89.8	90.9	91.8	93.4	93.3
5000	86.9	87.3	87.2	89.2	90.2	91.2	92.2	93.1	92.3
6300	86.6	86.9	87.5	89.1	90.0	90.9	91.9	92.2	90.9
8000	87.2	86.6	87.2	88.9	90.2	91.4	91.5	91.7	90.0
10000	86.7	86.8	87.1	88.4	89.6	90.3	90.9	90.8	88.6
12500	86.3	86.3	86.5	88.2	89.1	89.8	90.1	89.3	87.6
16000	86.1	86.1	86.2	87.8	88.7	89.3	89.3	88.1	85.5
20000	85.1	85.2	85.4	86.7	87.7	88.1	87.9	86.6	83.7
25000	84.7	85.1	85.0	86.2	87.6	87.4	86.9	85.6	82.9
31500	84.0	84.2	84.4	85.5	86.5	86.8	85.8	84.3	81.6
40000	83.7	84.0	84.3	85.1	85.6	86.0	84.9	83.1	80.4
50000	83.4	83.4	84.0	85.2	85.3	85.4	84.2	82.4	79.8
63000	83.3	83.7	84.3	84.9	85.5	85.3	83.9	82.3	79.9
80000	83.8	83.8	84.3	85.1	85.3	85.0	83.7	81.9	79.7
TSPL	99.0	99.1	99.5	100.8	101.5	102.2	102.9	104.2	105.7
SSPL	98.8	98.9	99.3	100.7	101.5	102.1	102.9	104.1	105.5

V_∞ = 199 fps
T_a = 55°F
RH_a = 71%
P_a = 14.27 psia

TABLE 4-IX

SAMPLE MODEL SCALE ACOUSTIC DATA

```
                    20036F DBTF JET NOISE TEST CONF. 1  2.2" DIA. NOZ.  TAPE 4914          10.2049

              STAND XARF   RIG ID VT=199   TEST DATE 05/21/76   SCALE RATIO   0.0/1   RUN NUMBER 3644   CONDITION  3644
**********************************************************************************************************************
                                 PRIMARY  FAN              PRIMARY  FAN                          PRIMARY   FAN               PRIMARY   FAN
                   AREA   SQFT    0.0     0.0      SQM  0.0      0.0      MASS FLOW  LB/S     0.0       0.0  KG/S     0.0       0.0
                   P.R.           1.82    0.0           1.82     0.0      THRUST,IDL   LB    65.2       0.0     N   290.1       0.0
                   TEMP    (K)  707.0      0.0     (K)  392.8     0.0      THRUST,MEA   LB             0.0          N            0.0
                   RHO  LB/FT3  0.067    0.0    KG/M3  1.070    0.0      AREA (MOD) SQFT    0.03      0.0   SQM  0.003     0.0
                   VEL     FPS 1154.0     0.0     M/S  351.7     0.0      W (MODEL)  LB/S     1.8       0.0  KG/S    0.8       0.0
**********************************************************************************************************************

                             1/3 OCTAVE BAND MODEL  JET NOISE DATA   10.0FT RADIUS          THEORETICAL DAY SPL  -  (MODEL)
BAND
CENTER FREQ                                   MICROPHONE ANGLES IN DEGREES                                               POWER
(KHZ)   70     80     90    100    110    120    130    140    150                                                      1E-12W

.050    0.0    0.0    0.0    0.0    0.0    0.0    0.0    0.0    0.0                                                        0.0
.063    0.0    0.0    0.0    0.0    0.0    0.0    0.0    0.0    0.0                                                        0.0
.080    0.0    0.0    0.0    0.0    0.0    0.0    0.0    0.0    0.0                                                        0.0
.100   79.4   78.8   76.4   76.7   71.0   69.1   71.8   75.8   82.3                                                       94.8
.125   76.0   77.4   74.7   73.8   69.4   71.2   71.9   74.2   81.0                                                       93.1
.160   73.8   76.3   73.6   73.9   71.4   71.3   71.4   74.8   78.5                                                       92.3
.200   74.7   76.5   73.8   75.8   72.6   73.7   76.6   78.2   77.8                                                       93.9
.250   75.3   66.2   76.5   76.4   77.7   77.0   76.9   81.0   79.5                                                       95.3
.315   76.4   79.1   79.2   78.7   77.8   77.6   78.0   80.6   86.8                                                       97.8
.400   79.4   78.9   78.7   79.2   78.2   78.4   81.5   83.2   87.7                                                       98.9
.500   78.8   77.8   78.8   79.1   79.4   81.3   83.4   86.8   90.7                                                      100.8
.630   80.2   80.1   80.4   81.0   81.4   82.6   84.4   87.4   92.2                                                      102.2
.800   85.4   82.3   83.1   84.0   83.3   83.8   86.3   90.2   94.9                                                      104.7
1.00   83.1   84.9   85.2   86.1   85.2   85.4   87.0   91.0   95.7                                                      105.6
1.25   84.4   84.8   84.4   86.4   87.2   87.3   88.8   92.2   96.1                                                      106.7
1.60   85.0   85.2   85.8   87.4   88.4   88.6   90.0   92.7   96.0                                                      107.5
2.00   85.6   86.6   88.1   89.0   88.9   89.7   91.6   93.6   95.7                                                      108.4
2.50   86.2   86.3   86.5   88.6   89.4   90.1   91.5   93.6   95.1                                                      108.3
3.15   86.3   86.7   87.5   88.7   89.4   90.2   91.8   93.5   94.6                                                      108.3
4.00   86.6   86.7   86.8   88.6   89.8   90.9   91.8   93.4   93.3                                                      108.3
5.00   86.9   87.3   87.2   89.2   90.2   91.2   92.2   93.1   92.3                                                      108.5
6.30   86.6   86.9   87.5   89.1   90.0   90.9   91.9   92.2   90.9                                                      108.1
8.00   87.2   86.6   87.2   88.9   90.2   91.4   91.5   91.7   90.0                                                      108.0
10.0   86.7   86.8   87.1   88.4   89.6   90.3   90.9   90.8   88.6                                                      107.4
12.5   86.3   86.3   86.5   88.2   89.1   89.8   90.1   89.3   87.0                                                      106.7
16.0   86.1   86.1   86.2   87.8   88.7   89.3   89.3   88.1   85.5                                                      106.1
20.0   85.1   85.2   85.4   86.7   87.7   88.1   87.9   86.6   83.7                                                      105.0
25.0   84.7   85.1   85.0   86.2   87.6   87.4   86.9   85.6   82.9                                                      104.5
31.5   84.0   84.2   84.4   85.5   86.5   86.8   85.8   84.3   81.6                                                      103.6
40.0   83.7   84.0   84.3   85.1   85.8   86.0   84.9   83.1   80.4                                                      103.0
50.0   83.4   83.4   84.0   85.2   85.3   85.4   84.2   82.4   79.8                                                      102.6
63.0   83.3   83.7   84.3   84.9   85.5   85.3   83.9   82.3   79.9                                                      102.6
80.0   83.8   83.8   84.3   85.1   85.3   85.0   83.7   81.9   79.7                                                      102.5
100.    0.0    0.0    0.0    0.0    0.0    0.0    0.0    0.0    0.0                                                        0.0

                                                                                                            OAPWL =   120.0

OSPL   99.0   99.1   99.5  100.8  101.5  102.2  102.9  104.2  105.7
```

V_∞ = 199 fps
T_a = 55°F
RH_a = 71%
P_a = 14.27 psia

TABLE 4-X

SAMPLE FULL SCALE ENGINE ACOUSTIC DATA

```
                              20036F DBIF JET NOISE TEST CONF. 1  2.2" DIA. NOZ.  TAPE 4914            10.2049

                     STAND X&RF   X26 1D VT=199   TEST DATE 05/21/76   SCALE RATIO  22.5/1   RUN NUMBER 3644   CONDITION  3644
*****************************************************************************************************************************
                                     PRIMARY  FAN                 PRIMARY  FAN                          PRIMARY  FAN           PRIMARY  FAN
                       AREA   SQFT  13.67     0.0       SQM   1.270     0.0      MASS FLOW  LB/S  921.4        0.0  KG/S  417.9       0.0
                       P.R.          1.62     0.0             1.62      0.0      THRUST,IDL   LB33020.7        0.0     N*******       0.0
                       TEMP    (R)  617.6     0.0       (K)   342.6     0.0      THRUST,MEA   LB            0.0        N            0.0
                       RHO  LB/FT3  0.067    0.0     KG/M3   1.070    0.0        AREA (MOD) SQFT   0.03      0.0    SQM  0.003   0.0
                       VEL     FPS 1154.0     0.0       M/S   351.7     0.0      W (MODEL)  LB/S    1.8        0.0  KG/S    0.8       0.0
*****************************************************************************************************************************

FAA DAY                                1/3 OCTAVE BAND ENGINE JET NOISE DATA  150.0FT RADIUS           (SCALED ENGINE)
BAND
CENTER  FREQ                                         MICROPHONE ANGLES IN DEGREES                                                POWER
(KHZ)    70      80      90     100     110     120     130     140     150                                                     1E-12W

.050    87.9    88.3    87.9    89.9    90.7    90.8    92.3    95.7    99.6                                                     137.3
.063    88.5    88.7    89.3    90.9    91.9    92.1    93.5    96.2    99.5                                                     138.0
.080    89.1    90.1    91.6    92.5    92.4    93.2    95.1    97.1    99.2                                                     139.0
.100    89.7    89.8    90.0    92.1    92.9    93.6    95.0    97.1    98.6                                                     138.8
.125    89.8    90.2    91.0    92.2    92.9    93.7    95.3    97.0    97.5                                                     138.8
.160    90.1    90.2    90.3    92.1    93.3    94.4    95.3    96.9    96.6                                                     138.9
.200    90.4    90.8    90.7    92.7    93.7    94.7    95.7    96.6    95.8                                                     139.0
.250    90.1    90.4    91.0    92.6    93.5    94.4    95.4    95.7    94.4                                                     138.6
.315    90.6    90.0    90.6    92.3    93.6    94.6    94.9    95.1    93.4                                                     138.5
.400    90.1    90.2    90.5    91.8    93.0    93.7    94.3    94.2    92.0                                                     137.8
.500    89.7    89.7    89.9    91.6    92.5    93.2    93.5    92.7    90.4                                                     137.1
.630    89.5    89.5    89.6    91.2    92.1    92.7    92.7    91.5    88.9                                                     136.5
.800    88.4    88.5    88.7    90.0    91.0    91.4    91.2    89.9    87.0                                                     135.3
1.00    88.0    88.4    88.3    89.5    90.9    90.7    90.2    88.9    86.2                                                     134.8
1.25    87.2    87.4    87.6    88.7    89.7    90.0    89.0    87.5    84.8                                                     133.8
1.60    86.8    87.1    87.4    88.2    88.9    89.1    88.0    86.2    83.5                                                     133.1
2.00    86.4    86.4    87.0    88.2    88.3    88.4    87.2    85.4    82.8                                                     132.6
2.50    86.1    86.5    87.1    87.7    88.3    88.1    86.7    85.1    82.7                                                     132.5
3.15    86.4    86.4    86.9    87.7    87.9    87.6    86.3    84.5    82.3                                                     132.2
4.00     0.0     0.0     0.0     0.0     0.0     0.0     0.0     0.0     0.0                                                       0.0
5.00     0.0     0.0     0.0     0.0     0.0     0.0     0.0     0.0     0.0                                                       0.0
6.30     0.0     0.0     0.0     0.0     0.0     0.0     0.0     0.0     0.0                                                       0.0
8.00     0.0     0.0     0.0     0.0     0.0     0.0     0.0     0.0     0.0                                                       0.0
10.0     0.0     0.0     0.0     0.0     0.0     0.0     0.0     0.0     0.0                                                       0.0

                                                                                                                     OAPWL =  149.9

OSPL   101.7  101.9  102.3  103.7  104.6  105.3  105.9  106.9  107.6
PNL    109.9  110.1  110.5  111.6  112.2  112.4  112.0  111.4  110.0

                 200. SIDELINE
PNL    106.7  107.2  107.8  106.8  106.9  106.4  106.6  104.6  101.1

                 370. SIDELINE
PNL    100.7  101.3  101.8  102.8  103.0  102.4  100.9   98.7   95.3

                 800. SIDELINE
PNL     92.4   93.0   93.7   94.7   94.9   94.2   92.9   91.6   87.4

                2128. SIDELINE
PNL     80.6   81.3   81.8   83.0   83.4   83.1   81.9   79.9   75.8
```

The ambient values of tunnel velocity, V_∞; temperature, Ta; relative humidity, RH_a, and pressure, P_a, present during the model test are listed on the right hand side of each data page, Tables 4-VI to 4-X.

Below the title are the tabulated, as measured model scale one-third octave band sound pressure levels at a 3.05 m (10 ft) polar distance under free-field measurement conditions during a "theoretical day" with the tunnel background noise removed. The center frequencies of the 30 measured one-third octave bands from 100 Hz to 80K Hz are listed in the left hand column. The one-third octave band sound pressure levels for each microphone measuring angle 70° to 150° at each 10 degree increments are listed in the appropriate columns. Below the one-third octave band sound pressure level where the total sound pressure level (TSPL) is the integration from 100 Hz to 80K Hz and the sum of sound pressure level (SSPL) is the integration from 500 Hz to 80K Hz. For certain conditions of high tunnel flow and nozzle velocities in the low end of the test matrix, the frequencies below 500 Hz were contaminated by a background noise. Nominal tunnel background noise had been measured by running the nozzle and tunnel at exactly the same speed. This nominal background noise was removed from the measured data. The "extra" low frequency noise is thought to be to an interaction of the jet and tunnel flows (when the model and tunnel jet velocities were not equal) and could not be separated from the data. Thus, for the in-flight conditions, SSPL was used as the overall sound pressure level. Since this spurious noise was below 500 Hz in the model data, it would be present at frequencies only below 25 Hz for a full size engine. Therefore, it can be removed without introducing an error in the overall noise characteristics.

Table VII is a sample data page of the model data on a theoretical day with the shear layer and moving medium corrections. At the top of the page is listed the title for data identification. Below the title are listed the corrected angles and overall sound pressure levels (TSPL) and (SSPL) at a 3.05 m (10 ft) radius after the shear layer refraction correction. Below the shear layer refraction correction data are listed the corrected angles (i.e., noise emission angles) and overall sound pressure levels (TSPL) and (SSPL) at a 3.05 m (10 ft) radius after the moving medium correction.

Table 4-VIII is a sample page of the model data on a theoretical day with shear layer and moving medium corrections and with the noise data interpolated to the original angles (i.e., 70° to 150° at each 10 degree increments). At the top of the page is listed the title for data identification. Below the title are the interpolated, model scale one-third octave band sound pressure levels at a 3.05 m (10 ft) radius on a "theoretical day." The center frequencies of the 30 measured one-third octave bands from 100 Hz to 80K Hz are listed in the left hand column. The one-third octave band sound pressure levels for each microphone measuring angle 70° to 150° at each 10 degree increments are listed in the appropriate columns. Below the one-third octave band sound pressure levels are listed the 3.05 m (10 ft.) radius overall sound pressure level TSPL and SSPL for each angle.

Table 4-IX is a sample of a final data page. At the top of the page are listed the pertinent ambient and nozzle operating parameters in both U.S. customary units as well as the International System of Units (S.I.).

The left hand columns list the full scale primary and fan stream exhaust nozzle areas (AREA) as equal to zero to indicate that the noise data are in model scale form. In the same columns are found the stream total to ambient pressure ratio (P.R.) stream temperature (TEMP), and stream density (RHO), and the ideally expanded velocity (VEL). The right hand columns list the full scale mass flow (MASS FLOW) as equal to zero to indicate that the noise data are in scale model form. Also listed in this column are the model size ideal thrusts (THRUST, IDL), exhaust nozzle areas (AREA MOD), and mass flows (W MODEL).

Below the parameter listing which defines the test conditions are the tabulated, model scale one-third octave band sound pressure levels at a 3.05 m (10 ft) polar distance under free-field measurement conditions during a "theoretical day." The center frequencies of the 30 measured one-third octave bands from 100 Hz to 80K Hz are listed in the left hand column. The one-third octave band sound pressure levels for each microphone measuring angle, 70° to 150° for each 10° increments, at each one-third octave band are listed in the appropriate columns. This format is used both for the static data and the "simulated flight" data which are directly comparable.

The one-third octave band power levels (referenced to 10^{-12} watts) are listed at the extreme right hand side of the page. Below the one-third octave band sound pressure and sound power levels are listed the 3.05 m (10 ft) radius overall sound pressure level (OSPL) for each angle and the overall sound power level (OAPWL). The OSPL represents the total noise contained in the frequency range from 100 to 80K Hz and thus contains the spurious low frequency noise below 500 Hz discussed previously. The overall sound pressure excluding the spurious noise is the SSPL term in Table 4-VIII.

At selected test points, the theoretical day noise data were scaled to represent a full size SCAR engine having linear dimensions corresponding to a 1.27 m (50 in) equivalent nozzle diameter (22.5 times the model size). Thus, the "simulated flight" and static model SPLs were increased by 20 log 22.5 to produce full scale engine noise characteristics. The full scale SPLs were extrapolated to 45.7 m radius, and corrected from a "theoretical day" to a standard FAA day by applying the spherical divergence law, Δ dB = 20 log r_2/r_1 and the atmospheric attenuation corrections of SAE ARP 866 (Ref. 11). Overall sound pressure levels (OSPLs) were determined by integrating the SPLs from 100 Hz to 8000 Hz.

For these selected test points, perceived noise levels (PNLs) were computed according to SAE ARP 865A (Ref. 12) from the SPL spectra and extrapolated to various sideline distances at zero altitude. As with all of the data in this report, the acoustic levels are based on free field conditions. Sound power level spectra and overall power level were determined individually for the model data and data scaled to full size by spatial integration over the nine microphone positions from the listed SPLs and OASPLs assuming symmetry about the jet axis of the noise generation. Since the theoretical day model scale data represent the noise that would be measured if no atmospheric absorption were present, the power levels represent noise generation at the source. The full scale data, however, represent noise that would be measured on a standard FAA day. Thus the full scale power levels represent an integration of the far field noise levels on a standard FAA day, reflecting the common method for comparing full scale data. The actual power level calculations employed were:

$$\text{PWL} = 10 \log \left(\frac{W}{W_{ref}} \right) = \text{sound power level, in decibels}$$

where: $W = \sum_{i=1}^{n} \frac{P_i^2}{\rho_o C} \Delta A_i$ = the acoustic power, in watts

$W_{ref} =$ 10^{-12} watts = the reference power level

$P_i^2 =$ $10^{\left(\frac{SPL}{10}\right)}$ P_{ref}^2 = mean square sound pressure

$P_{ref} =$ 20×10^{-6} N/m^2 = reference acoustic pressure

$\rho_o =$ atmospheric density

$C =$ atmospheric speed of sound

$n =$ number of microphones

$\Delta A_i =$ surface of spherical segment associated with ith microphone.

- **for the first microphone**

$$\Delta A_i = 2\pi r^2 \left[\cos\theta_1 - \cos\left(\frac{\theta_1 + \theta_2}{2}\right)\right] \qquad i = 1$$

- **for intermediate microphones**

$$\Delta A_i = 2\pi r^2 \left[\cos\left(\frac{\theta_{i-1} + \theta_i}{2}\right) - \cos\left(\frac{\theta_i + \theta_{i+1}}{2}\right)\right] \qquad i = 2, \ldots .\, n-1$$

- **for the last microphone**

$$\Delta A_i = 2\pi r^2 \left[\cos\left(\frac{\theta_{i-1} + \theta_i}{2}\right) - \cos\theta_i\right] \qquad i = n$$

where: r = distance of microphone from nozzle

As the characteristics of the test facility ensure far-field acoustic signals free from ground reflections, all acoustic values calculated from the measured data are also free field. The extrapolated values do not include extra ground attenuation.

The acoustic data for the full scale engine are compiled on computer output sheets in the Comprehensive Data Report. Table 4-X is a sample data page. This data page has the same format as does the final model data page (Table 4-IX) except for the following.

1) In the heading, the AREA represents the nozzle area of the full scale engine.

2) The noise data are for a standard FAA day.

3) Below the OSPLs are listed the perceived noise levels (PNL) at a 45.7 m (150 ft) polar and at various sideline distances from 61 m (200 ft) to 648.6 m (2128 ft). These PNLS include air attenuation per reference 11. Extra ground attenuation corrections have not been applied.

4.3 COMPARISON WITH OUTDOOR RESULTS

In order to establish the validity of the noise data measured in the acoustic wind tunnel, results from the static runs were compared with the outdoor results from Task IV of contract NAS3-17866. In NASA CR-2628 (Reference 1), it was shown that the reference convergent nozzle data and the coannular nozzle data for conditions where the coannular nozzle was operated as a conventional turbofan (i.e., $V_f < V_p$) agreed with established predictions. In order to validate the current results, the Reference 1 data were scaled to represent the nozzle size and microphone location used in the acoustic tunnel tests. Comparisons of the one-third octave band SPL spectra at 90° and 150° and OASPL directivity are shown in Figure 4.3-1 A and B for the convergent nozzle at subsonic and supersonic conditions, respectively. Results of the static runs from the two test facilities (acoustic wind tunnel and outdoor) showed good agreement. At both subsonic and supersonic jet conditions, a difference of less than 2 dB is observed around the peak jet noise frequencies and elsewhere the difference is less than 4 dB. In terms of OASPL directivity, the data agree within 2 dB for all angles. Similar results were obtained for the 0.75 and 1.2 area ratio coannular nozzles. Typical comparisons are shown in Figure 4.3-2A and B for 0.75 area ratio coannular nozzle at subsonic and supersonic fan conditions. From these comparisons, it can be concluded that the data obtained in the acoustic wind tunnel compare well with data obtained from the outdoor facility.

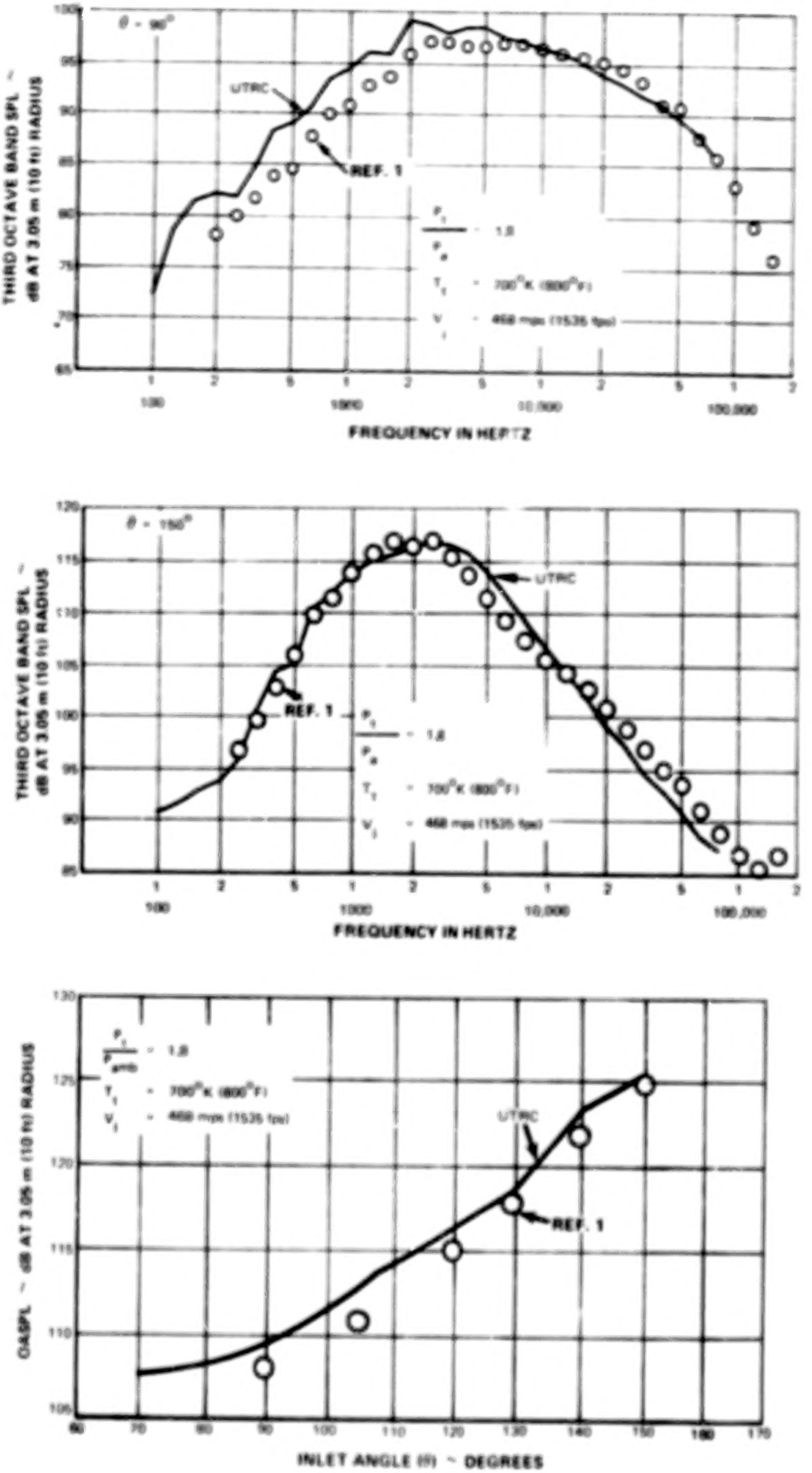

Figure 4.3-1A *Comparison of Wind Tunnel (UTRC) and Outdoor Stand (Ref. 1) Static Data for Convergent Nozzle Model Data at Subsonic Jet Velocity, Nozzle Exit Area, A_T = .0025 in^2 (3,89 in2)*

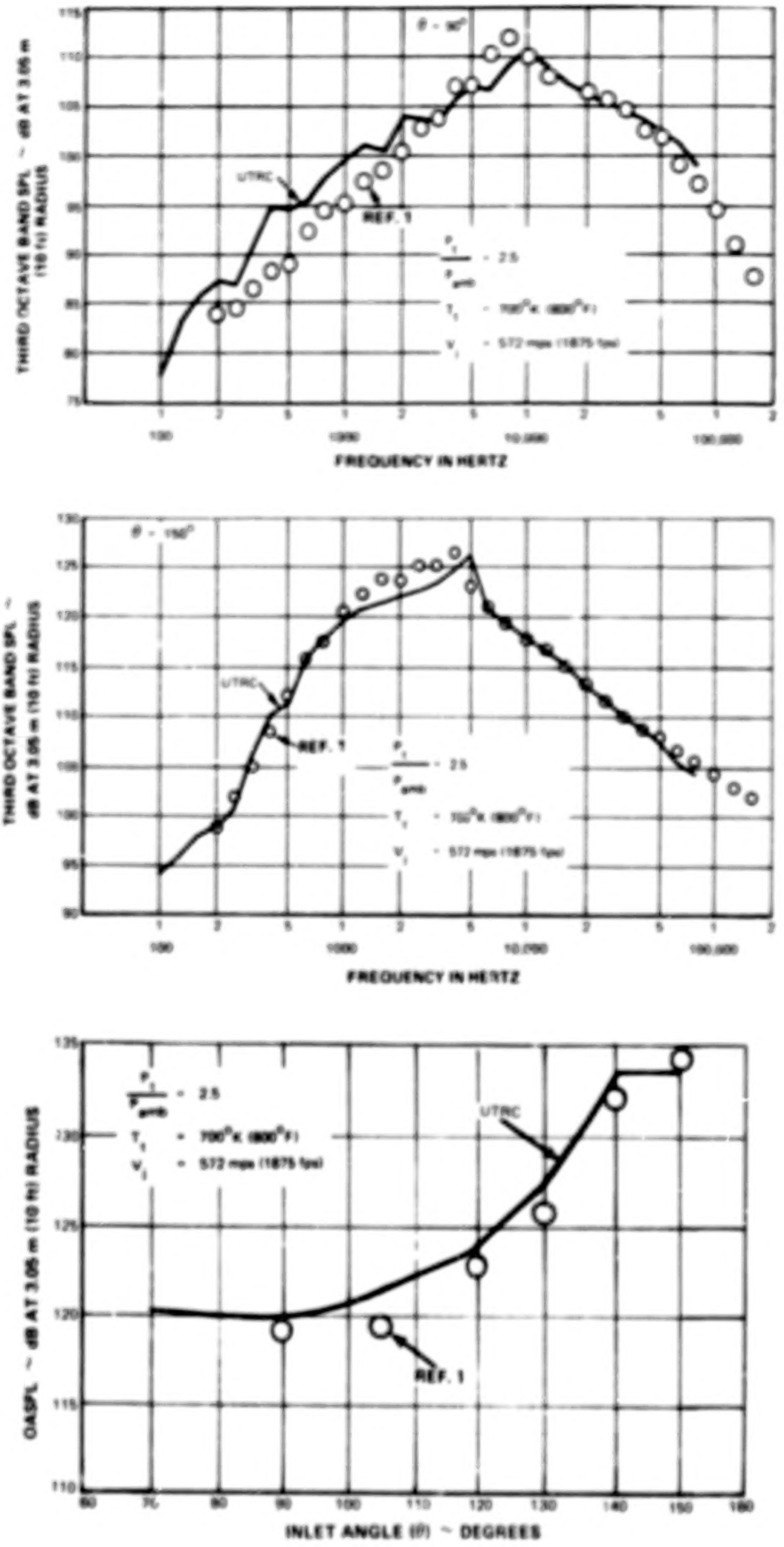

Figure 4.3-1B *Comparison of Wind Tunnel (UTRC) and Outdoor Stand (Ref. 1) Static Data for Convergent Nozzle Model Data at Supersonic Jet Velocity, Nozzle Exit Area,* $A_T = .0025$ *in*^{2} *(3.89 in*^{2}*)*

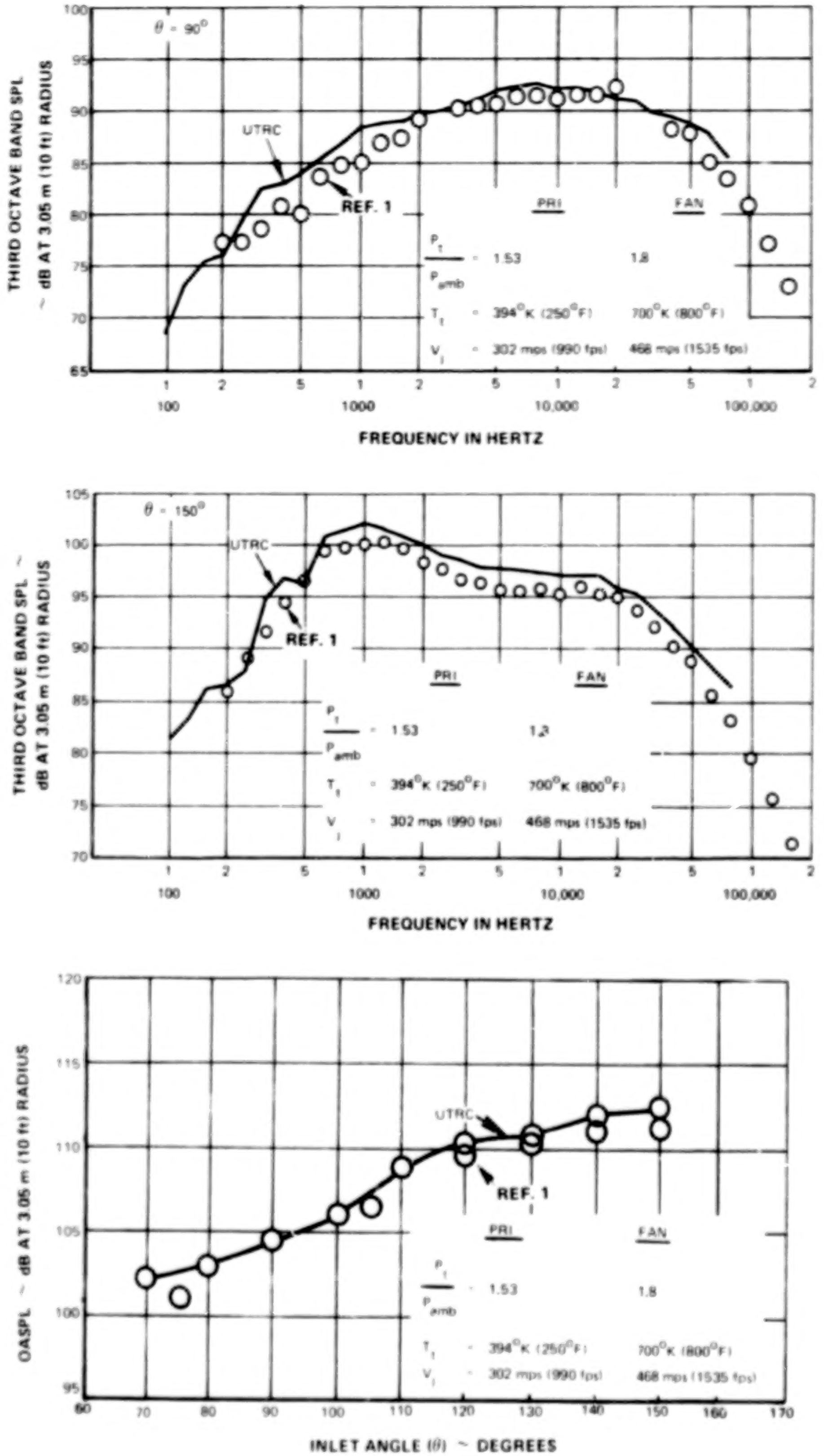

Figure 4.3-2A Comparison of Wind Tunnel (UTRC) and Outdoor Stand (Ref. 1) Static Data for 0.75 Area Ratio Coannular Nozzle Model Data at Subsonic Fan Jet Velocity Nozzle Exit Area, A_T = .0025 in ^{2} (3.89 in ^{2})

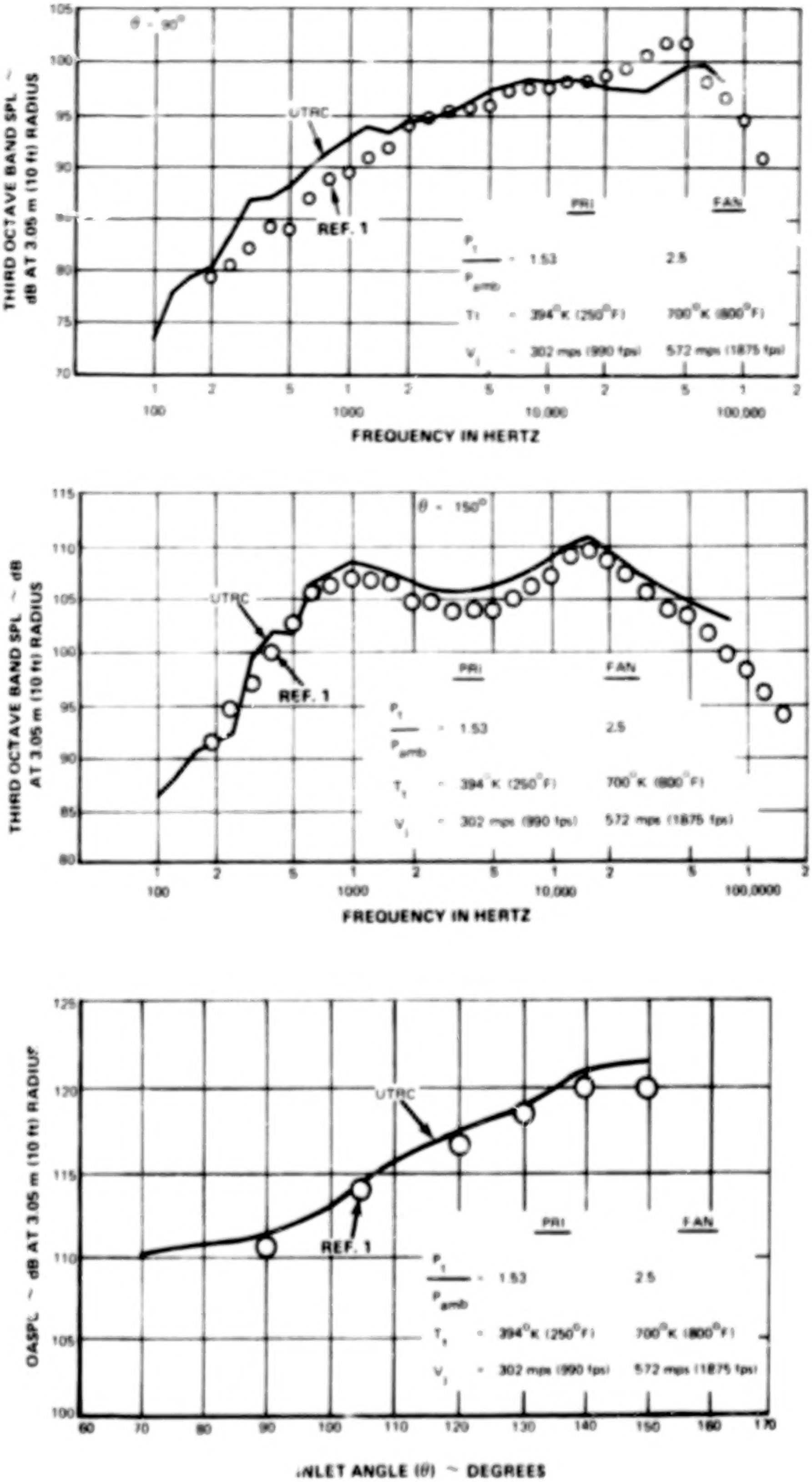

Figure 4.3-2B Comparison of Wind Tunnel (UTRC) and Outdoor Stand (Ref. 1) Static Data for 0.75 Area Ratio Coannular Nozzle Model Data at Supersonic Jet Velocity Nozzle Exit Area, $A_T = .0025\ in^2\ (3.89\ in^2)$

4.4 COANNULAR NOISE SYNTHESIS

This procedure estimates the sound power level from a coannular nozzle to be equal to the sum of the sound power levels from two independent convergent nozzle single jets whose areas are the same as the fan and primary nozzle areas, as shown in Figure 4.4-1. The operating conditions of the individual jets are taken to be equal to the fan and primary conditions, respectively, of the coannular nozzle. To allow accurate prediction on this basis, the reference convergent nozzle was tested at all of the fan and primary conditions in the coannular nozzle test matrix. The convergent nozzle test data were scaled in level to the appropriate exhaust areas, and scaled for frequency to the equivalent circular diameters of the primary and fan nozzle areas, respectively. The scaled data were then added logarithmically, as shown in Figure 4.4-1.

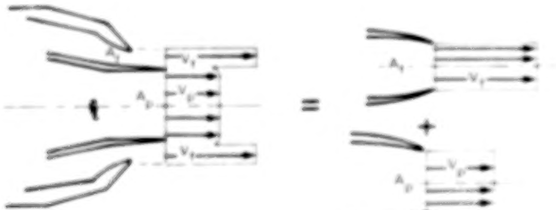

- SYNTHESIZED NOISE OF COANNULAR NOZZLE = SUM OF NOISE FROM INDEPENDENT CIRCULAR JETS AT PRIMARY AND FAN STREAM CONDITIONS
- $(\text{POWER LEVEL})_{\text{SYN}} = 10\,\text{LOG}\left[\text{LOG}^{-1}\left(\frac{\text{PWL}}{10}\right)_p + \text{LOG}^{-1}\left(\frac{\text{PWL}}{10}\right)_f\right]$
- $\text{PERCEIVED NOISE LEVEL (PNL)} = 10\,\text{LOG}\left[\text{LOG}^{-1}\left(\frac{\text{PNL}}{10}\right)_p + \text{LOG}^{-1}\left(\frac{\text{PNL}}{10}\right)_f\right]$

Figure 4.4-1 Coannular Jet Noise Synthesis Procedure

It has been shown in Reference 1 that the synthesis provides a reasonable prediction of the coannular noise (for $V_f/V_p > 1$) only at very low and very high frequencies, and significantly over estimates the noise in the middle frequency range. The synthesis, however, is useful as a base against which to compare results. Therefore, the synthesis was extended to handle the in-flight case using the simulated in-flight convergent nozzle data. Typical overall sound pressure level predictions based on this synthesized model are shown in Figure 4.4-2 for the 0.75 area ratio coannular model at the subsonic and supersonic fan conditions. The measured data are also shown in the figures for comparison. The measured levels are substantially lower (up to 10 dB) for both subsonic and supersonic fan conditions. These differences, which had been reported previously (ref. 1), based on static conditions are now seen to be retained in-flight. Similar results were observed for the 1.2 area ratio coannular nozzle. A more detailed discussion of the comparison of predictions based on the synthesis and measured data is presented in Section 5.1.2.

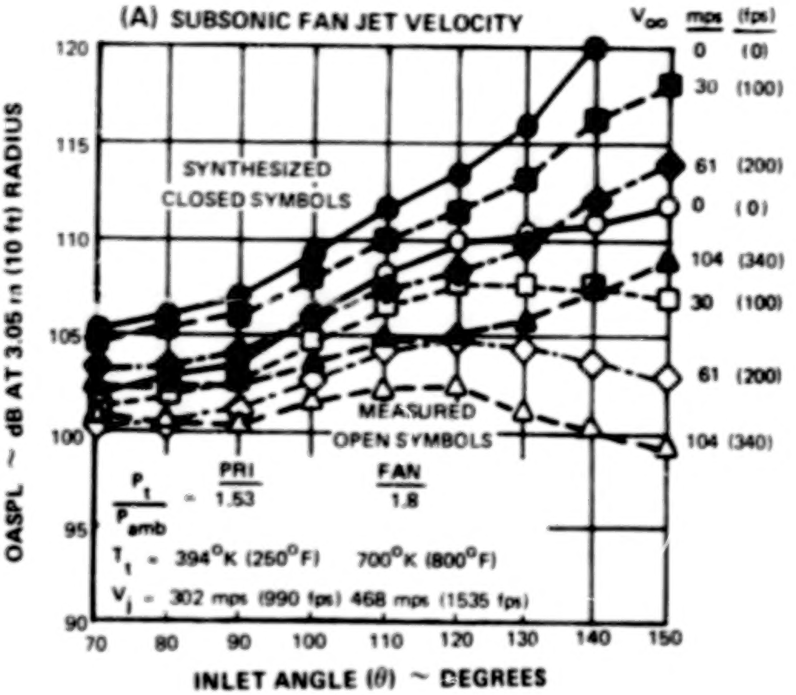

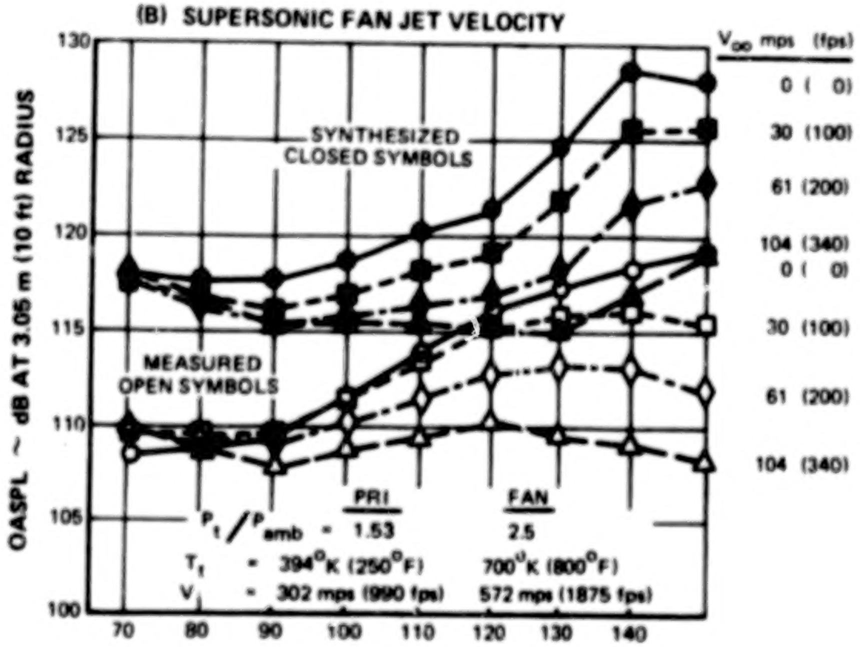

Figure 4.4-2 *Comparison of Measured and Synthesized OASPL Directivity for 0.75 Area Ratio Coannular Nozzle Model*

5.0 RESULTS AND DISCUSSION

The acoustic and aerodynamic results obtained from this program are presented in this section. The results are discussed at test conditions selected to best illustrate important characteristics and conclusions. The complete acoustic and aerodynamic data are contained in the Comprehensive Data Report, (Ref. 9).

5.1 DISCUSSION OF ACOUSTIC RESULTS

This experimental investigation produced data showing the effects of relative velocity typical of VSCE jet exhausts on jet noise of several coannular nozzles. In the following sections, a discussion of the relative velocity effects on the various configurations is presented. The noise characteristics of the various configurations are presented in terms of one-third octave band sound pressure spectra, overall sound pressure level directivity, and relative velocity exponents. A correlation of noise and measured velocity profiles is included. The data are presented in model scale and have been corrected to a theoretical day and "simulated flight" conditions (with tunnel shear layer refraction and moving medium corrections applied). A complete listing of the overall sound pressure levels for each angle and the overall power level is contained in Appendix A (Part 1) for all configurations at all operating conditions.

In this test program an arrangement of eight tabs was placed symmetrically around the nozzle lip of each configuration in order to suppress shock screech. A detailed discussion on the lip modification investigation is contained in Appendix B.

5.1.1 Acoustic Results

5.1.1.1 Reference Convergent Nozzle

The reference convergent nozzle tests provided data not previously available, namely the determination of the effect of flight on the noise of a conical jet at supersonic operating conditions free of the presence of shock screech. In addition, the data were used in the coannular synthesis noise prediction discussed in Section 4.4. The effect of increasing flight speed on the jet noise spectrum for a single jet at subsonic conditions is shown in Figures 5.1.1-1A and B for the 90° and 150° angles, respectively. These data are representative of all the subsonic jet data obtained during the tests and show two important effects. First, the noise reductions are much larger at rear angles than at the side angles. Secondly, the spectral comparisons show more noise reduction obtained in the lower frequencies, especially for the aft angles. The increase in SPL at high values of frequency for the static spectrum is thought by the authors to be caused by the application of theoretical air absorption corrections. This increase occurred for conditions of high chamber temperatures and very low humidity, where the theoretical corrections are very large. The actual existence of the increased SPLs at high frequency is questionable. However, in order to maintain consistency in presentation of the data, the atmospheric absorption corrections have been applied as defined in reference 11. The effect on OASPL of the SPL increase at very high frequencies is small since most of the contribution to OASPL derives from the range of frequencies below 30K. Appendix C contains a complete discussion on this topic.

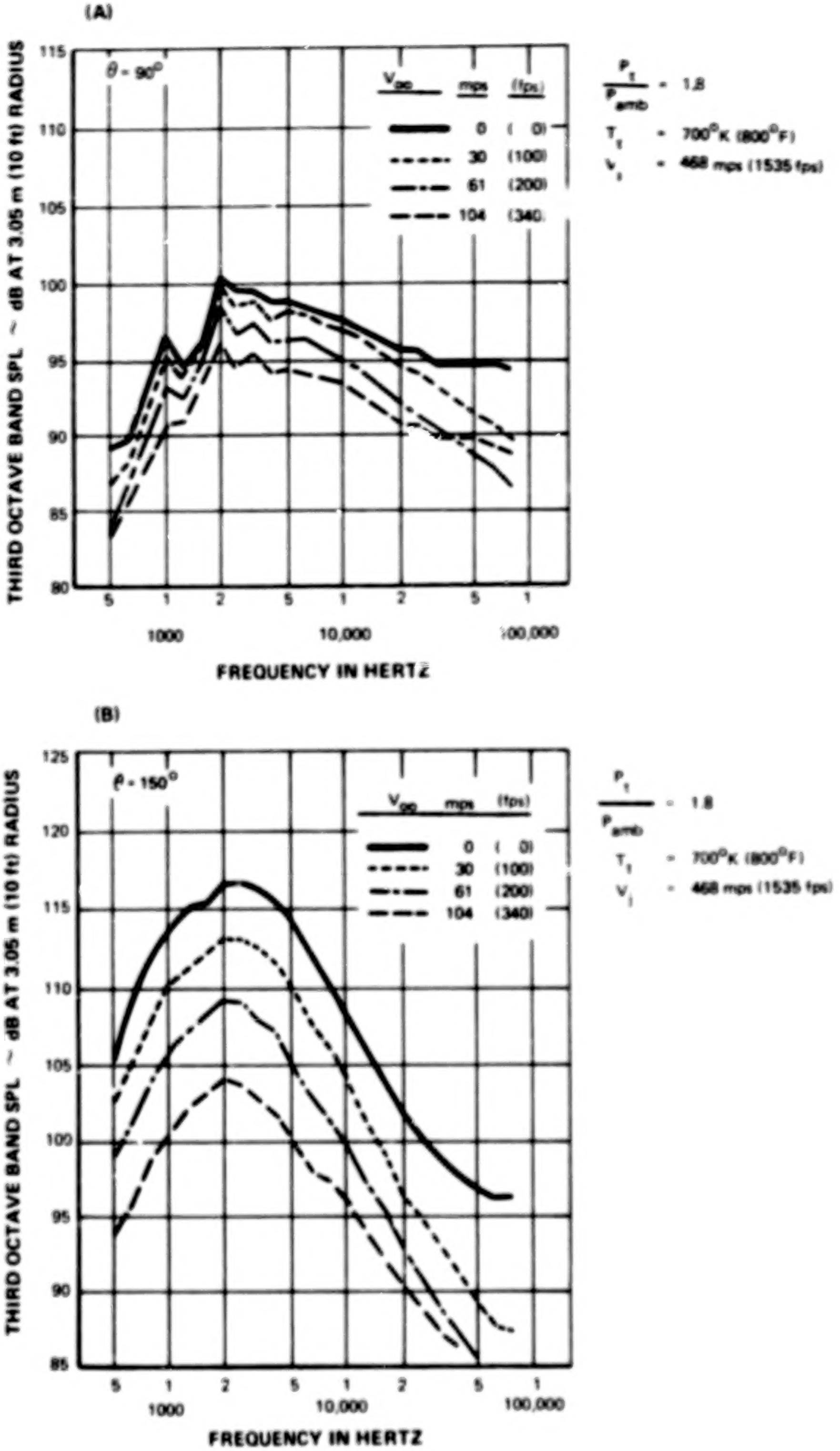

Figure 5.1.1-1 Effect of Relative Velocity on Spectra of Convergent Nozzle Model At Subsonic Jet Velocity

Polar OASPL directivity plots are shown in Figure 5.1.1-2 for the convergent nozzle over the range of external velocities tested. This figure shows that the OASPLs at all angles are reduced with increasing tunnel velocity and that the reductions are larger at the aft angles. These subsonic jet noise results agree well with the previous investigation as reported in reference 4.

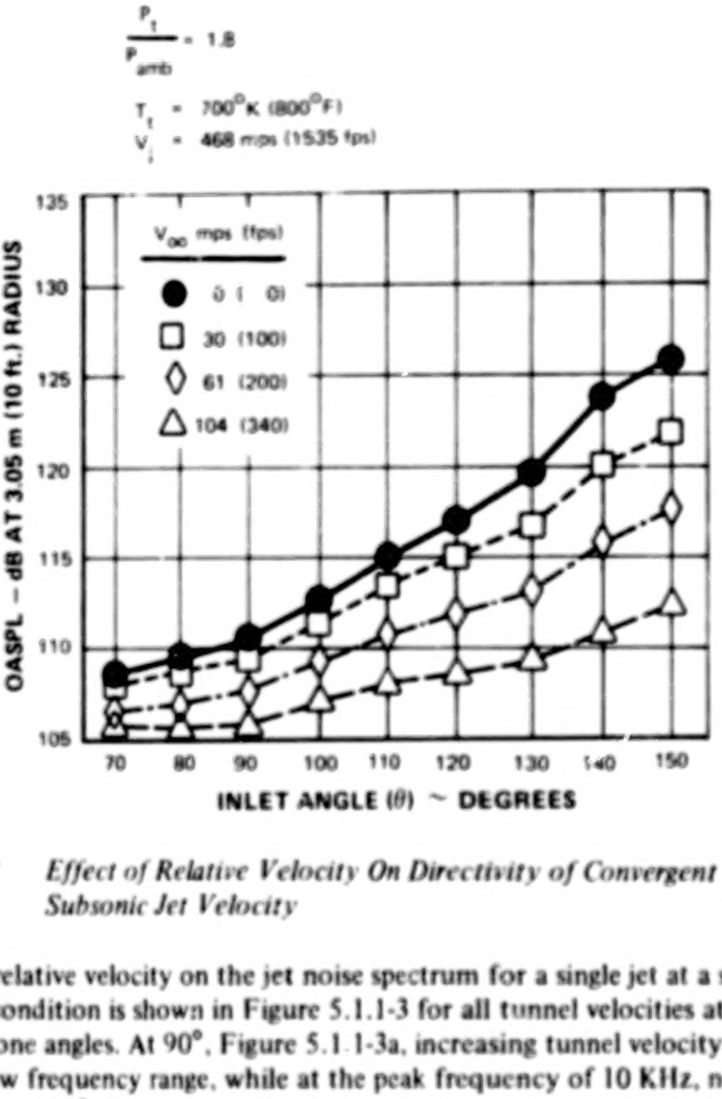

Figure 5.1.1-2 Effect of Relative Velocity On Directivity of Convergent Nozzle Model At Subsonic Jet Velocity

The effect of relative velocity on the jet noise spectrum for a single jet at a supersonic nozzle operating condition is shown in Figure 5.1.1-3 for all tunnel velocities at the 90° and 150° microphone angles. At 90°, Figure 5.1.1-3a, increasing tunnel velocity decreased the levels in the low frequency range, while at the peak frequency of 10 KHz, no change in level occurred. At θ = 150°, Figure 5.1.1-3b, the levels were reduced with increasing tunnel velocity at all frequencies. The effect of tunnel velocity on OASPL directivity, shown in Figure 5.1.1-4, shows a consistent decrease in noise level at angles greater than 100°, and small changes forward of 90°. Also, the noise reduction due to tunnel velocity is seen to increase with increasing angle similar to the subsonic case discussed previously. The noise level is essentially unchanged in the most forward angles due to the lack of reduction in the peak frequency levels as was illustrated for θ = 90° in Figure 5.1.1-3a. This broadband noise is produced by the interaction of turbulence with the shock system produced by the underexpanded jet. (It is not to be confused with shock screech noise, which is characterized by a series of discrete tones produced by a coherent feedback mechanism present in some model jet tests.) As discussed in Appendix B, the model nozzles were designed to eliminate shock

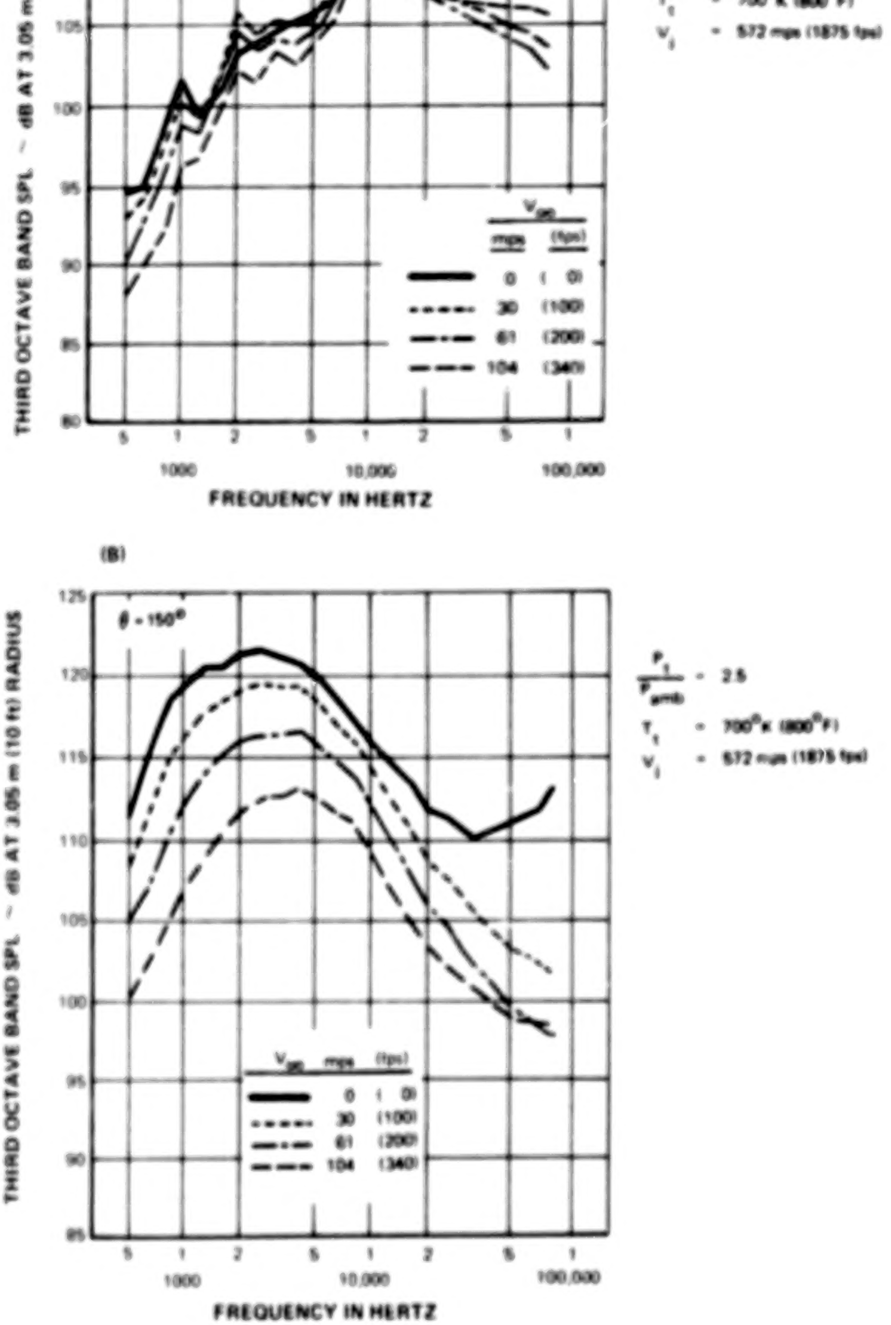

Figure 5.1.1-3 Effect of Relative Velocity On Spectra of Convergent Nozzle Model At Supersonic Jet Velocity

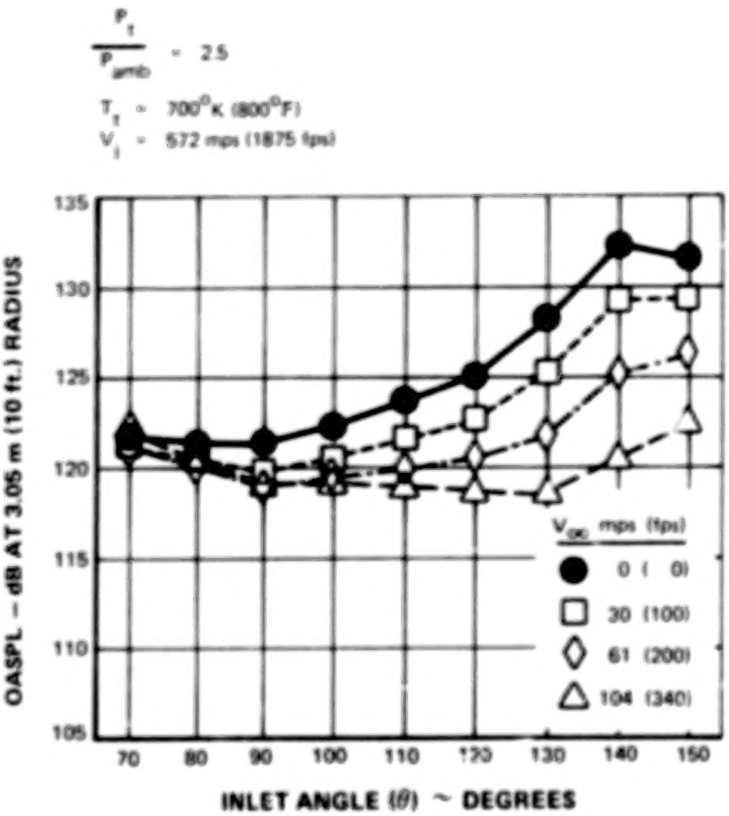

Figure 5.1.1-4 Effect of Relative Velocity On Directivity of Convergent Nozzle Model At Supersonic Jet Velocity

screech. The broadband shock noise present in the spectrum was compared to predictions using the method of Harper-Bourne and Fisher (Ref. 13) in Figure 5.1.1-5. The broadband lump in the data is accurately predicted by this shock noise procedure. The difference observed in the low frequencies is due to the jet mixing noise present in the data (which is not accounted for in the predicted spectra), and the difference in the higher frequencies is attributed to the atmospheric air attenuation correction.

To summarize the results presented in this section, the jet mixing noise of the reference convergent nozzle was reduced at all angles with tunnel speed, while the shock noise component was either unchanged or amplified depending on the angle.

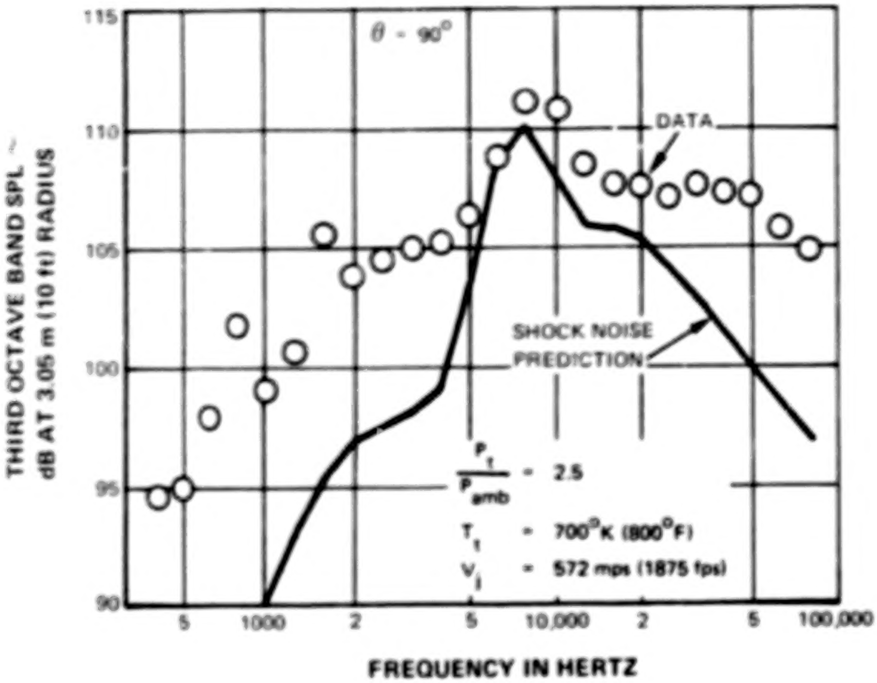

Figure 5.1.1-5 Comparison of Convergent Nozzle Model Data With Broadband Shock Noise Prediction From Reference 13, At Static Conditions

5.1.1.2 0.75 Area Ratio Coannular Nozzle

The effect of relative velocity on the jet noise spectrum of the 0.75 fan to primary area ratio coannular nozzle at a subsonic fan condition is shown in Figures 5.1.1-6a and b for 90° and 150°, respectively. The noise reduction at 90° is similar to that of the reference convergent nozzle configuration. However, the coannular nozzle noise is reduced more at low frequencies and less at high frequencies compared to the single jet results. At 150°, the coannular jet noise spectrum shows the double peak characteristics typical of coannular nozzles having $V_f > V_p$. As discussed in References 1 and 3, the low frequency peak is generated by the merged jet well downstream of the nozzle and the high frequency peak is generated by the premerged fan jet close to the nozzle. The portion of the spectrum caused by the merged jet shows more noise reduction than that due to the pre-merged jet because of the merged jet's lower velocity, which makes it more sensitive to tunnel velocity. The polar OASPL directivity for the subsonic fan condition is shown in Figure 5.1.1-7. It shows noise is reduced with tunnel velocity and the reduction increases for aft angles as was seen for the single jet. Typical spectra for the supersonic fan condition at 90° and 150° are shown in Figure 5.1.1-8a and b, respectively. At 90°, the high frequency noise increases with tunnel velocity, while the noise at the lower frequencies is reduced with tunnel velocity. This high frequency noise has been tentatively identified as the broadband shock noise generated by the interaction of turbulence with the shocks present in the underexpanded supersonic fan exhaust. It is similar to the shock noise present in the reference convergent nozzle data at supersonic conditions but occurs at higher frequencies due to the smaller characteristic dimension of the annular nozzle compared to that of the single circular jet nozzle. At 150°, the noise spectrum is dominated by the jet mixing noise and thus shows decreases at all frequencies with tunnel speed, similar to the results at subsonic conditions.

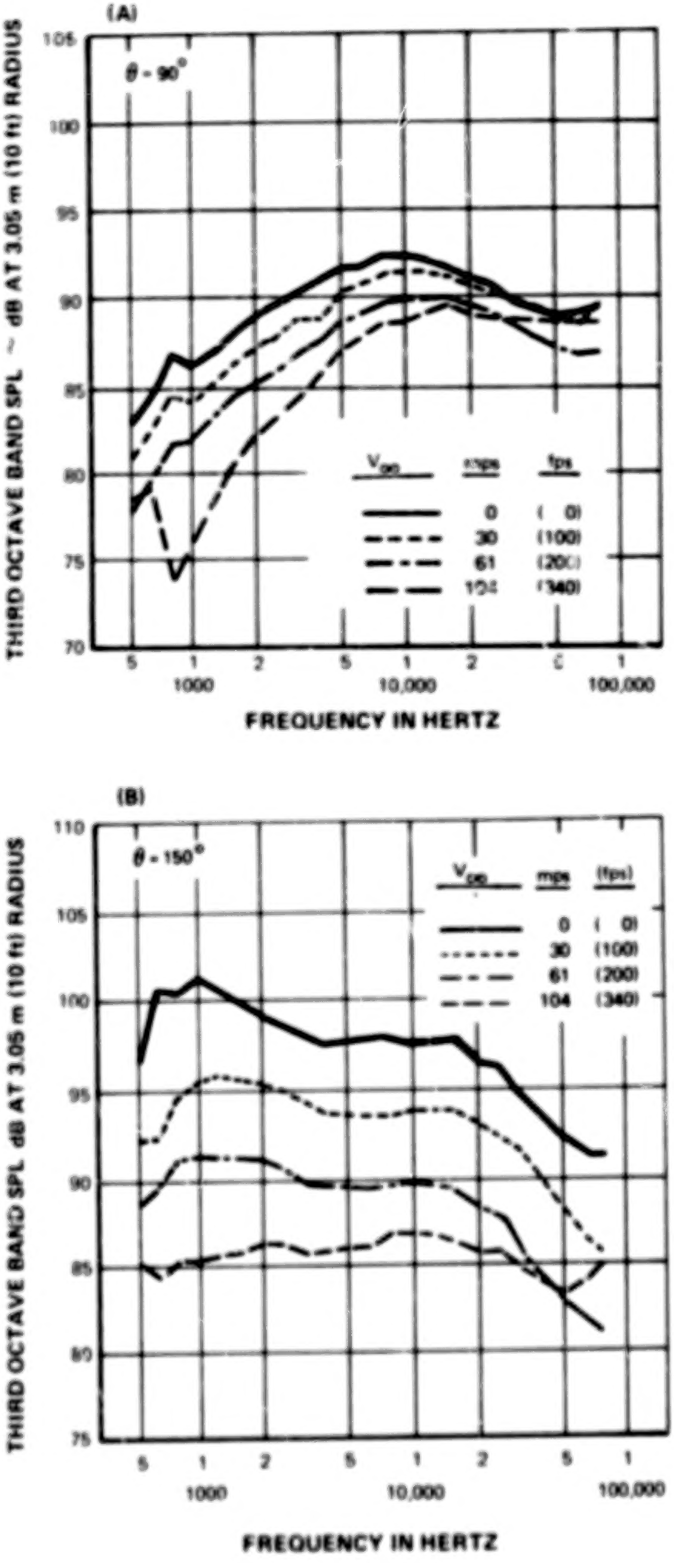

		PRI	FAN
$\frac{P_t}{P_{amb}}$	=	1.53	1.8
T_t	=	394°K (250°F)	700°K (800°F)
V_j	=	302 mps (990 fps)	468 mps (1535 fps)

		PRI	FAN
$\frac{P_t}{P_{amb}}$	=	1.53	1.8
T_t	=	394°K (250°F)	700°K (800°F)
V_j	=	302 mps (990 fps)	468 mps (1535 fps)

Figure 5.1.1-6 Effect of Relative Velocity On Spectra of 0.75 Area Ratio Coannular Nozzle Model At Subsonic Fan Jet Velocity

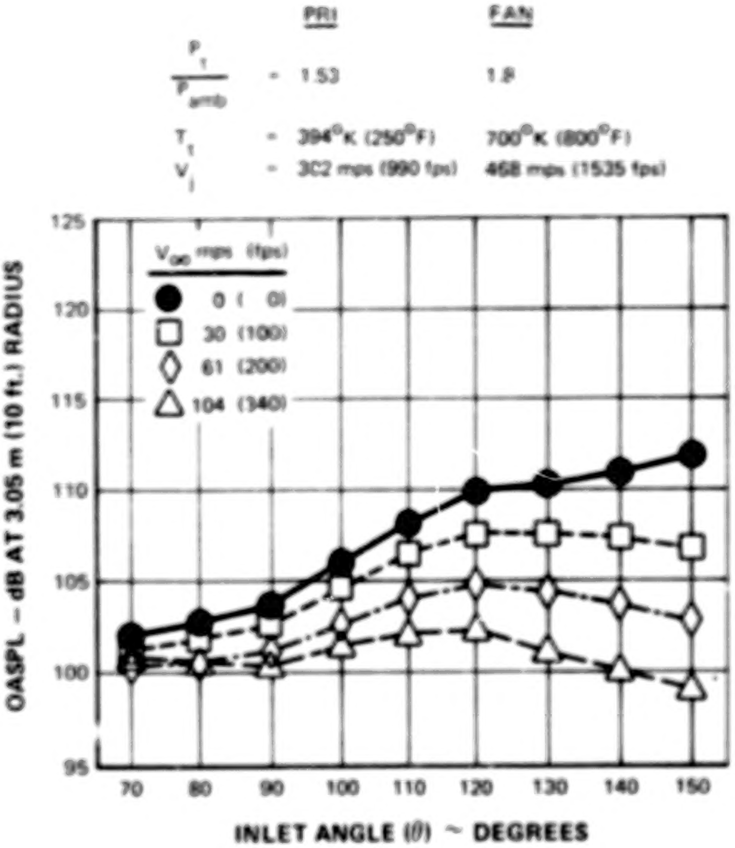

Figure 5.1.1-7 *Effect of Relative Velocity On Directivity of 0.75 Area Ratio Coannular Nozzle Model At Subsonic Fan Jet Velocity*

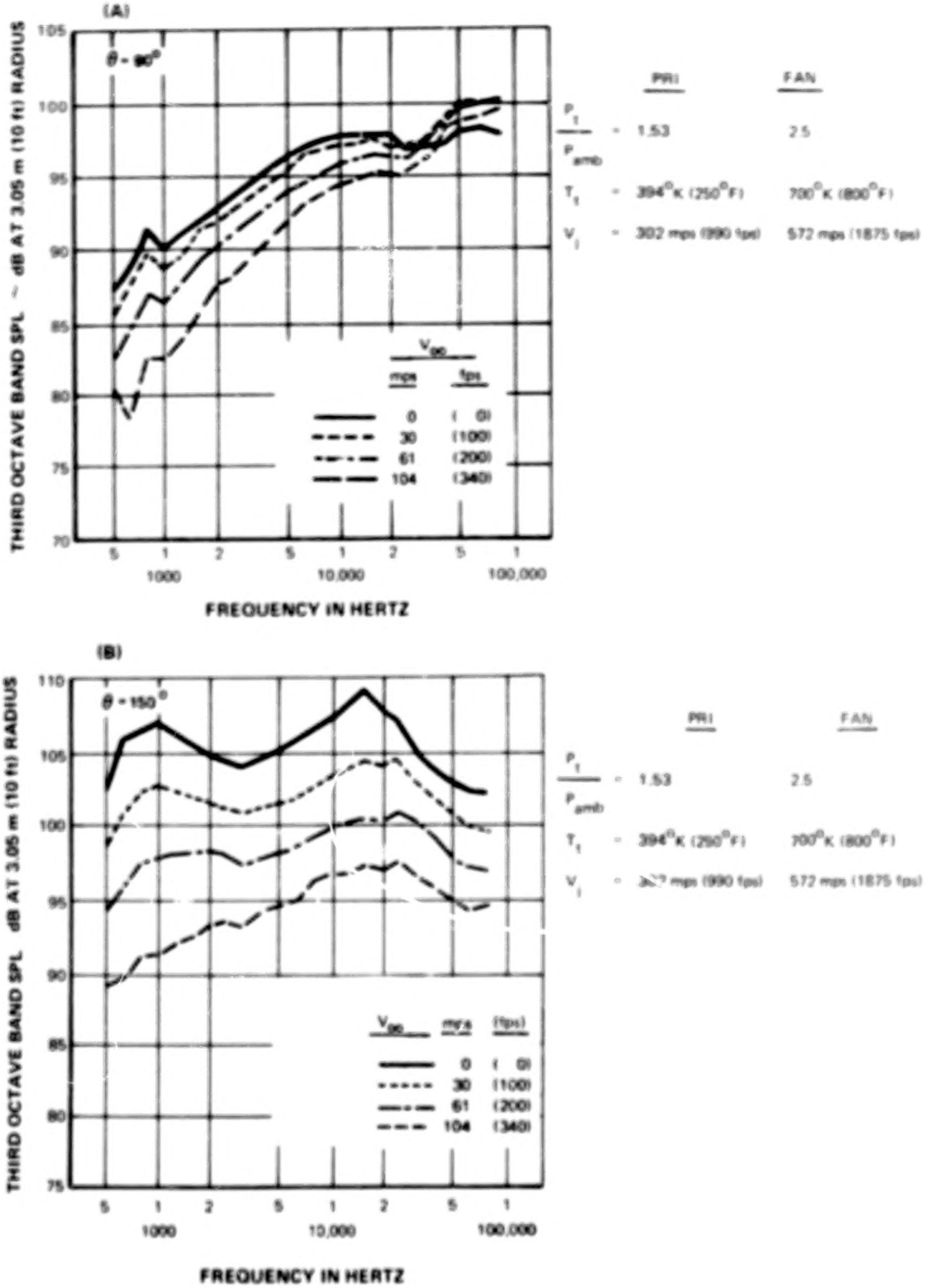

Figure 5.1.1-8 Effect of Relative Velocity On Spectra of 0.75 Area Ratio Coannular Nozzle Model At Supersonic Fan Jet Velocity

Polar OASPL directivity curves for the supersonic fan condition are shown in Figure 5.1.1-9. The noise reduction due to the relative velocity effect can be seen to increase toward the jet axis, whereas at the forward angles noise increases with flight due to the amplification of the broadband shock noise in the fan exhaust stream.

Thus, the effects of relative velocity on the jet mixing and shock components of the noise generated by the 0.75 area ratio coannular nozzle were seen to be generally similar to the results obtained for the reference convergent nozzle.

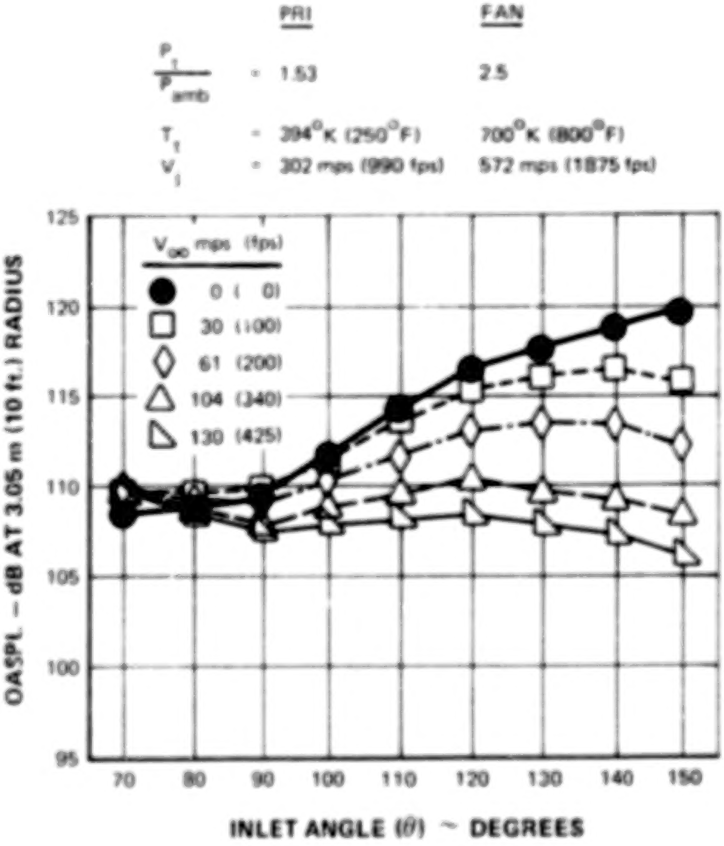

Figure 5.1.1-9 Effect of Relative Velocity On Directivity of 0.75 Area Ratio Coannular Nozzle Model At Supersonic Fan Jet Velocity

5.1.1.3 0.75 Area Ratio Coannular Nozzle With Hardwall Ejector

Before presenting the effects of relative velocity on the 0.75 area ratio coannular nozzle with hardwall ejector, the effect of the ejector at static conditions will be described relative to the basic coannular nozzle. The spectra at 90° and 150° at a typical subsonic fan condition are shown in Figures 5.1.1-10a and b. At 90°, the addition of the ejector caused additional noise in the mid frequencies as compared to the no-ejector configuration. The spectra at 150° show that the ejector caused a large reduction in the high frequency noise levels. In order to interpret these spectral changes due to the ejector, and be able to infer whether the changes are due to modification of the noise sources or the radiation characteristics, a study of the sound power spectra illustrated in Figure 5.1.1-10c is most helpful. The sound power spect represent the noise generated by the jet, and thus the radiation characteristics are eliminate As shown in the power spectra, the ejector causes a small increase in generated acoustic pow in the mid-frequency range, but not of the magnitude indicated by the 90° SPL spectra of Figure 5.1.1-10a. For frequencies above 10 KHz, the ejector causes a small (1 dB) reductio in generated power. Therefore the large reduction in high frequency noise measured at the 150° microphone, as was shown in Figure 5.1.1-10b, is primarily due to a redirection of the noise to other angles rather than to a reduction of the noise generated. This effect has been documented (Ref. 1) in previous ejector nozzle tests.

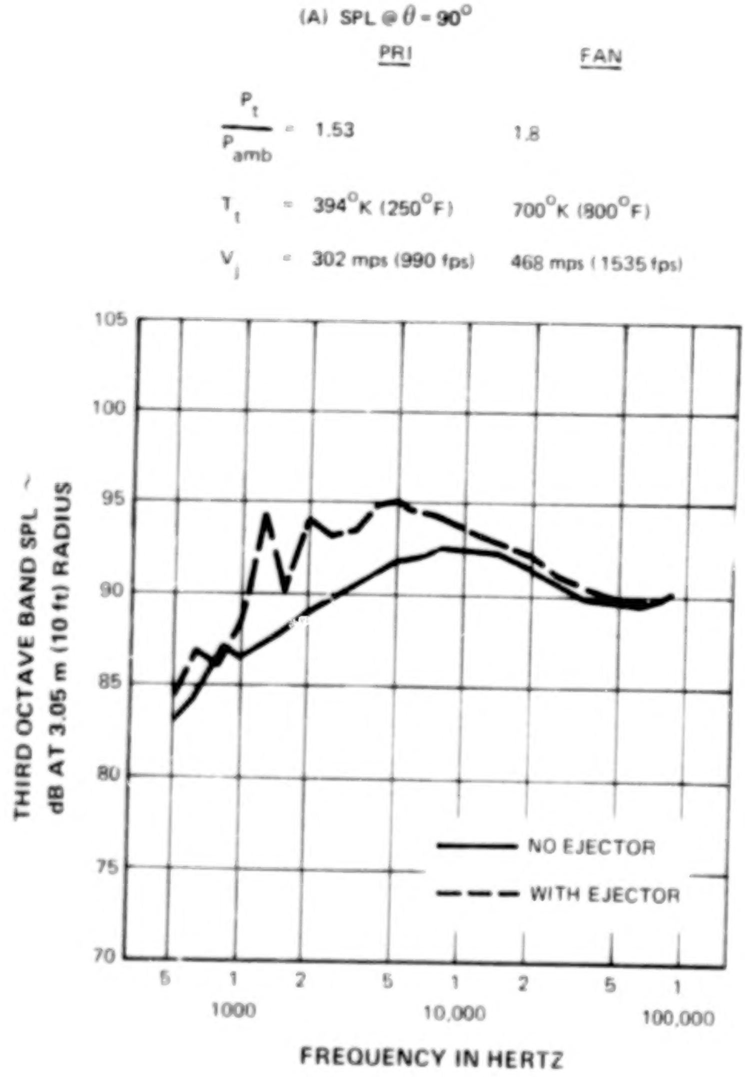

Figure 5.1.1-10 Effect of Ejector On SPL and PNL Spectra of 0.75 Area Ratio Coannular Nozzle Model At Static Condition

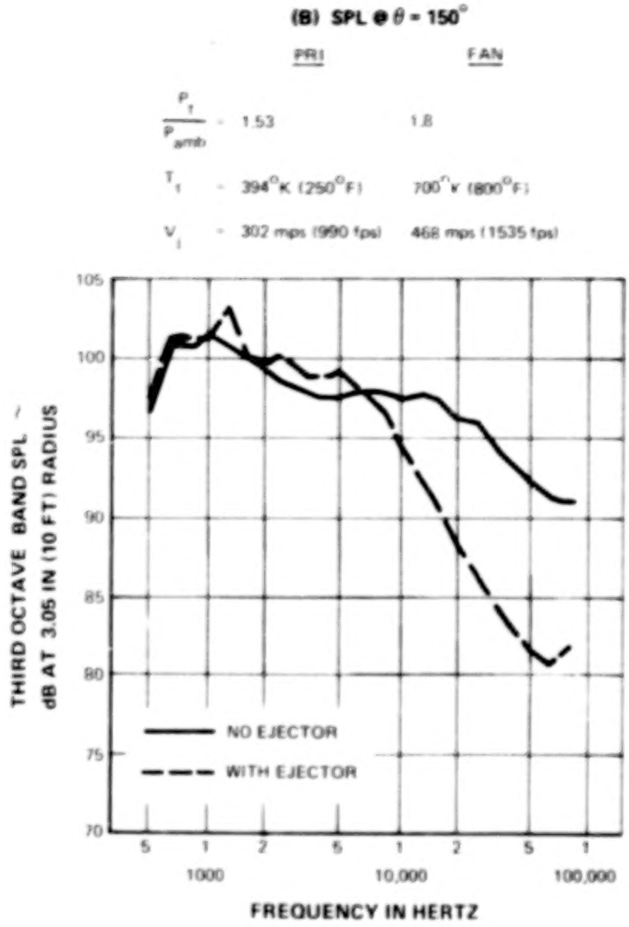
(B) SPL @ θ = 150°

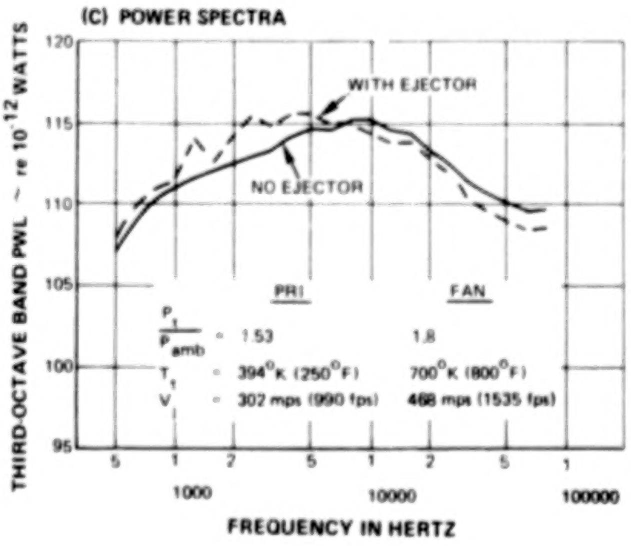
(C) POWER SPECTRA

Figure 5.1.1-10 Effect of Ejector On SPL and PNL Spectra of 0.75 Area Ratio Coannular Nozzle Model At Static Condition (Continued)

It is postulated that the slight increase in noise in the mid-frequency range is the result of an interaction of the fan stream shear layer with the ejector trailing edge. The relatively low stream velocities simulated in this test cause the low and mid-frequency jet mixing noise to be lower than that generated for a properly simulated VSCE cycle having higher velocities, therefore causing the ejector generated noise to be visible in the noise spectrum. It is expected that at higher stream velocities the ejector generated noise would not be significant and it is anticipated a hardwall ejector would not introduce any appreciable noise level change.

The effect of relative velocity on the jet noise spectrum for the 0.75 area ratio coannular nozzle with ejector is shown in Figure 5.1.1-11a and b for the subsonic fan condition at the 90° and 150°, respectively.

As illustrated, a discrete tone occurs at 1250 Hz. A similar tone was present in the earlier phase of this program (Ref. 1) for the same nozzle configuration, when operated at subsonic fan nozzle pressure ratio. The presence of this tone was thought to be due to an instability caused by the jet impinging on the ejector. It is to be noted that the OASPL or PNL values change by negligible amounts if the tone is analytically eliminated, so the presence of the tone can be ignored in the evaluation of OASPL and PNL. As illustrated, this tone disappears with increasing tunnel velocity, possibly because the jet flow is stabilized by the external flow. At 90°, (Figure 5.1.1-11a), the noise is reduced at all frequencies with increasing tunnel velocities, with larger reduction at the lower frequencies than at the high frequencies. At 150°, (Figure 5.1.1-11b), the noise reduction in the low frequencies is significant, whereas the high frequency noise reduction is minimal. A polar OASPL directivity is shown in Figure 5.1.1-12 for the subsonic fan condition. The noise reduction at the forward-most angles is minimal, but increases toward the jet axis reaching a value of 11 dB at 150°.

The effect of relative velocity on the jet noise spectrum for the supersonic fan condition is shown in Figures 5.1.1-13a and b. At 90°, the low frequency noise is reduced with tunnel speed while the noise at frequencies above 40K Hz is increased. As was the case for the non-ejector configuration described earlier, this result is explained by the presence of, and amplification of, shock noise.

The noise spectra at 150° (Figure 5.1.1-13b) shows large reductions with tunnel speed for frequencies below 20K Hz, similar to the results of the non-ejector configuration. Above 25K Hz, however, little or no noise reduction occurs. A lump of broadband noise, centered at 25K Hz, is seen to become more apparent with increasing tunnel speed. This noise appears to be shock noise which is uncovered at this angle due to the combined effects of relative velocity noise reduction and the ejector caused redirection of the noise.

The OASPL directivity for the supersonic fan condition is shown in Figure 5.1.1-14, which again illustrates the relative velocity amplification of the broadband shock noise in the forward angles.

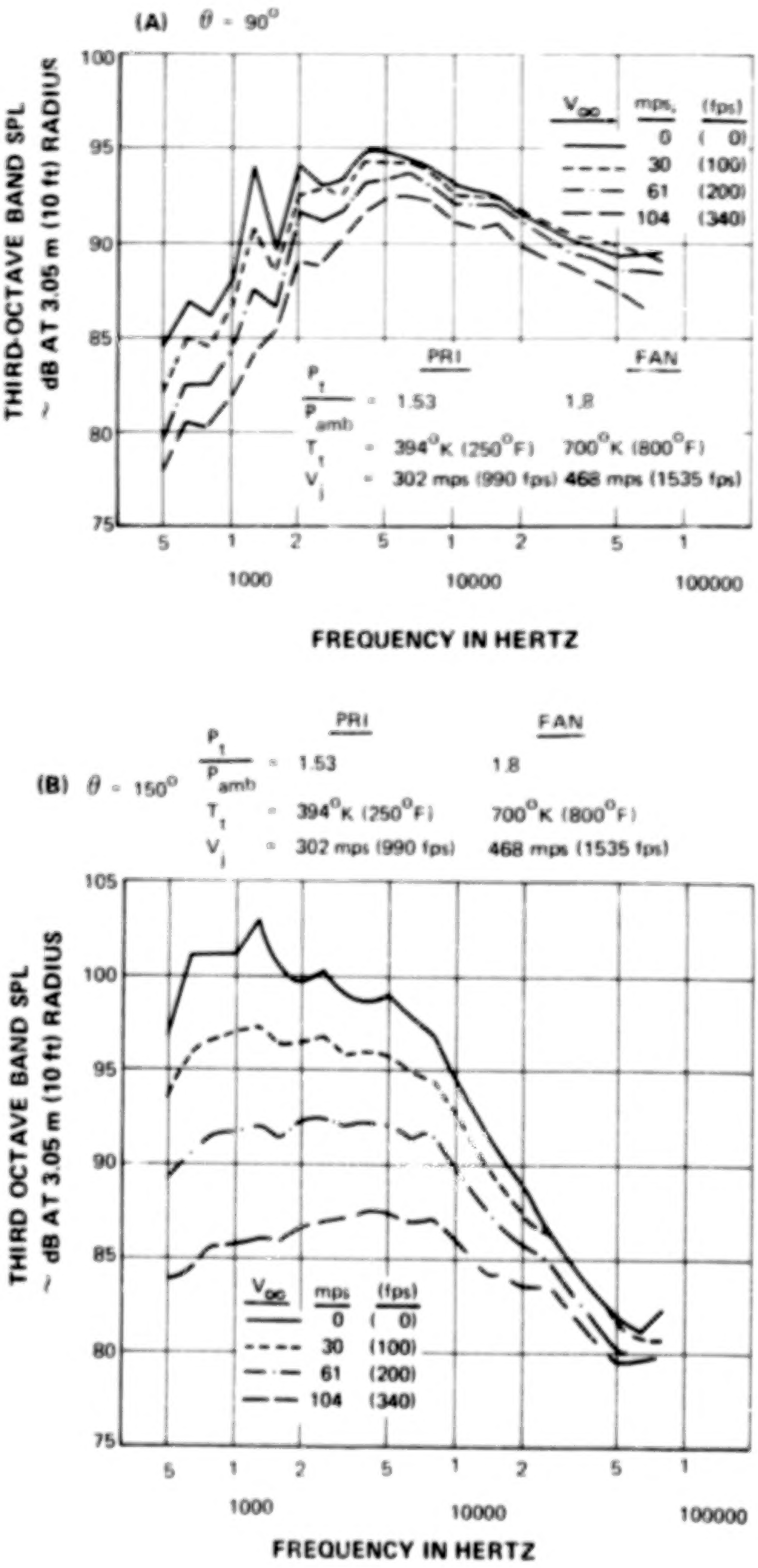

Figure 5.1.1-11 Effect of Relative Velocity On Spectra of 0.75 Area Ratio Coannular Nozzle Model With Ejector At Subsonic Fan Jet Velocity

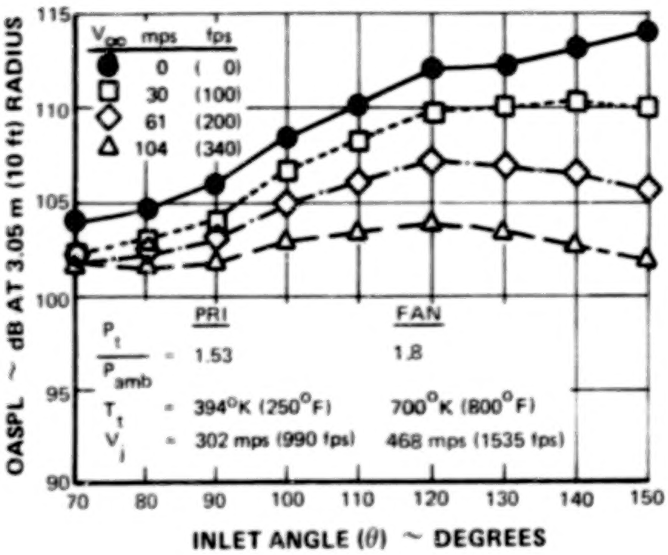

Figure 5.1.1-12 Effect of Relative Velocity On Directivity of 0.75 Area Ratio Coannular Nozzle Model With Ejector At Subsonic Fan Jet Velocity

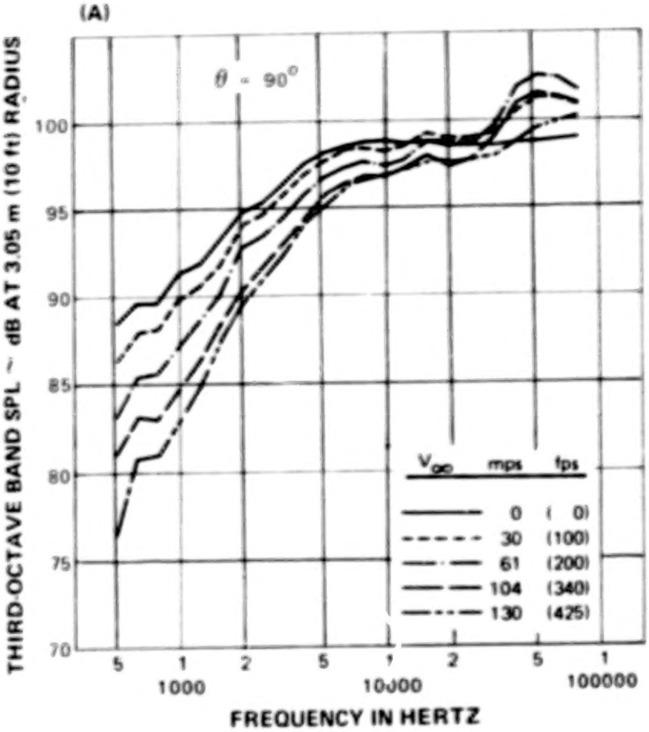

		PRI	FAN
$\frac{P_t}{P_{amb}}$	=	1.53	2.5
T_t	=	394°K (250°F)	700°K (800°F)
V_j	=	302 mps (990 fps)	572 mps (1875 fps)

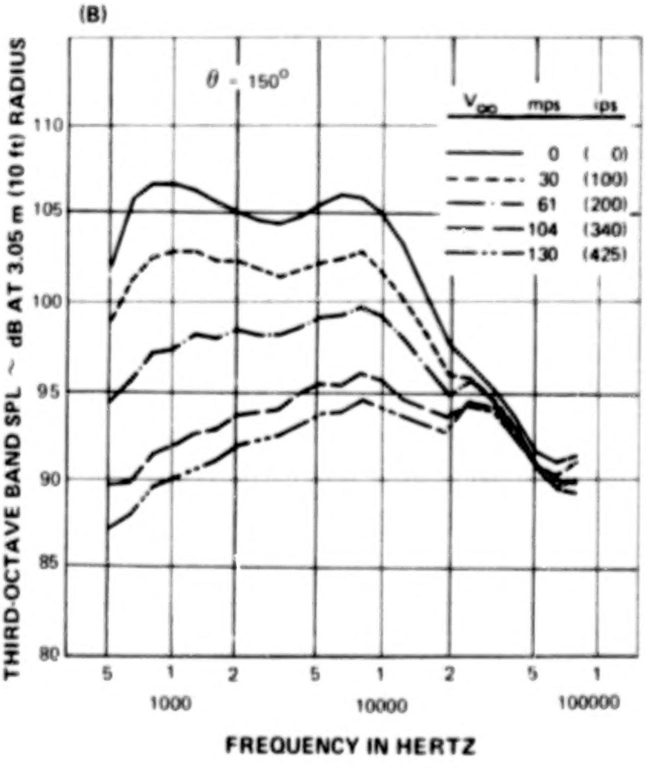

		PRI	FAN
$\frac{P_t}{P_{amb}}$	=	1.53	2.5
T_t	=	394°K (250°F)	700°K (800°F)
V_j	=	302 mps (990 fps)	572 mps (1875 fps)

Figure 5.1.1-13 Effect of Relative Velocity On Spectra of 0.75 Area Ratio Coannular Nozzle Model With Ejector At Supersonic Fan Jet Velocity

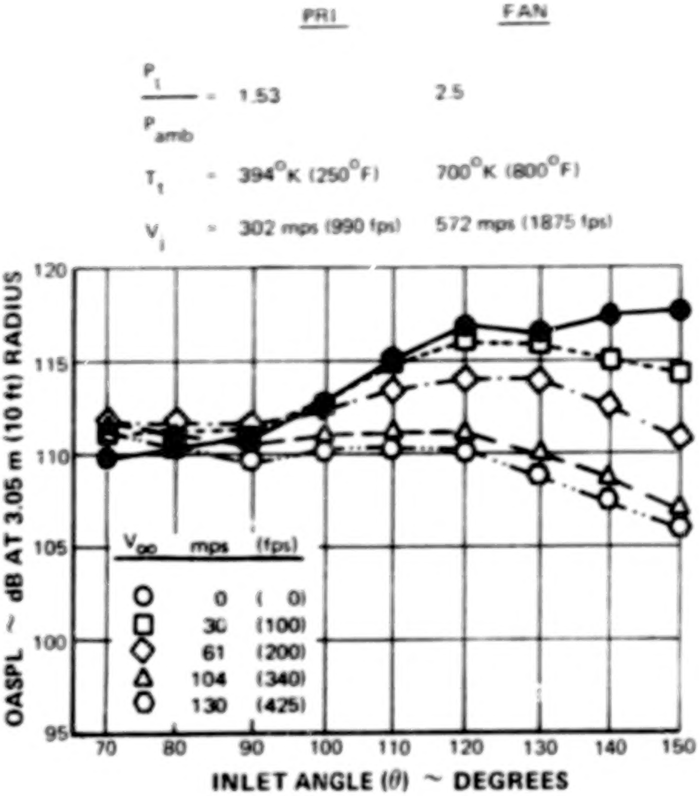

Figure 5.1.1-14 Effect of Relative Velocity On Directivity of 0.75 Area Ratio Coannular Nozzle Model With Ejector At Supersonic Fan Jet Velocity

A direct comparison of the relative velocity effect on the 0.75 coannular nozzle with and without ejector is shown in Figure 5.1.1-15A. The OASPL directivity at static and 104 mps (340 fps) tunnel speed are shown for both configurations at a fan velocity of 570 mps (1876 fps). At the flight condition, the ejector configuration has higher noise levels than the non-ejector configuration at all angles forward of 140°. This result is due to the extra noise generated at mid-frequencies by the ejector, as described earlier in this section. At a higher fan velocity more representative of a VSCE engine envisioned for use in a supersonic cruise aircraft, the presence of an ejector reduces the noise of the coannular nozzle in-flight. This result is shown in Figure 5.1.1-15B.

Thus, the noise of the 0.75 coannular nozzle with ejector was reduced at all frequencies and angles with increasing tunnel velocity for subsonic fan conditions. At a supersonic fan condition, the noise was reduced at low frequencies at all angles, while the broadband shock noise at high frequencies increased at forward angles and were essentially unchanged at aft angles with increasing tunnel velocity. Compared to the non-ejector nozzle, the SPL spectra at 90° were similar. At 150° the ejector caused large reductions in high frequency noise at static conditions. These reductions decreased with increasing tunnel velocity such that at 104 mps (340 fps) the 150° spectra of the two configurations were similar. The presence of extra mid-frequency noise caused the ejector configuration to be up to 3 dB noisier than the non-ejector configuration at 104 mps (304 fps) tunnel velocity and 572 mps (1876 fps) fan jet velocity. However, at a higher jet velocity, 635 mps (2082 fps) which is more representative of a VSCE under takeoff operation, the ejector configuration was quieter than the non-ejector configuration.

(A) MODERATE FAN PRESSURE RATIO

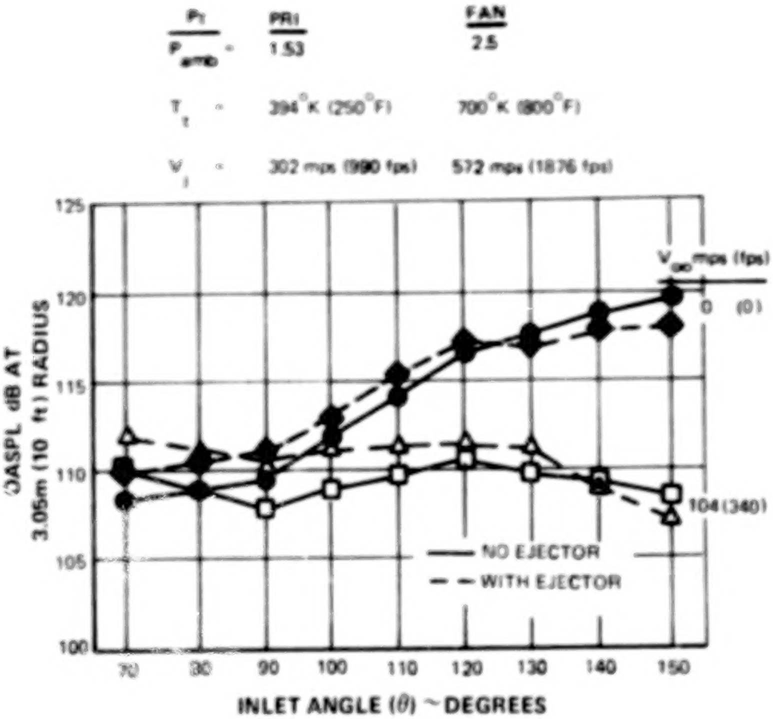

(B) HIGH FAN PRESSURE RATIO

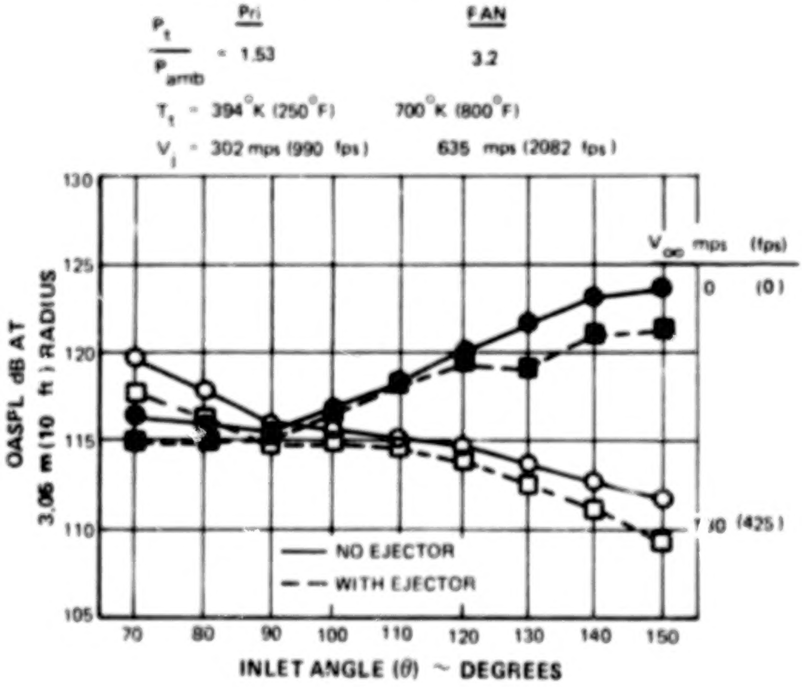

Figure 5.1.1-15 Effect of Ejector On Directivity of 0.75 Area Ratio Coannular Nozzle Model At Two Supersonic Fan Jet Velocities

5.1.1.4 1.2 Area Ratio Coannular Nozzle

Typical jet noise spectra and OASPL directivity for the 1.2 area ratio coannular nozzle are shown in Figures 5.1.1-16 to 19. The sound pressure level spectra for a subsonic fan nozzle condition is shown in Figure 5.1.1-16a and b for the 90° and 150° angles. At 90°, increasing tunnel speeds caused large noise reductions at low frequencies and small or negligible reductions at high frequencies. At 150°, large reductions in noise occurred at all frequencies. The OASPL directivity at all tunnel speeds, presented in Figure 5.1.1-17, shows large noise reductions with increased tunnel speed at aft angles, and small reductions at forward angles.

The sound pressure level spectra for supersonic fan nozzle conditions is shown in Figure 5.1.1-18a and b for angles of 90° and 150°. At 90°, increasing tunnel speed caused large noise reductions at low frequencies, and either small reductions or increases at high frequencies. At 150°, large noise reductions are seen at all frequencies. The OASPL directivity curve, Figure 5.1.1-19, shows large noise reductions at aft angles, and very small reductions at the 70° angle. It is seen that the noise spectra and OASPL directivity behave similarly to those of the 0.75 area ratio coannular nozzle.

A direct spectral comparison of the two configurations at a subsonic fan condition is shown in Figure 5.1.1-20. The 1.2 area ratio coannular nozzle produces slightly higher broadband noise levels due to the larger fan area. For the subsonic fan flow, this difference in noise level is essentially uniform for all frequencies and all angles and changes slightly with tunnel velocities. To illustrate this effect, an OASPL directivity comparison is shown in Figure 5.1.1-21 for both static and flight conditions.

At supersonic fan conditions, the 1.2 area ratio coannular nozzle also produces higher broadband noise levels for all angles and frequencies, as illustrated in Figure 5.1.1-22. In addition, the broadband shock noise from the fan stream of the 1.2 area ratio coannular nozzle is much stronger than the 0.75 area ratio coannular nozzle. The effect of area ratio on OASPL directivity is shown in Figure 5.1.1-23 at the supersonic fan condition for both static and flight conditions. In the forward angles, the noise levels of the 1.2 area ratio coannular nozzle is as much as 5 dB above that of the 0.75 nozzle, while at the aft angles, the increase is on the order of 2 dB. This trend is seen in both static and flight conditions. The high shock broadband noise levels of the 1.2 area ratio nozzle may have an impact on the selection of area ratio of a VSCE powerplant. However, these results must be considered with proper respect to real VSCE cycle conditions. The ratio of shock to mixing noise for the limited conditions tested in the current program is larger than for a VSCE cycle, since the VSCE has higher fan and primary stream velocities and temperatures. Thus, for VSCE cycles, the shock noise may be dominated by the mixing noise and the effect of area ratio on the jet noise, as defined by these results, may be misleading. To properly assess these effects, it is necessary to develop separate correlations from this data for shock and mixing noise, and to then apply these correlations individually to estimate the noise of a VSCE cycle.

Thus, except for differences in the shock noise which dominates the noise at forward angles for the test conditions run during this program, the effect of relative velocity on the noise of the coannular nozzle is essentially independent of an area ratio change from 0.75 to 1.2.

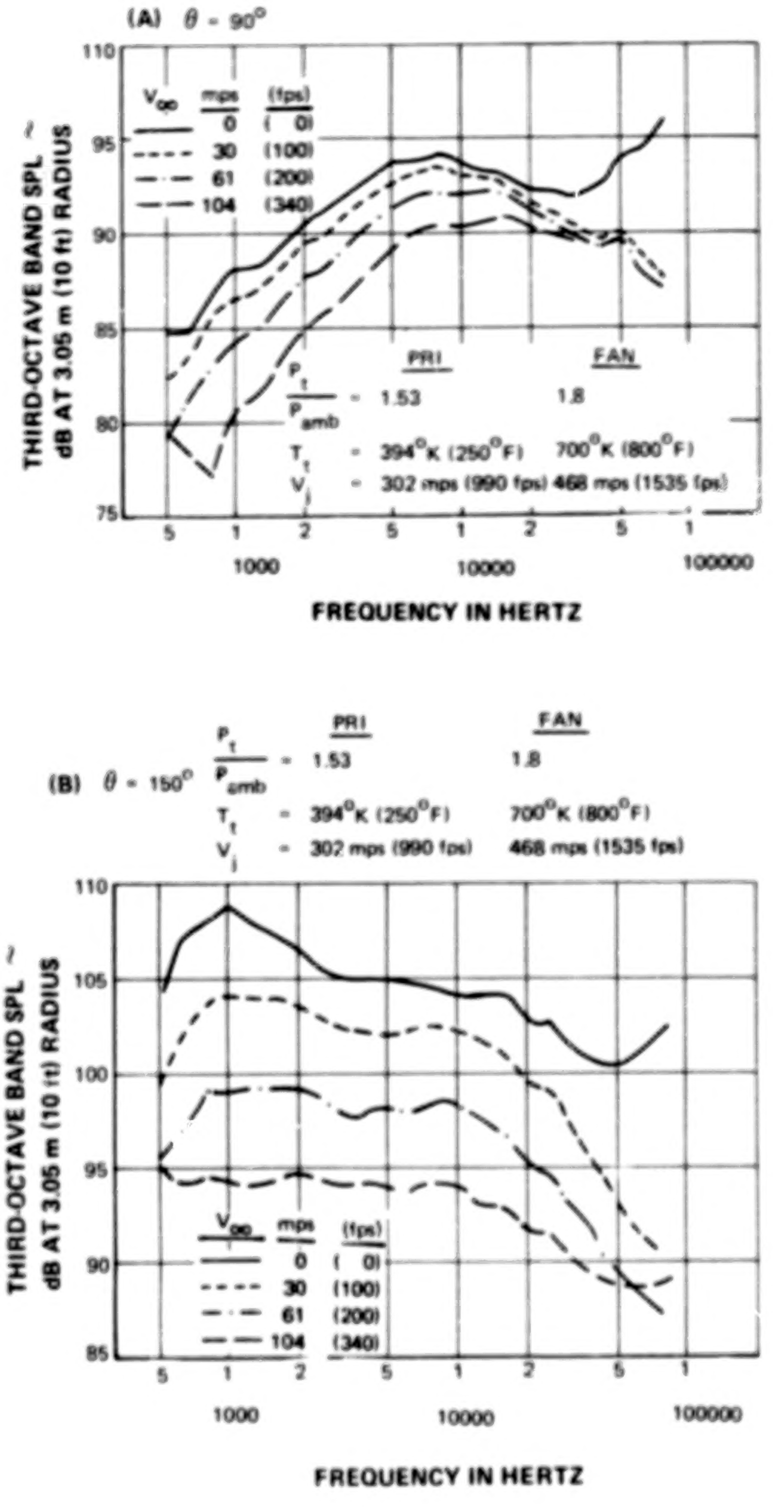

Figure 5.1.1-16 Effect of Relative Velocity On Spectra of 1.2 Area Ratio Coannular Nozzle Model At Subsonic Fan Jet Velocity

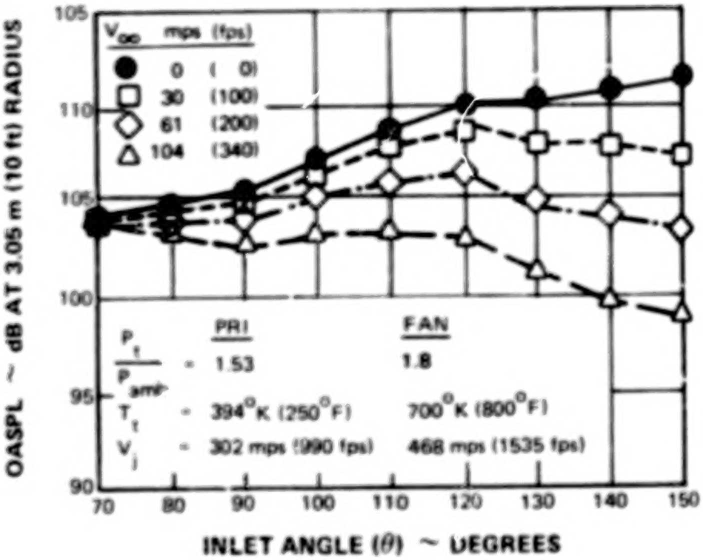

Figure 5.1.1-17 Effect of Relative Velocity On Directivity of 1.2 Area Ratio Coannular Nozzle Model At Subsonic Fan Jet Velocity

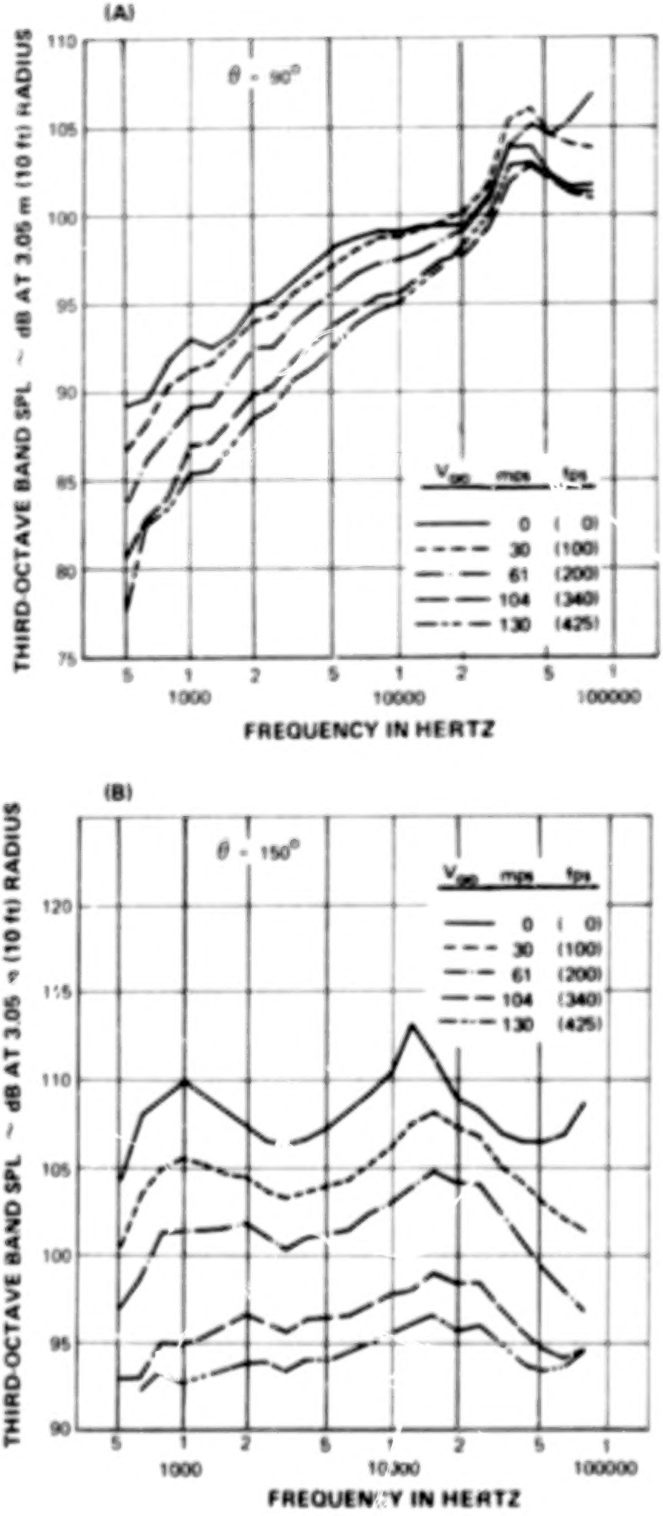

		PRI	FAN
P_t / P_{amb}	=	1.53	2.5
T_t	=	394°K (250°F)	700°K (800°F)
V_j	=	302 mps (990 fps)	572 mps (1875 fps)

		PRI	FAN
P_t / P_{amb}	=	1.53	2.5
T_t	=	394°K (250°F)	700°K (800°F)
V_j	=	302 mps (990 fps)	572 mps (1875 fps)

Figure 5.1.1-18 Effect of Relative Velocity On Spectra of 1.2 Area Ratio Coannular Nozzle Model At Supersonic Fan Jet Velocity

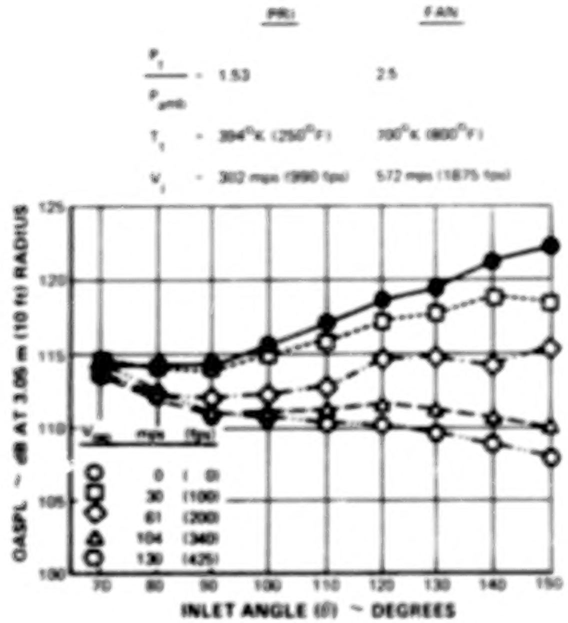

Figure 5.1.1-19 Effect of Relative Velocity On Directivity of 1.2 Area Ratio Coannular Nozzle Model At Supersonic Fan Jet Velocity

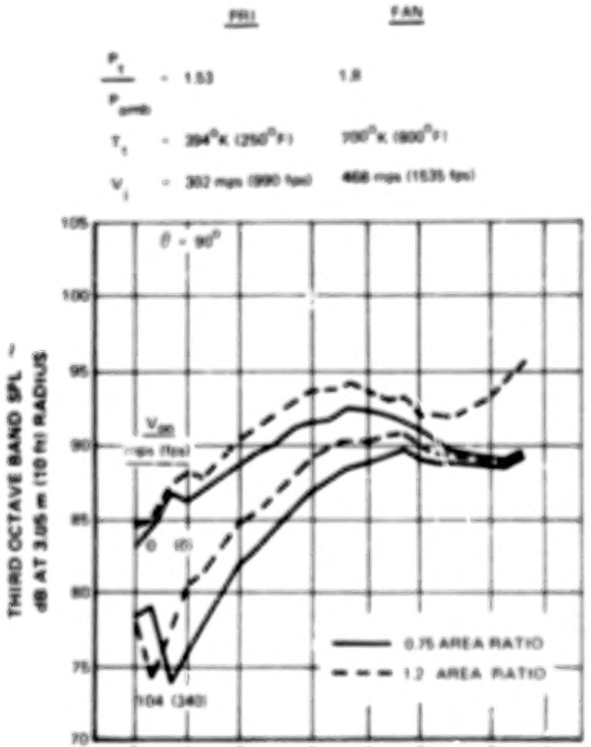

Figure 5.1.1-20 Effect of Area Ratio On Spectra of Coannular Nozzle Model At Subsonic Fan Jet Velocity

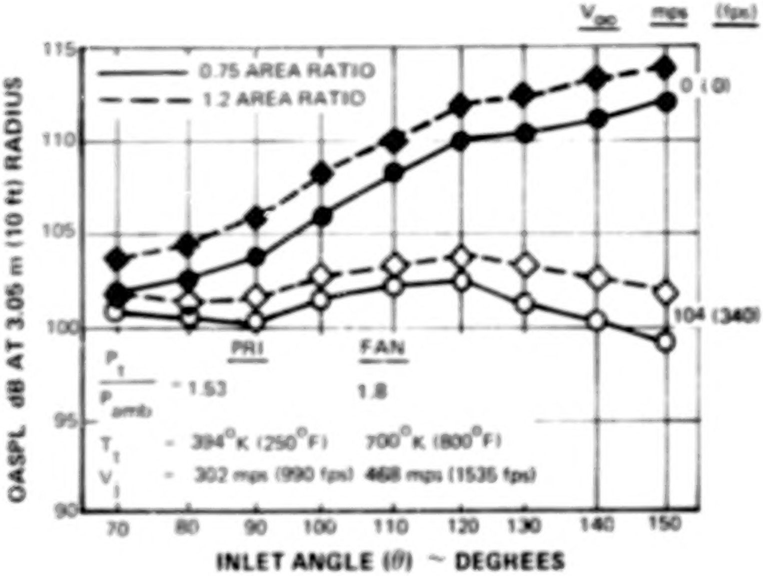

Figure 5.1.1-21 Effect of Area Ratio On Directivity of Coannular Nozzle Model At Subsonic Fan Jet Velocity

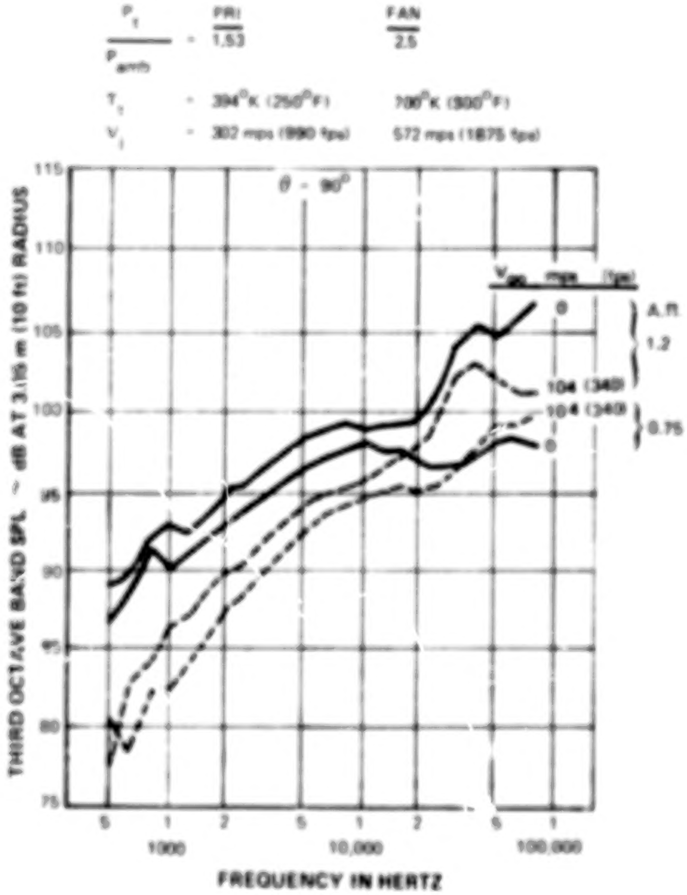

Figure 5.1.1-22 Effect of Area Ratio On Spectra of Coannular Nozzle Model At Supersonic Fan Jet Velocity

TABLE OF CONTENTS

Section	Title	Page No.	
1.0	SUMMARY	1	1/B4
2.0	INTRODUCTION	3	1/B6
	2.1 Background	3	1/B6
	2.2 Program Description	4	1/B7
3.0	APPARATUS	6	1/B9
	3.1 Acoustic Wind Tunnel	6	1/B9
	3.1.1 Adapter Section	8	1/B11
	3.1.2 Instrumentation Section	9	1/B12
	3.1.3 Exit Plane Traverse Instrumentation	10	1/B13
	3.1.4 Acoustic Instrumentation	11	1/B14
	3.2 Aerodynamic Wind Tunnel	12	1/C1
	3.3 Nozzle Configurations	14	1/C3
	3.3.1 Reference Convergent Nozzle	14	1/C3
	3.3.2 Coannular Nozzles	15	1/C4
	3.3.3 Ejector	17	1/C6
4.0	DATA	18	1/C7
	4.1 Aerodynamic Data Reduction	20	1/C9
	4.1.1 Thrust Coefficients and Flow Coefficients	26	1/D1
	4.1.2 Surface Static Pressure	27	1/D2
	4.1.3 Exit Profiles and Ejector Inlet Total Pressures	28	1/D3
	4.2 Acoustic Data Reduction	31	1/D6
	4.3 Comparison With Outdoor Results	46	1/E12
	4.4 Coannular Noise Synthesis	51	1/F3
5.0	RESULTS AND DISCUSSION	53	1/F5
	5.1 Discussion of Acoustic Results	53	1/F5
	5.1.1 Acoustic Results	53	1/F5
	5.1.2 Correlation of OASPL Noise Reduction with Relative Velocity Exponents	82	2/A8
	5.1.3 Velocity Profile Correlation	109	2/C7
	5.2 Application of Acoustic Results	113	2/C11
	5.2.1 Comparison of Results with Synthesis	114	2/C12
	5.2.2 Results Scaled to Full Size	120	2/D4
	5.2.3 Application of Results to SCAR Noise Predictions	123	2/D7
	5.3 Aerodynamic Performance	131	2/E1
	5.3.1 Convergent Nozzle	131	2/E1
	5.3.2 Coannular Nozzles	132	2/E2
	5.3.3 Flow Coefficients	136	2/E6
6.0	SUMMARY OF RESULTS	140	2/E10
	6.1 Acoustic Results	140	2/E10
	6.2 Aerodynamic Performance Results	141	2/E11

TABLE OF CONTENTS (Cont'd.)

Section	Title	Page No.
REFERENCES		143 2/E13
APPENDIX A		145 2/F1
Part 1	Model Scale Overall Sound Power Level and Overall Sound Pressure Level Directivity on Theoretical Day	145 2/F1
Part 2	Relative Velocity and Convective Exponents	153 2/G3
APPENDIX B	Supersonic Screech Elimination	155 2/G5
APPENDIX C	Theoretical Day Atmospheric Absorption Correction	163 2/G13
APPENDIX D	Shear Layer Refraction Correction	170 3/A8
LIST OF ABBREVIATIONS		180 3/B4

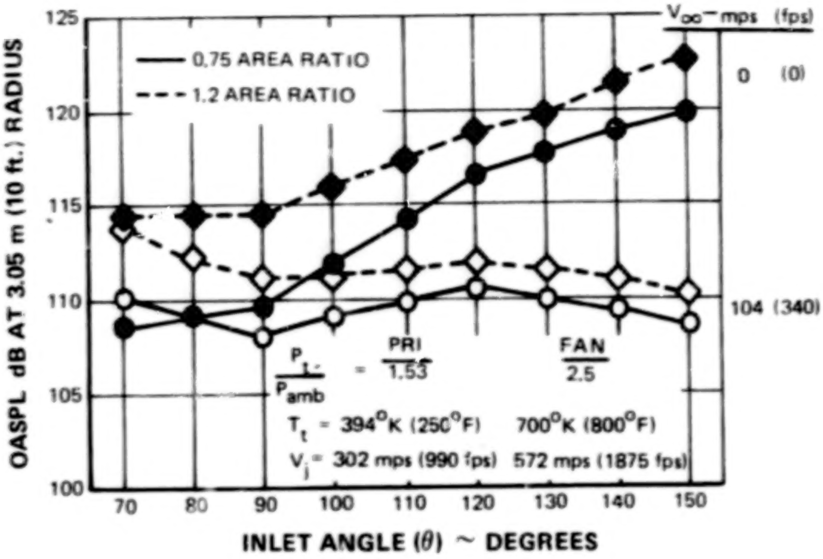

Figure 5.1.1-23 Effect of Area Ratio On Directivity of Coannular Nozzle Model At Supersonic Fan Jet Velocity

5.1.1.5 Comparison of Annular and Coannular Nozzles

In this section, the acoustic data of the 0.75 area ratio coannular nozzle with the primary stream turned off (annular jet) are compared to the data from the same nozzle with both streams flowing (coannular jet). These comparisons are useful in determining the influence of the primary stream on the coannular nozzle noise characteristics. The fan stream was set at the same conditions for both tests. Although the primary flow control valves were turned off during the annular nozzle tests, a small amount of leakage (≈3% of the fan stream flow) was present. An OASPL directivity comparison of the annular and coannular nozzle is shown in Figure 5.1.1-24 for a subsonic fan flow condition under both static and flight conditions. At the static condition, the OASPL of the annular jet is slightly lower than the coannular jet for the angles less than 120°. The annular jet is noisier for angles larger than 120°. At all angles, at a flight speed of 104 mps (340 fps), the OASPLs for the annular jet are higher than those of the coannular jet. Spectral comparisons at 90° and 150° are shown in Figures 5.1.1-25a and b for the subsonic fan condition. At the 90° angle, the peak SPL of the annular jet is lower than the coannular jet in the static condition, whereas in the flight condition, the SPLs of the annular jet are higher at the high frequencies. At the 150° angle, the SPLs of the annular jet are significantly higher than the coannular jet for all frequencies in both static and flight conditions. The double peak spectra is present for the annular case which is in reality a very low primary flow coannular stream.

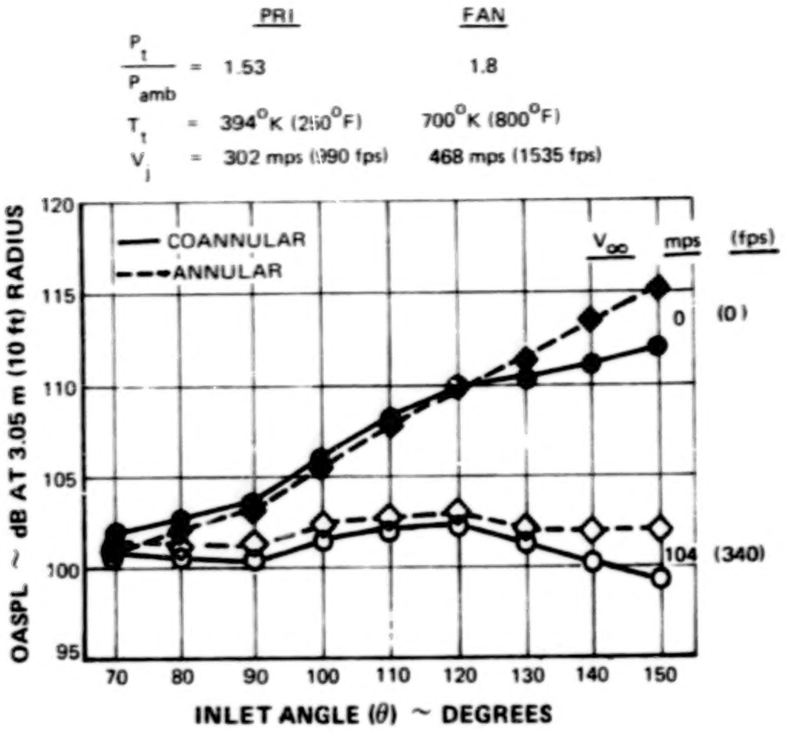

Figure 5.1.1-24 *Effect of Primary Stream On Directivity of 0.75 Area Ratio Coannular Nozzle Model At Subsonic Fan Jet Velocity. Primary stream operating conditions apply to coannular case only ($V_p \approx 0$ for annular case)*

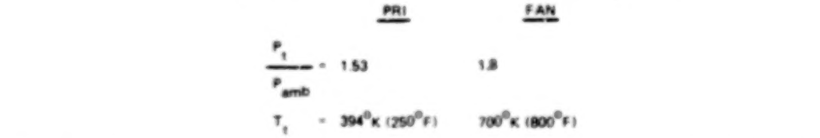

Figure 5.1.1-25 *Effect of Primary On Spectra of 0.75 Area Ratio Coannular Nozzle Model At Subsonic Fan Jet Velocity. Primary stream operating conditions apply to coannular case only ($V_p \approx$ for annular case)*

The OASPL directivity comparison of the annular and coannular nozzles is shown in Figure 5.1.1-26 for a supersonic fan flow case at both static and flight conditions. At all angles, the OASPLs for the annular jet are higher than the coannular jet at both static and flight conditions. Spectral comparisons, presented in Figures 5.1.1-27a and b indicate that the noise generation process is quite different for the annular and coannular jets. At the 90° angle, the annular jet is slightly noisier than the coannular jet at the low and high frequencies at both static and flight conditions. At the 150° angle, the annular jet noise spectra are significantly different from the double-peaked characteristic of the coannular jet. In fact, in the static case, the annular jet noise spectrum is similar to that of a single circular jet, with a peak SPL value significantly larger than the coannular flow case. Figure 5.1.1-28 shows the noise spectra from the coannular, annular and convergent nozzle at the same supersonic condition, for the same high velocity jet exhaust area. As shown, at low and mid-frequencies, the annular jet is quieter than the convergent nozzle, but the coannular jet is significantly quieter than the annular jet. In flight, the annular jet spectrum begins to approach the double-peaked shape exhibited by the coannular nozzle under static conditions. This observation can be explained by comparing the velocity profiles measured approximately 2 nozzle diameters downstream. The velocity profiles from the coannular and annular configurations with supersonic fan flow are shown in Figures 5.1.1-29 and 30. In the static condition, the velocity profile of the annular jet is relatively flat compared to the profile of the coannular jet. This difference in profile shape indicates that the annular jet does not decay as rapidly as the coannular jet since the annular jet profile resembles a circular flow. At a tunnel velocity of 105 mps (340 fps), the velocity profile of the annular jet approaches that of the coannular jet. The annular jet at this condition shows the double-peaked noise spectrum also characteristic of the coannular jet.

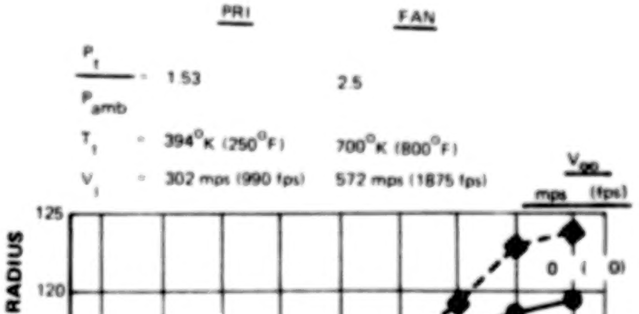

Figure 5.1.1-26 Effect of Primary Stream On Directivity of 0.75 Area Ratio Coannular Nozzle Model At Supersonic Fan Jet Velocity. Primary stream conditions apply to coannular case only (V_p ≈ for annular case)

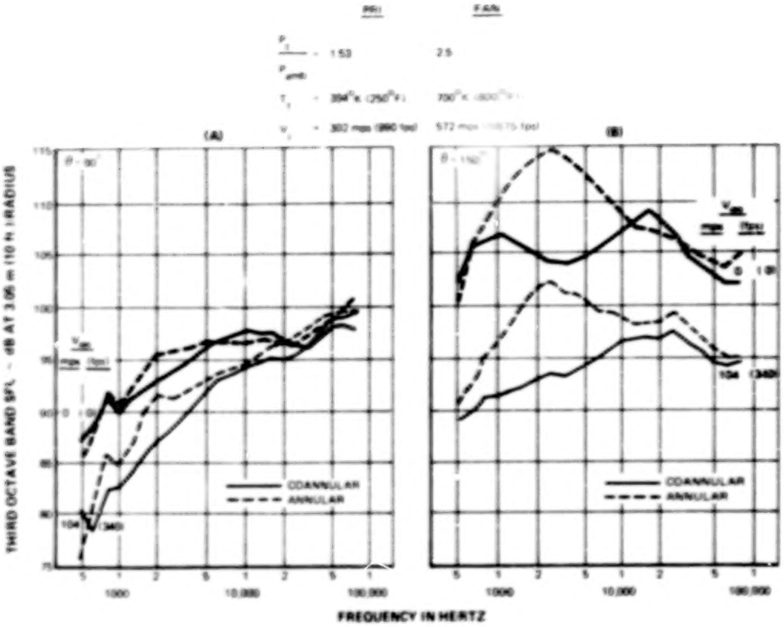

Figure 5.1.1-27 *Effect of Primary Stream On Spectra of 0.75 Area Ratio Coannular Nozzle Model At Supersonic Fan Jet Velocity. Primary stream operating conditions apply to coannular case only ($V_p \approx 0$ for annular case)*

SYMBOL	CONFIGURATION	PRI $\frac{P_t}{P_{amb}}$	PRI T_t	PRI V_j	PRI A	FAN $\frac{P_t}{P_{amb}}$	FAN T_t	FAN V_j	FAN A
— · —	CONVERGENT	2.5	700°K (800°F)	572 mps (1875 fps)	.00108m² (1.67 in²)				
- - -	ANNULAR					2.5	700°K (800°F)	572 mps (1875 fps)	.00108m² (1.67 in²)
——	COANNULAR	1.53	394°K (250°F)	302 mps (990 fps)	.00143m² (2.22 in²)	2.5	700°K (800°F)	572 mps (1875 fps)	.00108 m² (1.67 in²)

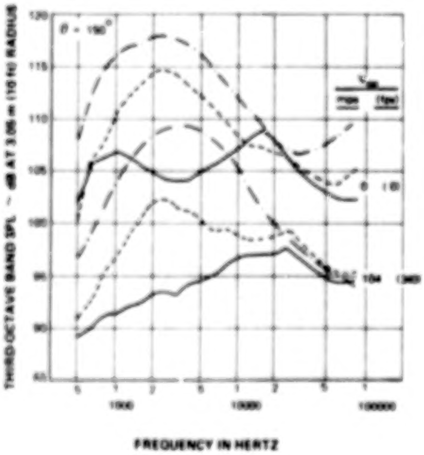

Figure 5.1.1-28 *Spectral Comparison of Coannular, Annular and Convergent Nozzle Model At Supersonic Jet Velocity*

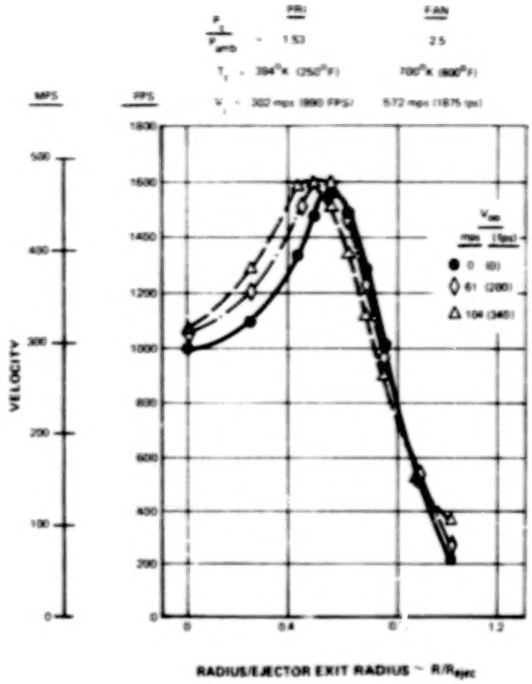

Figure 5.1.1-29 *Effect of Relative Velocity On Exit Velocity Profiles of 0.75 Area Ratio Coannular Nozzle Model. Velocity profiles measured 2 nozzle diameter downstream of nozzle esit.*

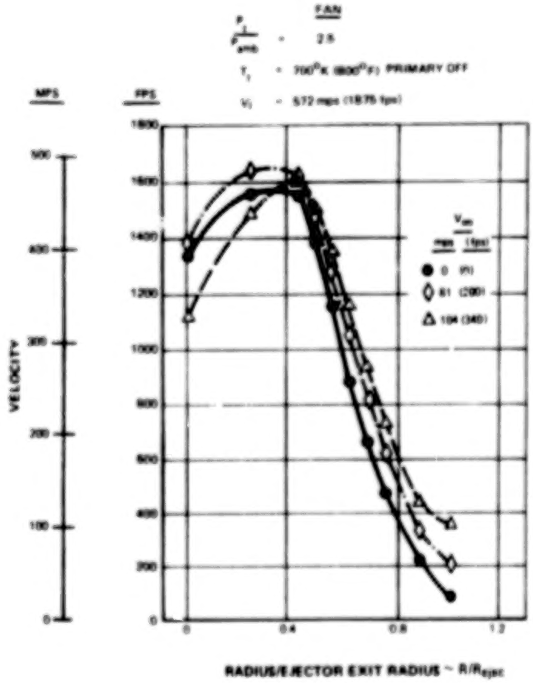

Figure 5.1.1-30 *Effect of Relative Velocity On Exit Velocity Profiles With Annular Flow Only Nozzle Model. Velocity profile measured 2 nozzle diameters downstream of nozzle exit.*

Based on these results, it appears that a coannular jet having a fan velocity substantially larger than its primary velocity is quieter than an annular jet operating at the velocity of the fan stream portion of the coannular jet. The annular jet is quieter than a single circular jet operating at the same conditions. These noise differences are basically retained in the flight condition.

5.1.2 Correlation of OASPL Noise Reduction with Relative Velocity Exponents

The OASPL noise reductions measured during this program were correlated by the use of two types of relative velocity exponents. The first exponent, n_1, (called here relative velocity exponent) is used to quantify the OASPL noise reductions due to the overall relative velocity effect of flight speed and it has found widespread use among current researchers in the field. The second exponent, n_6, (called here convection exponent) was defined to attempt to separate, in a simple fashion, the effects of flight on both source noise reduction and convective amplification. The results of the exponent correlations are presented in this section.

5.1.2.1 Definition of Relative Velocity Exponent, n_1 and Convection Exponent n_6

It is assumed that the sound intensity $\overline{p^2}(\theta_i)$, generated by a jet with or without an external flow (i.e., in forward flight or in a wind tunnel) at any angle, θ_i, is proportional to the product of the absolute jet velocity V_j, and the relative velocity, V_j-V_∞, each raised to a certain power (Ref. 14).

$$\overline{p^2}(\theta_i) \,\alpha\, V_j^{\,m(\theta_i)} \, (V_j - V_\infty)^{n_1(\theta_i)} \qquad (5\text{-}1)$$

The relative velocity exponent $n_1(\theta_i)$ can be defined in terms of the reduction in overall sound pressure level (Δ OASPL) where ΔOASPL is defined as the difference between static and in-flight levels:

$$\Delta\text{OASPL} = \text{OASPL}_{V_\infty = 0} - \text{OASPL}_{V_\infty} \qquad (5\text{-}2)$$

and using the general definition of OASPL α 10 log $\overline{p^2}$,

$$\Delta\text{OASPL} = \left[10 \text{ Log } \overline{p^2}(\theta_i)\right]_{V_\infty = 0} - \left[10 \text{ Log } \overline{p^2}(\theta_i)\right]_{V_\infty}$$

$$= 10 \text{ Log } \frac{\left[\overline{p^2}(\theta_i)\right]_{V_\infty = 0}}{\left[\overline{p^2}(\theta_i)\right]_{V_\infty}} \qquad (5\text{-}3)$$

Combining Eq. (5-1) & (5-3) gives:

$$\Delta\text{OASPL} = 10 \text{ Log } \frac{V_j^{\,n_1(\theta_i)}}{(V_j - V_\infty)^{n_1(\theta_i)}} = 10 \text{ Log } \left[\frac{V_j}{V_j - V_\infty}\right]^{n_1(\theta_i)} \qquad (5\text{-}4)$$

When testing in the acoustic wind tunnel, simulation of the static case results in a slight tunnel velocity, V_{To}, on the order of 7 mps due to pumping action by the model nozzle jet. To account for this small effect, the equation (5-4) for ΔOASPL is rewritten in the following form:

$$\Delta \text{OASPL} = 10 \text{ Log } \left[\frac{V_j - V_{To}}{V_j - V_\infty} \right]^{n_1(\theta_i)} \qquad (5\text{-}5)$$

Equation (5-5) was, therefore, used to obtain the values of relative velocity exponents $[n_1(\theta_i)]$ in this program.

The exponents developed by recent investigators using this procedure have shown general agreement, especially for subsonic jets. One significant result has been the strong dependence of the exponents on angle. At 90°, the exponent value has been generally about 4, while at an aft angle of 150°, the exponent is typically on the order of 10. In order to attempt to determine if the large angular dependence of the relative velocity ΔOASPL exponent is due to noise source effects or convective amplification effects, a second exponent, which we call convection exponent, n_6, was defined (Ref. 15).

If the jet noise source strength reduction due to relative velocity is non-directional (i.e., does not vary with angle of noise radiation), the angular dependence of the measured noise reductions must be due to convective amplification effects caused by the relative motion between the noise sources and the tunnel flow. In this case, the noise intensity, $\overline{p^2}(\theta_i)$, can be written as:

$$\overline{p^2}(\theta_i) \propto \frac{V_j^{m(\theta_i)} (V_j - V_\infty)^n}{(1 - M_\infty \cos \theta_i)^{n_6(\theta_i)}} \qquad (5\text{-}6)$$

where n does not vary with angle.

For this formulation to be correct, the convective amplification effects would be contained in the $(1 - M_\infty \cos \theta_i)^{n_6(\theta_i)}$ term.

In order to evaluate $n_6(\theta_i)$, the following procedure is used.

From (5-6)

$$\text{OASPL}_{\theta_i, V_\infty} \propto 10 \text{ Log } \overline{p^2}(\theta_i) \, \alpha \, 10 \text{ Log } \frac{V_j^{m(\theta_i)} (V_j - V_\infty)^n}{(1 - M_\infty \cos \theta_i)^{n_6(\theta_i)}} \qquad (5\text{-}7)$$

and for the static case,

$$\text{OASPL}_{\theta_i,\, V_\infty = o} \simeq 10 \text{ Log } [V_j^{m(\theta_i) + n}] \qquad (5\text{-}8)$$

The noise change from static to flight is:

$$\Delta \text{ OASPL} = \text{OASPL}_{V_\infty = o} - \text{OASPL}_{V_\infty}$$

$$= 10 \text{ Log } [V_j^{\,m(\theta_i)}\ V_j^{\,n}] - 10 \text{ Log} \left[\frac{V_j^{m(\theta_i)} (V_j - V_\infty)^n}{(1 - M_\infty \cos \theta_i)^{n_6(\theta_i)}} \right]$$

$$= 10 \text{ Log } \left[\frac{V_j^n}{\dfrac{(V_j - V_\infty)^n}{(1 - M_\infty \text{ COS } \theta_i)^{n_6(\theta_i)}}} \right]$$

$$= 10 \text{ Log } \left\{ \left(\frac{V_j}{V_j - V_\infty} \right)^n \left(1 - M_\infty \text{ COS } \theta_i \right)^{n_6(\theta_i)} \right\} \qquad (5\text{-}9)$$

Further, at $\theta_i = 90°$,

$$\Delta \text{ OASPL}_{90°} = 10 \text{ Log } \left(\frac{V_j}{V_j - V_\infty} \right)^{n_1(90°)} \qquad (5\text{-}10)$$

Therefore, from (9) and (10)

$$\Delta \text{ OASPL}_{\theta_i} - \Delta \text{ OASPL}_{90°} = 10 \text{ Log} \left\{ \left(\frac{V_j}{V_j - V_\infty} \right)^{n_1(90°)} (1 - M_\infty \text{ COS } \theta_i)^{n_6(\theta_i)} \right\}$$

$$- 10 \text{ Log} \left(\frac{V_j}{V_j - V_\infty} \right)^{n_1(90°)} \qquad (5\text{-}11)$$

$$= 10 \quad n_6(\theta_i) \text{ Log } (1 - M_\infty \text{ COS } \theta_i) \qquad (5\text{-}12)$$

Rearranging equation (12),

$$n_6(\theta_i) = \frac{\Delta \text{ OASPL}_{\theta_i} - \Delta \text{ OASPL}_{90^\circ}}{10 \text{ Log}(1 - M_\infty \text{ COS } \theta_i)} \qquad (5\text{-}13)$$

Thus, the n_6 convection exponent can be determined from the measured OASPL data using equation 5-13. That is, the noise reduction at any angle, θ_i, relative to the noise reduction at $\theta = 90°$ is expressed as being due to convective amplification effects.

If this formulation was completely correct, the value of n_6 would not depend on the angle, θ_i, since in the theory on convective amplification (Ref. 15) all angular effects are contained in the $(1 - M_\infty \text{ COS } \theta_i)$ term. However, this is a simplified approach in that it assumes that the jet noise sources under static conditions are at rest with respect to the ambient and, thus, have no convective amplification term $(1 - M \text{ COS } \theta_i)^{n_6}$, where the noise sources are assumed to travel upstream at a Mach number of $1 - M \text{ COS } \theta$ relative to the external stream. A more precise theoretical formulation of the effect of flight is discussed in Reference 16, in which the effects of the changes in source convection velocities are included. However, the theoretical formulation of Reference 16 requires the knowledge of turbulent characteristics which have not yet been measured for high speed hot jets. Therefore, the simple formulation involving the exponent, n_6, was done in an attempt to correlate the convective amplification effect on a simple basis not requiring knowledge of the flow turbulence behavior.

The method of least squares was employed in determining the exponents from the experimental data. For example, the relative velocity exponent $n_1(\theta_i)$ was obtained for each angle for each jet operating condition by using a least squares straight line fit to the data plotted as OASPL versus $10 \log [(V_j - V_{To})/(V_j - V_\infty)]$. The slope of the resulting line is then the value of n_1 for the particular value of angle and jet velocity. This straight line was determined by including the origin as one of the data points. Because all the data points were weighted equally in the calculation, the resulting straight line did not necessarily pass through the origin in the plot. The values of $n_6(\theta_i)$ were also determined in a similar fashion. A computer program was written to facilitate calculation of the exponents n_1 and n_6, and the resulting values are tabulated in Appendix A, Part 2 for the conditions at which exponents were calculated.

The two exponents, n_1 and n_6, calculated from the wind tunnel acoustic data are presented in the following sections for all configurations tested during the program.

5.1.2.2 Reference Convergent Nozzle

The reference convergent nozzle data are presented in Figures 5.1.2-1 through 5.1.2-3. Changes in the overall sound pressure levels are seen to correlate quite well with the parameter $10 \log_{10} [(V_j - V_{To})/(V_j - V_\infty)]$ for a subsonic jet of pressure ratio equal to 1.8, and total temperature of 700°K (800°F) (Figure 5.1.2-1a). For a supersonic jet with pressure ratio of 2.5, and a total temperature of 700°K (800°F) (Figure 5.1.2-1b), the correlation is not as good, probably due to the presence of strong shock-associated noise which does not scale with relative velocity.

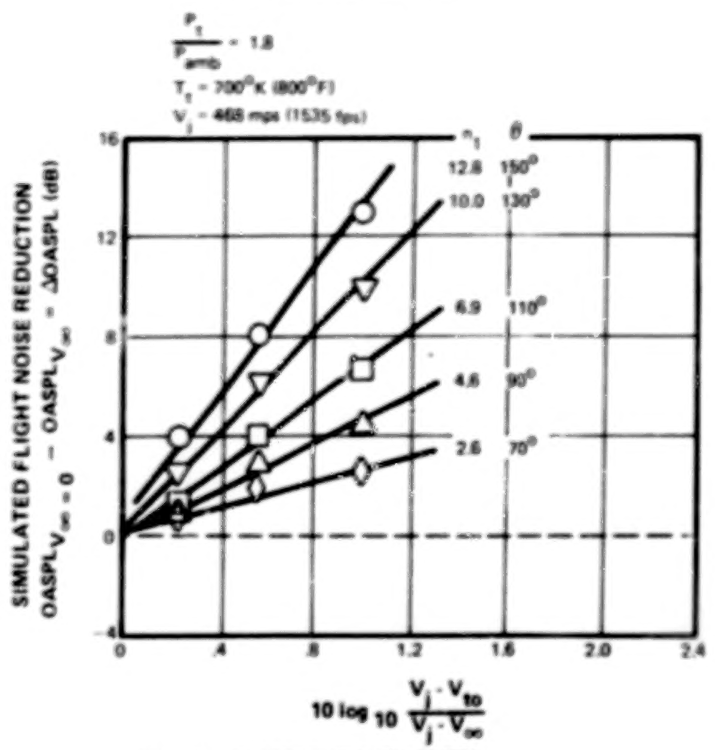
(A) SUBSONIC JET VELOCITY

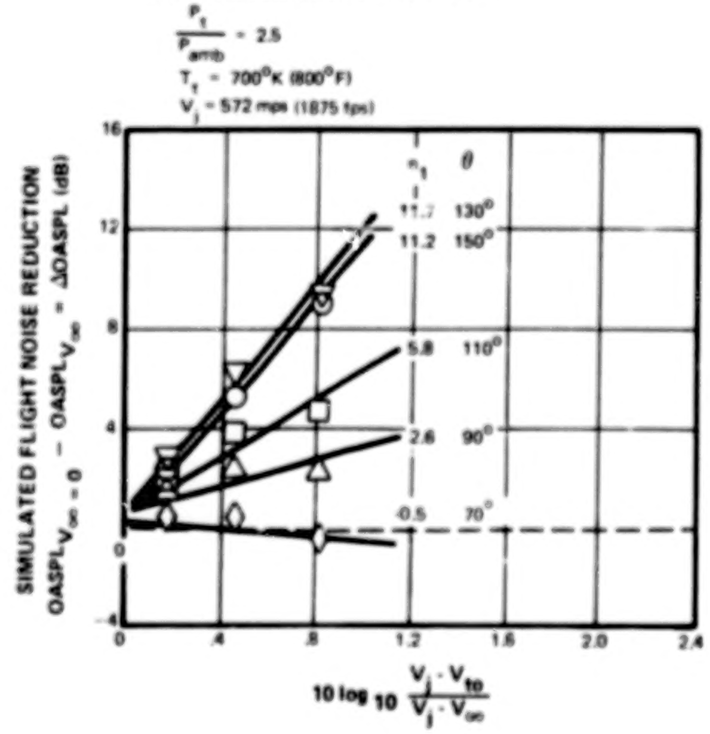
(B) SUPERSONIC JET VELOCITY

Figure 5.1.2-1 Correlation of Relative Velocity Effect On OASPL for Convergent Nozzle Model

(A) T_1 = 394°K (250°F)

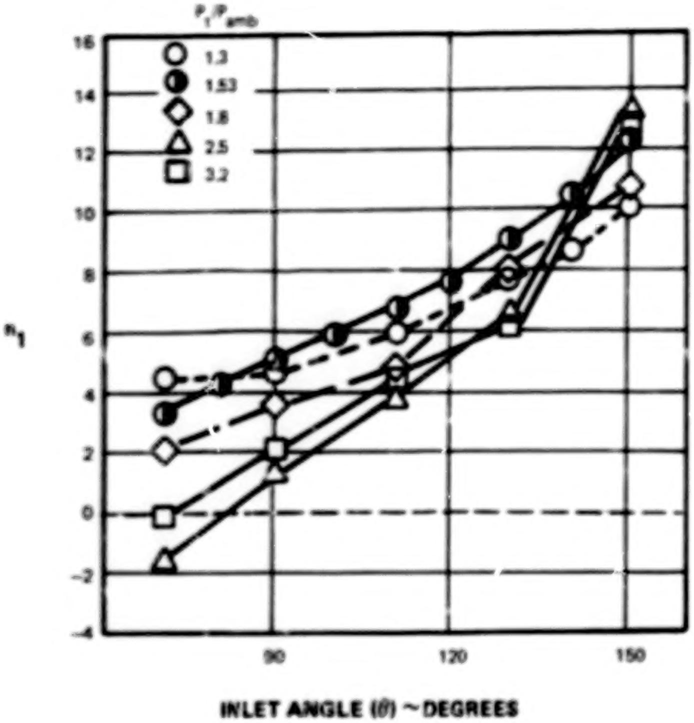

(B) T_1 = 589°K (600°F)

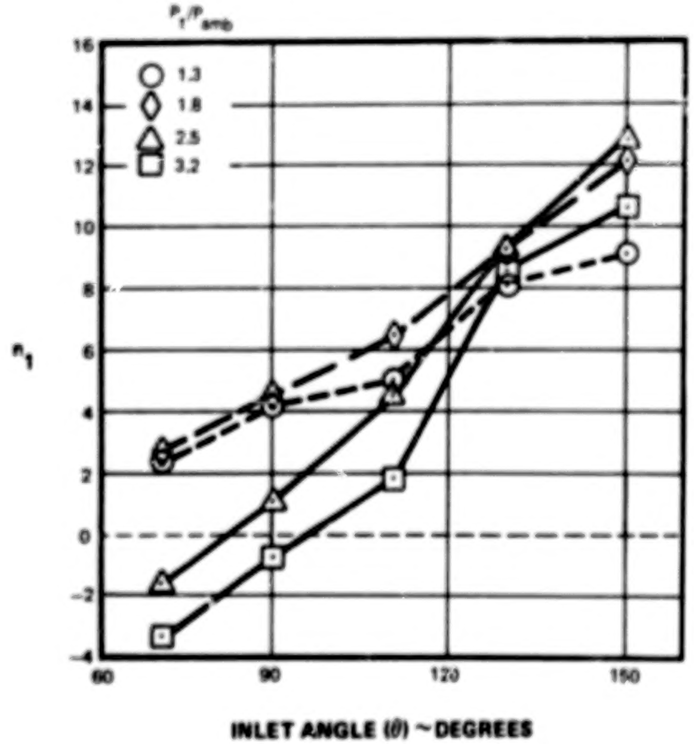

Figure 5.1.2-2 *Relative Velocity Exponents n_1 for Convergent Nozzle At Different Nozzle Pressure Ratio and Temperatures*

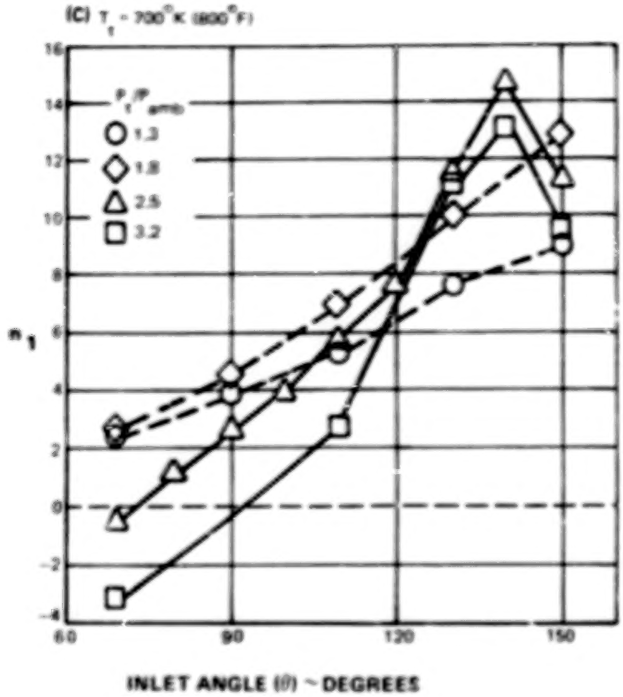

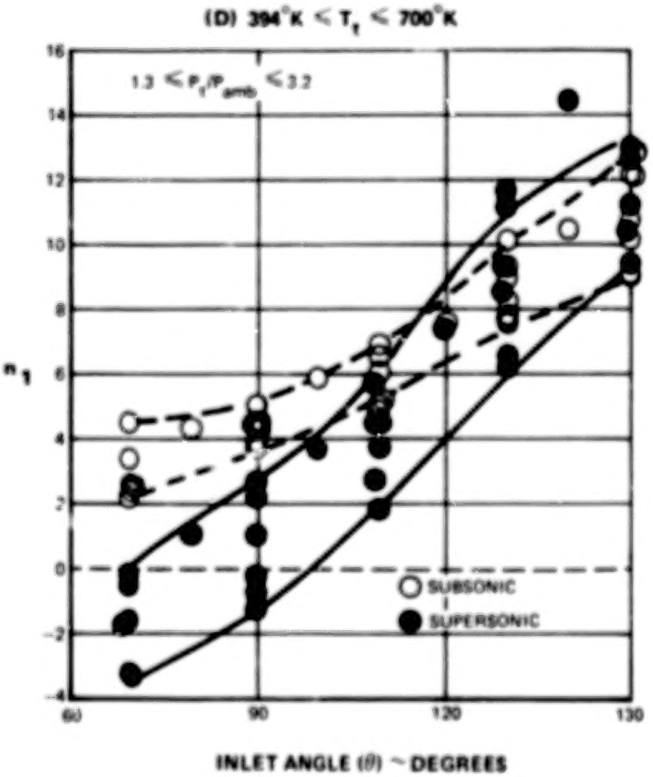

Figure 5.1.2-2 Relative Velocity Exponents n_1 for Convergent Nozzle At Different Nozzle Pressure Ratio and Temperatures

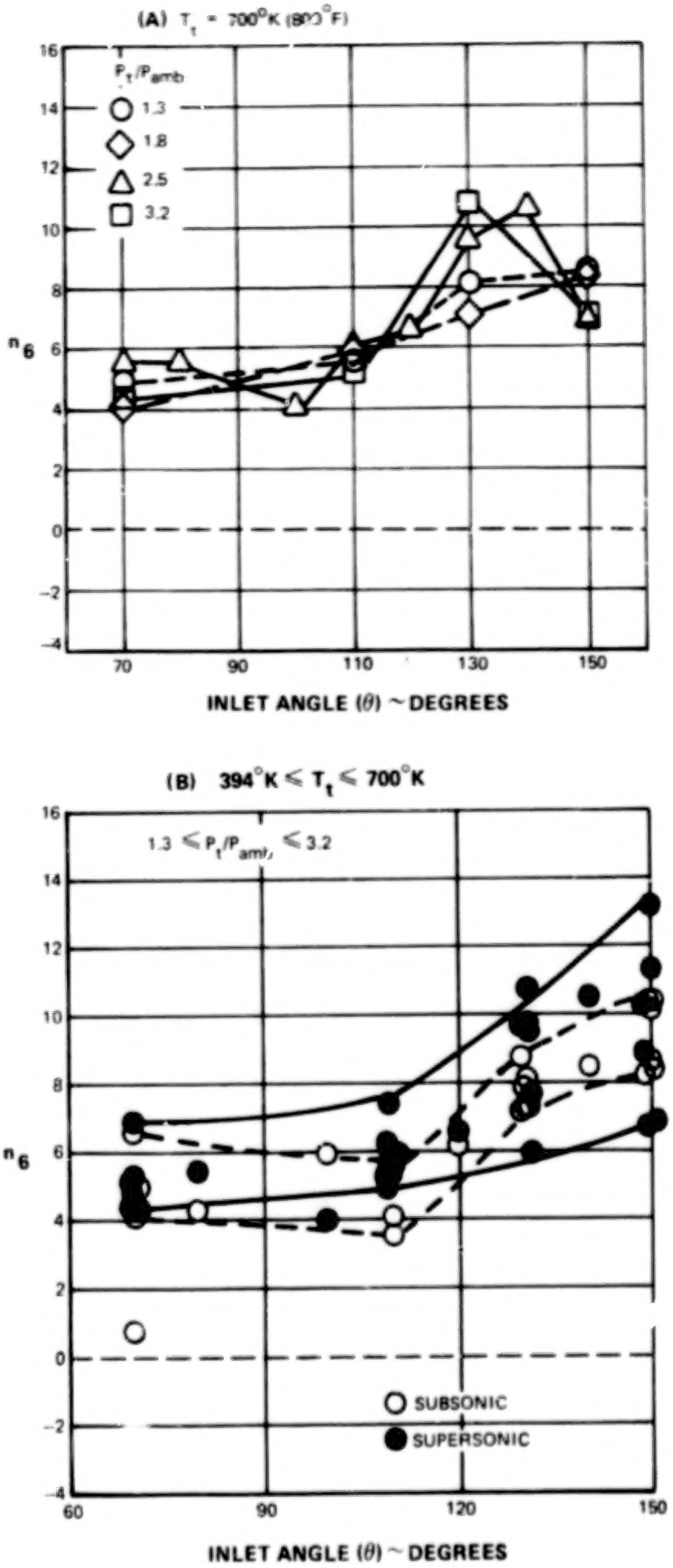
(A) T_t = 700°K (800°F)

(B) 394°K ≤ T_t ≤ 700°K

Figure 5.1.2-3 Convection Exponents n_6 for Convergent Nozzle At Different Nozzle Pressure Ratios

The variation in relative velocity exponent, n_1, with angular position for a range of pressure ratios at three jet total temperatures of 394°K (250°F), 589°K (600°F), and 700°K (800°F) is shown in Figures 5.1.2-2(a), (b) and (c), respectively. In general, the exponent n_1 increases with increasing inlet angle. For the subsonic cases (pressure ratio equal to 1.3, 1.53, and 1.8), the value of n_1 varies from 2 to 4.5 at $\theta_i = 70°$ and 9 to 13 at $\theta_i = 150°$. For the supersonic cases, (pressure ratios of 2.5 and 3.2), the exponent n_1 varies from -3.2 to 0 at $\theta_i = 70°$ and in the same range as the subsonic cases at 150°. The reason for n_1 peaking at $\theta_i = 140°$ for the supersonic conditions at $T_t = 700°K$ (800°F) (Figure 5.1.2-2c), is not known. The negative value of n_1 at the forward angles ($\theta_i < 90°$) indicates that the shock-associated noise was amplified by the tunnel flow at these angular positions. These observations are consistent with results reported elsewhere (References 4 and 17).

The n_1 exponent data for all operating conditions are plotted in Figure 5.1.2-2d. Although there are distinctly different trends for subsonic and supersonic conditions, the data scatter is significant, indicating that a single n_1 curve cannot universally represent the flight effect on jet noise.

The values of the n_6 exponent versus angle for a series of nozzle pressure ratios are shown in Figure 5.1.2-3 for one jet temperature. Since the exponent varies with angle, these data indicate that either, the source strength reduction due to flight is not constant for different noise emission angles, and/or, this simple approach used in an attempt to account for convective amplification of the jet noise under static conditions is not valid, and more sophisticated methods are required.

The values of n_6 for all nozzle operating conditions are shown in Figure 5.1.2-3b. The data spread in the n_6 correlation appears smaller than the data spread in the n_1 correlation shown in Figure 5.1.2-20, and thus at first glance, n_6 might be considered a better correlation for prediction purposes than would n_1. However, it must be remembered that in order to use n_6 for predictions one first must define the noise reduction at 90° since n_6 is based on the static-to-flight ΔOASPL at the various angles relative to the static-to-flight ΔOASPL at 90°. Thus, n_1 at $\theta = 90°$ must first be chosen. So, in reality, the n_1 data spread at 90° must be added to the n_6 data spread before judging the relative goodness of the n_1 and n_6 correlations. It thus appears that neither n_1 or n_6 exponents are completely reliable for use in predicting the effects of flight on jet noise. Although a detailed statistical assessment of the n_1 and n_6 exponents in terms of prediction accuracy was not carried out, it appears to the authors that the n_6 exponent provides no additional benefits for prediction purposes over the use of the n_1 exponent alone.

5.1.2.3 Coannular Nozzles

The exponent correlations for the coannular nozzles were carried out using three characteristic velocities: the primary velocity, V_p, the fan flow velocity, V_f, and the mixed (mass-flow average) velocity V_m of the two streams. The three correlations are shown in Figures 5.1.2-4 to 5.1.2-6 using the data from the 0.75 area ratio coannular nozzle without ejector.

(A) SUBSONIC FAN JET VELOCITY

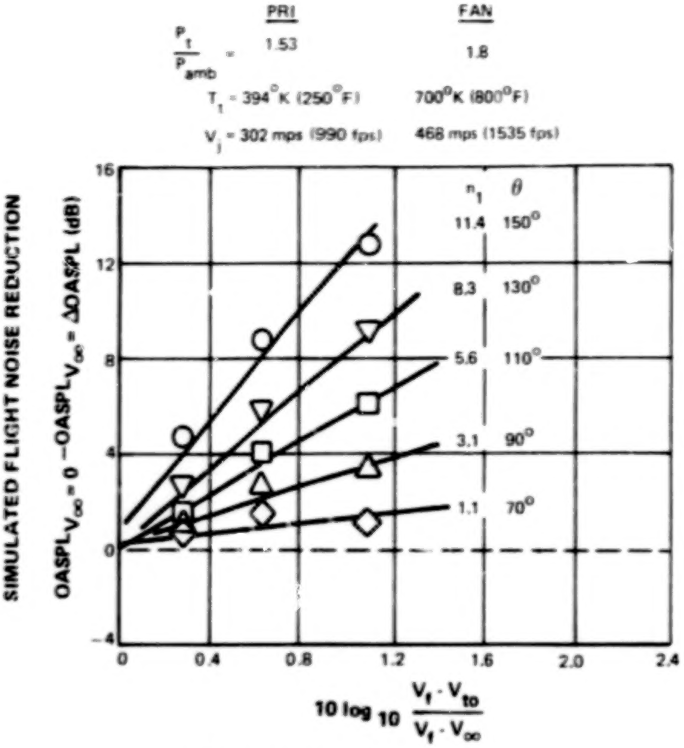

(B) SUPERSONIC FAN JET VELOCITY

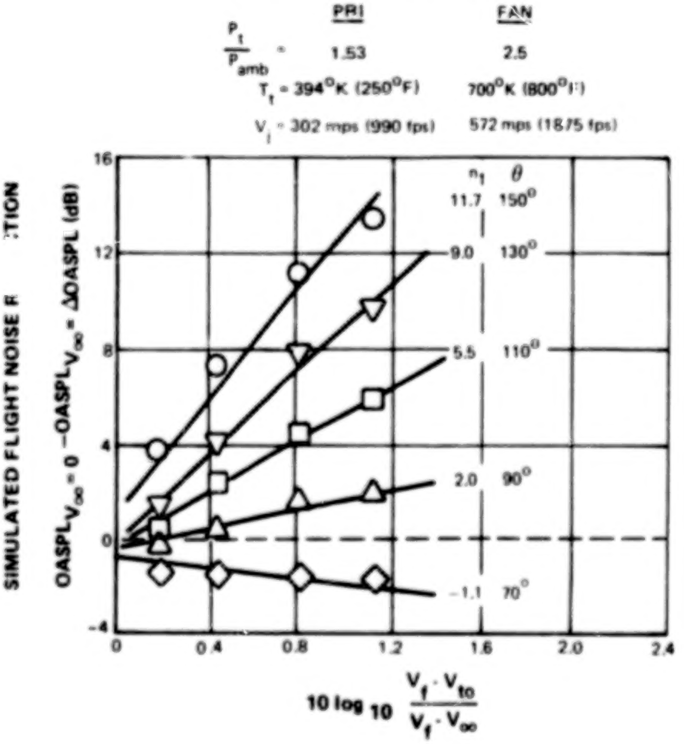

Figure 5.1.2-4 Correlations of Relative Velocity Effect On OASPL Using Fan Jet Velocity for 0.75 Area Ratio Coannular Nozzle

(A) SUBSONIC FAN JET VELOCITY

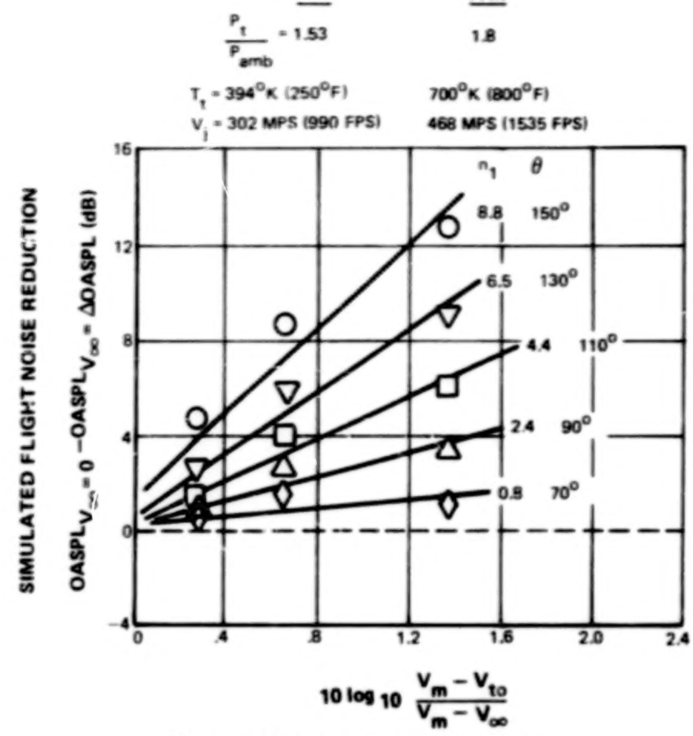

(B) SUPERSONIC FAN JET VELOCITY

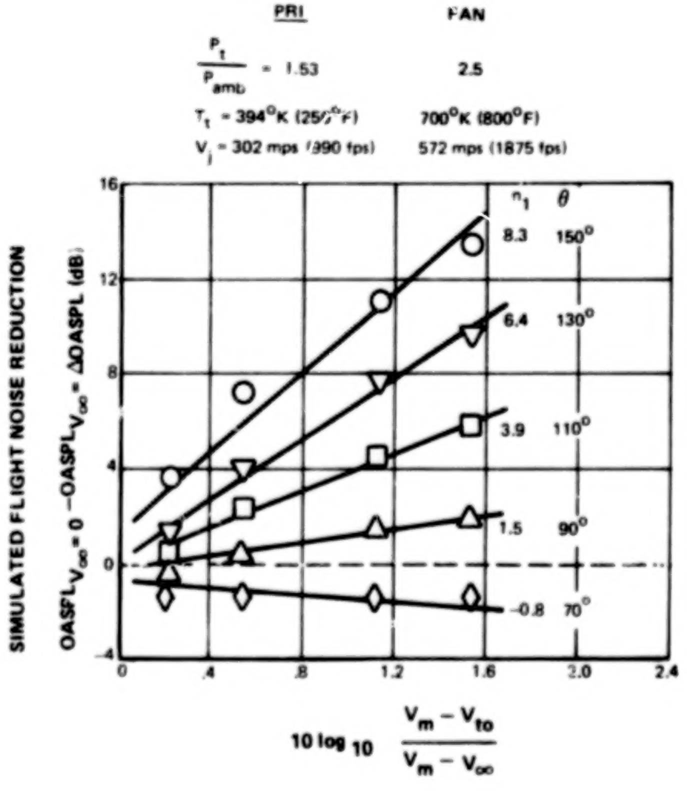

Figure 5.1.2-5 Correlations of Relative Velocity Effect On OASPL Using Mixed Jet Velocity of 0.75 Area Ratio Coannular Nozzle Model

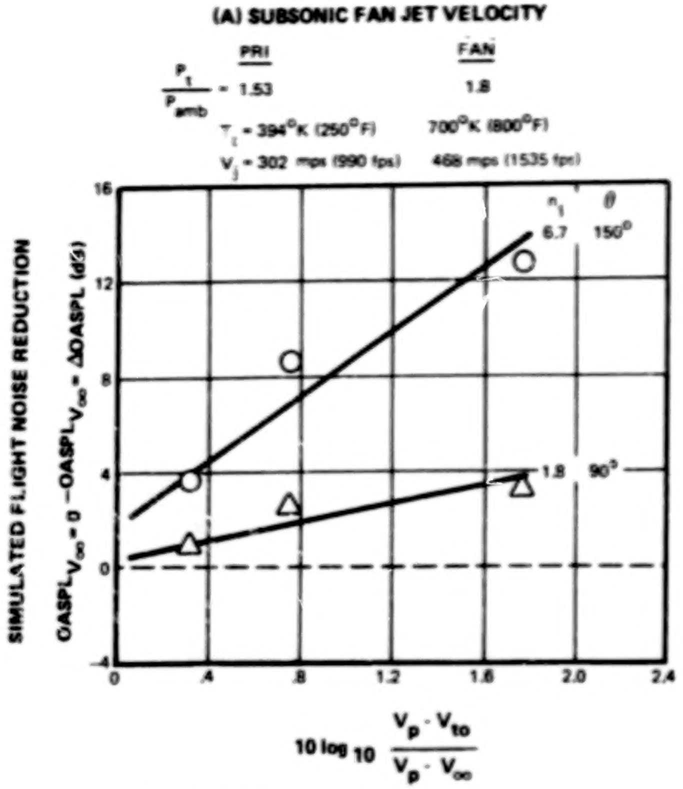

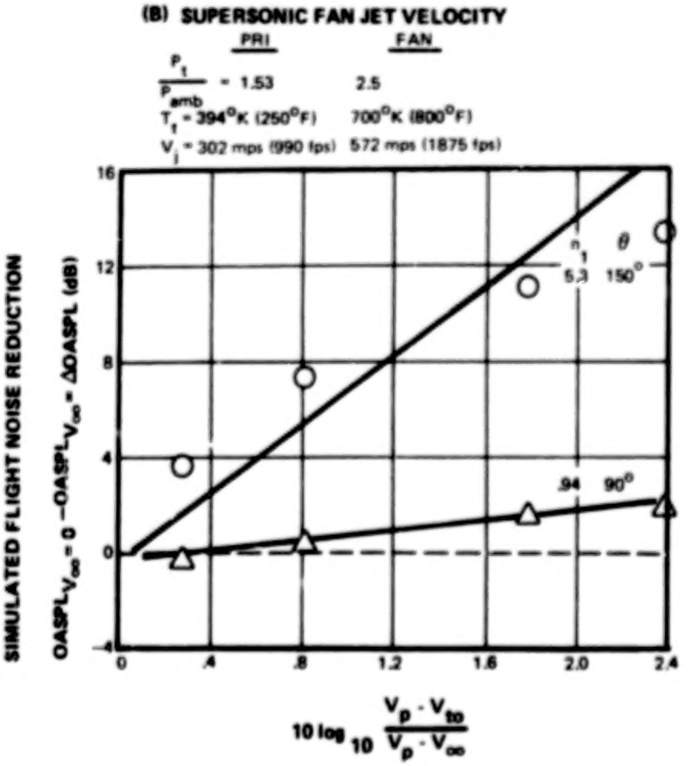

Figure 5.1.2-6 Correlations of Relative Velocity Effect On OASPL Using Primary Jet Velocity of 0.75 Area Ratio Coannular Nozzle Model

Figures 5.1.2-4a and 4b show the correlations with the fan flow velocity at subsonic and supersonic fan flow conditions. Figures 5.1.2-5 and 5.1.2-6 show correlations based on the mixed velocity and the primary flow velocity, respectively. The use of the mixed and fan velocities produce equally good collapse of the data; the use of primary velocity produces a less acceptable correlation. Since the fan velocity is a basic parameter for the coannular jet, the use of the fan velocity in the correlation is considered a more useful method for eventual prediction purposes. In addition, the fan velocity is a major correlation parameter for the noise of the coannular jet noise as shown in reference 1, while mixed velocity is not.

The results of the correlations for the coannular nozzle with ejector are shown in Figures 5.1.2-7 to 5.1.2-9. As was the case without the ejector, the data collapses well when either the fan or mixed velocity is used as the correlating parameters for both subsonic and supersonic fan velocities, as shown in Figures 5.1.2-7 and 5.1.2-8. The use of the primary velocity produced the data collapse shown in Figure 5.1.2-9, which was not quite as good as the other two velocities.

The results of the correlations for the 1.2 area ratio coannular nozzle are shown in Figure 5.1.2-10. The use of fan and mixed velocities both produce about the same data collapse as shown in Figures 5.1.2-10 and 11. The use of primary velocity also produced a reasonable data collapse as shown in Figure 5.1.2-12.

Thus, the exponent data show good collapse for all the coannular configurations when either the fan or mixed velocities are used as the correlating velocity, and fair collapse was achieved when the primary velocity was used. As mentioned previously, the exponents resulting from the fan velocity were considered the most useful for prediction use since it is an independent parameter.

The dependence of the relative velocity exponent, n_1, on the noise radiation angle, θ_i, is shown in Figures 5.1.2-13 to 15 for the three coannular nozzles, where

$$n_1 = \frac{\mathrm{OASPL}_{V_\infty = 0} - \mathrm{OASPL}_{V_\infty}}{10 \operatorname{Log} \dfrac{V_F}{V_F - V_\infty}}$$

The results for the 0.75 coannular nozzle, in Figure 5.1.2-13 show characteristics similar to those of the convergent nozzle seen earlier. For a subsonic fan flow, the exponents are positive for all measured angles, although the values decrease to a value of 1.0 at 70°. At the aft angles, the exponent levels are larger at the higher fan velocity. At a supersonic fan velocity, the exponents are larger at the aft angles, but are lower at the forward angles, actually showing negative values forward of 80° for a fan pressure ratio of 2.5 and forward of 100° for a 3.2 fan pressure ratio. These negative exponents are consistent with the increase in noise due to forward velocity at forward angles for supersonic fan conditions. As discussed previously, the broadband shock noise in the fan jet tends to increase with increasing tunnel speed at the forward angles, thus resulting in the exponents becoming more highly negative with increasing fan jet pressure ratio.

(A) SUBSONIC FAN JET VELOCITY

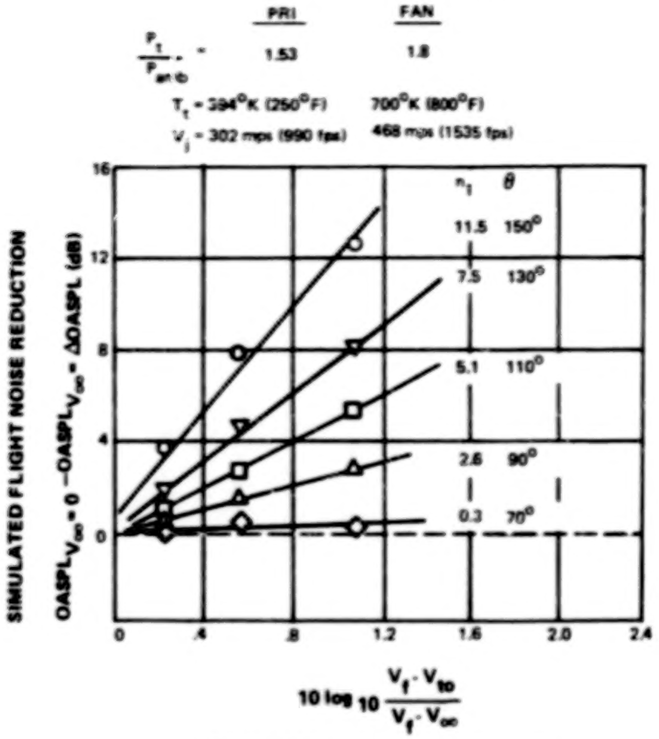

(B) SUPERSONIC FAN JET VELOCITY

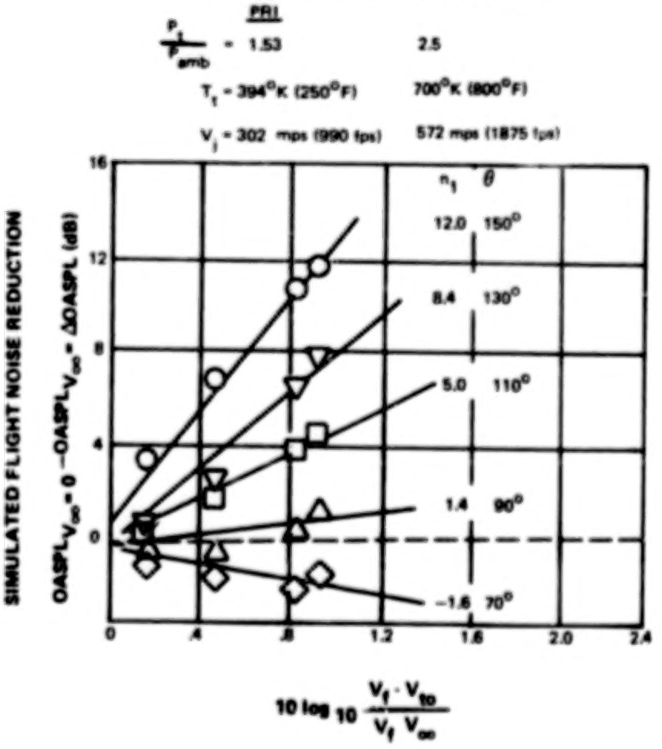

Figure 5.1.2-7 Correlations of Relative Velocity Effect On OASPL Using Fan Jet Velocity of 0.75 Area Ratio Coannular Nozzle Model With Ejector

(A) SUBSONIC FAN JET VELOCITY

	PRI	FAN
$\frac{P_t}{P_{amb}}$	= 1.53	1.8
T_t	= 394°K (250°F)	700°K (800°F)
V_j	= 302 mps (990 fps)	466 mps (1535 fps)

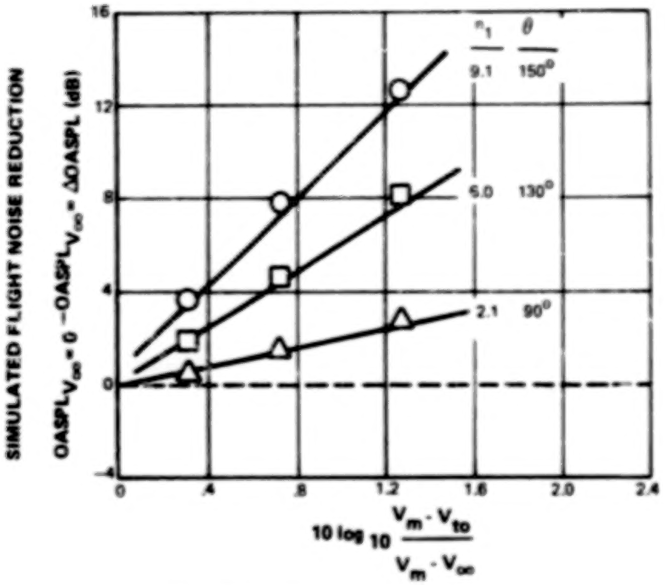

(B) SUPERSONIC FAN JET VELOCITY

	PRI	FAN
$\frac{P_t}{P_{amb}}$	= 1.53	2.5
T_t	394°K (250°F)	700°K (800°F)
V_j	= 302 mps (990 fps)	572 mps (1875 fps)

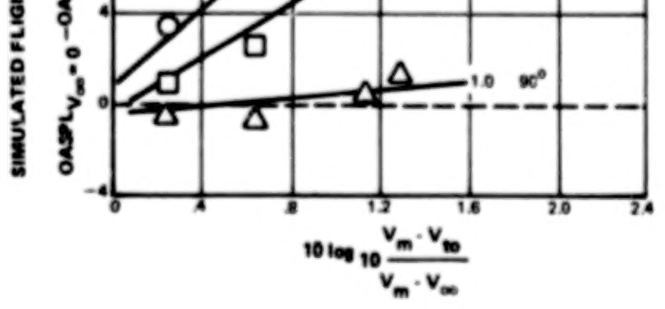

Figure 5.1.2-8 *Correlations of Relative Velocity Effect On OASPL Using Mixed Jet Velocity of 0.75 Area Ratio Coannular Nozzle Model With Ejector*

(A) SUBSONIC FAN JET VELOCITY

	PRI	FAN
P_t / P_{amb} =	1.53	1.9
T_t =	394°K (250°F)	700°K (800°F)
V_j =	302 mps (990 fps)	466 mps (1535 fps)

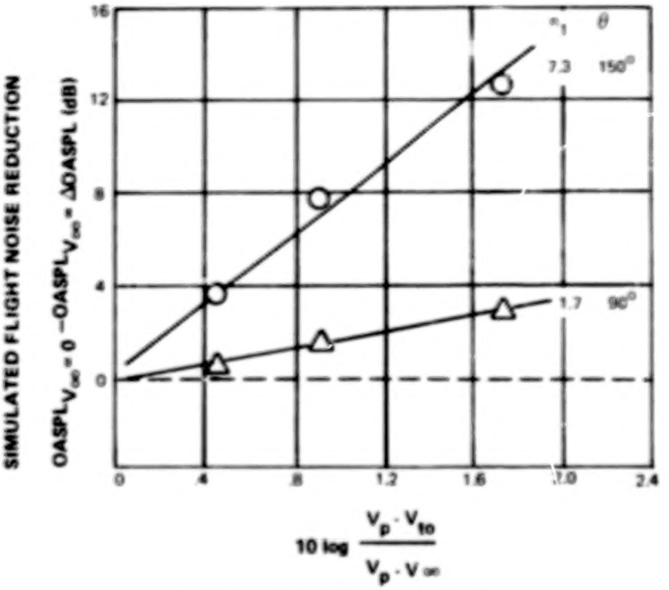

(B) SUPERSONIC FAN JET VELOCITY

	PRI	FAN
P_t / P_{amb} =	1.53	2.5
T_t =	394°K (250°F)	700°K (800°F)
V_j =	302 mps (990 fps)	572 mps (1875 fps)

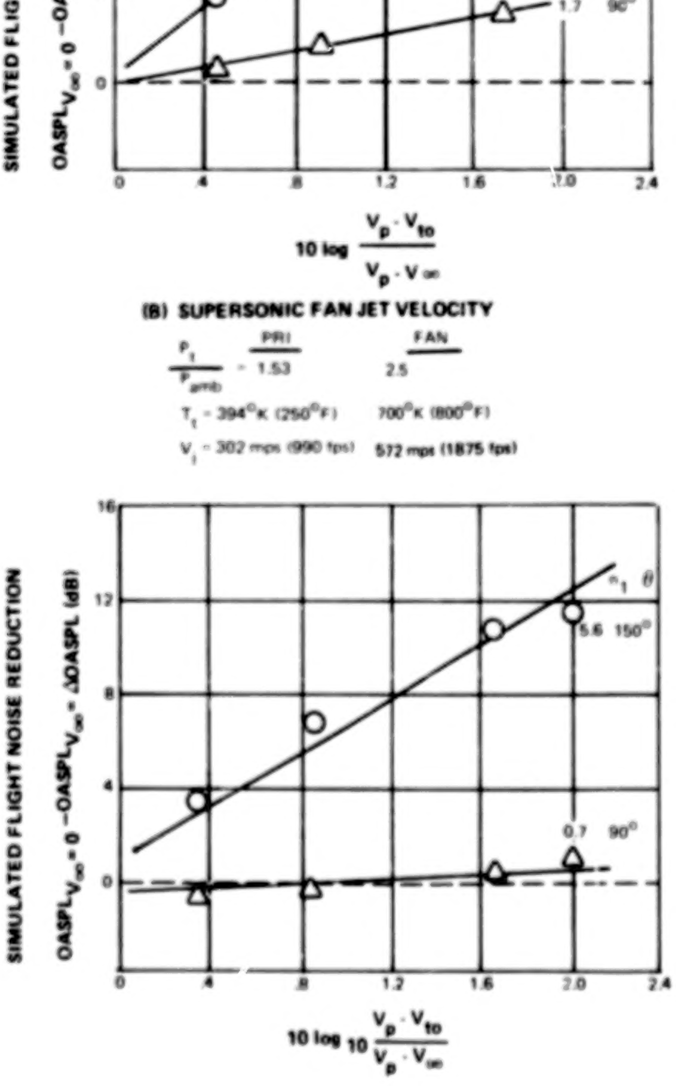

Figure 5.1.2-9 *Correlations of Relative Velocity Effect On OASPL Using Primary Jet Velocity of 0.75 Area Ratio Coannular Nozzle Model With Ejector*

(A) SUBSONIC FAN JET VELOCITY

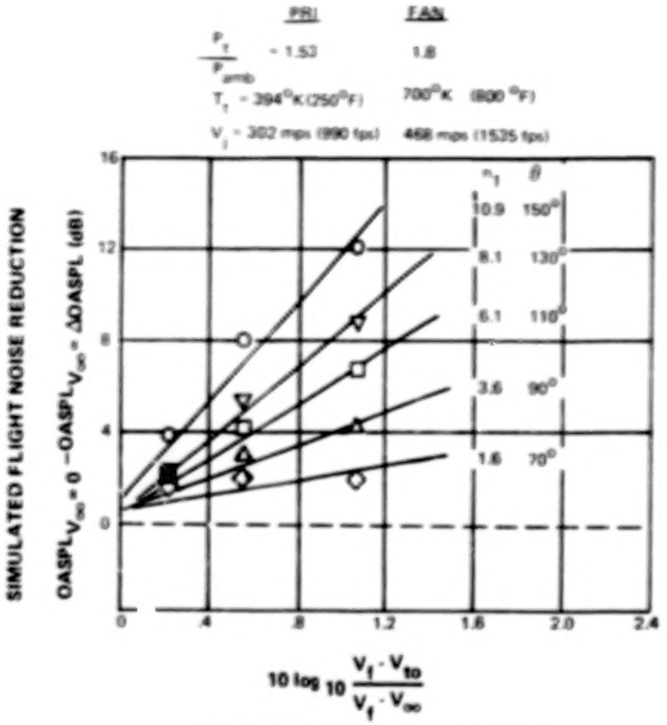

(B) SUPERSONIC FAN JET VELOCITY

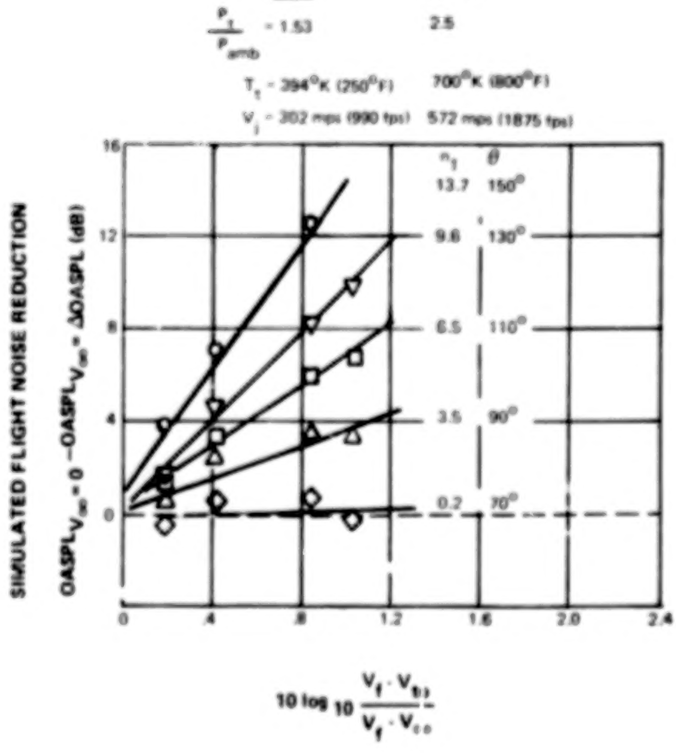

Figure 5.1.2-10 Correlation of Relative Velocity Effect On OASPL Using Fan Jet Velocity of 1.2 Area Ratio Coannular Nozzle Model

(A) SUBSONIC FAN JET VELOCITY

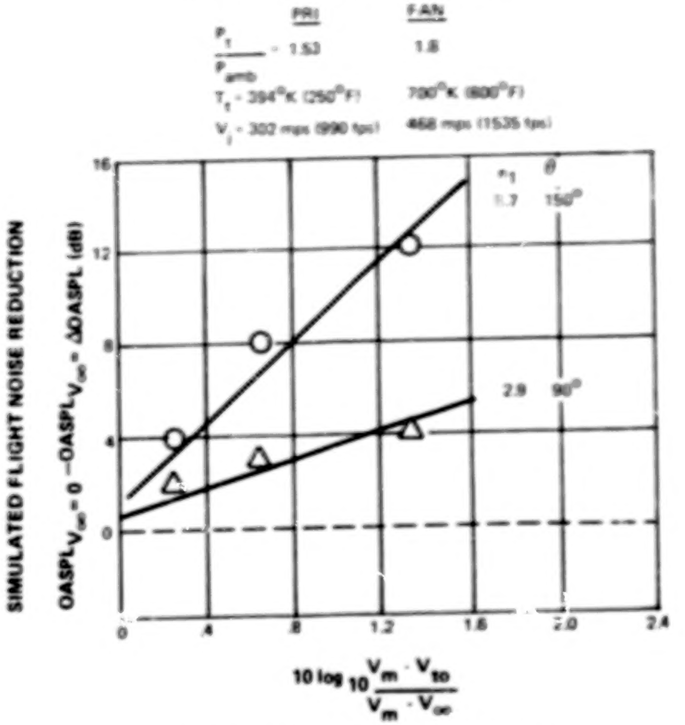

(B) SUPERSONIC FAN JET VELOCITY

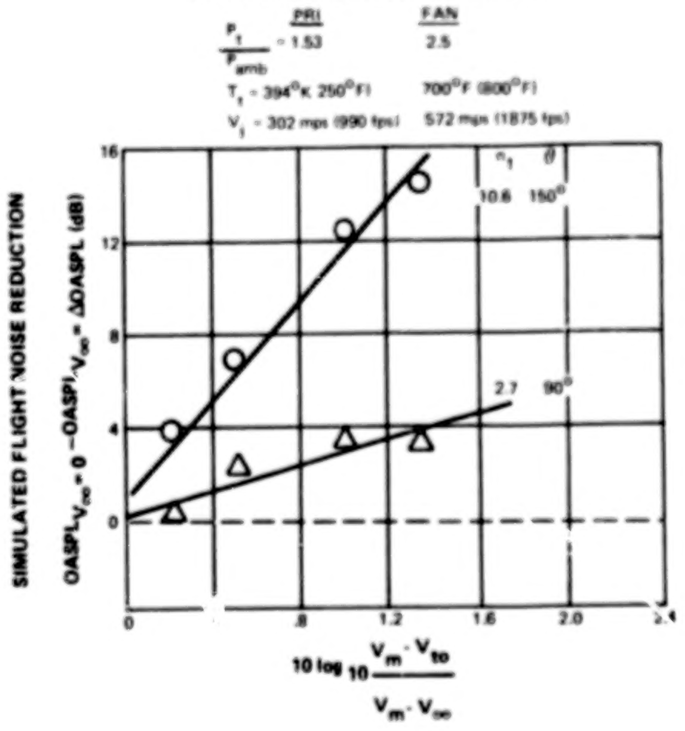

Figure 5.1.2-11 Correlations of Relative Velocity Effect On OASPL Using Mixed Jet Velocity of 1.2 Area Ratio Coannular Nozzle Model

(A) SUBSONIC FAN JET VELOCITY

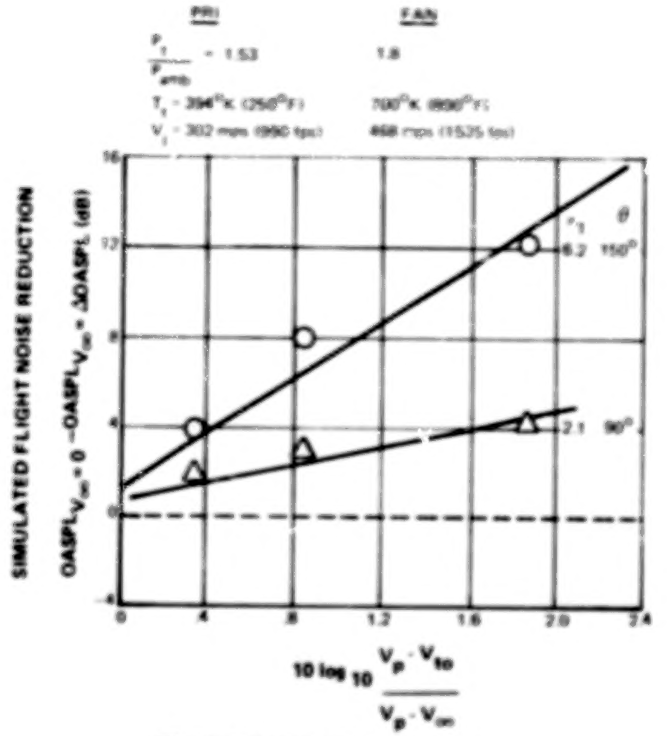

(B) SUPERSONIC FAN JET VELOCITY

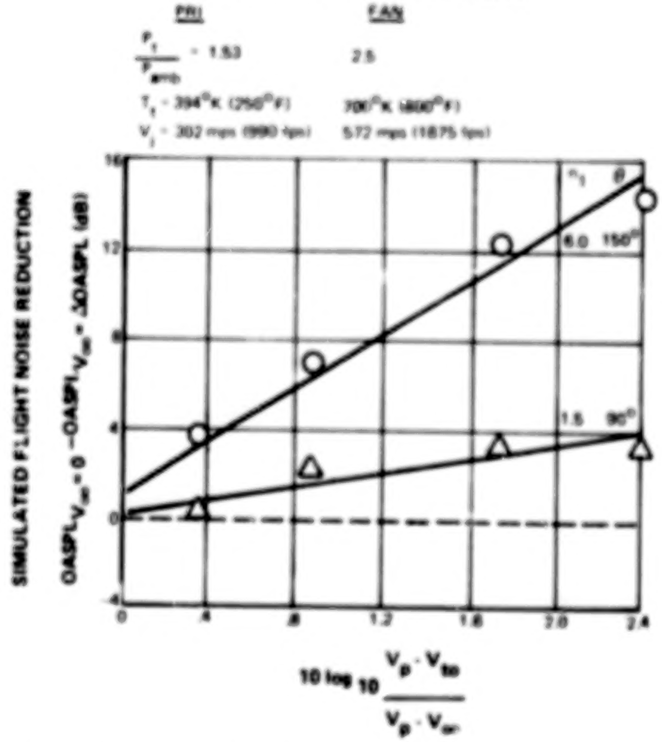

Figure 5.1.2-12 Correlations of Relative Velocity Effect On OASPL Using Primary Jet Velocity of 1.2 Area Ratio Coannular Nozzle Model

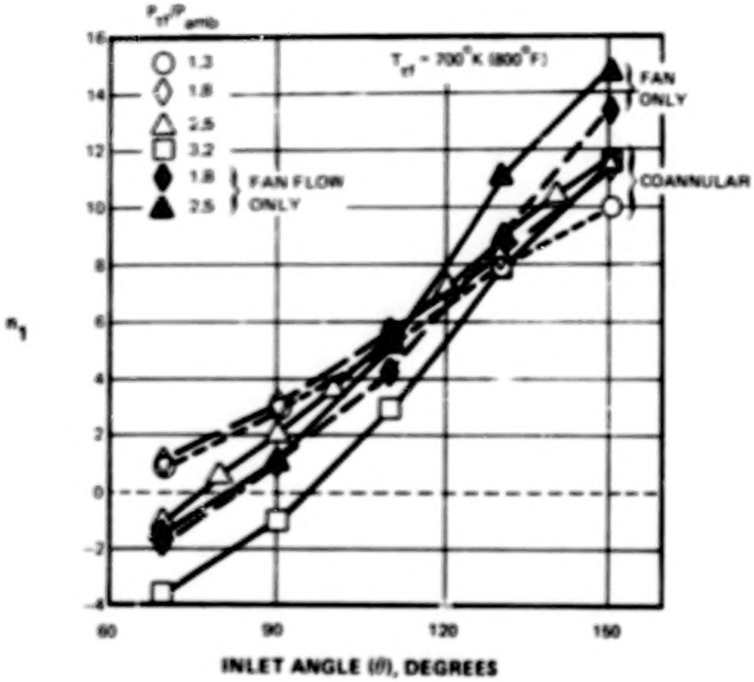

Figure 5.1.2-13 Relative Velocity Exponents As Function of Angular Position for 0.75 Area Ratio Coannular Nozzle; n_j Based on Fan Jet Velocity

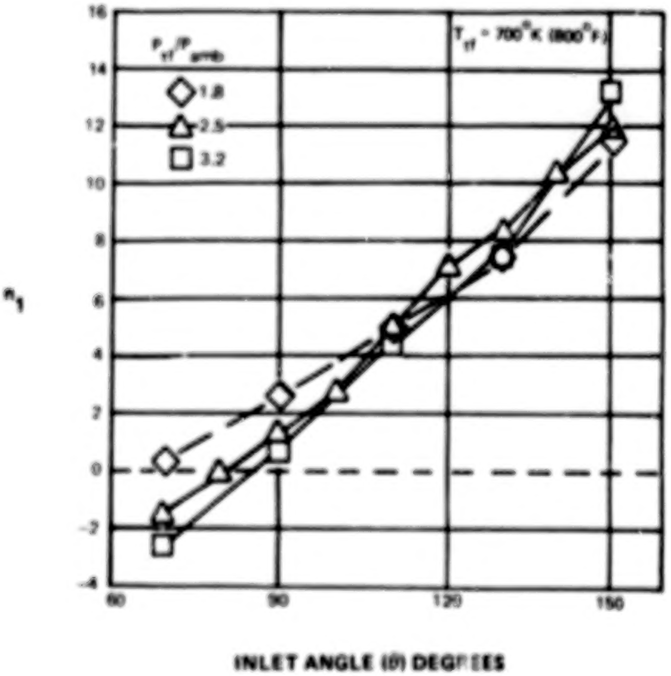

Figure 5.1.2-14 Relative Velocity Exponents As Function of Angular Position for 0.75 Area Ratio Coannular Nozzle With Ejector; n_j Based On Fan Jet Velocity

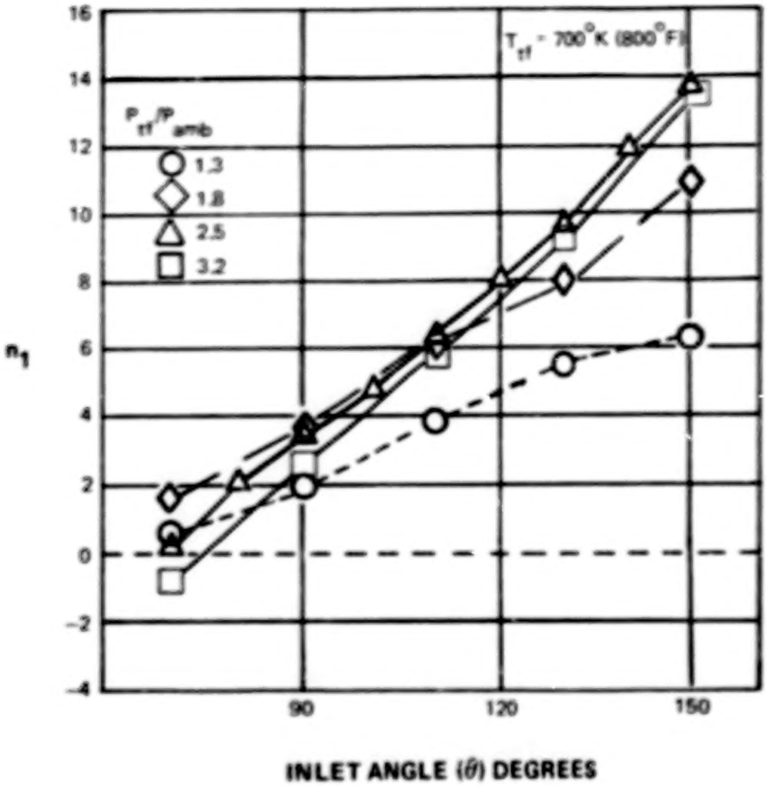

Figure 5.1.2-15 Relative Velocity Exponents As Function of Angular Position for 1.2 Area Ratio Coannular Nozzle; n_1 Based On Fan Jet Velocity

The impact of turning-off the primary stream (fan only) is also shown in Figure 5.1.2-13. The exponents for this care are larger at the aft angles than in the dual flow case, but lower at the forward angles.

The results for the coannular nozzle with ejector are shown in Figure 5.1.2-14. These results are similar to the results of this nozzle without the ejector. At forward angles the exponents are positive for subsonic fan conditions and negative for a supersonic fan. Figure 5.1.2-15 shows the results for the 1.2 area ratio nozzle, and the same general trends as seen for the other configurations are repeated.

The angular dependence of the convection exponent, n_6, for the coannular nozzles at one value of fan temperature is shown in Figures 5.1.2-16 to 5.1.2-18. The exponent, n_6, increases with inlet angle, also similar to the reference convergent nozzle result previously described. It varies from 4 to 6.5 at $\theta_i = 70°$ and from 8 to 10.5 at $\theta_i = 150°$ for all those coannular nozzle configurations. Values of n_6 for other nozzle operating conditions are listed in Appendix A. The data spread is on the same order as was seen previously for the convergent nozzle.

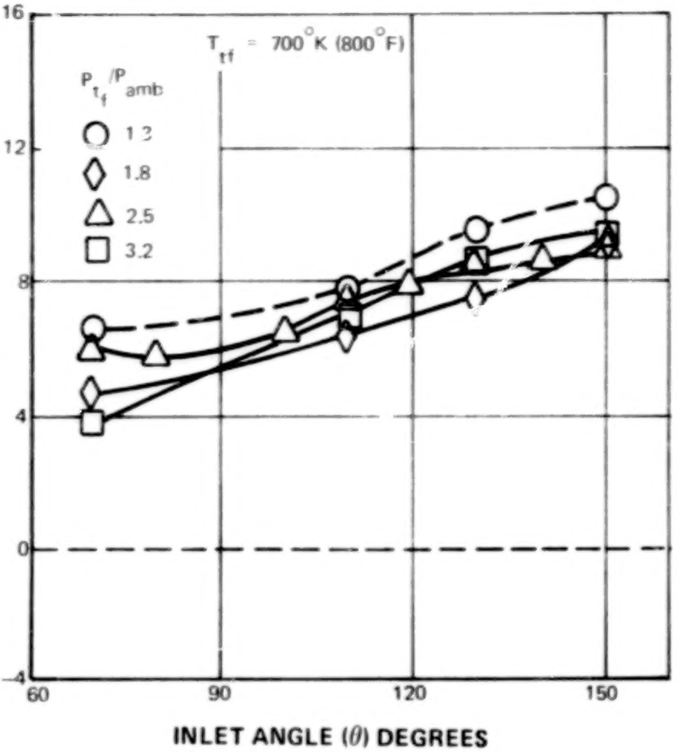

Figure 5.1.2-16 Convection Exponents As Function of Angular Position for 0.75 Area Ratio Coannular Nozzle

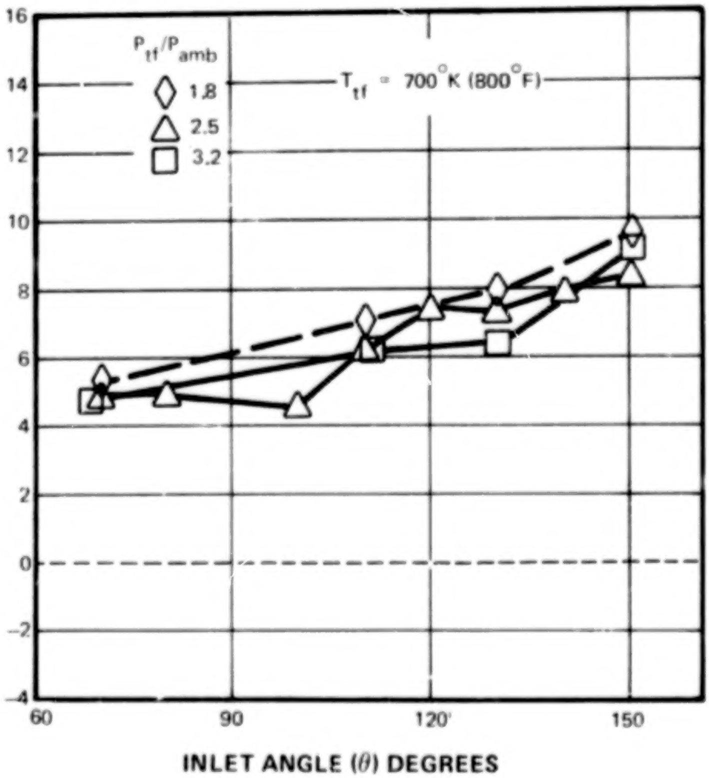

Figure 5.1.2-17 Convection Exponents As Function of Angular Position for 0.75 Area Ratio Coannular Nozzle With Ejector

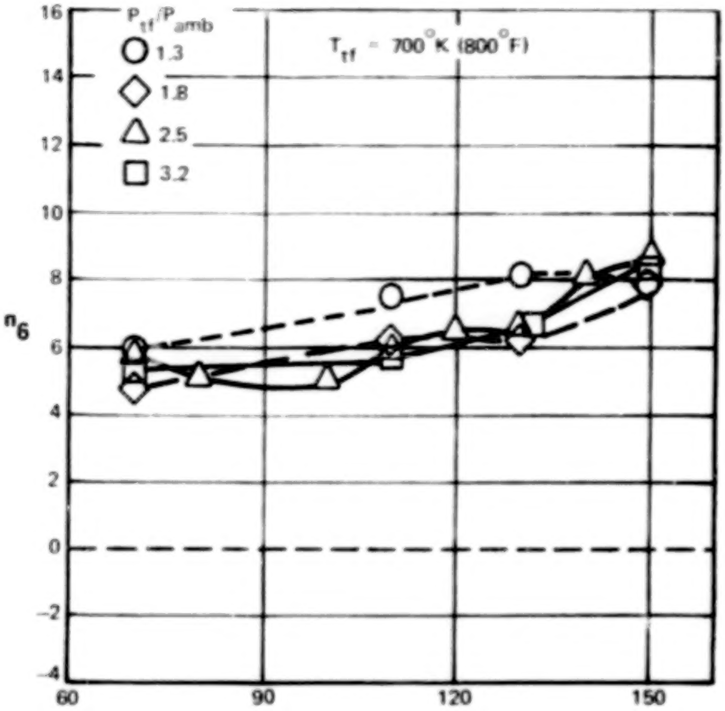

INLET ANGLE (θ) DEGREES

Figure 5.1.2-18 Convection Exponents As Function of Angular Position for 1.2 Area Ratio Coannular Nozzle

As was the case for the single stream convergent nozzle discussed previously, it is the authors opinion that for prediction purposes the use of the n_6 exponent in conjunction with the 90° n_1 exponent appears to offer no additional advantage over the use of the n_1 exponent curves alone. In a later section, the n_1 exponents are used to estimate the flight effects on the jet noise of a VSCE-502 engine. Since the exponent data had a large amount of scatter, n_1 values used for the predictions were based on those determined for nozzle operating conditions closest to the engine operating conditions rather than on averages of all the exponent data. Preliminary predictions also were made using a new approach based on separating the flight effects on the merged, pre-merged and shock noise components.

Effects of Nozzle Configuration

To illustrate the effect of nozzle configuration on the in-flight jet noise reductions, the values of the relative velocity exponent, n_1, for the four test nozzles are compared in Figures 5.1.2-19 at one subsonic fan stream condition, and in Figure 5.1.2-20 for one supersonic fan stream condition. The values of n_1 for the coannular nozzles are generally lower than those for the reference convergent nozzle, although the differences are small. An exception to this occurs at large inlet angles (θ_i = 130° to 150°) for the supersonic condition. At this condition, the reference convergent nozzle data show an irregular behavior as noted in the earlier discussion. In addition, although the coannular data do not completely collapse, the differences between those configurations are not considered significant. Also, the effect of nozzle configuration on n_1 at constant operating condition is much smaller than was the effect of operating condition for any one configuration.

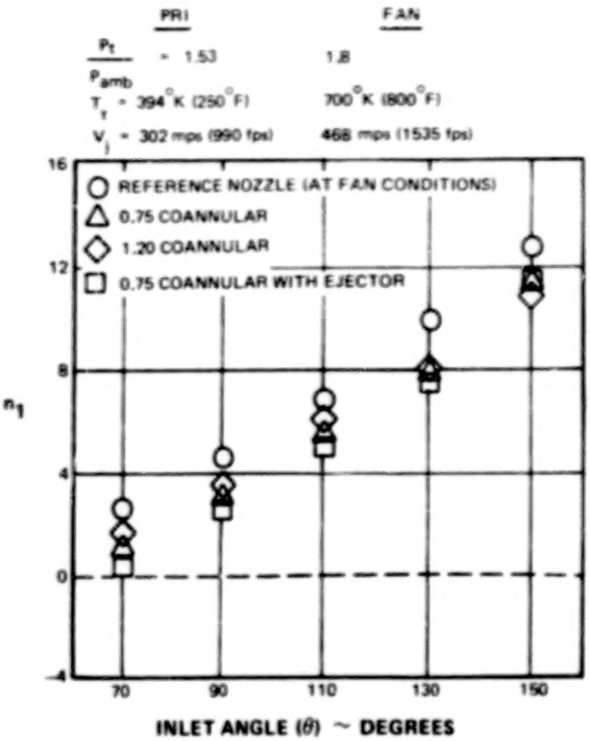

Figure 5.1.2-19 Effect of Nozzle Configuration On Relative Velocity Exponents At Subsonic Jet Velocity; n_1 Based On Fan Jet Velocity

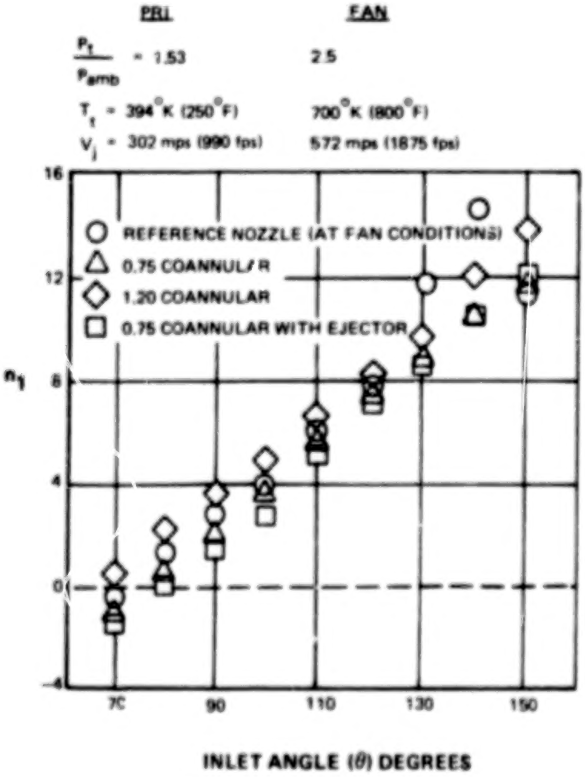

Figure 5.1.2-20 Effect of Nozzle Configuration On Relative Velocity Exponents At Supersonic Jet Velocity; n_1 Based On Fan Jet Velocity

Effects of Jet Temperature and Jet Pressure Ratio

For the reference convergent nozzle, the relative velocity exponent, n_1, increases slightly with jet temperature at pressure ratios of 1.8 (Figure 5.1.2-21) and 2.5 (Figure 5.1.2-22). For the coannular nozzle of area ratio 0.75 and a fan pressure ratio of 1.8, the highest values of n_1 in most angular positions are associated with the highest fan flow temperatures (Figures 5.1.2-23). Similar results can be observed for the fan pressure ratio of 2.5 in Figure 5.1.2-24. The changes of n_1 with fan temperature, however, are not as systematic as for the reference convergent nozzle. It must be recognized that at constant pressure ratio, increasing jet temperature corresponds to increased jet velocity. Thus, for constant values of pressure ratio, the effect of temperature described above is also true for the effect of increasing jet velocity.

5.1.2.4 Summary of Exponent Studies

The major findings of the exponent correlations are:

1) The annular (fan) stream velocity has been identified as the characteristic velocity most suitable for use in defining the relative velocity exponents for the coannular nozzles having $V_f > V_p$, although the use of mixed jet velocity also produced an acceptable data collapse.

2) At subsonic fan conditions, the exponents were positive at all angles, while for supersonic fan flow the exponents become negative at the forward angles.

3) The relative velocity exponents are slightly lower for the coannular nozzles than for the convergent nozzle, and the effects of area ratio and ejector were not significant.

4) At constant pressure ratio, the exponent values were highest at the highest value of temperature (velocity).

5) The separation of source strength and convective amplification effects was not completely modeled by the assumption of a simple convective amplification model.

6) A single universal exponent curve to define the effect of flight on the jet noise was not developed due to the large spread of data with nozzle operating conditions.

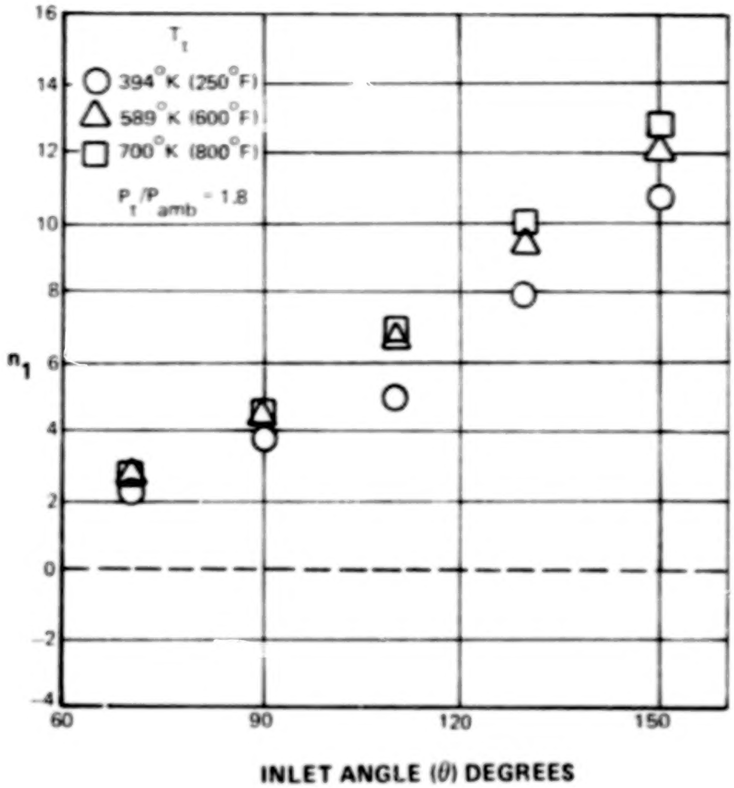

Figure 5.1.2-21 Effect of Jet Temperature On Relative Velocity Exponents for Convergent Nozzle At a Pressure Ratio of 1.8

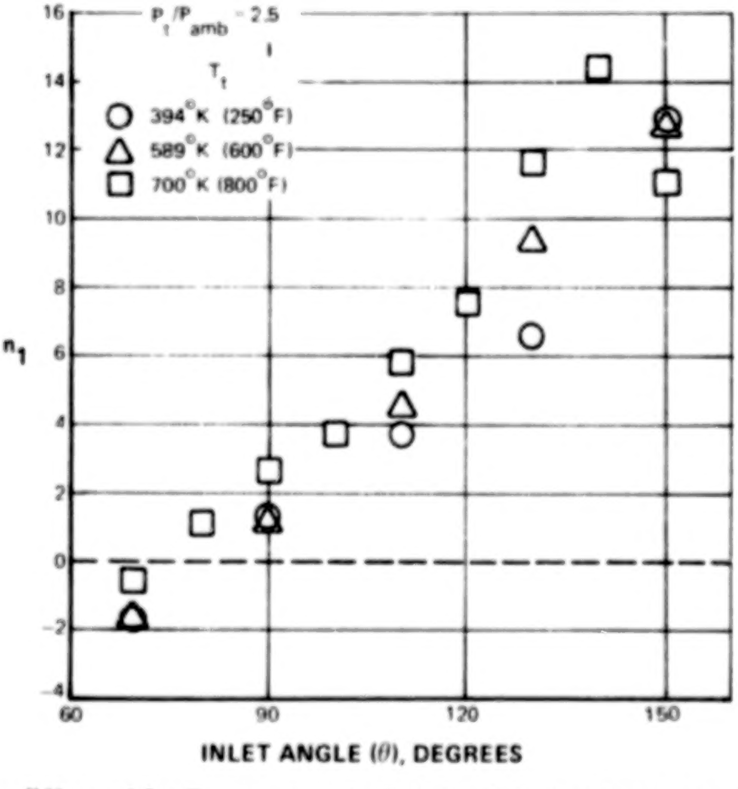

Figure 5.1.2-22 Effect of Jet Temperature In Relative Velocity Exponents for Convergent Nozzle At a Pressure Ratio of 2.5

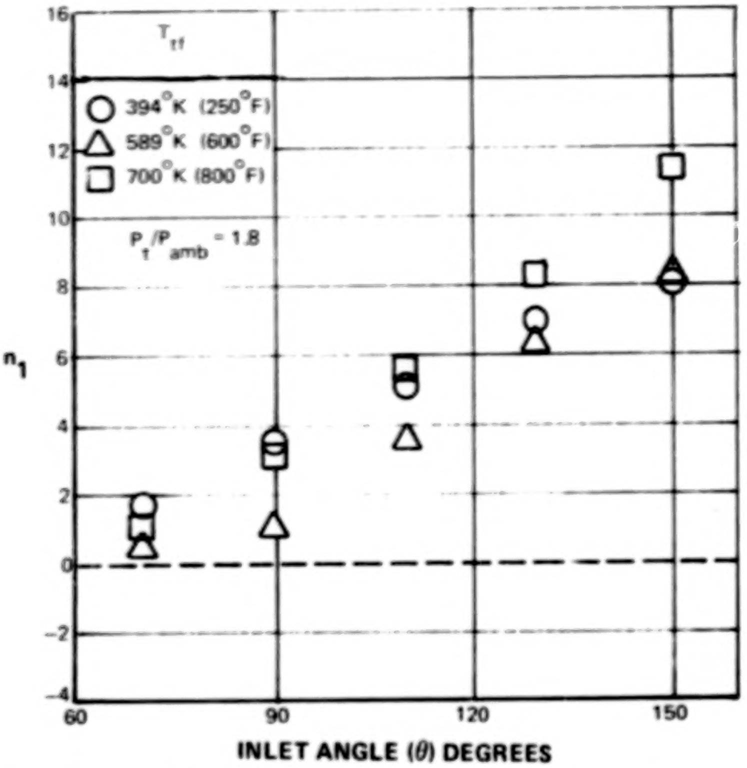

Figure 5.1.2-23 Effect of Jet Temperature On Relative Velocity Exponents for 0.75 Area Ratio Coannular Nozzle At a Fan Pressure Ratio of 1.8; n_1 Based On Fan Jet Velocity

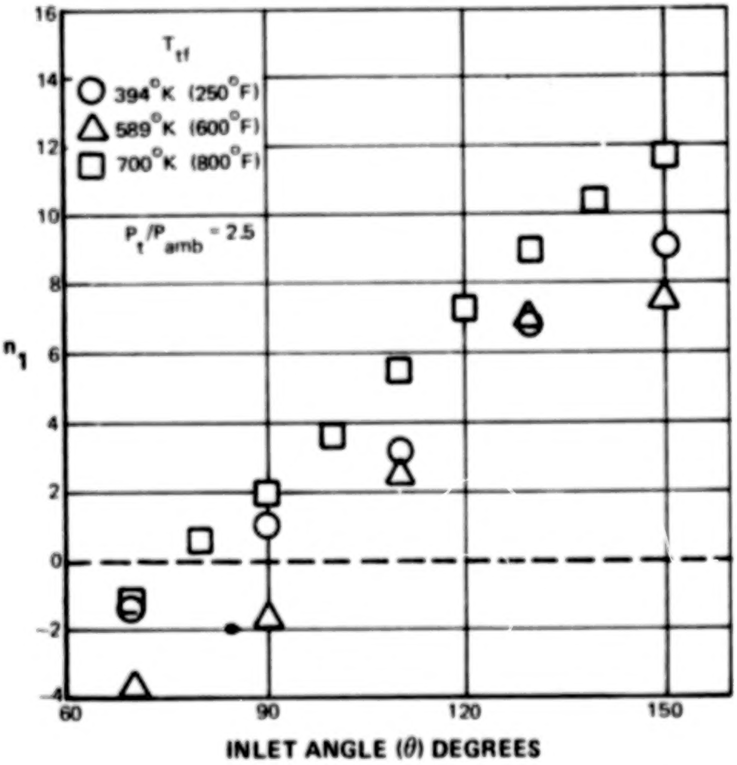

Figure 5.1.2-24 Effect of Jet Temperature On Relative Velocity Exponents for 0.75 Area Ratio Coannular Nozzle At a Fan Pressure Ratio of 2.5; n_1 Based On Fan Jet Velocity

5.1.3 Velocity Profile Correlation

A separate correlation was developed to relate the noise of the various configurations to the jet plume characteristics in the relative velocity field. This correlation follows a similar correlation of the coannular nozzle static data as presented in Reference 1. The basis for this correlation is the work of Chen (Ref. 18) in which he demonstrated that jet noise can be approximated by a spatial integration across the jet volume of a large number of radiating noise elements (or turbulent eddies). Each of the elements generates approximately as the eighth power of the local mean velocity. A velocity parameter, ϕ_V, which is a function of the absolute and relative maximum fan and primary stream velocity, each raised to different exponents (Ref. 5), and the fan-to-primary stream area ratio, was defined as shown below to model the characteristic velocity in the noise generation process.

$$\phi_V = 10\ \mathrm{LOG}\left(\left[\frac{V_{f\,max}{}^{3}\,(V_{f\,max} - V_{\infty})^{5}}{V_{ref}{}^{8}}\right]\left[\frac{A_f}{A_p}\right] + \frac{V_{p\,max}{}^{3}\,(V_{p\,max} - V_{\infty})^{5}}{V_{ref}{}^{8}}\right) + 10\ \mathrm{LOG}\left(\frac{1 + (A_f/A_p)_{ref}}{1 + (A_f/A_p)}\right)$$

where V_{ref} and $(A_f/A_p)_{ref}$ are arbitrary values.

The measurements of velocity profiles at the ejector exit plane located two diameters downstream of nozzle exit (whether or not an ejector was used) were correlated with the measured noise power levels of the various configurations. Typical velocity profiles for all configurations tested at comparable operating conditions are shown in Figures 5.1.3-1 and 2 for the static and simulated flight conditions. At both static and flight conditions, results showed the velocity decaying much faster in the coannular nozzles than the convergent nozzle. In the static condition, the velocity profiles showed only slight differences among the coannular nozzles. In the flight condition, the velocity profiles are significantly different. As shown, the fan stream of the 1.2 area ratio coannular nozzle and 0.75 area ratio coannular nozzle without ejector were moved effectively toward the centerline as compared with the static condition, while the profile of the ejector configuration was not appreciably altered. The correlations of noise level with the velocity parameter are shown in Figure 5.1.3-3 at a constant fan pressure ratio of 2.5. In the non-ejector configurations, the correlation is excellent. The maximum deviation from the mean line was within 1 dB. However, the data from the ejector configuration do not correlate along the same line. The noise levels are higher, and the slope of the data is lower than for the non-ejector configurations. Since the ejector configuration was traversed at fan pressure ratios of 1.3, 1.8 and 3.2 in addition to the 2.5 fan pressure ratio traversed for the other configurations, the effect of this variable on the correlation can be defined from the data. Figure 5.1.3-4 shows this correlation.

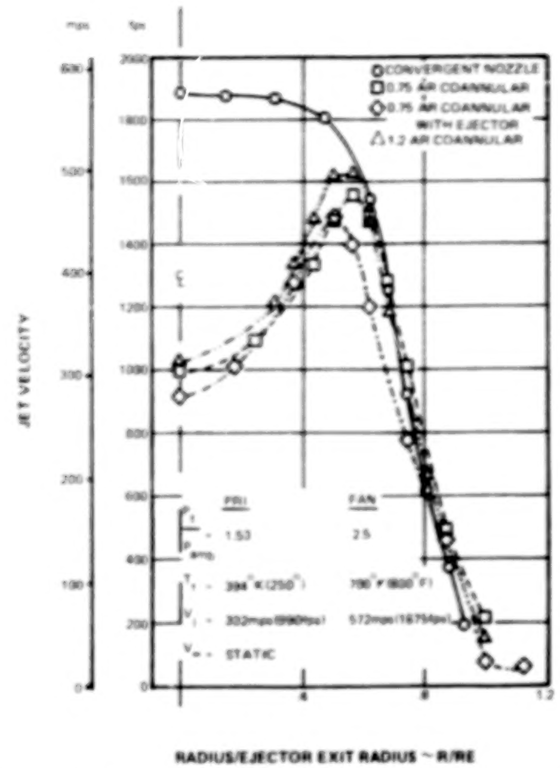

Figure 5.1.3-1 ***Velocity Profiles Measured Two Nozzle Diameters Downstream of Nozzle Exit For Various Nozzle Configurations At Static Condition***

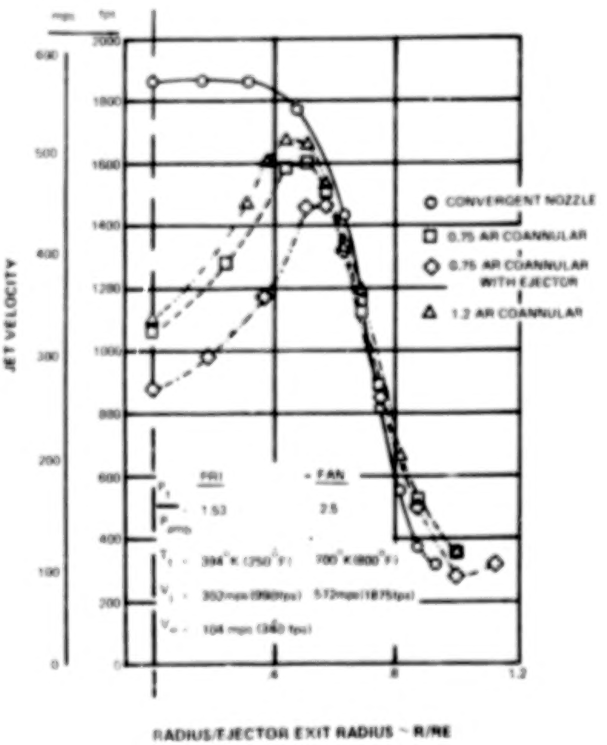

Figure 5.1.3-2 ***Velocity Profiles Measured Two Nozzle Diameters Downstream of Nozzle Exit for Various Nozzle Configurations At a Simulated Flight Speed of 104 mps (340 fps)***

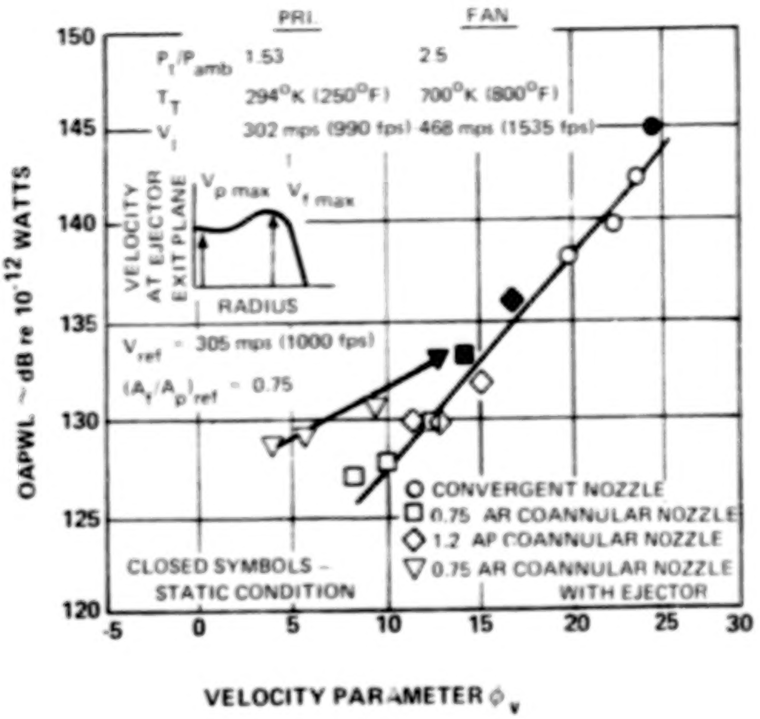

Figure 5.1.3-3 *Correlation of OAPWL and Velocity Profile Parameter for Constant Primary and Fan Conditions*

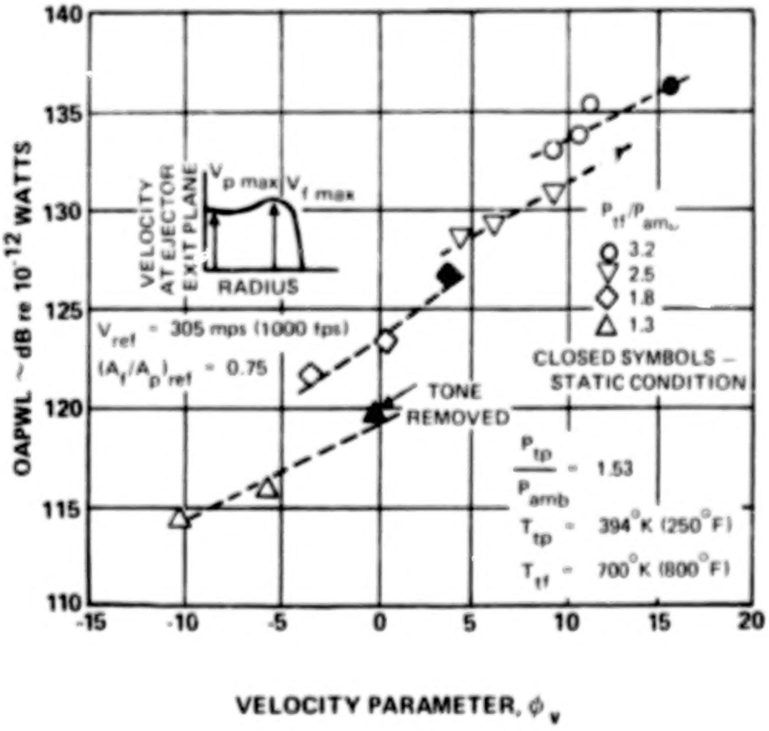

Figure 5.1.3-4 *Correlation of OAPWL and Velocity Profile Parameter for 0.75 Area Ratio Coannular Nozzle Model With Ejector*

The correlation stratifies along lines of constant fan pressure ratio, and the slopes of the data at each fan pressure ratio are approximately equal. Also, the slope of the static data (closed symbols) is approximately the same as the slope of data from the non-ejector configurations (Figure 5.1.3-3). Additional information is provided by the power spectra of the .75 coannular nozzle with and without ejector for both subsonic and supersonic fan stream conditions (P_{tf}/P_{amb} = 1.8 and 2.5) shown in Figures 5.1.3-5 and 6. In the subsonic fan condition, Figure 5.1.3-5, the ejector configuration showed more noise at the low and peak frequencies, and this excess noise was probably generated by the ejector. With tunnel velocity, this excess noise is more dominant indicating that it is subjected to less relative velocity effect. The supersonic fan condition, Figure 5.1.3-6, also showed similar results.

As discussed in Section 5.1.1.3, this excess noise is only significant at these test velocities, which are relatively low because of a temperature limitation in the test facility. At operating conditions more typical of supersonic cruise aircraft propulsion cycles, the ejector noise is expected to have only minor influence on the noise at either static or take-off speeds.

Thus, the jet noise power levels of the reference convergent and non-ejector coannular nozzles were correlated with the measured velocity profiles in the jet plume by use of a relative velocity parameter. The noise of the ejector configuration did not correlate with the same parameter due to the noise generated by the ejector which is not affected in-flight in the same manner as jet noise.

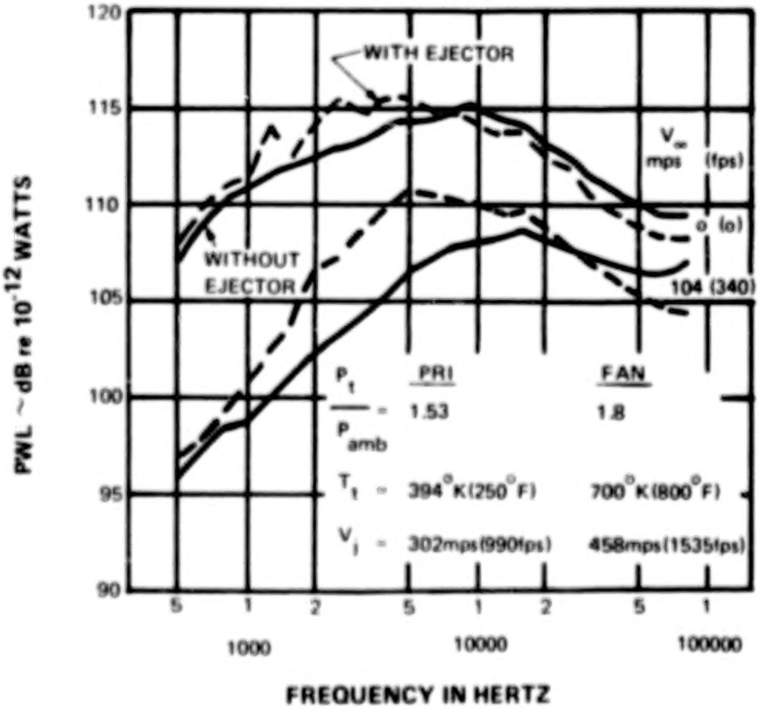

Figure 5.1.3-5 Effect of Ejector On PNL Spectra of 0.75 Area Ratio Coannular Nozzle Model At Subsonic Fan Jet Velocity

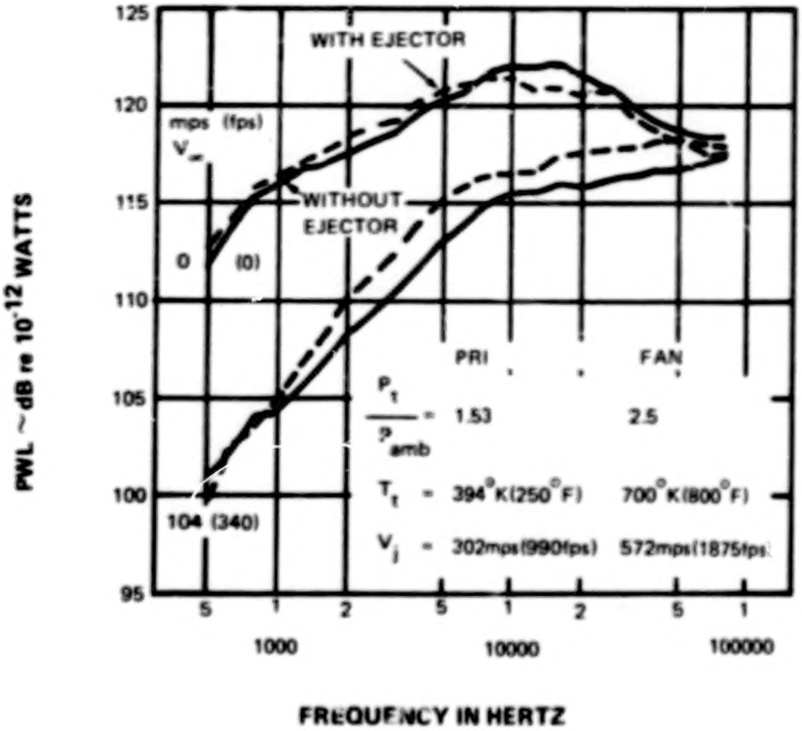

Figure 5.1.3-6 Effect of Ejector On PNL Spectra of 0.75 Area Ratio Coannular Nozzle Model At Supersonic Fan Jet Velocity

5.2 APPLICATION OF ACOUSTIC RESULTS

The acoustic results presented in the preceding sections comprise a data base to be used to define the effects of forward speed on the jet noise of VSCE coannular nozzle exhausts. In this section, the data is applied in a number of ways to gain an improved insight as to what the results imply with respect to the earlier results obtained from the static test phase of the program (Ref. 1).

Section 5.2.1 contains a comparison of the measured noise reductions due to flight speed and the noise reductions estimated on a synthesis basis. In order to assess the flight noise reductions expected for a full scale engine based on the model results, data from a limited number of test points were scaled in size to allow an evaluation of perceived noise level reductions due to flight. These results are presented in section 5.2.2.

The final section, 5.2.3, contains descriptions of two prediction methods developed using the model data which allow the flight noise reductions to be estimated at engine operating conditions typical of VSCE engines envisioned for supersonic cruise aircraft. Predictions for the VSCE-502 engine based on the two methods were carried out and are presented in this section.

5.2.1 Comparison of Results with Synthesis

As described in Section 4.4, the coannular noise synthesis was used in the early part of the AST studies to predict the noise of a VSCE exhaust system since no better procedure was available. The coannular model test program (Ref. 1) conducted by P&WA showed that the noise of a coannular nozzle having $V_f > V_p$ was significantly lower than the synthesized values. The noise characteristics of the coannular nozzle were subsequently documented in terms of a noise reduction (or noise benefit) relative to the synthesized levels. Thus, in order to describe the effect of forward speed on the coannular noise benefit, the results are presented in this section on the same basis as were the static results. That is, the noise of the coannular jet under flight conditions will be characterized as a Δ OASPL noise benefit obtained by subtracting the measured coannular noise from the synthesized levels at each wind tunnel velocity. For the flight synthesis, the convergent nozzle data obtained at the same wind tunnel speed as the coannular nozzle data were used as input. Thus, as in the static synthesis, the primary and fan streams are considered to be isolated circular jets. Specifically, any real effects of flow interaction and shielding are not considered in the synthesis procedure.

5.2.1.1 0.75 Area Ratio Coannular Nozzle

A comparison of the measured and synthesized OASPLs for the 0.75 area ratio coannular nozzle at a subsonic fan condition is presented in Figure 5.2.1-1a for flight velocities ranging from static to 104 mps (340 fps). The difference between the measured and synthesized OASPLs, (Δ OASPL) is shown in Figure 5.2.1-1b as a function of angle for all tunnel velocities. In the aft angles, the measured levels are substantially lower than the synthesized levels. A 10 dB difference is observed at 150° and the difference reduces to 2 dB for the angles less than 120°. The Δ OASPL relative to the synthesized noise remains constant for all tunnel velocities, which indicates that the coannular noise advantages defined in the manner described above, is preserved under flight conditions. As shown in Figure 5.2.1-2, a substantial difference is observed in the Δ OASPL as a function of angle for supersonic fan flow compared to the subsonic case. The OASPL noise reduction of the measured data relative to the synthesized levels in the aft angles is similar to the subsonic fan condition, but the reduction is much larger in the forward angles. This difference is due to the dominance of broadband shock noise in the forward angle, which in turn, is much stronger in the convergent nozzle spectra used in the synthesis than in the coannular nozzle data. This also indicates that the noise reduction of the coannular nozzle relative to the synthesis is slightly reduced with tunnel velocities (less than 2dB), although no distinct trend with flight speed can be observed.

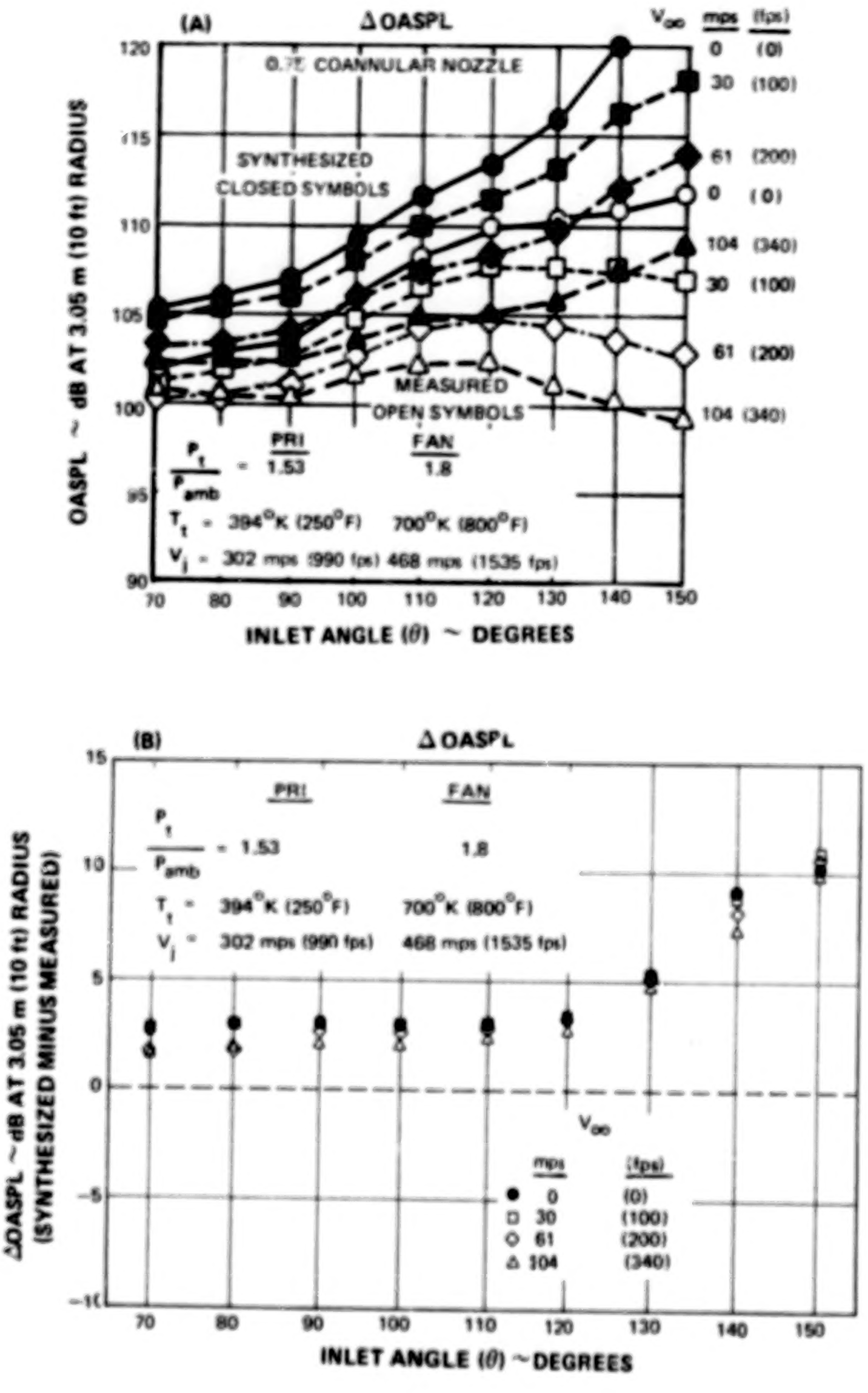

Figure 5.2.1-1 Comparison of Measured and Synthesized OASPL Directivity for 0.75 Area Ratio Coannular Nozzle Model At Subsonic Fan Jet Velocity

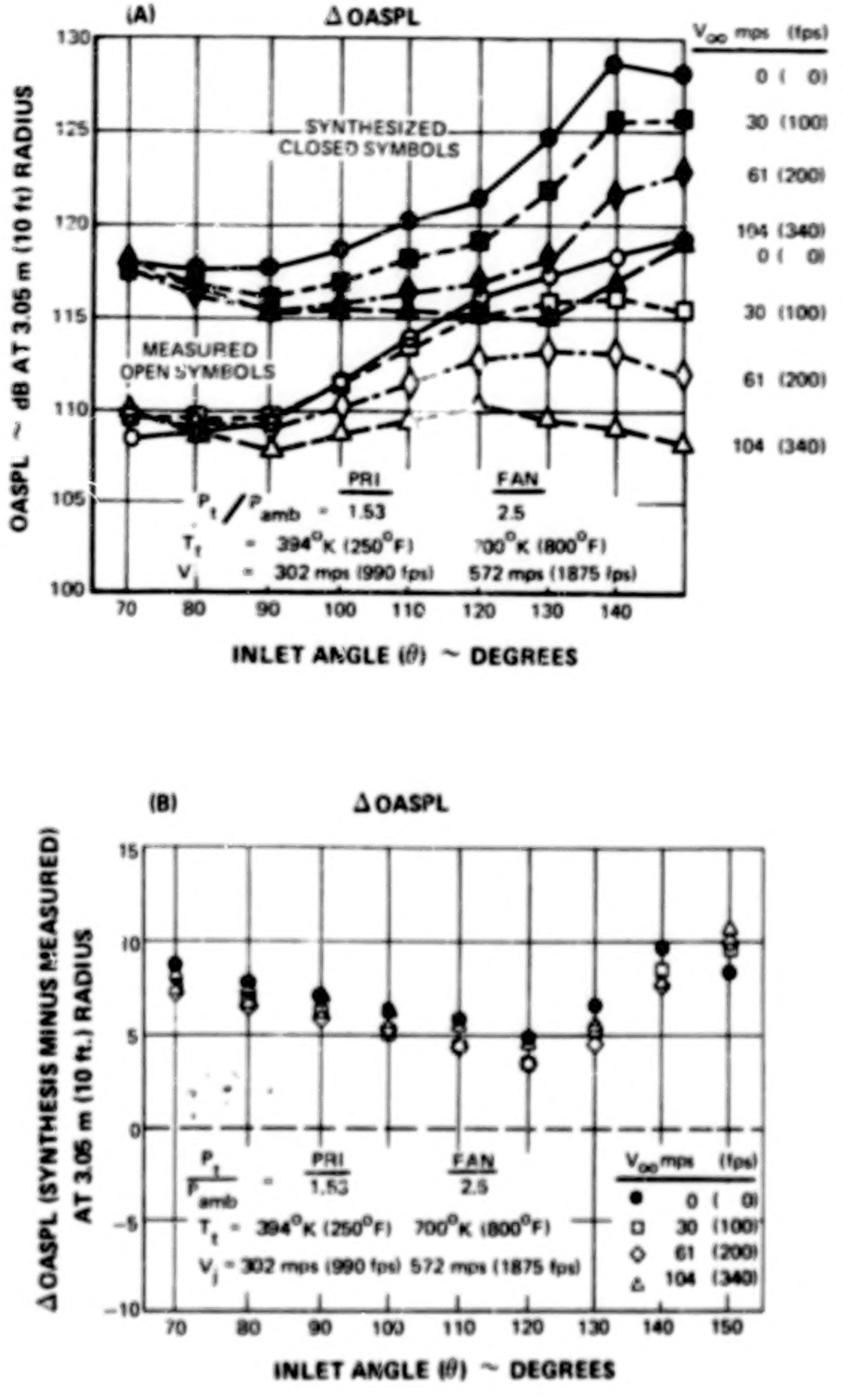

Figure 5.2.1-2 Effect of Relative Velocity On OASPL Benefit of 0.75 Area Ratio Coannular Nozzle Model At Supersonic Fan Jet Velocity

5.2.1.2 0.75 Area Ratio Coannular Nozzle with Ejector

A similar comparison of synthesized and measured OASPLs was made for the 0.75 area ratio coannular nozzle with the ejector. The synthesized OASPLs are the same with and without ejector since ejector effects are not considered in the synthesis model. The Δ OASPL relative to the synthesized noise for the subsonic fan flow case at all tunnel velocities is shown in Figure 5.2.1-3. In the aft angles, the results are similar to the non-ejector configuration. In the forward angles, there is less noise reduction of the measured data relative to the synthesis compared to the non-ejector configuration. This difference is due primarily to an increase of low frequency jet noise caused by the angular redistribution of acoustic energy by the ejector and also by a small increase in noise generation due to the presence of the ejector. These effects were previously described in Section 5.1.1.3. The figure also indicates that the noise reduction of the coannular nozzle with ejector relative to the synthesis is reduced slightly (from 0 to 3 dB) with increased tunnel velocity at most angles. The Δ OASPL for the supersonic fan flow case for all tunnel velocities is shown in Figure 5.2.1-4. These results are quite similar to the results from the non-ejector configuration, except that the loss of suppression with flight is slightly greater, relative to the synthesized value.

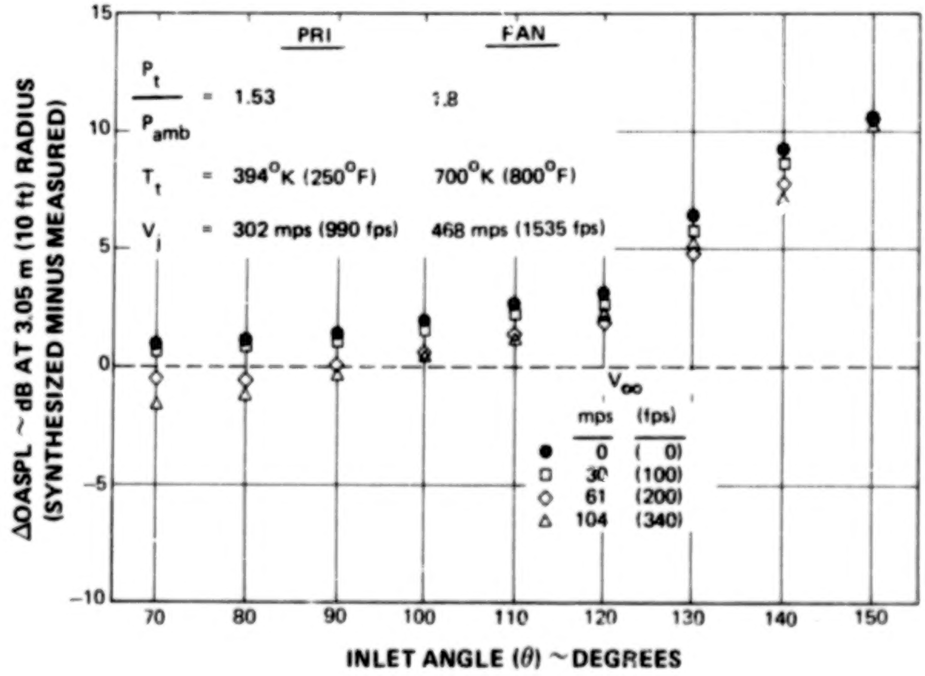

Figure 5.2.1.3 Effect of Relative Velocity On OASPL Benefit of 0.75 Coannular Nozzle Model With Ejector At Subsonic Fan Jet Velocity

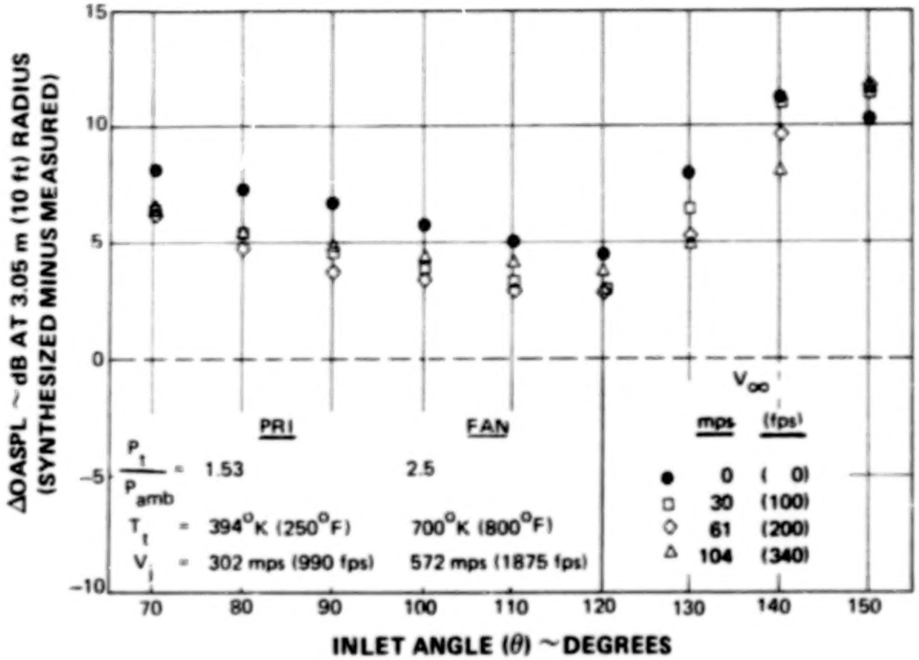

Figure 5.2.1-4 Effect of Relative Velocity On OASPL Benefit of 0.75 Coannular Nozzle Model With Ejector At Supersonic Fan Jet Velocity

5.2.1.3 1.2 Area Ratio Coannular Nozzle

A comparison of synthesized and measured OASPL was made for the 1.2 area ratio coannular nozzle. The Δ OASPL noise reduction relative to the synthesis as a function of directivity angle is presented for the subsonic and supersonic fan flow cases for all tunnel velocities in Figures 5.2.1-5 and 5.2.1-6. In the subsonic fan condition, the Δ OASPL directivity pattern is similar to the 0.75 area ratio coannular nozzle data, and the Δ OASPL is constant over the range of tunnel velocities tested. For the supersonic fan condition, the Δ OASPLs are smaller relative to the 0.75 coannular nozzle in the forward angles. This is due to the higher broadband shock noise generated by the 1.2 area ratio coannular nozzle. This broadband shock noise does not scale with the fan jet area in the same manner as does the jet mixing noise. As mentioned previously, the shock noise is a strong function of the pressure ratio. Over the range of tunnel velocities tested, the Δ OASPL changes slightly without a definite trend.

In general, the noise benefit observed under static conditions for each coannular nozzle configuration relative to the synthesized values was essentially retained under in-flight conditions.

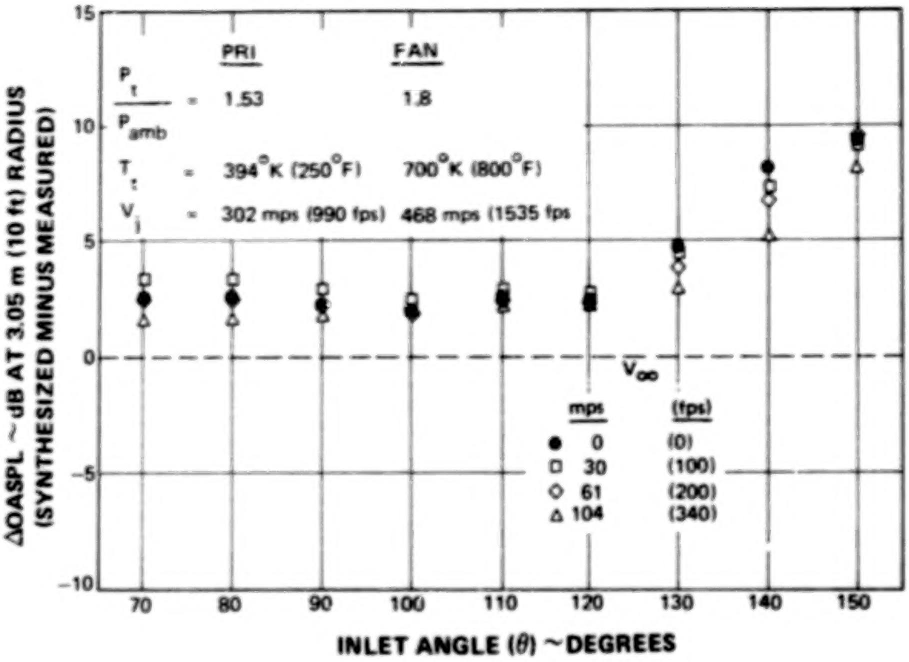

Figure 5.2.1-5 *Effect of Relative Velocity On OASPL Benefit of 1.2 Area Ratio Nozzle Model At Subsonic Fan Jet Velocity*

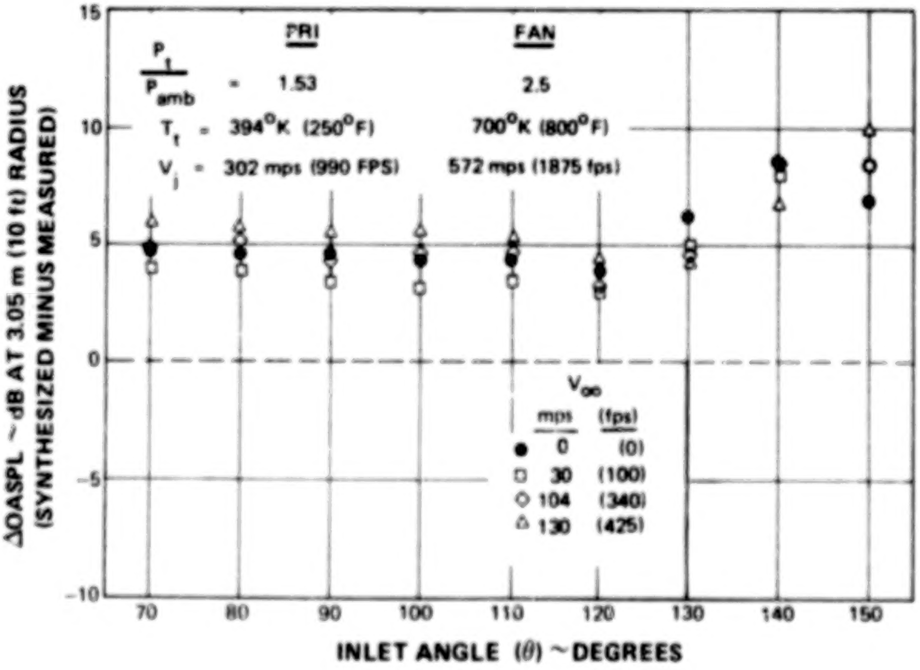

Figure 5.2.1-6 *Effect of Relative Velocity On OASPL Benefit of 1.2 Area Ratio Nozzle Model At Supersonic Fan Jet Velocity*

5.2.2 Results Scaled to Full Size

In aircraft noise studies, perceived noise level (PNL) is the most important measure of the noise under static conditions. During flight the PNL directivity, along with a duration factor, is used to compute the effective perceived noise level (EPNL). The EPNL is the noise parameter that is used in aircraft certification rules. From the current tests, a few model data points were selected and scaled (22.5X) in order to simulate a full scale engine jet exhaust. The scaling and extrapolation procedure were described in Section 4.2. It is to be noted that VSCE cycles currently being evaluated in the SCAR Program require nozzle flow conditions beyond the current test facility capability. For example, the VSCE-502 engine has primary stream temperatures and velocities up to 978°K (1300°F) and 609 mps (2000 fps), respectively, and fan stream temperatures and velocities up to 1866°K (2900°F) and 881 mps (2900 fps), respectively. As described in Section 3.1, the facility capabilities limited model primary stream temperatures to 394°K (250°F) and velocities to 304 mps (1000 fps) and fan stream temperatures to 700°K (800°F) and velocity to 635 mps (2088 fps). Thus, the full scale PNL information does not completely represent the noise characteristics of a full scale VSCE. However, the PNL results are helpful in gaining some insight as to whether the coannular nozzle noise benefits described earlier will also be true for noise on a PNL basis. In this experimental investigation, the models are 1/22-scale of typical Variable Cycle Engine for an AST application, and the measurable frequency range of the model noise is 80K Hz, which scales to 3600 Hz in full size. Thus, extrapolation to full scale suffers slightly in accuracy compared to a full frequency simulation. This slight loss in the high frequency noise does not significantly change the general behavior of PNL under relative velocity conditions. The full size PNL directivities calculated by scaling the model data include relative velocity effects. An EPNL for a specific airplant operation, such as take-off, could be calculated by applying the duration effects and Doppler frequency correction associated with the aircraft altitude and speed. A typical synthesized and measured PNL comparison is shown in Figure 5.2.2-1 for the 0.75 area ratio coannular nozzle with subsonic fan condition for all tunnel velocities. Similar to the OASPL directivity, the synthesized PNLs are significantly higher than the measured PNLs. In terms of PNL directivity, the measured noise peaks at 120° at the static condition and peaks at 100° for the flight speed of 104 mps (340 fps). The synthesized noise peaks at 140° at the static condition and peaks at 110° in the flight condition. The difference between the measured and synthesized PNL at 649 m (212 ft) sideline is presented in Figure 5.2.2-2 for all tunnel speeds. This PNL relative to the synthesized noise is very similar to the OASPL results, shown previously, in shape and level. As in the OASPL results, the noise benefit relative to the synthesis is essentially retained in flight. The PNL directivity of the synthesized and measured noise for the supersonic fan condition is shown in Figure 5.2.2-3. Both synthesized and measured PNL directivities are flatter in shape as compared with the subsonic fan condition. This change in shape is due to the strong influence of shock noise from the supersonic fan jet in the forward angles. Figure 5.2.2-4 shows the PNL reduction of the measured data relative to the synthesis for the supersonic fan condition. The results are also similar to the OASPL results presented in a previous section. Thus, for both subsonic and supersonic fan conditions, the PNL noise benefit of the coannular nozzle relative to the synthesis is retained under flight conditions.

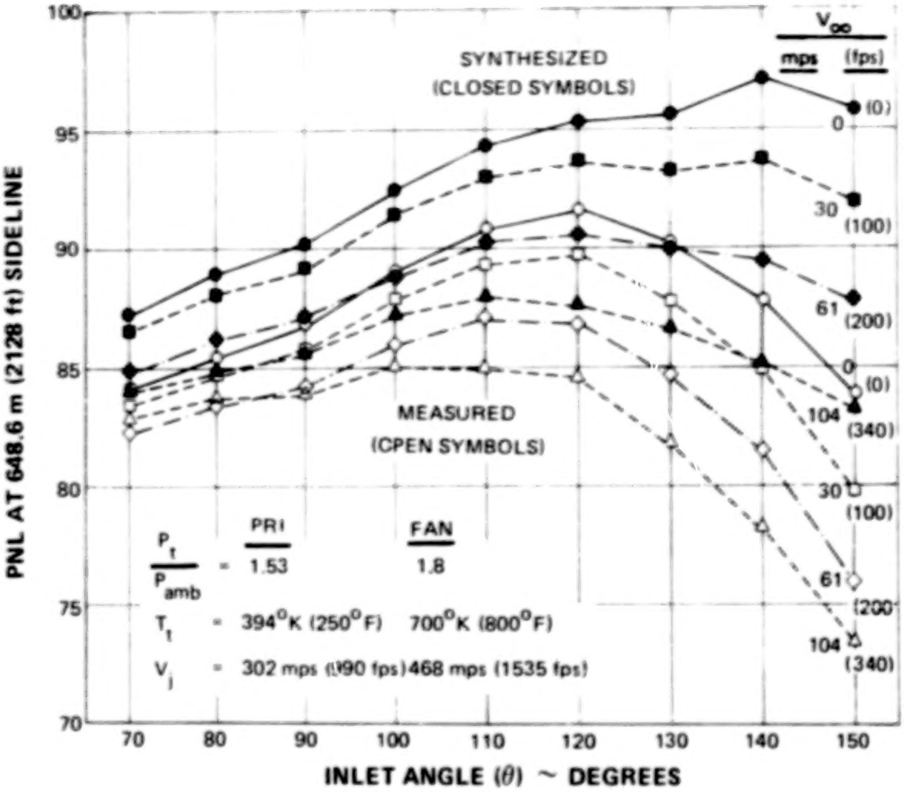

Figure 5.2.2-1 *Comparison of Measured and Synthesized PNL Directivity for 0.75 Area Ratio Coannular Nozzle Scaled to 1.27m (50 in.) Equivalent Diameter At Subsonic Fan Jet Velocity*

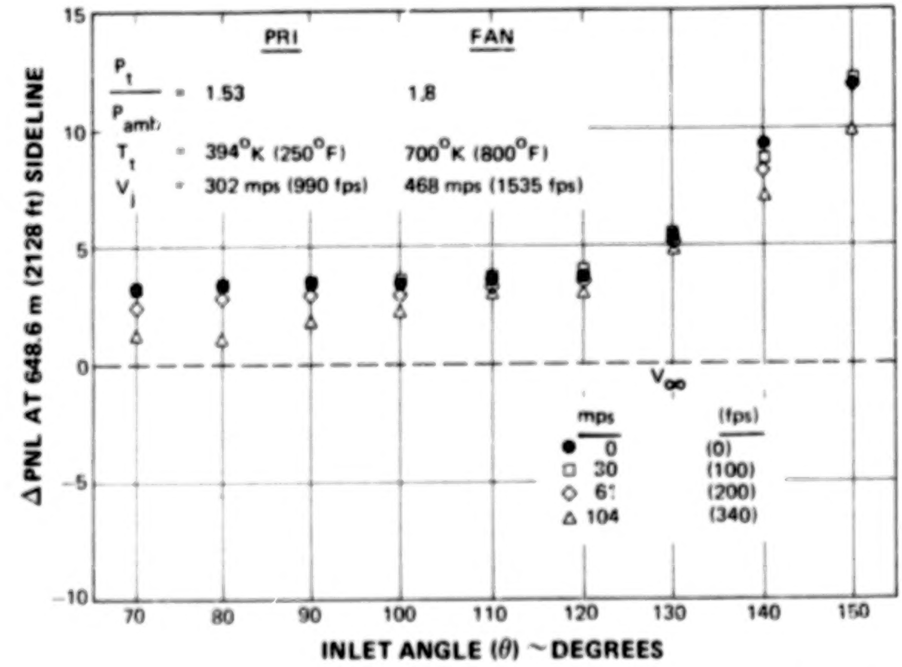

Figure 5.2.2-2 *Effect of Relative Velocity On PNL Benefit of 0.75 Area Ratio Coannular Nozzle Scaled to 1.27m (50 in.) Equivalent Diameter At Subsonic Fan Jet Velocity*

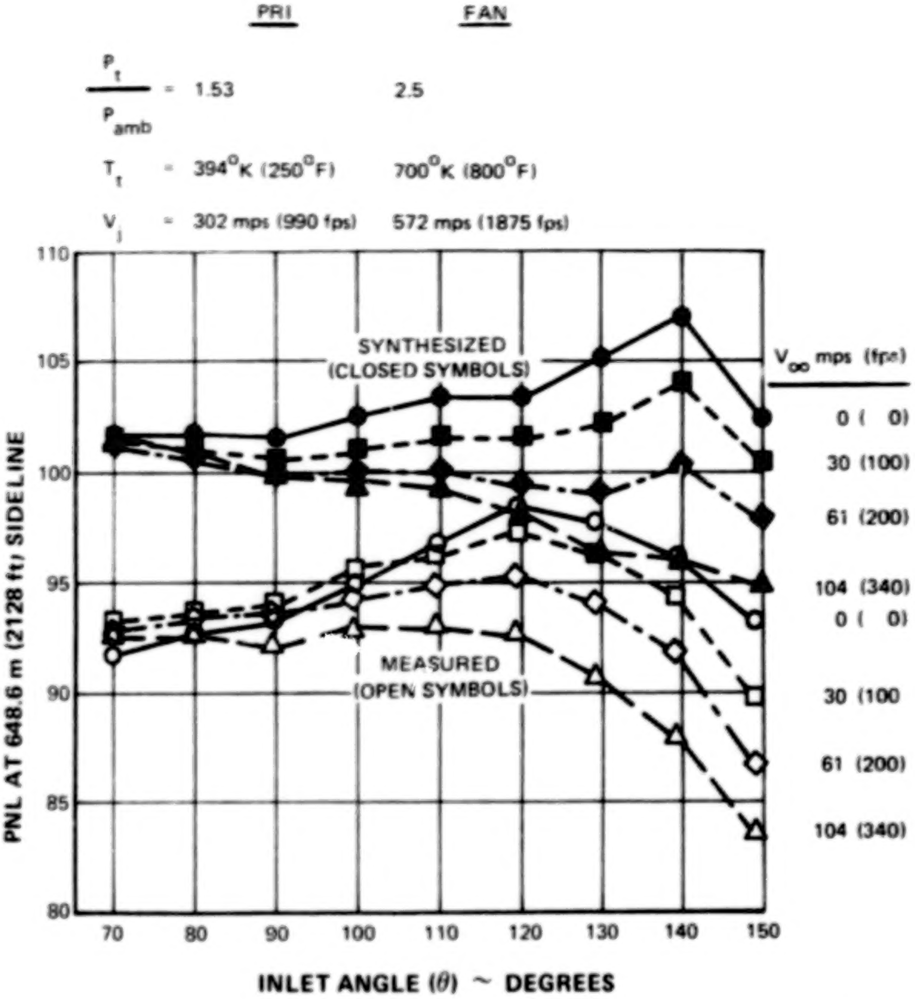

Figure 5.2.2-3 *Comparison of Measured and Synthesized PNL Directivity for 0.75 Area Ratio Coannular Nozzle Scaled to 1.27m (50 in.) Equivalent Diameter At Supersonic Fan Jet Velocity*

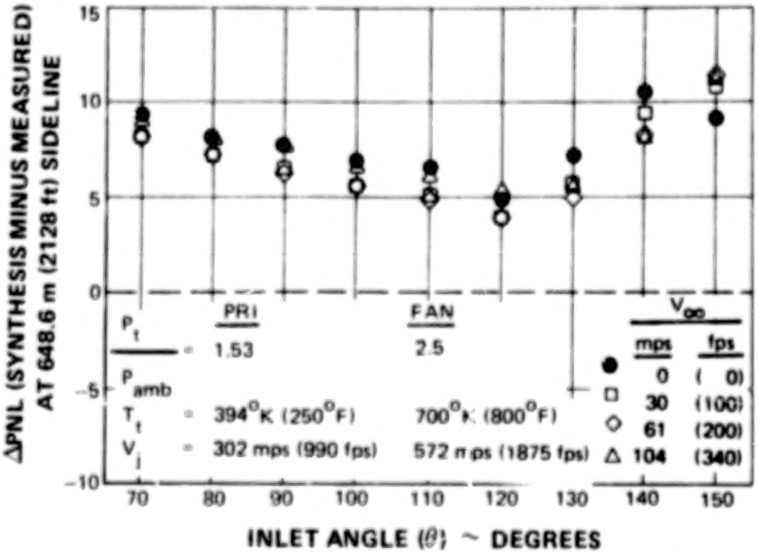

Figure 5.2.2-4 *Effect of Relative Velocity On PNL Benefit of 0.75 Area Ratio Coannular Nozzle Scaled to 1.27m (50 in.) Equivalent Diameter At Supersonic Fan Jet Velocity*

5.2.3 Application of Results to Scar Noise Predictions

A major objective of the relative velocity investigation was to acquire a data base which could be used to predict the effect of flight on the jet noise produced by the coannular exhaust nozzle of a Variable Stream Control Engine. There are two approaches that can be taken in utilizing the data base information for predictions of this type. These different approaches are discussed in the following section.

5.2.3.1 Prediction Based On Δ OASPL Exponents

The first and simplest approach is the direct application of the ΔOASPL relative velocity exponents presented in Section 5.1.2. No simple universal exponent curve in either n_1 or n_6 was developed due to the large data scatter. Thus, in order to use the exponent results for prediction of the inflight jet noise of a Variable Stream Control engine, the exponents determined for specific fan pressure ratios representative of those in a VSCE-502 engine were used. The n_1 exponent results at two fan pressure ratios, one subsonic and the other supersonic, are shown in Figure 5.2.3-1. In both cases, the primary stream was subsonic. The major difference in the two exponent curves is seen to occur in the angles forward of 110°. At these angles, the exponents for the supersonic fan jet curve are of lower value (in fact, of negative value at 70°), compared to the subsonic results. It is noted that the temperatures of the VSCE-502 are in general substantially higher than those used in the testing from which these exponents were derived. The n_1 exponents are being used rather than the n_6 exponents since, in the authors judgement the n_6 exponents offer no advantage over the use of the n_1 exponents alone.

The exponent values from Figure 5.2.3.1 were used to predict the effect of flight on the jet noise for a VSCE 502 over the range of operating conditions shown in Table 5.2-I.

The elements of the prediction procedure are illustrated in Figure 5.2.3-2. The OASPL directivity for static conditions is predicted for the particular cycle under consideration based on an empirical procedure established from the results obtained during the first phase of this program (Ref 1). The Δ OASPL relative velocity exponents, n shown in Figure 5.2.3-1 are used to predict the Δ OASPL for the specific cycle and airspeed,

where: $$\Delta \text{ OASPL } (\theta) = 10 \text{ Log} \left(\frac{V_f}{V_f - V_a} \right)^{n_1 (\theta)}$$

and V_f = Fan Jet Velocity
V_a = Airspeed

The static-to-flight Δ OASPLs are then subtracted from the static values to determine the inflight noise levels. To extend the predictions to provide in-flight PNL estimates, it is assumed that the static-to-flight Δ PNL is approximately equal to the Δ OASPL (results shown in Section 5.2.2 indicate that this is a reasonable assumption). This is equivalent to assuming that changes in the jet noise spectrum caused by flight effects are small.

Before presenting the results of the predictions based on the Δ OASPL exponent method, the second approach to VSCE coannular nozzle jet noise prediction will be discussed. Then the results of the two prediction procedures will be compared.

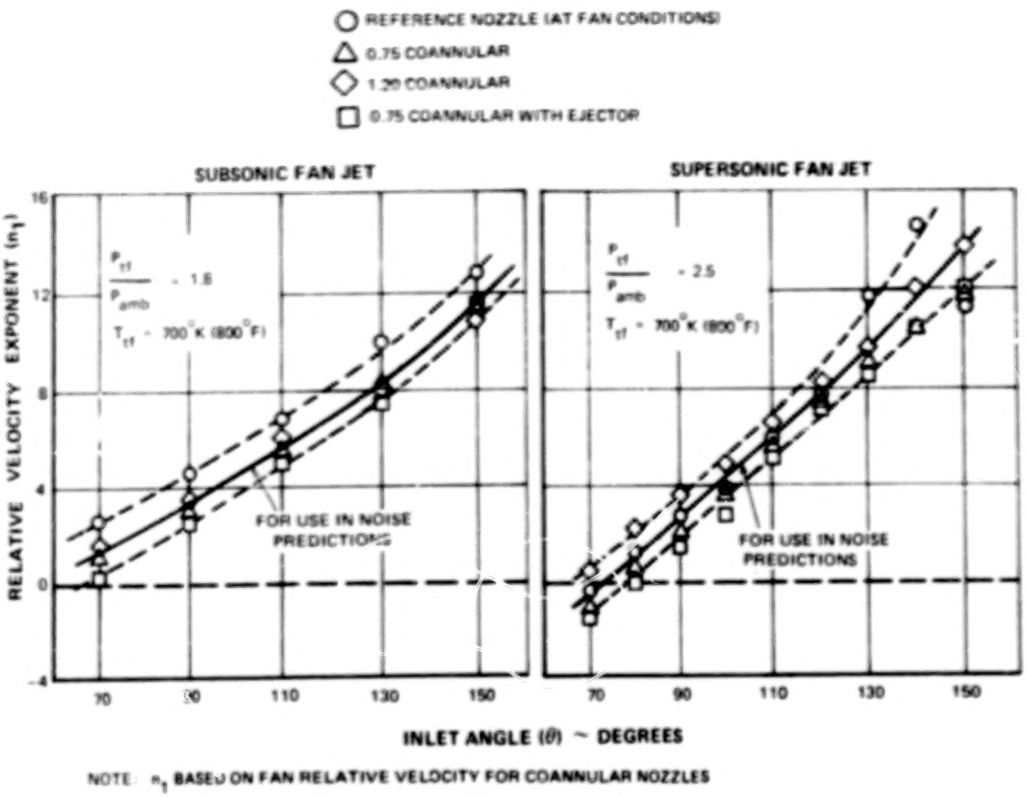

Figure 5.2.3-1 Relative Velocity Exponents As Function of Angular Position for Various Nozzle Configurations

TABLE 5.2-I

VSCE-502 OPERATING LINE

M_∞ = 0.3 At Sea Level Engine Airflow = 340 Kg/sec (750 lb/sec)

	F/A			
Fuel/Air Ratio	0.005	0.015	0.030	0.040
Fn N Net Thrust) (lbf)	124550 (28000)	164580 (37000)	209065 (47000)	226860 (51000)
V_f mps (fps)	541 (1776)	674 (2211)	814 (2672)	884 (2900)
V_p mps (fps)	337 (1106)	420 (1378)	506 (1661)	511 (1678)
T_t °K (°F)	631 (676)	979 (1302)	1436 (2125)	1706 (2610)
T_p °K (°F)	856 (1081)	891 (1144)	941 (1233)	944 (1240)

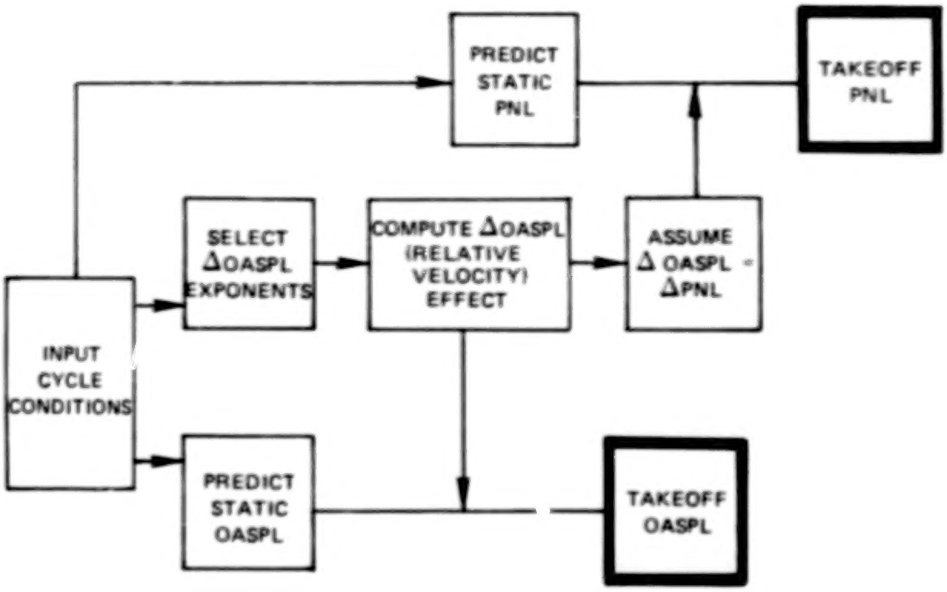

Figure 5.2.3-2 In-Flight Noise Prediction Procedure Based On Δ OASPL Relative Velocity Exponent Method

5.2.3.2 Predictions Based on Δ SPL Exponents (Separation of Jet Noise Components)

The second approach to prediction is based on separating the noise generation process of a VSCE jet exhaust into its major components and then assessing the effects of flight on each. As described in Reference 1 & 2, the noise generated by a coannular nozzle jet exhaust having $V_f > V_p$ can be separated into three major components, each generated in a specific region of the jet, and each producing noise at levels and frequencies relating to the flow properties in the respective regions of generation. Figure 5.2.3-3 is a schematic representation of the jet flow and the noise spectra. The noise generating components will be defined using static data. Flight corrections for each component will then be developed using the data from this program.

The simplified spectrum, shown for a given angle, is used to aid in the definition of the noise generation regions. In the actual data correlation, spectra at different angles were used to resolve the different noise components. Shown in Figure 5.2.3-3 are two types of velocity profiles. The profile close to the nozzle represents the velocity existing in the initial stage of the mixing process. The profile in this region is characterized by a high velocity annulus (fan stream) surrounding a low velocity central core (primary stream). The noise produced in this region is dominated by the mixing between the high velocity annulus and the ambient air and is called pre-merged jet noise. This noise appears in the spectrum as the middle peak. The level and frequency of this noise has been shown to correlate with the fan stream properties, with a modifying influence of the primary stream. The second type of profile, existing downstream in the plume, represents the velocity after the fan and primary streams mix and lose their individual identities. The profile in this region is typical of a single stream jet. The noise generated in this region is shown as the low frequency peak in the noise spectrum and is called merged jet noise. The level and frequency of this noise has been shown to correlate with the merged jet velocity resulting from the mixing of the fan and primary jets.

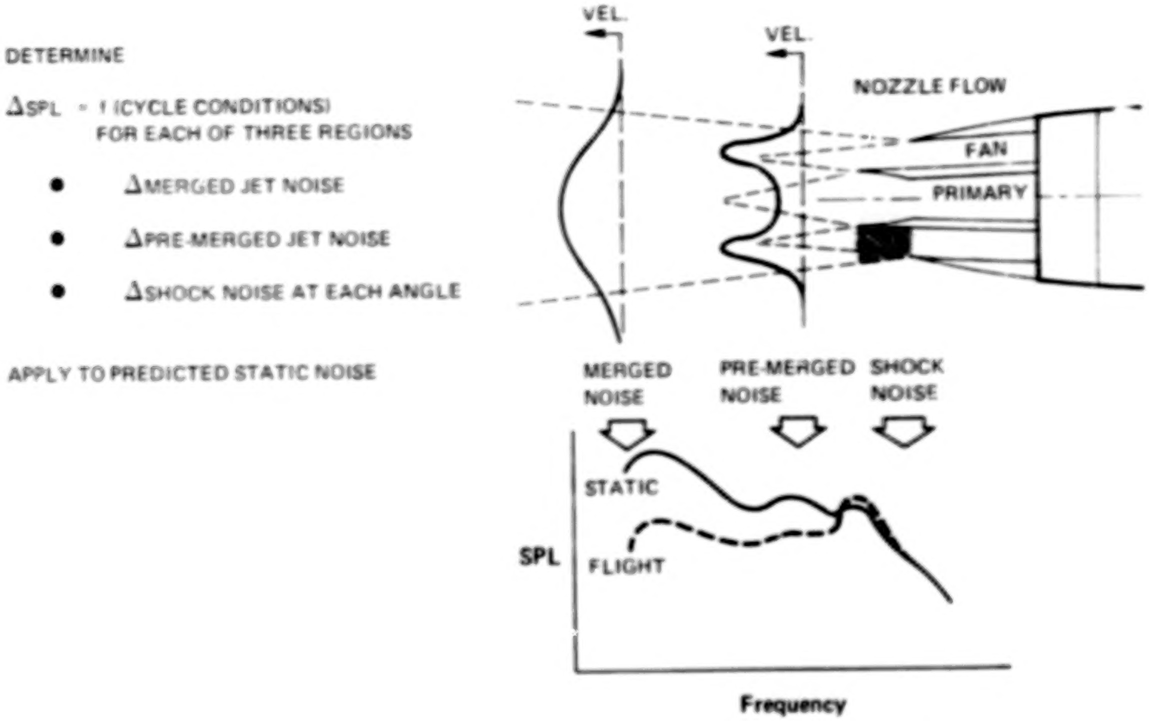

Figure 5.2.3-3 Model Based Separation of Jet Noise Components for Δ SPL Relative Velocity Exponents Method

The third component of jet noise shown in the spectrum as the high frequency peak is caused by the interaction of turbulence with shock waves existing in the exhaust of an underexpanded supersonic fan stream. This noise source can be predicted with reasonable accuracy for a single stream conical nozzle jet (Ref 13). The current program has produced sufficient additional static and flight data to allow a fair assessment of the shock noise contribution to VSCE coannular jet exhausts under both static and flight conditions. It is to be noted that this noise source is not present in the noise of subsonic jets or in ideally expanded supersonic jets.

Based on the separation and identification of the three components of VSCE coannular nozzle jet noise under static conditions, the effects of flight can be assessed with more preciseness than is possible with the simple Δ OASPL procedure discussed in the previous section. The dotted curve in Figure 5.2.3-3 represents the spectrum measured in the wind tunnel under simulated flight conditions. Preliminary correlation studies of the effects of flight have indicated that the three components of jet noise behave in a consistent and definable manner with respect to the free stream velocity. Based on this preliminary work, the following can be tentatively concluded:

1.) The low frequency noise generated by the merged jet is reduced in flight by an amount equal to the reduction in overall sound pressure level (ΔOASPL) of a subsonic single stream circular jet operating at the mixed conditions of the circular jet.

2.) The mid-frequency mixing noise generated by the pre-merged jet is reduced in flight by an amount equal to the reduction in overall sound pressure level (ΔOASPL) in mixing noise of a single stream circular jet operating at the fan stream conditions.

3.) The high-frequency broadband shock noise generated in the shock-cell region close to the fan nozzle exit did not appear to be affected by flight speed in the same manner as the shock noise of the single convergent nozzles. Since shock noise is directly related to nozzle pressure ratio (Ref. 13), the effect of flight on shock noise can be predicted by using the actual coannular nozzle data at the pressure ratio of interest. The actual change in the shock noise is found after separating the mixing noise from the shock noise component.

The above are recognized as preliminary conclusions. Complete correlations necessary for a comprehensive prediction procedure are beyond the scope of the current program. However, the data in the Comprehensive Data Report, NASA CR 135189, can be used to develop the correlations necessary in the development of an improved prediction procedure for use in advanced supersonic commercial aircraft studies.

Using the tentative conclusions listed above, static-to-flight changes in the jet noise of the VSCE-502 engine without ejector were predicted for the conditions shown previously in Table 5.2-1. Figure 5.2.3-4 shows the steps used in the prediction. The cycle conditions were input and the static jet noise spectra predicted for each jet noise component.

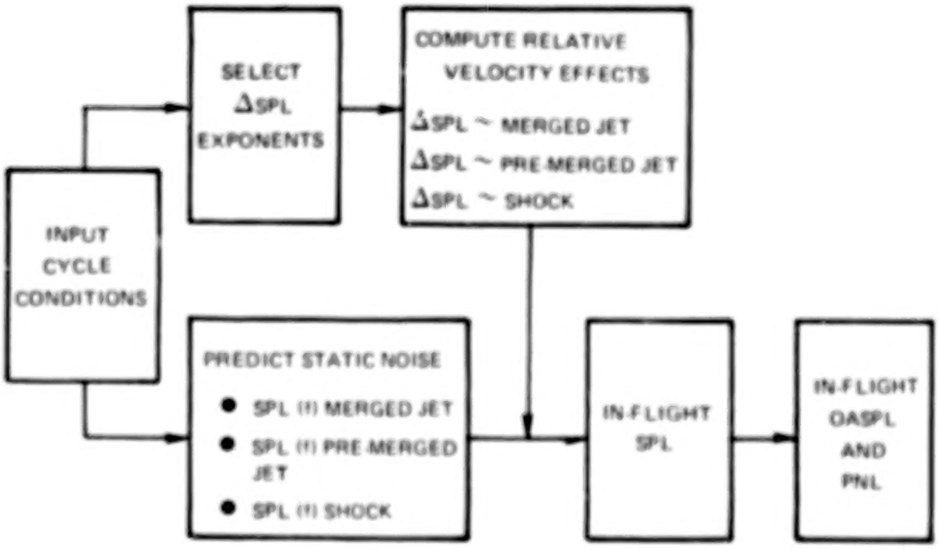

Figure 5.2.3-4 In-Flight Noise Prediction Procedure Based On Δ SPL Relative Velocity Exponents Method

The exponents for the merged and pre-merged mixing noise components were selected based on a preliminary correlation of convergent nozzle data for which the mixing and shock noise components were separated by inspection of the SPL spectra. The exponents determined for pressure ratios simulating the VSCE-502 engine were used for the predictions. The shock noise component SPLs measured at the static and simulated flight conditions for the fan nozzle pressure ratio representative of the VSCE-502 engine were used to determine the shock noise ΔSPL for the engine noise predictions. The ΔSPL's due to flight then were applied to the static predictions to produce predicted takeoff noise spectra. As was the case for the ΔOASPL exponent prediction method, it is noted that the noise data used to develop these predictions were measured for test conditions having nozzle temperatures much lower than those present in the VSCE-502 engines. The reliability of the predicted levels can be determined only when data from the high temperatures present in the engine becomes available.

Figure 5.2.3-5 shows the predicted effect of flight speed on the spectrum at 150° for a low duct-burner fuel to air ratio, F/A, of 0.005. The solid curve with symbols is the static prediction. The dashed lines represent the predicted spectra of merged, pre-merged, and shock noise contributing to the total static spectrum. After applying the static-to-flight Δ SPL exponents for each noise component, the flight spectra of the three noise components shown by the dash-dotted lines result. The solid curve without symbols is the total flight spectrum resulting from adding the flight spectra of the individual components. The same procedure was used to predict the noise spectra at the other angles. Figure 5.2.3-6 illustrates the Perceived Noise Level (PNL) directivity for static and flight conditions. Also shown on this figure is the prediction based on the Δ OASPL exponent method described in section 5.1.2. The agreement between the two methods is good at the 90° and 120° angles. At 150°, the Δ OASPL method over-predicts the noise reduction compared to the more detailed Δ SPL component method. Inspection of the spectral curves shown in Figure 5.2.3-5 indicates that the difference is due to the presence of shock noise in the flight spectrum. The level and frequency of this noise has little influence on the OASPL level in the Δ OASPL method, and thus does not impact the PNL derived from the Δ OASPL method. However, the PNL resulting from the spectrum predicted from the Δ SPL method is significantly affected by shock noise, which is particularly pronounced in a frequency region having a large annoyance factor.

The results of the same prediction procedure applied to another VSCE-502 condition, having an intermediate fuel-to-air ratio of 0.030, are shown in Figure 5.2.3-7. In this case the agreement between the two prediction methods is good.

In terms of peak PNL, there was good agreement between both methods at all four of the operating conditions. A summary of the peak PNL predictions based on the component Δ SPL method at static and at a take-off speed of 104 mps (340 fps) for the four VSCE-502 conditions is shown in Figure 5.2.3-8. The peak PNL at 649 m (2128 ft) sideline distance and zero altitude is plotted versus net thrust. The approximately constant noise reduction at all thrusts due to flight speed can be traced to the varying dominance of noise from each of the three jet noise components as thrust varies. At low thrust, the shock noise is very important. The large expected reductions in jet mixing noise due to low jet velocity is counteracted by the shock noise, which does not decrease in flight. At high thrust, the merged jet noise component dominates, while at mid-thrusts the pre-merged and merged jet each contribute important amounts. The net effect is to produce the approximately constant flight noise reductions for all thrusts. This result is not considered to be a universal result for VSCE engines, but rather should be recognized as being characteristic of this particular engine cycle.

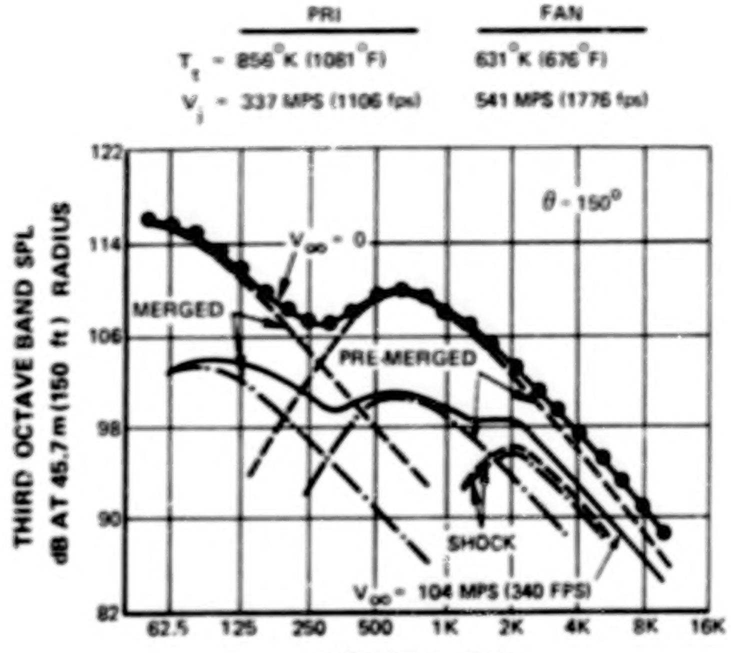

Figure 5.2.3-5 *In-Flight Noise Spectra Prediction Based On Δ SPL Relative Velocity Exponent Method for VSCE-502 At Fuel to Air Ratio of 0.005*

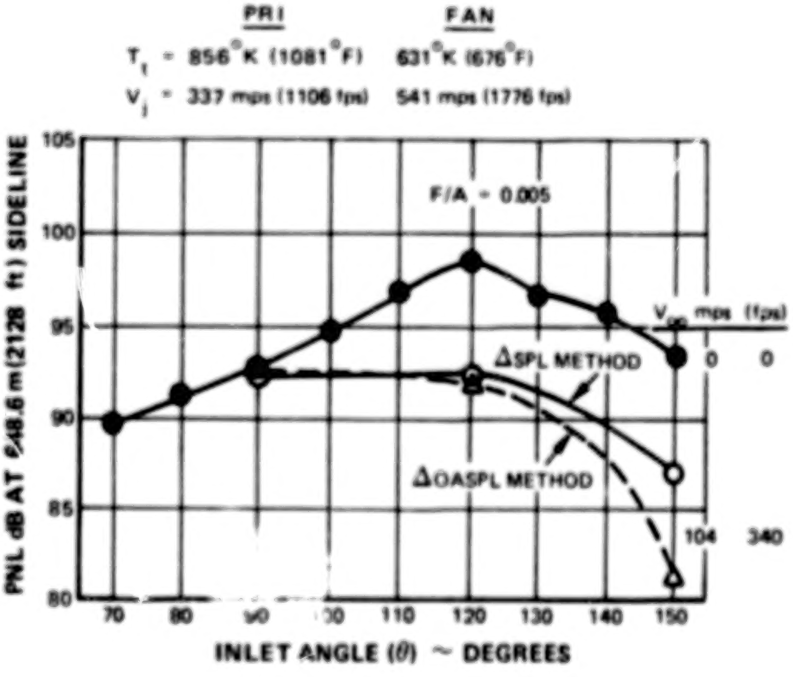

Figure 5.2.3-6 *Comparison of In-Flight Noise Prediction Methods for VSCE-502 At Fuel to Air Ratio of 0.005*

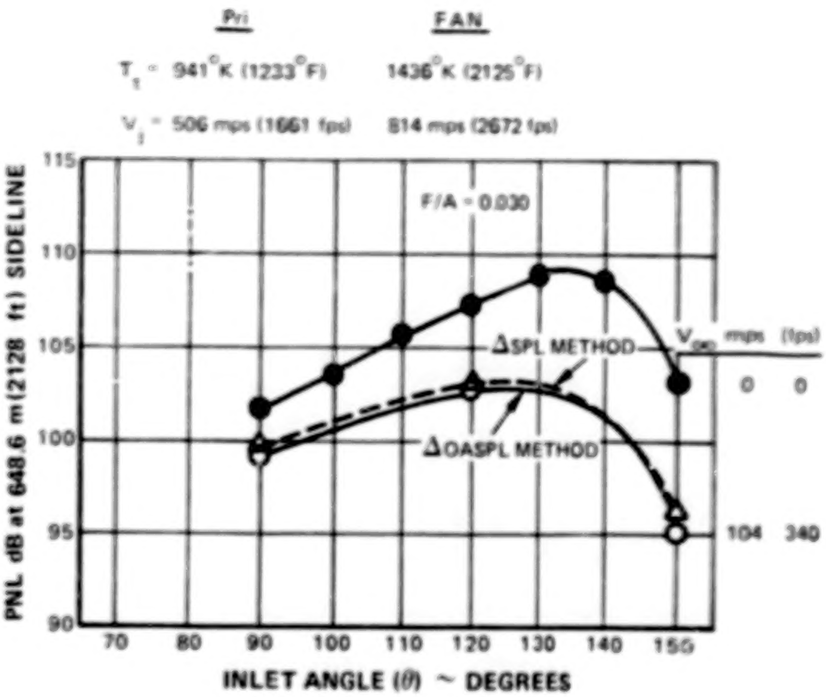

Figure 5.2.3-7 Comparison of In-Flight Noise Prediction Method for VSCE-502 At Fuel to Air Ratio of 0.030

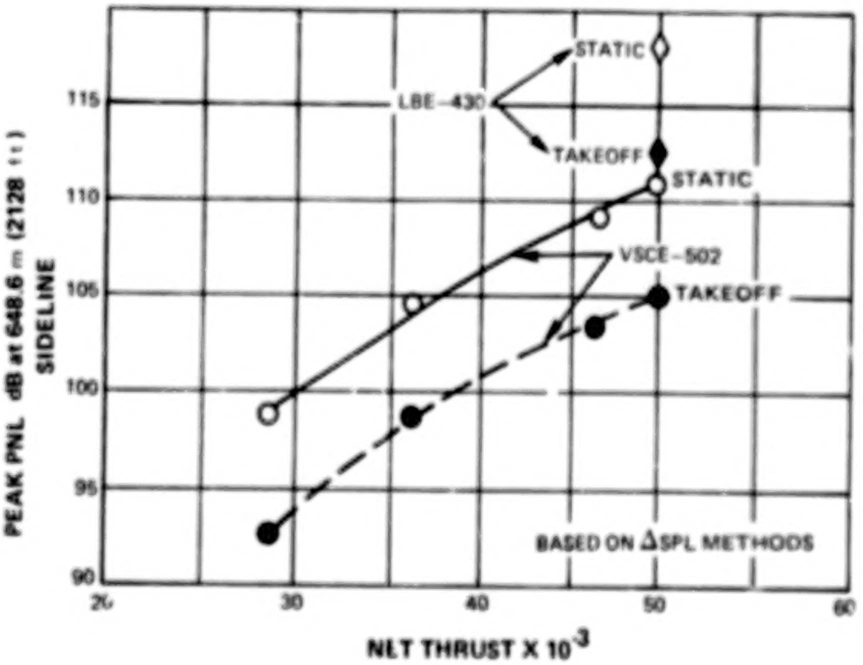

Figure 5.2.3-8 Peak PNL Predictions Based On Δ SPL Relative Velocity Exponents Method for VSCE-502 and LBE-430 Engines

Also shown on this figure are the predictions for the LBE-430 engine, which is a very low bypass turbofan engine. The noise of this engine was predicted by the SAE method of Reference 11 assuming that the exhaust would be fully mixed. This assumption produces slightly lower predicted noise levels than if the streams were unmixed. The predictions indicate a 6 PNdB noise reduction of the VSCE relative to the LBE-430 for both static and flight conditions. By adding a treated ejector on the VSCE coannular nozzle, an additional 2 PNdB reduction can be expected.

Thus, the results of the acoustic wind tunnel testing accomplished during this program have led to a data base which can be used to predict the static-to-flight effects on jet noise of variable cycle and turbojet engines for supersonic cruise aircraft. For the VSCE-502 engine, predictions based on ΔOASPL exponents agreed reasonably well with preliminary predictions based on the ΔSPL's of the individual jet noise components. Both methods indicated that the coannular noise benefits present under static conditions were retained in flight. It is recommended that a comprehensive procedure based on detailed correlations of the changes to the individual noise component levels due to flight speed (i.e. the ΔSPL method) to provide the most accurate noise predictions for coannular nozzle exhaust noise.

5.3 AERODYNAMIC PERFORMANCE

The aerodynamic performance characteristics of the four test model nozzles are presented in this section. The thrust characteristics are presented in terms of the nozzle thrust coefficient (C_F) which is the ratio of actual thrust produced by the model (including external boattail drag) to the total ideal thrust available. The flow properties of the nozzle are presented in terms of flow coefficient (C_D) for each stream.

The measured performance levels are presented for each of the nozzles, representing all the test points for that configuration. An analysis of the thrust losses in each system are described and appropriate adjustments made available to provide a more complete indication of the performance potential of the test nozzles. The performance data are not adjusted for any full scale effects since the physical full scale exhaust system characteristics have not been established.

In the following discussion the thrust coefficients of the reference convergent nozzle are presented first, followed by the thrust coefficients of the coannular configurations. The flow coefficients for all the nozzles are then presented.

5.3.1 Convergent Nozzle

The thrust coefficients, as measured with the convergent nozzle, are presented in Figure 5.3-1 at all of the test conditions. The performance level at static conditions ($V_\infty = 0$) is consistent with that generally accepted for a convergent nozzle, tested in this manner. In these tests the instrumentation was located upstream of the nozzle exit (as described in Section 3.1), causing the performance level to be slightly low because of the internal friction losses. At a pressure ratio of 2.0, these losses were estimated to be 0.35% (ΔC_F). Adjusting the measured level for this loss would result in the expected performance of a convergent nozzle. The repeatability of the test facility can be seen by comparing the duplicate or repeat points obtained at various operating conditions. The introduction of a free stream velocity (V_∞) reduces the performance level as illustrated. The loss at a typical take-off velocity, $V_\infty = 104$ mps (340 fps), was approximately 0.7% (ΔC_F) relative to the static value.

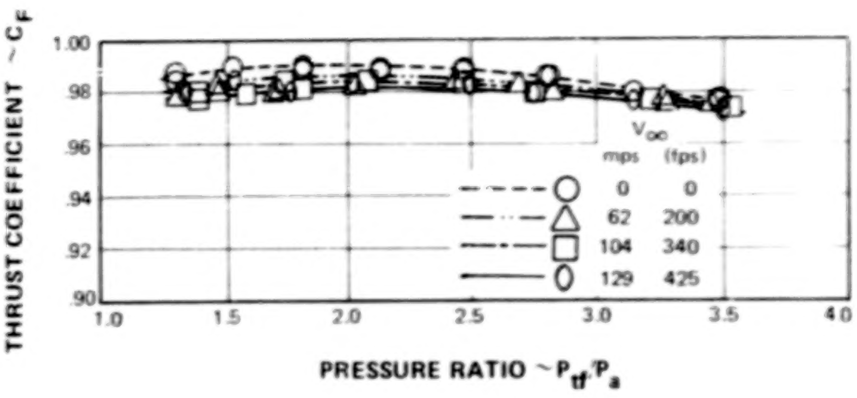

Figure 5.3-1 Aerodynamic Performance of Reference Convergent Nozzle

5.3.2 Coannular Nozzles

The performance of the 0.75 area ratio coannular configuration is presented in Figure 5.3-2 at all of the test conditions, as a function of fan nozzle pressure ratio and tunnel speed. At a typical fan pressure ratio of 2.5, the performance loss between $V_\infty = 0$ and 104 mps (0 and 340 fps) is approximately 1.0% (Δ C_F). At static conditions the primary flow was turned off (i.e., fan stream only operating) in order to complement the earlier acoustic investigation. As indicated, a loss of 4-5% resulted.

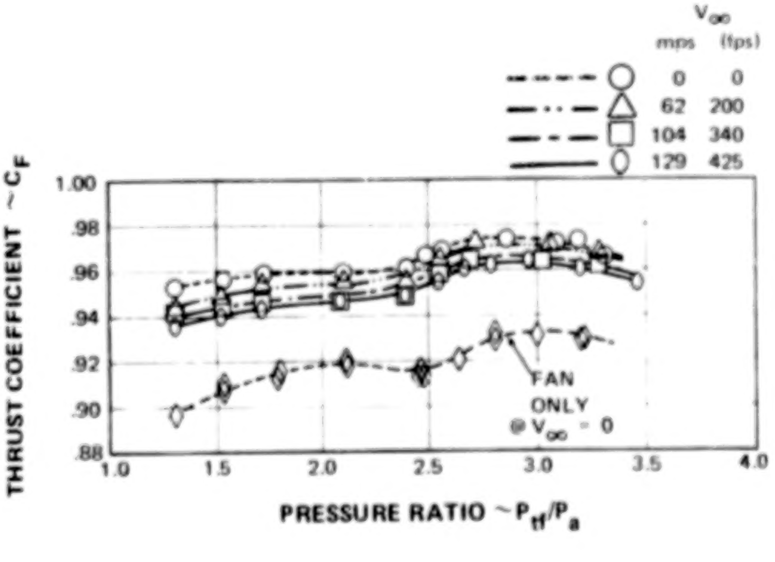

Figure 5.3-2 Aerodynamic Performance of 0.75 Area Ratio Coannular Nozzle At a Primary Pressure Ratio of 1.53

The performance level of the 0.75 area ratio coannular nozzle with the ejector addded is illustrated in Figure 5.3-3. The performance trends with fan pressure are similar to the basic coannular nozzle. At a fan pressure ratio of 2.5 the performance loss of the ejector configuration between $V_\infty = 0$ and 104 mps is approximately 2.0% (ΔC_F). At static conditions these two configurations (i.e., with or without the ejector) have essentially the same performance level; however, at a nominal take-off speed of 104 mps the ejector configuration is approximately 1.0% (ΔC_F) lower than the basic nozzle. This difference is not believed to be inherent with the type of ejector required in this application. It does indicate that the particular ejector tested requires some slight modification to minimize the drag penalty at take-off conditions.

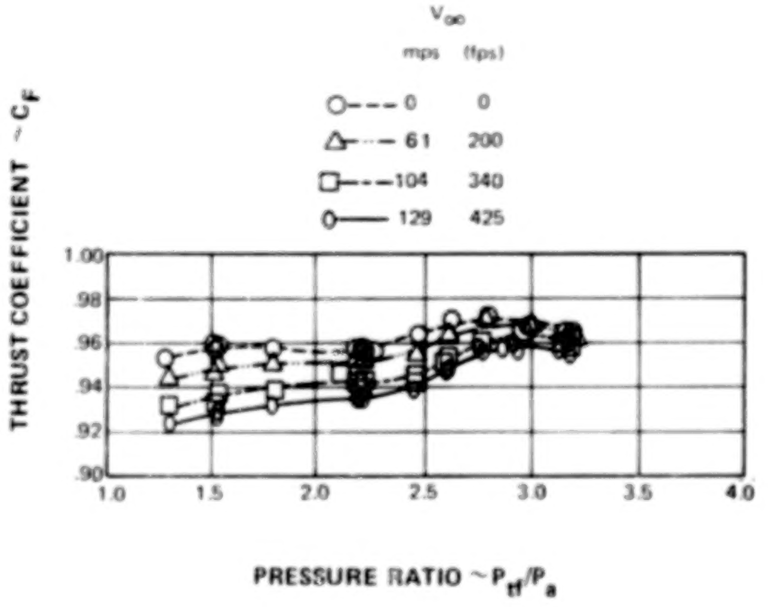

Figure 5.3-3 *Aerodynamic Performance of 0.75 Area Ratio Coannular Nozzle With Ejector At a Primary Pressure Ratio of 1.53*

The performance of the 1.2 area ratio coannular nozzle is presented in Figure 5.3-4 at all the test conditions. The performance trend with fan nozzle pressure ratio is somewhat different than exhibited on the 0.75 area ratio nozzle. Although the two nozzles are geometrically similar, the increase in area ratio results in a more dominant fan stream and causes a different interaction between the fan and primary streams. Since the primary nozzle is a low area ratio convergent-divergent nozzle, the impact of the surrounding fan stream is important. The overall performance level of a coannular nozzle is therefore a function of the proportions of the fan and primary streams, the exact geometry of the nozzles in each stream and the operating conditions in each stream.

The effect of external flow on the 1.2 area ratio nozzle is slightly less than with the 0.75 area ratio nozzle. The performance difference between $V_\infty = 0$ and 104 mps is approximately 0.5% (ΔC_F) at a fan nozzle pressure ratio of 2.5.

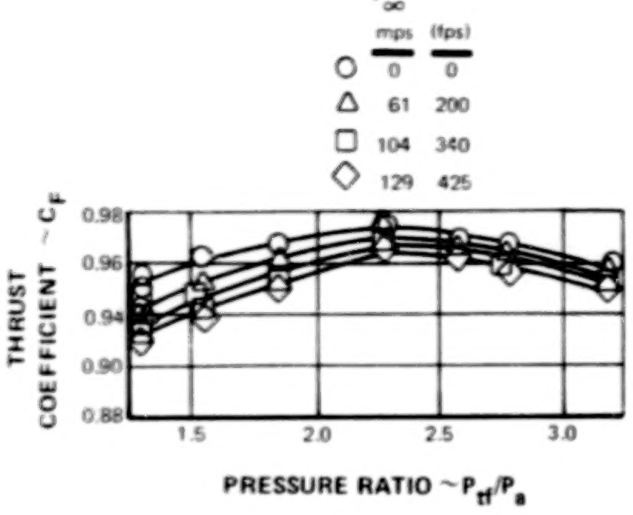

Figure 5.3-4 *Aerodynamic Performance of 1.2 Area Ratio Coannular Nozzle At a Primary Pressure Ratio of 1.53*

It should be noted that during the complete aerodynamic test matrix the primary stream pressure ratio was maintained at 1.53. Since the primary nozzle is a convergent-divergent nozzle with an area ratio of 1.1, it will be generally overexpanded at a pressure ratio of 1.53. The nozzle was based on an early design employing fixed geometry which was biased for high speed cruise operation. Current designs incorporate variable geometry which would eliminate this problem. The impact of this primary stream overexpansion on overall nozzle performance has been estimated for both coannular nozzles, as illustrated in Figure 5.3-5, along with the impact of the total pressure loss between the internal instrumentation and the exit of the nozzle. If the combined effect of overexpansion and total pressure loss were incorporated into the measured performance levels, a better indication of the performance potential of the nozzle configurations under study would be obtained. The adjusted performance level is illustrated typically for the 0.75 area ratio coannular nozzle in Figure 5.3-6.

The impact of external velocity is summarized for the coannular nozzle configuration in Figure 5.3-7. It is presented using both the as-measured data and the performance levels adjusted for pressure loss and primary overexpansion. As illustrated, the performance decay with external velocity is a function of nozzle geometry. The higher area ratio nozzle (i.e., 1.2) is somewhat less effected by external speed than the 0.75 area ratio configuration. The impact of the ejector increases at the higher velocities; however, as discussed earlier it is believed that further refinement of the ejector design could minimize this effect. It should be noted that the performance difference between the 0.75 area ratio configuration and the 1.2 area ratio nozzle as originally measured is nearly halved when the primary overexpansion correction is considered. The primary stream contributes a larger percentage of the overall nozzle thrust in the 0.75 area ratio nozzle than in the 1.2 area ratio nozzle and therefore an adjustment of this type is more significant than in the nozzle with the larger area ratio.

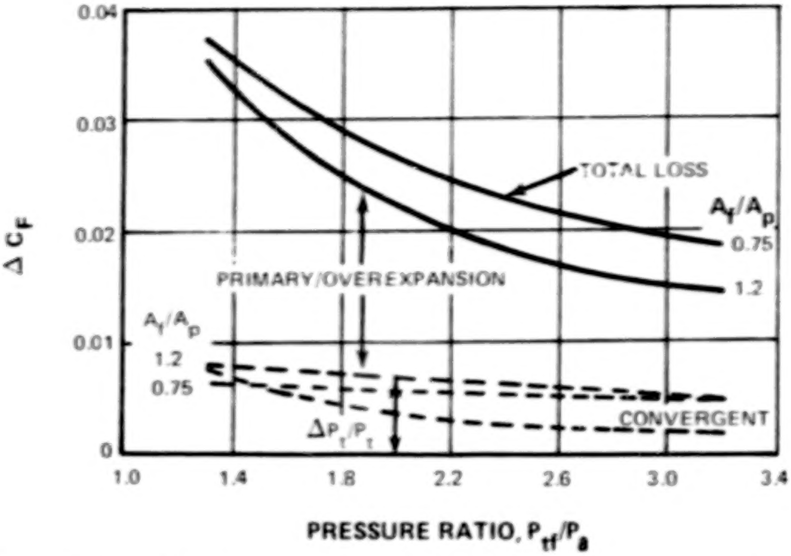

Figure 5.3-5 *Internal Performance Losses for Reference Convergent Nozzle and Coannular Nozzles*

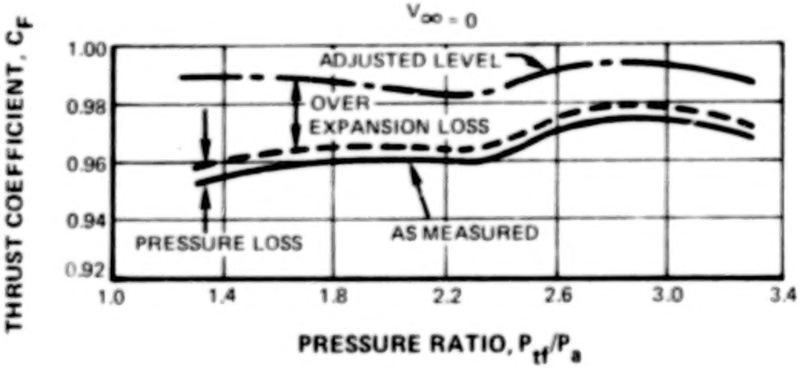

Figure 5.3-6 *Comparison of Measured and Adjusted Aerodynamic Performance of 0.75 Area Ratio Coannular Nozzle At a Primary Pressure Ratio of 1.53*

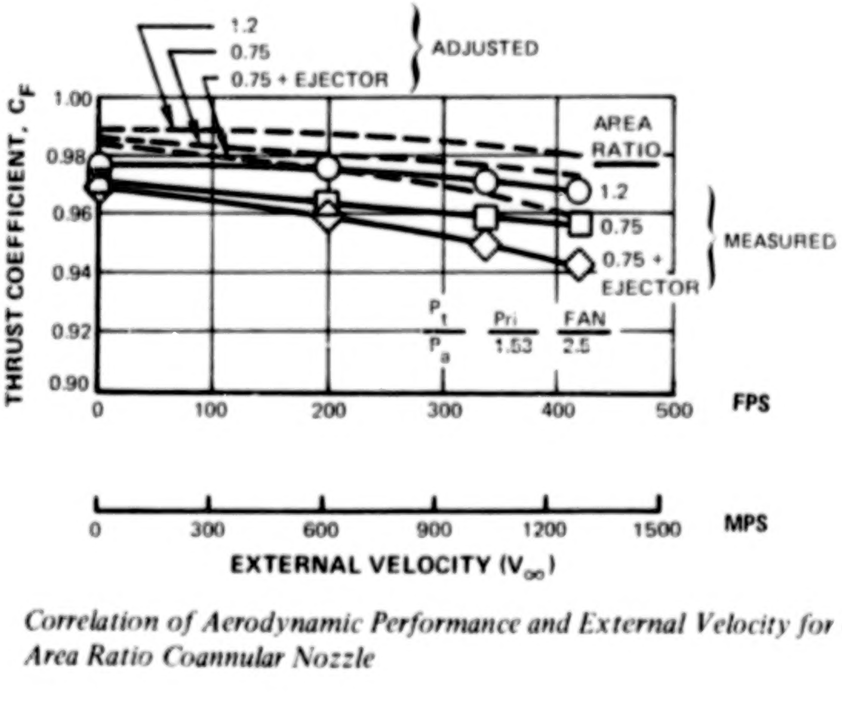

Figure 5.3-7 *Correlation of Aerodynamic Performance and External Velocity for 0.75 Area Ratio Coannular Nozzle*

The trend in performance with nozzle area ratio is illustrated in Figure 5.3-8 for a representative set of stream pressure ratios at both static and take-off conditions (V_∞ = 104 mps). When the basic data are corrected for internal losses (i.e., total pressure loss and primary stream overexpansion), there is no significant trend at static conditions, but there is a slight trend toward higher performance levels at V_∞ = 104 mps as the nozzle area ratio is increased. This occurs because the higher area ratios produce a larger exhaust plume resulting in lower overall closure drag. As a convenience, the data have been extrapolated to the area ratio required for one of the currently most promising engines (VSCE-502B) being considered for advanced supersonic cruise aircraft.

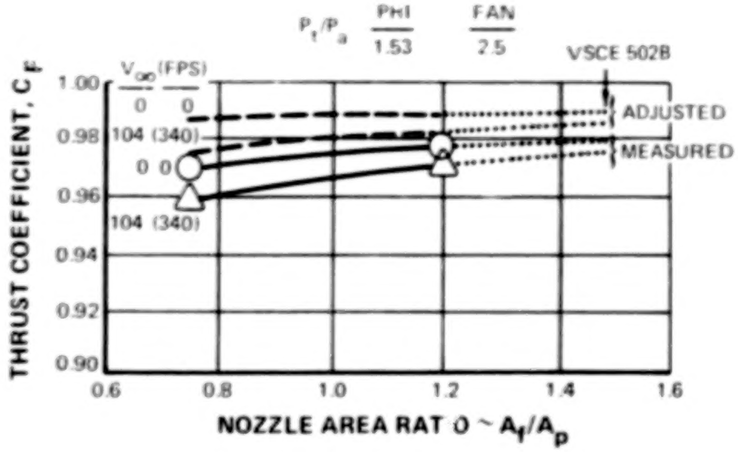

Figure 5.3-8 *Correlation of Aerodynamic Performance and Nozzle Area Ratio of Coannular Nozzles*

5.3.3 Flow Coefficients

The flow coefficients of the convergent nozzle, illustrated in Figure 5.3-9, have a conventional trend with pressure ratio. Increasing the external velocity (V_∞) reduces the flow coefficients in the low pressure ratio, unchoked range as expected.

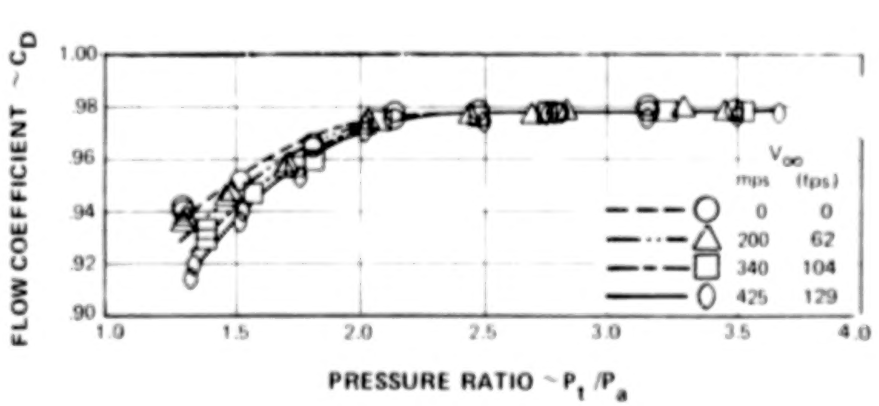

Figure 5.3-9 *Flow Coefficients for Reference Convergent Nozzle*

The flow characteristics of the basic 0.75 area ratio coannular nozzles are illustrated in Figure 5.3-10. The fan stream exhibits a conventional trend, but is independent of external velocity. An examination of the local static pressures in the vicinity of the nozzle exit showed that because of the steep external contour near the nozzle exit, the external flow is probably seperated and the effect of low external velocities is nullified. The primary stream (which is nominally at a pressure ratio of 1.53) exhibits a level of flow coefficient greater than unity at the low fan pressure ratios because it is being aspirated by the fan stream. At the higher fan pressure ratios, the primary flow becomes influenced by the external velocity. This is associated with the changing interaction between fan stream expansion, external flow field and primary nozzle discharge. In other words, a changing static pressure field is imposed on the primary stream as the fan pressure ratio increases in combination with increasing external velocity. As will be seen on the other coannular configurations, this fluctuation in primary flow coefficient is also a function of nozzle geometry.

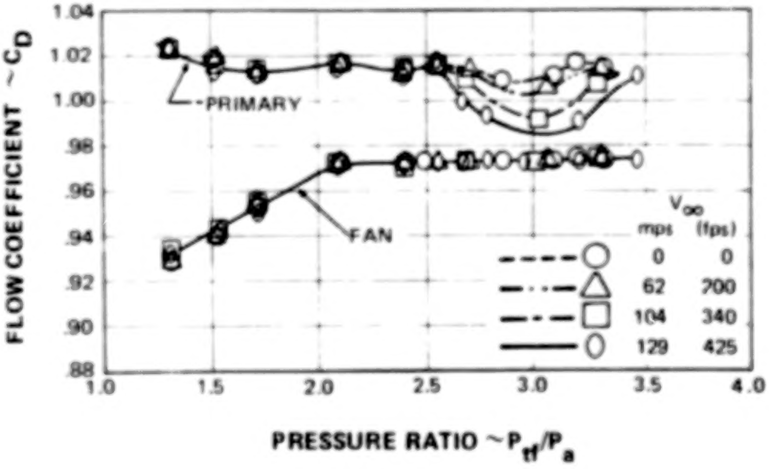

Figure 5.3-10 *Flow Coefficients for 0.75 Area Ratio Coannular Nozzle At a Primary Pressure Ratio of 1.53*

The flow characteristics of the 0.75 area ratio nozzle when the ejector was added are presented in Figure 5.3-11. The fan nozzle in this configuration now reflects the introduction of external velocity. This is due to the large reduction in pressure distribution around the fan nozzle when the ejector is added as illustrated in Figure 5.3-12 at both $V_\infty = 0$ and $V_\infty = 104$ mps (340 fps).

The level of fan stream flow coefficient for the 0.75 area ratio with ejector at high fan stream pressure ratios is slightly higher than the other 0.75 area ratio configuration. Since these are physically different models, the difference is attributed to manufacturing tolerances. Because the ejector also changes the local flow field surrounding the primary nozzle, the variation in primary flow coefficient at the high pressure ratios, associated with external velocity is greatly reduced.

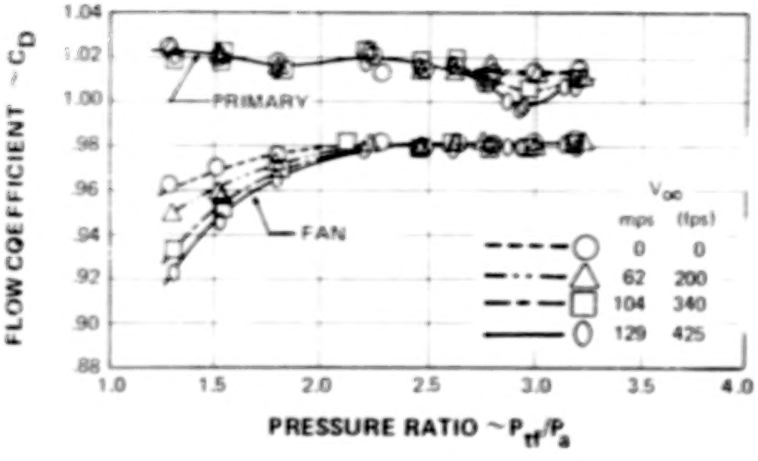

Figure 5.3-11 *Flow Coefficients for 0.75 Area Ratio Coannular Nozzle With Ejector At a Primary Pressure Ratio of 1.53*

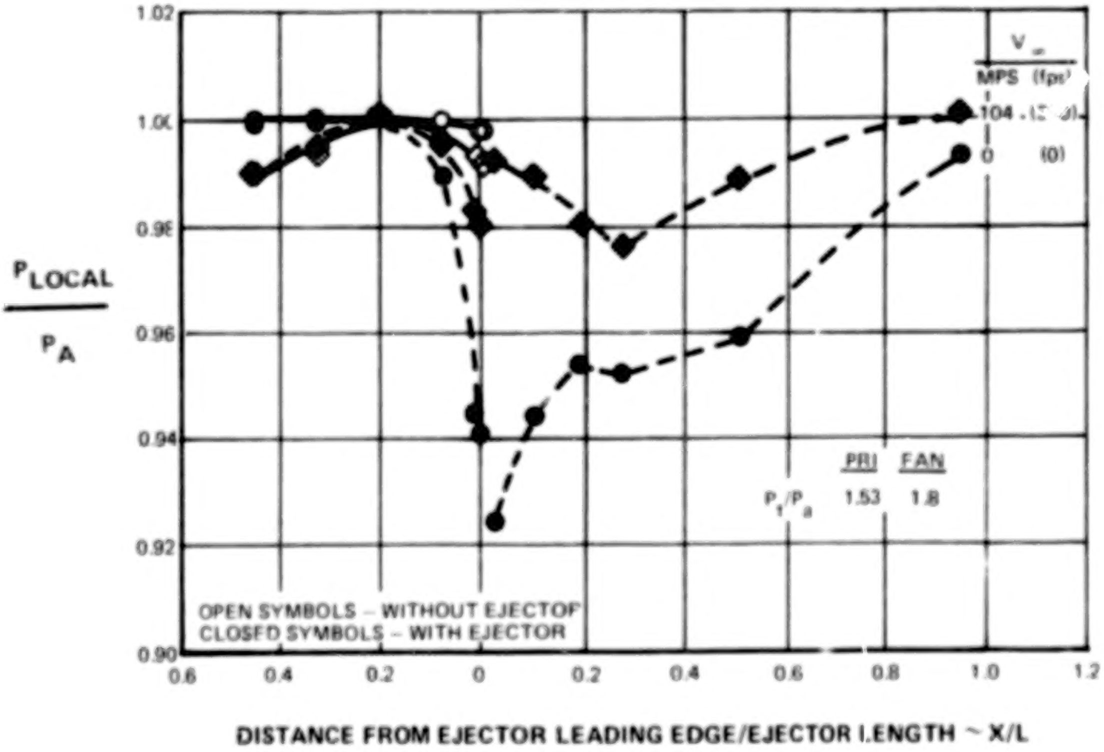

Figure 5.3-12 *Typical Static Pressure Distribution for 0.75 Area Ratio Coannular Nozzle With Ejector*

The flow coefficients of the 1.2 area ratio coannular nozzle are illustrated in Figure 5.3-13. The general trends and basic levels are similar to the 0.75 area ratio configuration; however, the primary stream is seen to be independent of external velocity. The increase in fan stream area was enough to change the flow field around the primary nozzle and eliminate any interaction with the external flow (in the pressure ratio range considered).

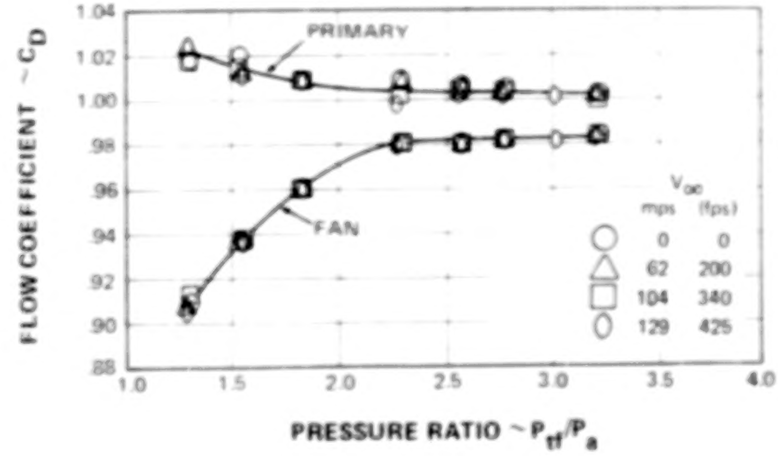

Figure 5.3-13 *Flow Coefficients for 1.2 Area Ratio Coannular Nozzle At a Primary Pressure Ratio of 1.53*

6.0 SUMMARY OF RESULTS

The effect of forward flight on the jet noise characteristics of coannular exhaust nozzles (suitable for Variable Stream Control Engines) was investigated under simulated flight conditions in a series of wind tunnel tests.

Models of approximately 1/22 size having an equivalent diameter of 0.057 m were tested over a range of conditions. The external velocity (flight speed) was varied from 0 to 129 mps. During the acoustic tests, the fan stream velocity was varied from 240 to 630 mps and the fan stream temperature was varied from 394 to 700°K. The primary stream properties were maintained constant, with the velocity equal to 300 mps and the temperature equal to 394°K. A total of 230 acoustic data points were obtained. Radial pressure and temperature traverses were made at selected conditions.

During the aerodynamic performance tests the same range of tunnel speeds and nozzle presure ratios were covered on each of the nozzle configurations. The flow temperatures were near ambient, since the test facility employed an unheated air supply. A total of 80 test points were taken.

All of the detailed acoustic and aerodynamic performance data obtained are reported in the companion Comprehensive Data Report, NASA CR-135189.

6.1 ACOUSTIC RESULTS

The more significant results from the acoustic tests are summarized in this section.

- The effect of flight on the reference convergent nozzle agrees with the results of previous investigations. At subsonic nozzle conditions, the noise was reduced at all angles. At supersonic nozzle conditions, noise increased at forward angles due to broadband shock noise amplification.
- The noise of the coannular nozzles was reduced in flight by 0 - 2 dB less than the noise of the reference convergent nozzle operating at the fan stream conditions. Effects of fan-to-primary stream area ratio on the results were minor.
- The presence of a hard wall ejector on the coannular nozzle produced small additional decreases in the noise reductions due to flight compared to the results obtained without an ejector for some nozzle operating conditions. Projecting the results to exhaust conditions simulating a supersonic cruise aircraft propulsion system indicates that the presence of an ejector has no impact on the noise reductions due to flight.
- Essentially eliminating the primary stream flow caused noise increases relative to the basic coannular nozzle levels both statically and at flight velocities. However, the noise levels were still below that of an equivalent convergent nozzle operating at the fan conditions.

- The noise reductions due to flight were correlated by the use of ΔOASPL relative velocity exponents. For the coannular nozzles having $V_f > V_p$, the exponents were based on the fan stream velocity although correlations using the mixed velocity produced similar collapse of the data. No consistent effect of temperature was indicated.

- A convection exponent was defined to attempt to quantify the effects of convective amplification. The results of this exponent correlation indicated no distinct advantage compared to the use of ΔOASPL relative velocity exponents for in-flight jet noise predictions.

- Correlations were developed which related the acoustic power of the various configurations with the mean velocity profile measured in the jet plume.

- The coannular nozzle OASPL and PNL noise reductions observed statically relative to synthesized values were essentially retained in flight.

- The data were used to provide preliminary estimates of the effect of flight on jet noise for the VSCE exhaust system envisioned for a supersonic cruise aircraft application.

- It is recommended that the data obtained during this program be used to develop a more sophisticated prediction procedure to account for the effects of flight on the noise of inverted velocity profile ($V_f > V_p$) jets. The procedure envisioned would require the separation and correlation of the low frequency merged jet mixing noise, the high frequency pre-merged jet mixing noise, and the high frequency broadband shock noise.

6.2 AERODYNAMIC PERFORMANCE RESULTS

The results from the aerodynamic performance tests are summarized in this section.

- Measured thrust coefficients for all the nozzle configurations were obtained and are identified in the text. The coannular configuration had thrust coefficients ranging from approximately 0.965 to 0.975 at a fan nozzle pressure ratio of 2.5, with the potential for as much as 2% more if the configurations could be altered. In addition, flow coefficients for all the nozzles are also documented.

- The aerodynamic performance of the coannular configurations tested at simulated take-off speeds decreased from 0.75 to 2% relative to the static performance levels.

- Analysis of the observed performance data indicated large reductions of the performance losses associated with take-off speeds are likely through primary nozzle redesign, ejector refinement, and increased fan/primary area ratios. Losses of approximately 0.5% are anticipated with refined exhaust system configurations suitable for the Variable Stream Control Engines.

- The test results illustrated the need for variable geometry in the primary stream. This would eliminate over expansion losses at low pressure ratio operation.

- The importance of the primary stream was further identified when the primary stream was turned off. An additional performance loss of approximately 5% was observed at static conditions when the primary stream was turned off.

REFERENCES

1. Kozlowski, H., Packman, A. B., "Aero-Acoustic Tests of Duct-Burning Turbofan Exhaust Nozzles," Final Report NASA CR-2628, July 1976.

2. H. Kozlowski, A. B. Packman, and O. Gutierrez, "Aeroacoustic Performance Characteristics of Duct Burning Turbofan Exhaust Nozzles," AIAA Paper 76-148.

3. A. B. Packman, H. Kozlowski, and O. Gutierrez, "Jet Noise Characteristics of Unsuppressed Duct During Turbofan Exhaust System," AIAA Paper No. 76-149.

4. Packman, A. B., Ng, K. W., and Paterson R. W., "Effect of Simulated Forward Flight on Subsonic Jet Exhaust Noise, " J. Aircraft, Vol. 13, No. 12, December 1976, pp. 1007–1013.

5. Cocking, B., and Bryce, W., "Subsonic Jet Noise in Flight Based on Some Recent Wind Tunnel Tests," AIAA Paper 75-462, 1975.

6. Strout, F. G., "Flight Effects on Noise Generated By the JT8D-17 Engine in a Quiet Nacelle and a Conventional Nacelle as Measured in the NASA-AMES 40 X 80-Foot Wind Tunnel," Contract Report NAS2-8213, January 1976.

7. Merriman, J.E., Good, R. C., Low, J.K.C., Yee, P.M., and Blankenship, G. L., "Forward Motion and Installation Effects on Engine Noise," AIAA Paper 76-584, 1976.

8. Amiet, R. K., "Correction of Open Jet Wind Tunnel Measurements for Shear Layer Refraction," AIAA Paper 75-532, 1975.

9. Packman, A. B. and Kozlowski, H., "Flight Effects on the Aerodynamic and Acoustic Characteristics of Inverted Velocity Profiles Coannular Nozzles - Comprehensive Data Report," NASA CR-135189, 1978.

10. Paterson, R. W., Vogt, P. G., and Foley, W. M., "Design and Development of the United Aircraft Research Laboratories Acoustic Research Tunnel," J. Aircraft, Vol. 10, No. 7, July 1973, pp. 427-433.

11. Society of Automotive Engineers: Aerospace Recommended Practice, ARP 866A, March 15, 1975.

12. Society of Automotive Engineers: Aerospace Recommended Practice, ARP 865A, August 1969.

13. Harper-Bourne, M., and Fisher, M. J., "The Noise from Shock Waves in Supersonic Jets," Paper No. 11, Agard CP-131, Noise Mechanisms, Fluid Dynamics Specialists Meeting, Brussels, Belgium, 1973.

14. Cocking, B. J. and Bryce, W. D. "An Investigation of the Noise of Cold Air Jets Under Simulated Flight Conditions," NGTE Report 334, Sept., 1974.

15. Private Communication, O. Gutierrez to A. B. Packman, August, 1976.

16. Larson, R. S. McColgan, C. J., Packman, A. B, "Jet Noise Source Modification due to Forward Flight," AIAA Paper 77-58, January 1977.

17. deBelleval, J. F., C. Y. Chen, and M. Perulli: "Investigation of In-Flight Jet Noise Based on Measurements in An Anechoic Wind Tunnel," Presented at 6th International Congress on Instrumentation in Aerospace Simulation Facilities, Ottawa, Canada, September 22-24, 1975.

18. Chen, C.Y., "Calculations of Far-field and Near-Field Jet Noise, AIAA Paper No. 75-93, 1975.

APPENDIX A

PART 1

MODEL SCALE OVERALL SOUND POWER LEVEL AND OVERALL SOUND PRESSURE LEVEL DIRECTIVITY ON THEORETICAL DAY

- Flight data are presented in the "simulated-flight" mode (i.e., corrected for shear layer refraction and moving medium effect).
- Peak perceived noise levels are shown on a 648.6 M sideline, at 22.5 X model scale for an FAA day ambient condition.
- "Theoretical Day" data are the noise that would be measured at the microphone if no noise were lost through atmospheric absorption.

TEST CONDITIONS					ACOUSTIC DATA													
									OASPL at 3.05m Radius									
Run No.	P_t/P_{amb}	T_t (°K)	V_j (mps)	V_{wt} (mps)	Ambient Temp (°K)	RH (%)	Peak PNL* at 648.6m Sideline	OAPWL	θ = 70°	80°	90°	100°	110°	120°	130°	140°	150°
Configuration 1 Convergent Nozzle																	
3603	2.52	590.0	525.5	9.4	305	10.0	106.8	142.4	120.6	119.9	119.4	120.4	121.6	122.4	124.6	129.9	142.5
3604	2.52	583.9	523.0	31.4	296	10.0	104.5	140.1	120.8	119.7	115.8	119.5	120.4	120.8	121.7	126.0	127.6
3605	2.52	586.7	524.3	61.9	297	12.0	101.8	138.1	121.3	119.7	116.4	116.6	116.8	116.9	118.9	121.8	124.0
3606	1.81	591.7	432.2	61.3	297	15.0	90.6	127.4	104.6	104.9	105.4	107.2	108.6	109.5	110.5	112.6	114.5
3607	1.81	588.3	430.4	30.8	297	17.0	93.3	130.4	105.5	106.2	106.9	109.1	110.9	112.2	113.8	116.5	118.6
3608	1.81	592.8	431.9	9.4	310	15.0	95.8	133.4	106.4	107.1	108.2	112.5	112.6	114.5	116.6	120.4	123.0
3609	1.30	597.7	296.3	9.4	305	14.0	81.2	119.8	95.1	95.6	96.4	98.5	100.4	101.7	103.2	105.8	108.1
3610	1.31	594.4	297.5	31.7	290	15.0	78.9	116.8	93.7	93.9	94.9	96.7	98.2	99.0	99.9	101.8	103.1
3611	1.31	590.0	296.3	61.6	287	17.0	75.5	113.2	92.1	92.0	92.6	93.9	94.9	95.2	95.7	97.0	98.2
3612	2.53	589.4	526.4	103.3	294	40.0	105.3	136.7	122.0	119.9	118.4	117.9	117.5	117.0	115.9	116.9	119.0
3613	1.81	587.8	430.7	103.0	294	58.0	87.2	123.4	103.1	102.7	102.6	104.1	105.0	105.4	105.7	107.0	108.7
3614	1.31	595.7	297.2	102.7	284	64.0	73.6	113.4	91.9	90.3	89.6	90.7	91.7	91.1	90.0	90.6	92.0
3615	3.23	592.2	583.7	103.9	283	68.0	114.4	143.2	126.2	126.4	124.9	124.7	124.2	123.7	122.1	122.9	125.2
3616	3.22	702.2	636.4	103.3	283	69.0	111.9	144.3	125.6	126.8	125.6	125.5	125.5	124.9	124.5	126.0	127.6
3617	2.52	700.0	573.9	103.6	283	70.0	105.9	138.2	122.1	120.4	119.1	119.2	119.1	118.8	118.7	120.6	122.6
3618	1.82	702.6	471.8	103.6	283	71.0	90.5	126.7	105.8	105.7	105.9	107.2	108.2	108.7	109.4	110.9	112.6
3619	1.30	702.8	321.6	103.0	283	71.0	75.4	114.5	94.0	92.8	92.5	93.7	94.5	94.2	93.8	94.6	96.1
3620	3.23	592.8	584.0	61.9	292	70.0	110.3	143.0	127.1	125.9	124.7	124.9	124.9	124.9	124.4	127.4	129.1
3621	3.23	594.4	584.9	31.4	294	70.0	109.8	145.5	125.6	125.8	124.9	125.5	125.9	126.2	126.9	131.3	131.8
3622	3.23	592.8	583.7	9.8	326	70.0	110.5	146.4	125.4	124.8	124.1	124.8	125.5	126.4	128.9	131.9	133.5
3623	3.23	695.0	633.4	61.6	299	3.0	110.4	144.9	127.3	126.1	124.9	125.2	125.5	125.4	126.8	129.6	130.1
3624	3.22	699.4	635.2	31.4	297	3.0	110.3	146.6	126.7	126.0	125.2	125.9	126.7	126.9	130.1	133.0	132.5
3625	3.23	700.3	635.6	9.8	331	1.0	112.4	148.2	126.3	125.8	125.3	126.2	127.4	128.2	132.4	135.4	134.4
3626	2.52	696.7	571.8	61.3	289	6.0	105.0	139.8	121.3	120.1	119.0	119.5	120.0	120.5	121.8	125.2	126.3
3627	2.52	698.9	573.6	30.5	294	8.0	106.3	142.2	121.2	120.5	119.8	120.6	121.8	122.7	125.3	129.2	[illegible]
3628	2.52	700.0	573.6	9.8	326	7.0	109.7	144.7	121.8	121.4	121.4	122.4	123.9	125.1	128.2	132.4	131.7
3629	1.81	696.7	468.8	61.7	289	8.0	93.0	130.0	106.6	107.0	107.6	109.3	110.9	111.9	113.2	115.7	117.6
3630	1.81	701.1	470.6	30.2	299	10.0	96.3	133.5	107.9	108.7	109.4	111.6	113.6	115.0	116.9	120.1	121.8
3631	1.82	701.1	472.7	9.4	314	9.0	99.1	136.3	108.7	109.5	110.5	112.7	115.1	116.9	119.5	123.8	125.8
3632	1.31	697.8	321.9	61.5	289	12.0	78.3	116.0	94.5	94.6	94.9	96.5	97.7	98.1	98.8	100.1	101.4
3633	1.31	701.1	323.4	30.8	289	14.0	81.6	119.5	96.2	96.6	97.1	99.2	100.9	101.7	102.8	104.8	106.0
3634	1.31	705.0	323.4	9.4	289	14.0	83.6	122.4	97.1	97.7	98.4	100.7	102.8	104.2	106.1	108.7	110.9
3635	3.24	396.7	476.7	9.1	299	37.0	109.0	144.2	125.6	125.3	124.5	124.9	124.8	125.7	124.7	127.6	131.5
3636	3.18	395.0	473.0	31.7	291	39.0	109.4	142.9	126.2	125.7	124.4	124.4	123.9	124.5	123.0	123.5	126.4
3637	3.21	393.9	474.0	61.3	287	48.0	109.3	142.1	126.6	125.7	124.1	123.7	122.8	122.8	121.5	120.7	122.1
3638	2.52	390.6	427.0	60.7	286	64.0	103.4	135.3	120.3	118.9	117.3	116.8	115.9	115.6	114.5	114.2	115.5

* **Engine Size: 22.5 X Scale Model**

Run No.	P_t/P_{amb}	T_t (°K)	V_j (mps)	V_∞ (mps)	Ambient Temp (°K)	RH (%)	Peak PNL* at 648.6m Sideline	OAPWL	OASPL at 3.05m Radius								
									θ = 70°	80°	90°	100°	110°	120°	130°	140°	150°
3639	2.52	396.7	430.1	30.8	287	66.0	103.2	136.6	[illegible]	119.0	118.0	117.8	117.4	117.6	116.9	118.1	120.7
3640	2.52	396.1	430.1	9.1	298	51.0	102.7	138.0	119.6	118.8	118.1	118.2	118.3	188.9	199.0	122.0	126.0
3641	2.03	393.3	380.1	9.1	297	40.0	92.5	130.1	107.3	107.2	107.3	108.6	109.8	111.2	113.0	116.0	119.4
3642	2.01	397.2	380.4	30.8	289	44.0	90.1	127.1	106.7	106.3	105.9	107.0	107.9	108.8	109.9	111.8	114.0
3643	2.02	371.7	278.8	60.7	286	60.0	89.4	124.1	105.9	105.1	104.3	104.9	105.3	105.7	106.2	107.4	109.1
3644	1.82	392.8	351.7	60.7	286	71.0	83.4	120.0	98.8	98.9	99.3	100.7	101.5	102.1	102.9	104.1	105.5
3645	1.84	396.7	353.3	30.5	286	72.0	86.6	123.5	103.6	101.0	101.5	103.3	104.6	105.6	106.8	108.6	110.6
3646	1.92	395.6	353.0	6.4	296	59.0	[illegible]	127.0	101.9	102.4	103.2	105.1	106.6	108.2	110.2	113.1	[illegible]
3647	1.54	396.1	304.5	9.1	296	50.0	83.0	120.9	96.3	97.0	97.9	99.9	101.4	102.7	104.3	106.7	109.5
3648	1.54	395.6	304.2	30.8	288	52.0	80.5	117.7	94.9	95.4	95.9	97.8	99.0	99.9	100.9	102.6	104.1
3649	1.54	393.9	303.3	60.7	286	59.0	77.0	114.0	93.3	93.2	93.5	94.7	95.5	96.0	96.4	97.5	98.6
3650	1.31	395.6	241.4	60.7	286	66.0	67.8	106.0	84.3	84.8	85.6	86.6	87.1	87.4	87.4	88.1	88.8
3651	1.31	396.1	242.0	29.9	285	68.0	71.8	109.6	87.6	88.1	88.6	90.2	91.1	91.8	92.4	93.7	94.7
3652	1.31	397.2	242.0	9.1	290	64.0	74.4	112.8	89.3	89.8	90.8	92.6	93.9	95.0	96.2	98.2	100.3
3656	3.21	395.6	474.9	102.4	283	76.0	108.4	140.1	125.8	124.9	122.3	121.2	120.1	119.5	118.1	117.1	117.6
3657	2.52	397.8	431.0	102.4	282	78.0	103.8	134.3	120.9	118.7	116.6	115.5	114.2	113.2	111.6	110.6	110.9
3658	2.02	395.0	379.8	102.4	282	80.0	87.8	121.0	104.3	102.7	101.6	101.8	101.5	101.5	101.4	101.9	103.3
3659	1.81	394.4	351.7	102.4	282	60.0	79.6	117.1	96.5	96.3	96.3	97.2	97.5	97.7	98.1	98.7	99.5
3660	1.54	396.7	304.8	102.4	282	81.0	73.2	114.5	90.7	90.3	90.3	91.1	91.8	91.5	91.1	91.6	92.7
3661	1.31	393.3	241.7	102.4	282	81.0	70.7	113.0	89.3	85.9	83.3	86.2	86.0	84.7	84.4	83.2	86.6

Run No.	P_{tp}/P_{amb}	T_{tp} (°K)	V_p (mps)	P_{ts}/P_{amb}	[illegible]	[illegible]	V_∞(mps)	Ambient Temp (°K)	RH (%)	Peak PNL at* 648.6 m Side Line	OAPWL	OASPL at 3.05m Radius θ = 70	80	90	100	110	120	130	140	150
Configuration 2 0.75 Area Ratio Coannular Nozzle Without [illegible]																				
3310	1.52	387.9	296.0	3.21	401.1	477.9	30.5	286	22.0	100.7	134.9	119.3	117.6	116.3	115.8	116.3	115.9	115.7	116.7	117.1
3311	1.52	387.8	297.2	3.20	400.4	477.0	60.4	283	25.0	101.0	133.9	118.7	117.4	115.6	114.9	115.1	114.4	113.8	114.4	114.5
3313	1.53	389.0	296.9	2.50	399.3	429.8	30.5	289	22.0	95.4	127.1	112.3	111.3	110.2	109.8	110.1	110.2	110.7	111.8	112.3
3315	1.53	396.5	302.2	2.51	404.3	433.4	60.4	285	24.0	95.4	128.0	112.6	111.1	109.5	108.9	108.8	108.4	108.4	109.2	109.5
3316	1.53	396.5	301.6	1.80	404.6	355.1	60.4	284	25.0	82.7	118.3	98.2	98.0	98.2	99.2	100.3	100.6	100.9	101.8	102.5
3317	1.53	394.8	301.1	1.80	407.1	356.0	30.2	285	26.0	85.3	121.2	99.2	99.5	100.1	101.5	103.2	103.6	104.3	105.6	106.0
3318	1.53	393.3	299.8	1.80	409.8	357.2	6.4	297	25.0	87.7	123.9	100.6	101.3	102.2	103.7	105.5	106.2	107.3	109.0	110.3
3319	1.53	391.6	299.7	1.53	410.8	308.2	6.4	299	24.0	84.4	120.9	98.3	98.9	99.6	100.8	102.5	102.8	103.9	106.1	107.9
3320	1.53	389.6	298.6	1.53	408.5	306.9	30.5	288	24.0	81.9	118.2	97.0	97.2	97.6	98.8	100.1	100.1	100.7	102.4	107.4
3321	1.52	385.0	296.4	1.54	404.1	306.3	60.4	285	25.0	79.4	115.2	96.1	95.8	95.8	96.5	97.2	96.9	97.0	98.0	98.9
3322	1.53	378.2	294.3	1.30	405.2	242.2	60.4	284	26.0	76.3	113.0	95.3	94.6	94.2	94.3	94.6	93.8	93.7	94.9	96.4
3323	1.52	371.8	290.8	1.30	418.5	245.8	29.6	285	27.0	78.9	115.3	95.5	95.4	95.5	96.2	97.1	96.7	97.2	99.2	100.6
3324	1.51	360.6	294.2	1.30	403.9	242.5	6.4	294	26.0	80.8	117.5	95.9	96.3	96.9	97.8	99.1	99.1	100.0	102.5	114.4
3325	1.53	392.8	300.4	3.21	388.9	470.6	01.5	281	33.0	101.6	133.5	119.5	117.6	115.7	114.7	114.1	112.9	111.1	110.4	110.3
3326	1.51	397.7	297.5	2.51	391.5	426.1	101.8	280	35.0	97.4	126.9	112.9	111.0	109.0	107.9	107.1	106.0	104.7	104.5	104.9
3327	1.53	396.8	301.3	1.80	394.4	347.8	101.5	281	36.0	80.6	116.9	97.8	97.3	96.8	97.1	97.5	97.1	96.3	96.3	97.2
3328	1.53	392.8	300.6	1.53	393.9	301.6	101.8	281	41.0	79.3	115.5	96.6	–	95.5	94.7	94.8	94.1	93.1	93.1	94.4
3329	1.51	396.7	297.2	1.30	394.3	237.6	101.5	281	44.0	79.4	114.8	96.5	–	94.6	93.4	93.1	91.9	90.3	90.5	92.5
3330	1.52	398.4	301.5	1.31	575.6	266.1	101.2	290	56.0	80.4	115.2	97.5	–	96.1	95.4	95.2	94.5	92.8	92.8	94.0
3340	1.52	409.3	304.3	3.21	596.1	584.3	11.6	313	13.0	103.9	137.6	118.9	118.5	119.2	118.8	119.9	120.3	122.4	122.6	123.3
3341	1.54	402.7	306.3	3.21	577.9	575.5	31.1	300	12.0	101.1	136.0	117.8	117.0	116.0	116.3	117.3	117.7	119.7	119.4	118.9
3342	1.53	389.7	299.3	3.20	590.4	580.9	61.3	292	16.0	100.7	134.7	118.2	116.9	115.5	115.6	115.9	115.9	117.2	116.7	115.1
3343	1.52	386.8	295.4	2.49	635.7	530.0	61.0	291	23.0	94.5	129.1	110.8	109.8	109.1	109.6	110.7	111.4	112.8	112.1	110.6
3344	1.52	392.1	297.7	2.50	605.0	530.7	30.8	292	34.0	96.5	131.4	110.0	110.5	110.2	111.2	112.8	114.1	116.1	115.4	114.6
3345	1.49	397.6	293.2	2.49	602.4	524.3	6.7	311	30.0	97.4	132.3	109.7	109.6	109.8	111.2	113.0	115.0	117.1	117.2	118.1
3346	1.53	404.4	304.3	1.80	598.9	432.8	6.7	311	21.0	90.4	125.7	101.6	102.3	103.4	105.5	107.4	108.9	110.3	110.1	111.4
3347	1.52	410.8	304.3	1.79	600.0	429.8	31.1	296	21.0	88.6	123.8	100.7	101.4	102.2	104.2	106.0	107.0	109.1	107.6	107.0
3348	1.53	380.8	295.0	1.80	596.5	431.6	61.0	289	68.0	86.0	120.8	99.6	99.9	100.4	102.1	103.5	103.8	104.5	103.2	101.8
3349	1.54	384.3	299.8	3.21	638.2	479.1	6.4	330	53.0	100.0	135.1	117.4	116.9	115.9	115.8	116.1	116.4	117.6	117.9	119.2
3350	1.52	376.2	294.9	2.52	391.3	426.7	6.4	332	38.0	94.9	129.6	111.2	110.9	110.9	110.2	110.6	111.2	112.6	112.7	114.1
3351	1.53	402.8	303.9	1.30	576.3	290.3	6.7	336	21.0	81.7	118.9	96.5	96.9	97.5	99.1	100.3	100.9	102.2	103.8	106.0
3352	1.53	406.2	306.3	1.31	574.3	290.8	31.1	296	21.0	80.1	116.3	95.7	95.9	96.1	97.6	98.3	98.3	99.0	99.7	100.8
3353	1.56	409.7	313.6	1.30	569.3	288.4	61.6	292	24	78.8	114.4	96.2	95.7	95.2	95.9	96.1	95.4	95.5	95.4	96.1
3356	1.51	394.3	297.5	3.20	696.3	632.2	9.4	321	26.0	102.2	137.6	116.4	115.9	115.5	116.8	118.3	120.0	121.6	123.0	123.5
3359	1.53	402.2	304.7	3.20	692.6	630.3	31.1	299	26.0	102.8	137.5	118.5	117.9	117.2	118.0	119.0	119.7	120.7	121.4	120.6
3361	1.52	408.6	304.8	3.22	699.1	634.3	61.9	294	37.0	101.7	136.3	118.9	117.9	116.9	117.3	117.9	118.3	118.7	118.8	117.4
3362	1.52	401.8	300.6	2.51	701.5	573.3	61.6	292	56.0	95.1	129.9	110.1	109.5	109.2	110.4	111.8	113.1	113.5	113.4	112.2

Run No	P_{tp}/P_{amb}	T_{tp} (°K)	V_p (mps)	P_{tf}/P_{amb}	T_{tf} (°K)	V_j (mps)	**V_{ac}(mps)**	Ambient Temp (°K)	RH (%)	Peak PNL at* 648.6 m Side Line	OAPWL	θ = 70	OASPL at 3.05m Radius 80	90	100	110	120	130	140	150
Configuration 2 0.75 Area Ratio Coannular Nozzle Without Ejector																				
3363	1.53	394.6	301.8	2.50	703.9	573.3	**30.2**	295	57.0	94.7	132.0	109.9	109.8	109.9	111.7	113.7	115.4	116.1	116.4	115.7
3364	1.52	388.6	296.4	2.51	706.7	575.2	**9.4**	**317**	35.0	98.7	133.2	108.6	109.0	109.6	111.8	114.2	116.5	117.6	118.7	119.5
3365	1.53	377.5	294.4	1.81	699.4	467.9	**9.4**	314	27.0	91.7	126.3	101.9	102.7	103.7	106.0	108.2	109.9	110.3	111.0	111.9
3366	1.52	387.9	297.2	1.80	660.9	461.5	**30.8**	294	56.0	89.6	124.1	101.2	101.8	102.6	104.7	106.6	107.7	107.7	107.5	106.9
3367	1.52	402.2	302.7	1.80	674.4	456.1	**61.6**	306	55.0	86.9	121.4	100.3	100.5	101.1	102.7	104.1	104.8	104.5	103.8	102.8
3368	1.53	404.8	304.8	1.30	613.5	300.4	**61.3**	292	68.0	76.0	113.5	95.3	94.9	94.5	95.1	95.4	95.0	94.5	94.5	95.2
3369	1.54	372.6	294.2	1.31	617.6	307.6	**30.2**	292	65.0	79.8	116.1	95.9	95.8	96.0	97.3	98.2	98.3	98.4	99.3	100.3
3370	1.53	383.2	296.1	1.30	623.3	301.5	**6.4**	305	53.0	81.4	118.5	96.1	96.5	97.1	98.8	100.6	100.7	101.6	103.2	105.6
3371	1.51	389.1	295.5	3.24	706.3	637.6	**129.5**	290	64.0	101.8	134.3	119.7	117.8	116.0	115.7	115.2	114.7	113.6	112.7	111.7
3372	1.56	382.3	296.5	2.49	691.7	567.5	**129.5**	290	68.0	92.8	127.1	110.3	106.7	107.7	108.0	108.3	108.5	107.9	107.3	106.1
3373	1.52	386.7	295.4	2.50	705.6	573.9	**103.6**	290	71.0	93.5	127.8	110.1	109.0	108.0	109.0	109.7	110.5	109.8	109.3	108.4
3374	1.52	382.6	294.8	1.90	681.8	461.5	**103.3**	290	71.0	85.0	120.0	100.8	103.6	100.4	101.6	102.2	102.4	101.2	100.2	99.2
3375	1.52	375.7	292.7	1.31	633.2	305.4	**103.6**	290	72.0	78.1	115.7	95.9	94.9	93.4	93.2	92.8	92.1	93.4	93.9	91.8
3376				3.35	717.6	652.3	**103.9**	290	72.0	102.7	135.8	120.2	118.5	116.8	116.9	116.7	116.8	116.7	117.2	117.6
3377				2.61	714.8	589.2	**103.3**	290	73.0	95.7	129.8	112.3	111.1	110.1	110.9	111.2	111.4	111.4	112.5	113.4
3378				1.89	691.6	482.5	**103.6**	290	74.0	87.4	122.2	103.0	102.9	102.7	103.9	104.2	104.3	103.5	103.4	103.4
3379				1.36	656.3	335.3	**103.3**	289	74.0	78.3	115.9	95.4	95.0	94.5	94.8	94.8	94.8	94.1	93.5	92.9
3380				**3.25**	**710.9**	**642.5**	**9.4**	322	16.0	104.9	140.8	117.6	117.3	116.8	–	119.5	121.6	124.2	128.0	129.6
3381				3.26	727.8	651.1	**61.9**	295	18.0	101.7	137.2	118.9	118.0	116.7	117.3	117.9	118.8	119.9	121.6	122.2
3382				2.56	721.8	587.3	**61.0**	292	23.0	96.0	132.0	111.5	110.9	110.3	111.8	113.1	114.1	115.2	117.2	117.7
3383				2.51	733.7	586.7	**6.7**	315	22.0	100.6	136.2	110.2	110.4	110.9	113.1	115.2	117.5	119.9	[illegible]	124.6
3384				1.84	717.4	474.3	**9.4**	312	19.0	91.9	127.7	101.4	102.4	103.6	106.0	108.0	110.2	111.6	113.9	115.5
3385				1.84	701.1	476.4	**61.9**	294	23.0	87.9	123.2	101.7	102.3	102.5	104.2	105.3	106.2	106.3	107.0	107.1
3386				1.35	663.3	331.0	**61.3**	292	38.0	77.4	113.3	93.6	93.2	93.3	94.3	94.9	95.5	94.7	94.3	93.5
3388				1.33	668.2	314.2	**11.3**	296	47.0	77.1	113.4	90.1	91.1	91.9	93.7	95.2	96.5	97.0	98.2	98.5
Configuration 3 0.75 Area Ratio Coannular Nozzle With Ejector																				
3501	1.52	374.7	290.4	3.23	401.3	476.2	**9.1**	302	27.0	100.9	135.3	117.3	117.0	116.5	116.9	117.4	117.2	116.1	117.2	117.9
3052	1.52	375.4	291.4	3.20	398.2	475.5	**30.8**	294	29.0	100.3	134.1	117.5	116.9	116.0	116.0	116.2	115.6	113.8	113.9	113.5
3503	1.52	375.8	291.2	3.20	401.5	477.9	**61.3**	291	32.0	100.7	133.6	118.2	117.3	115.9	115.5	115.2	114.1	111.9	110.6	112.1
3504	1.50	376.0	286.7	2.44	404.4	427.6	**61.0**	290	37.0	97.2	130.3	114.1	113.7	113.1	112.7	112.0	110.5	108.3	106.6	106.0
3505	1.52	375.6	292.0	2.49	395.4	427.3	**29.9**	291	41.0	97.0	130.4	113.1	113.1	112.6	112.5	112.3	111.6	110.0	109.5	110.8
3506	1.52	374.6	291.8	2.50	397.2	428.9	**9.1**	301	37.0	97.2	131.0	112.4	112.4	112.4	112.8	113.2	112.7	112.0	113.2	114.4
3507	1.53	375.2	292.7	1.80	403.3	354.8	**9.1**	300	32.0	87.3	124.1	103.3	103.7	103.5	104.8	105.9	105.7	105.9	108.0	111.8
3508	1.52	375.7	292.7	1.80	397.4	351.4	**31.4**	292	34.0	85.3	121.4	102.2	102.0	102.2	103.0	103.6	103.2	102.6	103.2	106.7
3509	1.53	376.3	294.3	1.80	399.6	352.7	**61.0**	290	39.0	83.9	119.5	101.7	101.3	101.1	101.6	101.8	100.9	99.7	99.2	101.6
3510	1.53	376.9	295.2	1.53	400.6	304.6	**60.6**	290	42.0	81.2	117.0	99.5	98.9	98.8	99.2	99.2	97.9	96.3	95.9	99.0

								Ambient		Peak PNL at*						OASPL				
Run No.	P_{tp}/P_{amb}	T_{tp} (°K)	V_p (mps)	P_{tf}/P_{amb}	T_{tf} (°K)	V_f (mps)	V_{ac}(mps)	Temp (°K)	RH (%)	648 m Sideline	OAPWL	θ=70	80	90	100	110	120	130	140	150
3511	1.51	377.3	290.8	1.53	397.8	302.1	29.9	291	47.0	82.3	115.8	99.9	99.8	99.6	100.6	100.9	100.1	99.2	103.1	104.6
3513	1.52	377.9	293.5	1.53	392.8	296.5	8.5	299	31.0	86.7	124.8	107.5	110.0	104.9	105.9	104.1	103.0	103.8	106.6	109.7
3514	1.52	376.2	292.5	1.30	397.1	240.2	9.1	293	29.0	81.2	116.5	98.6	98.9	98.9	99.3	100.3	99.8	99.9	102.7	104.7
3515	1.53	376.1	294.6	1.31	395.9	241.3	30.8	292	30.0	79.9	116.0	97.0	97.0	97.1	97.8	98.3	97.5	96.6	98.3	99.4
3516	1.52	376.6	292.9	1.30	400.0	240.5	61.3	291	33.0	78.7	114.2	96.5	96.2	96.0	96.3	96.4	95.1	93.6	94.0	94.6
3517	1.52	377.5	292.5	3.20	396.1	474.6	103.3	290	59.0	101.1	132.9	118.5	117.0	115.6	114.7	113.7	112.2	109.7	109.0	106.8
3518	1.53	377.8	294.9	2.50	400.6	430.7	103.0	290	59.0	96.6	129.1	113.7	113.0	111.1	111.5	110.2	108.3	105.6	103.9	102.9
3519	1.52	377.2	293.0	1.80	402.1	353.0	103.0	299	66.0	93.0	119.2	101.3	100.3	99.8	97.8	99.3	98.0	96.3	96.0	96.2
3520	1.51	375.9	289.8	1.51	403.2	304.3	103.3	289	62.0	79.6	117.1	98.7	97.8	97.1	97.1	96.5	95.0	92.0	91.7	94.2
3521	1.53	379.0	292.8	1.31	399.8	243.6	103.3	289	64.0	77.2	116.0	95.8	95.1	94.6	94.6	93.8	92.3	89.7	89.6	93.4
3522	1.53	400.4	303.1	3.21	591.1	562.2	61.9	294	3.0	99.0	133.1	115.9	115.1	114.4	114.6	115.3	115.1	114.1	114.2	113.6
3523	1.53	397.2	302.2	3.20	564.4	577.9	30.2	297	4.0	100.2	134.5	115.7	115.3	114.9	115.5	116.6	116.9	116.5	117.3	117.0
3524	1.52	395.4	299.8	3.20	563.5	577.6	9.4	314	4.0	100.8	136.2	116.3	116.0	116.0	116.7	118.2	119.8	119.7	120.2	120.6
3525	1.52	392.2	298.8	2.50	590.6	521.3	9.4	315	4.0	97.6	132.4	111.2	111.4	111.8	113.0	114.5	115.8	115.2	116.3	116.9
3526	1.52	391.2	298.0	2.50	598.7	523.3	31.7	297	6.0	96.0	130.6	110.6	110.8	110.8	111.6	112.8	113.7	112.9	113.4	113.2
3527	1.52	392.1	298.0	2.49	593.5	524.0	61.3	294	8.0	95.8	129.4	111.2	111.1	110.7	111.2	111.6	111.8	110.6	110.3	109.5
3528	1.53	390.2	300.1	1.79	601.8	431.9	61.3	293	11.0	87.5	122.3	103.3	103.1	103.4	104.2	105.1	105.0	103.7	103.4	102.8
3529	1.52	388.2	295.9	1.60	590.2	427.9	30.8	295	14.0	89.3	124.2	103.7	103.8	104.4	105.7	106.9	107.4	106.3	106.8	106.6
3530	1.52	386.6	295.7	1.60	585.1	426.1	9.1	306	15.0	90.8	126.1	104.1	104.4	105.4	107.0	108.5	109.2	108.6	110.0	110.8
3531	1.52	383.2	294.0	1.30	587.4	293.0	9.1	304	16.0	84.9	124.6	105.1	104.8	106.7	105.3	102.9	101.7	102.1	106.5	107.2
3532	1.52	385.2	295.3	1.30	567.1	291.4	31.4	295	19.0	80.9	117.4	98.2	98.3	98.3	99.2	99.7	99.2	98.2	99.6	100.5
3533	1.52	384.9	295.5	1.30	562.8	289.9	61.3	292	23.0	79.3	115.4	97.6	97.2	97.1	97.6	97.8	96.8	95.0	95.1	95.6
3534	1.53	401.8	303.7	3.20	646.5	631.9	9.4	319	31.0	101.4	136.3	114.9	114.9	115.0	116.5	118.2	119.3	119.1	120.9	121.2
3535	1.52	402.7	302.8	3.21	683.5	629.1	31.1	299	31.0	102.4	136.3	116.5	116.7	116.3	117.6	118.9	119.4	118.4	119.1	118.5
3536	1.53	406.7	304.8	3.20	701.0	636.1	61.6 61.6	293	51.0	101.2	135.4	116.9	116.6	116.1	116.8	117.8	117.9	119.0	116.8	115.1
3537	1.52	413.7	302.2	2.45	706.0	565.3	61.6	292	69.0	96.4	131.0	111.5	111.7	111.5	112.4	113.4	114.0	114.0	112.3	110.8
3538	1.52	401.7	302.2	2.56	700.2	572.1	30.2	294	67.0	97.9	132.2	111.0	111.3	111.4	112.9	114.7	116.0	115.8	115.0	114.3
3539	1.52	401.0	302.5	2.54	691.7	571.8	9.4	315	37.0	99.6	132.9	109.8	110.3	110.9	112.8	115.0	116.8	116.5	117.4	117.6
3540	1.53	395.3	300.7	1.80	647.4	461.9	9.4	309	30.0	91.7	126.7	104.3	104.9	105.6	107.3	108.9	110.2	109.5	111.0	111.6
3541	1.50	393.8	294.9	1.81	684.4	463.3	31.1	297	34.0	90.5	125.3	104.1	104.6	105.0	106.5	107.9	108.9	107.6	108.0	107.6
3542	1.53	390.9	298.8	1.81	676.5	460.6	61.6	294	49.0	88.8	123.4	103.8	104.1	104.1	103.3	106.1	106.6	104.8	104.4	103.5
3543	1.52	382.2	293.9	1.30	647.6	306.0	61.6	292	66.0	79.6	115.8	97.8	97.6	97.3	99.0	98.2	97.5	95.7	95.7	95.8
3544	1.52	376.8	292.8	1.31	641.1	307.8	30.2	293	70.0	81.1	117.7	95.4	98.6	98.4	99.5	99.9	99.7	98.5	99.8	100.4
3545	1.52	376.8	292.4	1.30	643.5	306.0	9.1	303	56.0	84.1	123.6	104.8	108.1	106.4	105.8	101.7	101.9	102.2	105.4	107.0
3546	1.52	411.0	304.6	3.20	709.6	676.3	103.9	291	67.0	100.0	133.8	117.1	116.4	115.3	115.7	115.8	115.6	114.4	113.2	111.6
3547	1.52	417.3	306.6	3.20	705.5	637.0	129.8	290	80.0	106.2	133.1	117.6	116.3	114.7	114.8	114.6	113.8	112.6	111.1	109.3
3548	1.57	407.9	314.6	2.64	697.2	565.2	129.5	290	82.0	94.7	128.6	111.4	110.5	109.6	110.4	110.2	108.8	107.4	107.4	106.1
3549	1.53	404.2	303.6	2.50	697.6	570.0	103.9	290	64.0	95.5	129.1	111.8	111.2	110.5	111.1	111.2	111.2	110.0	108.7	107.0
3550	1.52	396.0	300.5	1.60	675.0	459.3	103.9	290	86.0	86.5	121.6	104.0	103.4	102.8	103.4	103.5	103.2	101.4	99.9	99.0
3551	1.52	367.4	295.8	1.30	635.6	302.6	103.6	290	86.0	80.8	116.6	98.4	97.6	96.6	97.2	96.5	95.6	93.6	91.9	90.8
3552	1.52	367.9	297.0	3.15	600.0	582.5	103.3	290	87.0	106.0	132.7	117.4	116.2	114.6	114.2	114.1	113.5	112.2	110.9	109.4
3553	1.53	394.9	296.5	2.51	601.5	530.0	103.9	290	89.0	96.0	126.4	112.4	111.6	110.3	109.9	109.9	109.5	108.0	106.6	105.4
3554	1.52	362.6	294.5	1.80	605.0	434.0	103.9	290	86.6	85.5	120.8	103.4	102.7	101.7	102.2	102.2	101.7	100.0	98.6	97.6

Run No.	P_{Tp}/P_{amb}	T_{Tp} (°K)	V_p (mps)	P_{Tf}/P_{amb}	T_{Tf} (°K)	V_f (mps)	V_∞ (mps)	Ambient Temp (°K)	RH (%)	Peak PNL dB* 648 m Sideline	OAPWL				OASPL					
												θ = 70	80	90	100	110	120	130	140	150
3888	1.52	390.6	292.5	1.30	914.3	[illegible]	103.3	290	80.0	79.5	116.3	97.7	[illegible]	95.9	96.2	96.0	94.6	92.1	90.7	90.0
Configuration 6 1.2 Area Ratio Coannular Nozzle																				
3401	1.52	389.3	295.9	3.20	710.6	638.6	9.4	326	80.0	105.7	141.2	120.5	120.3	120.5	121.3	122.0	123.3	124.5	126.2	126.6
3402	1.74	389.6	301.0	3.21	702.9	635.5	31.3	298	71.0	111.0	138.7	119.5	118.9	119.3	118.8	119.5	120.9	121.8	123.0	123.0
3403	1.52	363.4	299.0	3.20	698.5	633.4	61.6	294	13.0	103.2	137.3	120.0	119.1	118.0	118.1	116.3	119.0	119.4	120.0	119.3
3404	1.52	397.8	299.3	2.51	708.9	575.8	61.3	291	15.0	96.9	131.8	114.0	112.3	112.0	112.3	112.8	114.7	114.8	114.3	115.3
3406	1.52	394.4	295.6	2.51	700.0	572.1	30.8	295	22.0	99.6	134.5	114.6	114.2	113.9	114.9	115.8	117.2	117.7	118.8	118.5
3407	1.53	397.8	300.0	2.52	702.4	574.2	6.7	326	14.0	100.6	136.0	134.3	114.3	114.3	115.6	117.1	118.6	119.6	121.2	122.3
3408	1.52	389.3	297.5	1.81	705.1	470.3	6.7	322	10.0	93.7	128.4	103.9	106.0	108.4	110.1	112.0	112.3	112.3	113.2	114.0
3409	1.52	388.8	297.4	1.81	700.7	469.7	31.1	297	10.0	91.7	126.2	102.3	103.0	108.1	106.6	108.2	109.8	110.0	110.4	110.1
3410	1.52	391.5	299.0	1.81	698.5	467.9	61.3	291	15.0	89.0	123.7	101.8	102.2	103.0	104.9	106.0	107.2	106.9	106.6	105.7
3411	1.53	386.0	297.2	1.30	670.9	313.3	61.3	291	19.0	76.7	114.1	95.3	95.0	95.0	95.9	96.0	96.2	95.3	95.2	95.5
3412	1.53	384.6	296.7	1.30	670.2	311.6	30.8	291	22.0	80.7	116.8	96.1	96.1	96.5	98.1	98.8	99.4	99.1	100.0	100.5
3413	1.53	385.1	295.8	1.31	671.7	315.8	11.3	302	23.0	82.2	119.0	96.6	97.0	97.8	97.5	100.5	101.6	102.1	103.6	103.1
3414	1.53	401.2	303.5	3.20	590.2	590.9	103.6	299	86.0	103.1	135.2	130.4	118.8	117.2	116.6	115.9	115.4	114.5	114.1	113.5
3415	1.52	422.4	302.7	2.51	596.7	527.6	103.6	299	87.0	96.2	129.1	115.8	112.1	110.5	110.3	109.9	110.1	109.5	108.9	109.1
3416	1.53	430.7	302.9	1.80	606.3	434.6	103.9	299	87.0	84.9	120.2	100.3	100.1	100.2	101.4	101.7	102.1	101.5	100.8	100.3
3417	1.53	396.3	301.3	1.30	596.5	295.9	103.9	299	87.0	78.5	115.6	95.6	95.2	94.0	93.7	93.4	92.6	91.3	91.7	93.2
3418	1.54	407.5	307.5	3.20	705.6	636.4	130.5	299	87.0	107.7	133.5	[illegible]	119.9	117.3	116.9	116.1	115.6	115.4	114.7	113.4
3419	1.53	402.5	304.3	3.21	702.8	635.5	103.6	299	88.0	104.4	136.1	[illegible]	119.0	117.6	117.5	117.0	117.1	116.9	116.6	115.7
3420	1.53	394.2	300.0	2.47	707.2	570.6	103.9	298	67.0	96.2	129.9	113.7	112.0	110.9	111.1	111.2	111.6	111.2	111.7	109.9
3421	1.52	388.7	297.7	2.51	709.3	576.4	129.8	298	87.0	97.0	129.9	114.5	112.5	111.0	110.9	110.4	110.2	109.6	108.8	107.9
3422	1.51	380.6	292.1	1.80	690.7	464.2	102.1	299	88.0	96.2	121.9	101.5	101.6	101.8	102.9	103.4	103.9	103.5	102.7	101.9
3423	1.52	370.7	299.0	1.30	654.1	309.7	104.2	299	87.0	78.8	116.4	95.9	95.4	94.3	94.2	93.9	93.4	92.4	92.9	93.8
3424	1.53	379.6	296.7	3.20	586.3	579.1	61.3	278	26.0	103.3	137.1	120.6	119.7	118.5	118.5	118.3	118.5	118.2	118.7	118.3
3425	1.53	397.1	298.9	3.22	595.4	584.3	29.9	290	27.0	103.6	139.6	120.7	120.0	119.0	119.3	119.8	120.4	120.7	121.9	122.0
3426	1.53	392.1	300.3	3.21	591.1	581.9	6.7	319	29.0	103.8	139.4	119.9	119.4	119.0	119.6	120.2	121.4	122.0	123.8	125.2
3427	1.52	396.1	299.7	2.52	580.3	525.8	6.7	320	10.0	101.5	136.1	116.6	116.2	116.0	117.1	117.7	118.4	118.3	119.7	121.5
3428	1.53	397.6	302.1	2.51	588.6	524.3	31.1	295	10.0	97.7	132.7	113.0	112.7	112.4	113.2	113.9	115.4	115.6	116.7	117.0
3429	1.53	398.6	302.0	2.51	594.4	527.3	61.0	298	11.0	96.7	131.1	113.6	112.7	111.8	112.2	112.4	113.2	113.1	113.0	115.0
3430	1.53	399.3	303.8	1.81	607.3	436.8	60.4	297	12.0	87.6	122.5	100.7	101.2	101.8	103.7	104.7	105.9	105.8	105.4	105.8
3431	1.63	398.6	302.3	1.81	595.6	431.6	29.9	288	13.0	90.1	125.0	101.8	102.3	103.2	105.3	107.0	106.5	108.5	109.9	110.0
3432	1.53	397.1	301.3	1.81	580.3	431.0	6.7	310	12.0	92.7	127.7	103.5	104.5	105.4	107.7	109.3	111.0	111.3	112.4	113.5
3433	1.53	393.9	301.4	1.30	592.0	295.1	9.1	301	11.0	81.3	116.9	96.2	96.6	97.3	98.9	100.1	101.3	102.0	104.1	100.1
3434	1.53	393.4	300.1	1.31	598.7	297.3	30.8	290	12.0	79.4	116.3	95.1	95.2	95.6	97.0	97.8	98.6	99.6	100.1	101.1
3435	1.52	393.3	298.9	1.31	601.5	299.4	60.7	286	14.0	78.3	113.9	94.9	94.6	94.6	95.4	95.5	95.7	95.2	94.9	97.9
3436	1.52	385.1	295.9	3.21	600.0	477.6	60.4	282	52.0	104.2	136.4	121.2	120.3	118.8	118.2	117.5	116.9	114.8	114.1	114.6

Run No.	P_{tp}/P_{amb}	T_{tp} (°K)	V_p (mps)	P_{tf}/P_{amb}	T_{tf} (°K)	V_f (mps)	V_{eo}(mps)	Ambient Temp (°K)	RH (%)	Peak PNL at* 648.6m Side Line	OAPWL	OASPL at 3.05m Radius θ = 70	80	90	100	110	120	130	140	150
3437	1.53	385.7	297.8	3.21	399.4	477.0	30.5	294	57.0	103.9	137.0	120.9	120.1	118.9	118.6	118.4	118.1	116.6	117.0	118.3
3438	1.53	386.6	297.8	3.22	399.6	477.6	9.1	295	48.0	103.2	137.9	120.3	120.0	119.2	119.2	119.2	119.4	118.6	120.1	121.5
3439	1.53	385.1	297.6	2.52	400.6	432.2	9.1	295	41.0	98.2	133.1	115.5	114.7	114.5	114.3	114.2	114.7	114.5	115.7	117.0
3440	1.53	385.3	297.6	2.51	395.6	429.2	31.1	285	41.0	95.7	131.3	115.1	114.1	113.3	112.4	112.3	112.5	111.8	112.4	112.6
3441	1.53	385.0	297.4	2.52	395.6	429.2	60.4	283	44.0	97.6	130.0	115.2	113.7	112.1	111.4	110.6	110.3	109.1	109.0	108.8
3442	1.52	384.9	296.1	1.81	395.9	351.7	60.4	283	49.0	85.9	118.4	98.0	98.2	98.7	99.9	100.7	100.9	100.6	100.3	103.0
3443	1.53	385.0	298.5	1.81	397.9	353.6	29.6	284	51.0	85.8	121.5	99.4	99.8	100.5	102.3	103.3	104.1	104.3	104.9	107.8
3444	1.52	383.3	295.5	1.81	397.6	353.6	9.1	294	46.0	87.5	123.8	100.3	101.4	101.9	103.9	105.4	106.4	107.1	108.8	110.6
3445	1.53	383.3	296.7	1.54	393.3	302.2	9.1	292	37.0	83.5	120.1	97.2	77.6	98.4	100.1	101.5	102.3	103.0	105.2	107.4
3446	1.53	385.1	297.1	1.53	392.8	300.3	31.1	285	37.0	81.9	117.4	96.1	96.4	96.9	98.3	99.5	99.7	99.9	101.2	102.1
3447	1.53	387.3	299.1	1.54	397.4	305.1	60.4	282	41.0	86.0	114.8	95.5	95.5	95.6	96.5	97.0	96.8	96.3	96.7	97.3
3448	1.52	389.1	297.9	1.31	400.0	243.3	60.4	282	45.0	77.4	112.1	94.5	93.9	93.5	94.0	93.7	92.7	92.2	92.7	94.7
3449	1.52	390.4	298.5	1.30	396.3	241.1	29.6	282	49.0	76.9	114.7	94.7	94.7	94.8	95.8	96.4	96.2	96.5	98.1	100.7
3450	1.53	390.8	299.3	1.30	395.4	241.0	9.1	288	45.0	80.5	116.1	95.7	95.9	96.4	97.8	98.9	99.2	100.2	103.0	107.4
3451	1.53	393.8	300.2	1.31	398.2	243.8	102.1	281	45.0	77.6	115.7	95.0	93.3	92.5	92.1	90.9	89.6	88.6	88.5	89.2
3452	1.52	394.4	300.0	1.54	397.4	303.6	101.8	280	51.0	76.9	116.9	95.7	94.9	94.5	95.0	94.4	93.7	92.6	91.4	94.1
3453	1.52	396.4	300.4	1.81	394.1	332.0	101.8	280	57.0	82.3	118.5	97.9	97.4	97.3	98.2	97.9	[illegible]	96.8	96.2	96.7*
3454	1.53	390.4	299.0	2.50	396.5	428.9	101.8	280	64.0	97.3	128.8	115.2	113.0	111.1	109.9	106.7	107.6	[illegible]	104.2	105.4
3455	1.52	399.6	300.3	3.23	395.9	475.8	101.5	280	68	104.4	135.9	121.6	120.1	118.6	117.6	116.4	115.1	112.4	110.8	110.6

APPENDIX A

PART 2

RELATIVE VELOCITY AND CONVECTIVE EXPONENTS

RELATIVE VELOCITY EXPONENTS, $n_1(\theta) = \dfrac{\Delta OASPL_\theta}{10\log\left(\dfrac{V_j - V_{to}}{V_j - V_\infty}\right)}$

Configuration	$\frac{P_t}{P_{amb}}$	T_t(°K)	θ=70	80	90	100	110	120	130	140	150
1	1.3	394	4.46		4.59		5.99		7.73		10.02
1	1.53	394	3.42	4.35	5.01	5.95	6.73	7.63	8.98	10.45	12.29
1	1.8	394	2.21		3.65		4.83		7.89		10.68
1	2.5	394	- 1.61		- 1.32		3.70		6.57		13.04
1	3.2	394	- 0.14		2.15		4.52		6.26		12.94
1	1.3	589	2.43		4.26		5.04		8.14		9.10
1	1.8	589	2.64		4.43		6.49		9.33		12.10
1	2.5	589	- 1.60		1.05		4.56		9.39		12.74
1	3.2	589	- 3.29		- 0.73		1.84		8.57		10.59
1	1.3	700	2.36		3.81		5.17		7.58		8.93
1	1.8	700	2.63		4.56		6.92		10.03		12.80
1	2.5	700	- 0.49	1.09	2.64	3.73	5.79	7.58	11.66	14.50	11.18
1	3.2	700	- 3.20		- 0.35		2.75		11.11		9.49
	$\frac{P_{tf}}{P_{amb}}$	T_{tf}(°K)									
2	1.8	394	1.68		3.35		5.03		6.95		8.15
2	2.5	394	- 1.26		1.01		3.17		6.83		8.14
2	1.8	589	3.19		4.88		6.58		9.78		15.60
2	2.5	589	- 2.41		1.99		5.77		10.48		17.69
2	1.3	700	0.92		2.91		5.17		7.91		10.04
2	1.8	700	1.08		3.11		5.61		8.35		11.42
2	2.5	700	- 1.11	0.57	2.04	3.61	5.51	7.27	8.97	10.38	11.69
2	3.2	700	- 3.56		- 0.99		3.03		8.00		11.65
2 *	1.8	700	- 1.73		1.04		4.25		9.02		13.50
2 *	2.5	700	- 1.49		1.06		5.22		11.11		14.69
3	1.8	394	1.95		3.16		5.25		8.02		12.77
3	2.5	394	- 1.21		0.17		2.62		5.72		10.88
3	1.8	589	0.65		3.55		6.12		8.31		12.60
3	2.5	589	- 1.81		1.58		5.37		8.39		13.63
3	1.3	700	2.69		4.43		2.87		4.57		8.61
3	1.8	700	0.27		2.64		5.50		7.51		11.52
3	2.5	700	- 1.59	0.14	1.35	2.68	5.04	7.15	8.43	10.39	11.98
3	3.2	700	- 2.60		0.76		4.40		7.52		13.22
4	1.8	394	1.69		2.55		5.15		7.10		9.74
4	2.5	394	0.20		2.88		4.62		7.58		9.77
4	1.8	589	2.80		4.63		6.98		9.05		12.34
4	2.5	589	2.26		5.59		8.36		9.96		14.78
4	1.3	700	0.40		1.98		3.81		5.52		6.35
4	1.8	700	1.55		3.61		6.09		8.08		10.92
4	2.5	700	0.22	2.10	3.51	4.79	6.52	8.14	9.60	11.99	13.71
4	3.2	700	- 0.81		2.62		5.75		9.30		13.64

* Fan stream alone

$$\text{CONVECTIVE EXPONENTS, } n_6 = \frac{\Delta OASPL_{\theta} - \Delta OASPL_{90^\circ}}{10 \operatorname{Log}(1 - M_{\infty} \operatorname{Cos}\theta)}$$

Configuration	$\frac{P_t}{P_{amb}}$	$T_t(^\circ K)$	θ=70	80	100	110	120	130	140	150
1	1.3	394	0.71			6.16		7.57		10.02
1	1.53	394	5.08	4.35	5.97	5.77	6.13	7.35	8.54	10.33
1	1.8	394	4.34			4.07		7.99		10.31
1	2.5	394	6.86			6.25		7.69		13.23
1	3.2	394	4.99			5.81		5.59		11.40
1	1.3	589	6.58			3.41		8.74		8.48
1	1.8	589	4.22			5.42		7.21		8.69
1	2.5	589	5.05			7.39		9.80		10.38
1	3.2	589	4.26			4.78		9.76		8.92
1	1.3	700	4.90			5.35		8.05		8.48
1	1.8	700	4.04			5.50		7.12		8.26
1	2.5	700	5.40	5.47	3.97	5.97	6.56	9.45	10.55	6.75
1	3.2	700	4.32			5.23		10.72		6.99
	$\frac{P_{tf}}{P_{amb}}$	$T_{tf}(^\circ K)$								
2	1.8	394	5.55			6.01		7.17		7.42
2	2.5	394	5.63			5.85		8.75		8.05
2	1.8	589	3.63			3.84		6.08		10.16
2	2.5	589	6.89			6.16		7.55		10.98
2	1.3	700	6.52			7.70		9.46		10.52
2	1.8	700	4.67			6.36		7.42		9.07
2	2.5	700	5.91	4.68	6.36	7.37	7.79	8.25	8.54	8.99
2	3.2	700	3.74			6.85		8.55		9.34
2 •	1.8	700	5.22			6.70		9.22		11.01
2 •	2.5	700	4.12			7.27		9.76		10.17
3	1.8	394	3.27			6.17		7.79		11.60
3	2.5	394	3.20			6.41		8.04		11.59
3	1.8	589	6.20			6.14		6.36		9.28
3	2.5	589	5.89			7.32		7.28		9.89
3	1.8	700	5.35			6.04		6.86		9.64
3	2.5	700	4.79	4.92	4.58	6.72	7.44	7.26	7.98	8.44
3	3.2	700	4.92			6.19		6.36		9.25
4	1.8	394	2.68			8.71		8.51		10.12
4	2.5	394	6.57			4.73		7.04		8.05
4	1.8	589	4.06			5.76		5.99		8.02
4	2.5	589	6.00			5.54		4.69		7.61
4	1.3	700	5.85			7.46		8.17		7.93
4	1.8	700	4.65			6.18		6.22		7.95
4	2.5	700	5.74	4.97	4.94	6.05	6.38	6.70	8.09	8.70
4	3.2	700	5.37			5.59		6.67		8.46

• Fan stream alone

APPENDIX B

SUPERSONIC SCREECH ELIMINATION

The jet noise spectra of model nozzles operating at supercritical nozzle pressure ratios often contain "spikes" or discrete tones. These intense discrete tones, commonly known as shock screech, are generated from a feedback mechanism described as follows: turbulence in the jet shear layer interacts with the flow field shock waves, giving rise to an acoustic signal, which is then "feedback" to trigger another disturbance in the shear layer. The net effect of this process is the generation of a discrete tone on the sound field. Such shock screech tones are not present in full scale engine noise spectra because the physical irregularities that exist in full scale engines greatly weaken the feedback between sound and shear layer disturbance.

Typical noise spectra of the convergent nozzle operating at the various nozzle pressure ratios are shown in Figure B-1a and b for the 90° and 150° angles, respectively. It can be seen that the screech tones are not present for the subsonic jet condition. In the supersonic jet condition, the screech tones can be easily identified, and normally are present at two frequencies, the fundamental and first harmonic. The fundamental frequency of the screech tone from a convergent nozzle is given by the following relationship (Ref. B-1):

$$f = \frac{c}{3d\,(PR-1.89)^{1/2}}$$

where "f" is the frequency, "d" is the nozzle diameter, "PR" is the nozzle pressure ratio and "c" is the speed of sound. The measured screech frequencies at pressure ratios 2.5 and 3.2 agreed reasonably well with predictions from the preceding equation. These screech tones, in general, appear very intense along the side angles (80° - 110°) where the jet mixing noise is relatively low. At higher jet temperatures, for a given pressure ratio, the shock screech tones are not as dominant because of the increase in jet mixing noise caused by the higher jet velocity.

The noise spectra of a higher temperature jet demonstrating this effect are shown in Figures B-2a and b. The effects of relative velocity on the shock screech tones are shown in Figures B-3a and b for the 90° and 150° microphones, respectively. With relative velocity, it can be seen that the screech tones are amplified and broadened at the 90° angle. This effect is similar to the amplification of the broadband shock noise in the relative velocity field as described in Section 5.1. Since screech tones are not present in full scale engine noise the amplification and broadening of such tones would not simulate the noise characteristics in flight. Therefore, in order to obtain experimental results applicable to full size engines, an analytical and experimental investigation was conducted to study ways of eliminating the supersonic screech tone.

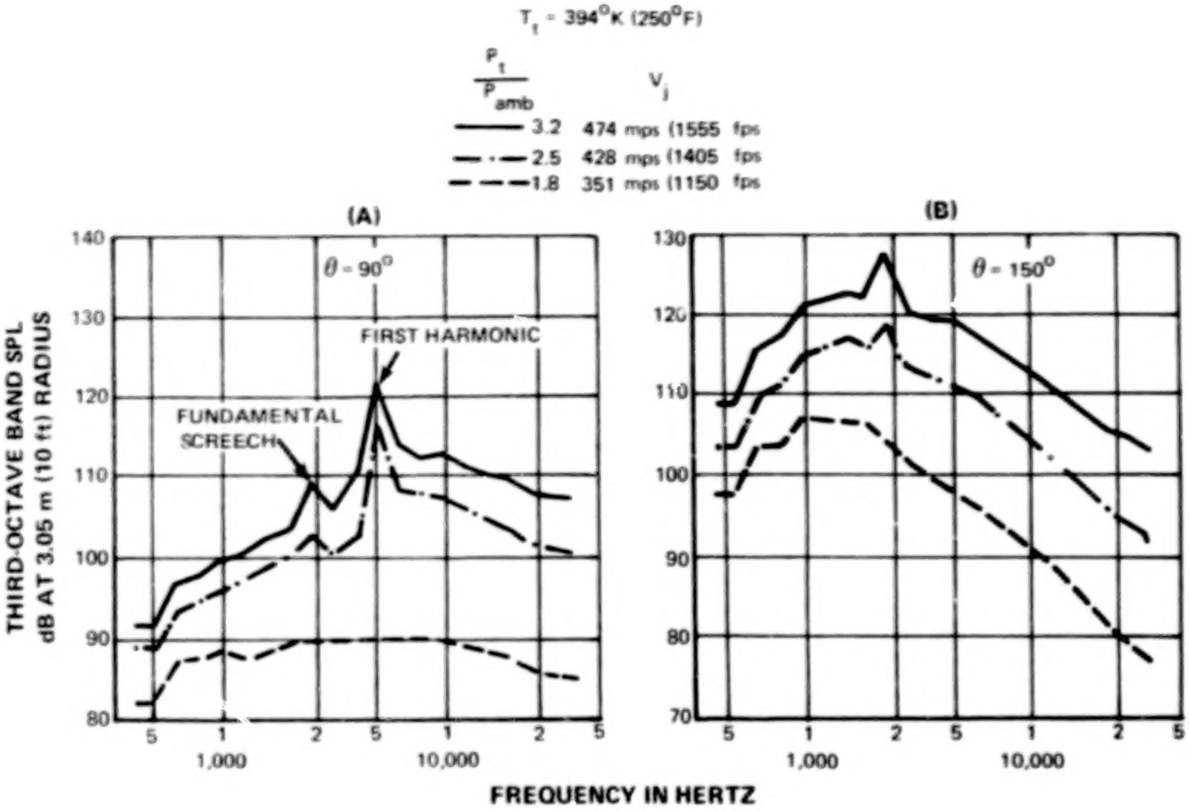

Figure B-1 *Effect of Screech Tone On SPL Spectra of Convergent Nozzle At a Jet Temperature of 394° K (250° F)*

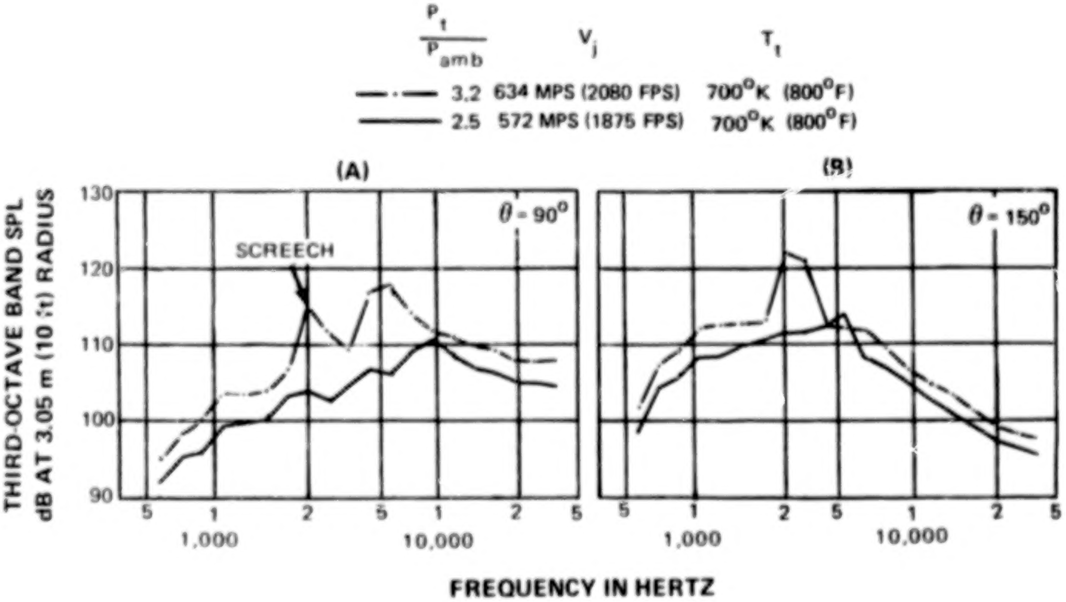

Figure B-2 *Effect of Screech Tone On SPL Spectra of Convergent Nozzle At a Jet Temperature of 700° K (800° F)*

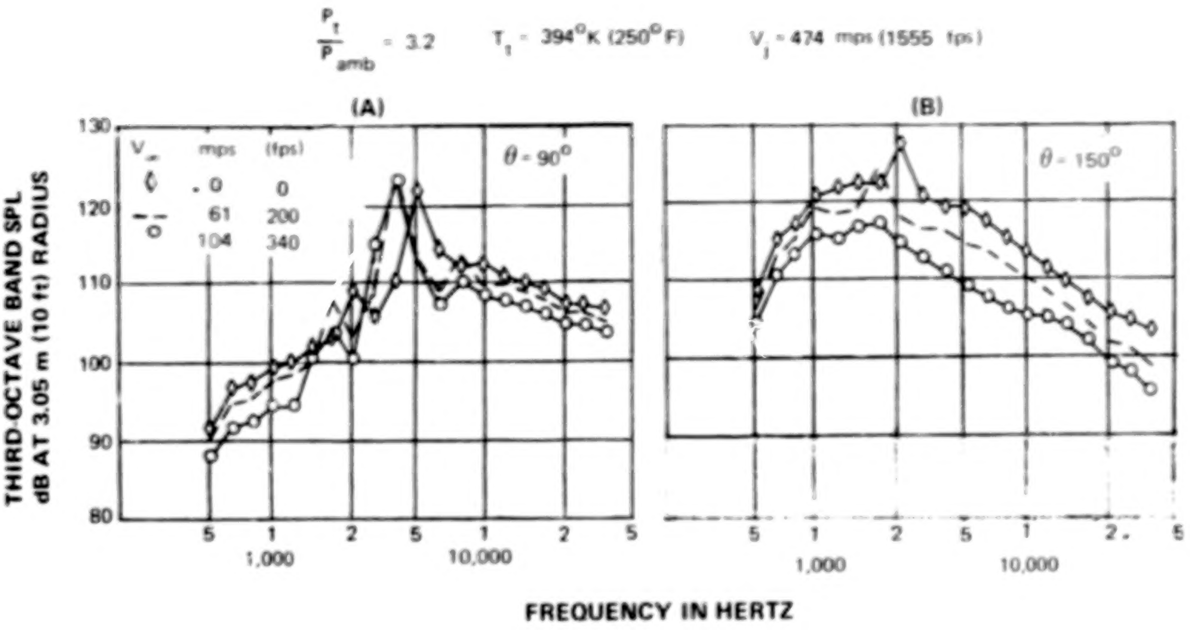

Figure B-3 *Effect of Relative Velocity On Shock Screech Tone of Convergent Nozzle Operating At Supercritical Nozzle Pressure Ratio*

The screech tones could be removed analytically by smoothing the noise spectra containing the tone. However, several problems and disadvantages are inherent in this approach. In the static condition, the tones can be easily removed because the tones are well defined. But in the flight case, the broadening of such tones makes the smoothing process more difficult and subject to individual interpretation. Also, based on previous results by Lockheed-Georgia (Ref. B-2) and DFVLR – Institute for Turbulent Research (Ref. B-3) suppression of screech tones in a jet result in changes to the broadband noise spectra. This change occurs because broadband mixing noise is found to be enhanced by the screech tone. Results from Reference B-2 demonstrating this effect are shown in Figure B-4. Thus, the interaction between the screech tone and the broadband noise makes the process of analytical smoothing extremely difficult since effects of interaction phenomenon must be known before the data can be properly corrected.

Experimentally, the screech tone can be eliminated by simulating full scale nozzle irregularities through the use of nozzle lip modifications. This has the advantage of suppressing the screech tone and the interaction between screech and the broadband noise. Various nozzle lip modifications were tested in order to determine the lip changes which would eliminate the screech tone and at the same time have negligible effect upon the jet subsonic noise spectrum, where screech effects are non-existant. Schematics of these changes are shown in Figure B-5. Two types of modifications were investigated: tabs which protruded into the jet flow, and tabs which impinged on the edge of, but did not protrude into the jet flow. In principle, these lip modifications destroyed the azimuthal symmetry of the flow structure and thus minimized the screech tone feedback mechanism. Typical results of the screech suppression with tabs protruding into the jet flow are shown in Figures B-6a and b. Generally, the tabs eliminated the screech tone successfully, but in varying degree, reduced the low frequency broadband jet mixing noise and increased the high frequency

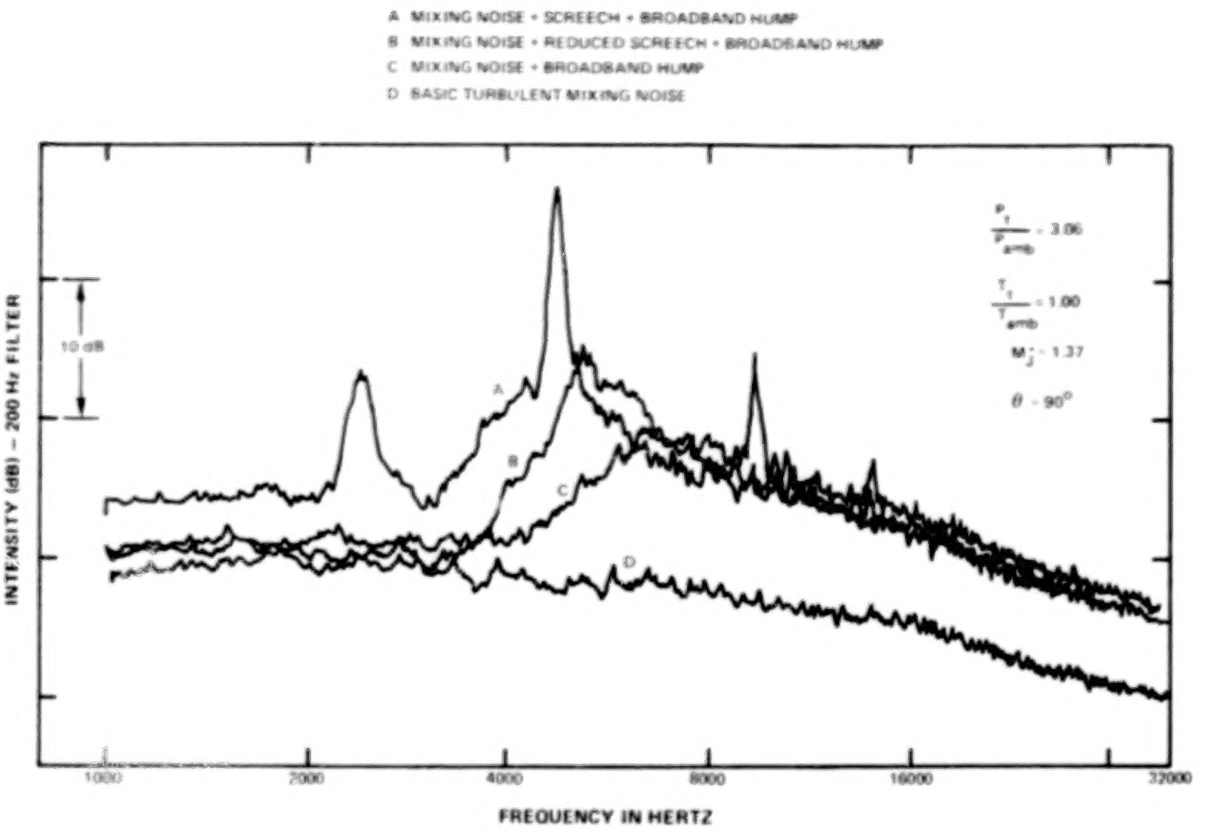

Figure B-4 *Effect of Shock Screech Tones On Broadband Noise Spectra*

noise slightly. The reduction in the low frequency jet mixing noise is probably due to an enhanced mixing process similar to the effect of multi-element jet suppression nozzles, whereas the increase in high frequency noise is associated with the generation of aerodynamic noise from the tabs. The results also show that the size and orientation of the tab has a significant effect on the noise spectra because of asymmetric jet plume development as discussed in Reference B-4. Results of lip modifications based on tabs which impinged on the edge of, but did not protrude into the jet flow are shown in Figures B-7a and b. These lip irregularities eliminated the screech tone successfully and showed less distortion on the noise spectra as compared with the protruding tabs configurations. The noise spectra of these lip irregularities also exhibited reduced low frequency broadband jet mixing noise while the high frequency noise was increased. The reduction in the low frequencies is similar to the results from References B-2 and B-3 in that the suppression of the screech tone results in changes to the low frequency broadband noise. The slight increase in the high frequency noise is probably due to the generation of aerodynamic noise associated with the lip irregularities. Among the nonprotruding lip modifications, the 0.25 cm (0.1 in) edged lip (i.e., modification #6, Figure B-5) showed the least distortion on the noise spectra while at the same time completely eliminating the tones.

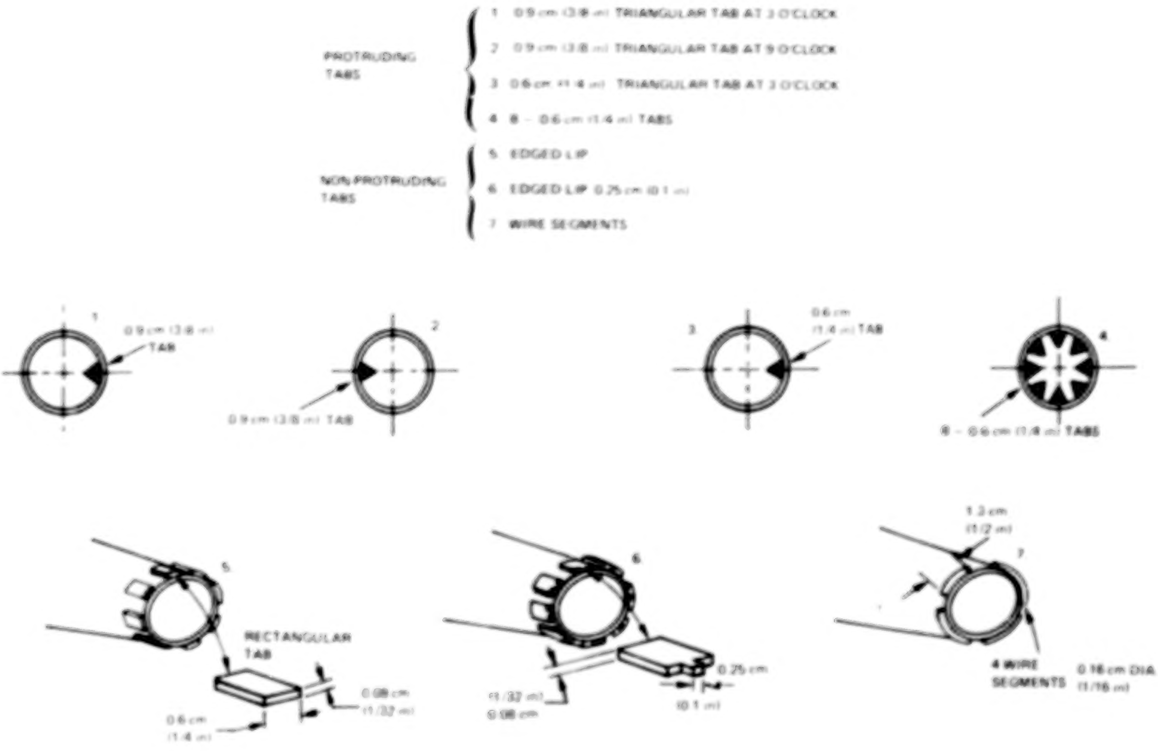

Figure B-5 *Schematic of Various Nozzle Lip Modifications Evaluated for Screech Tone Suppression*

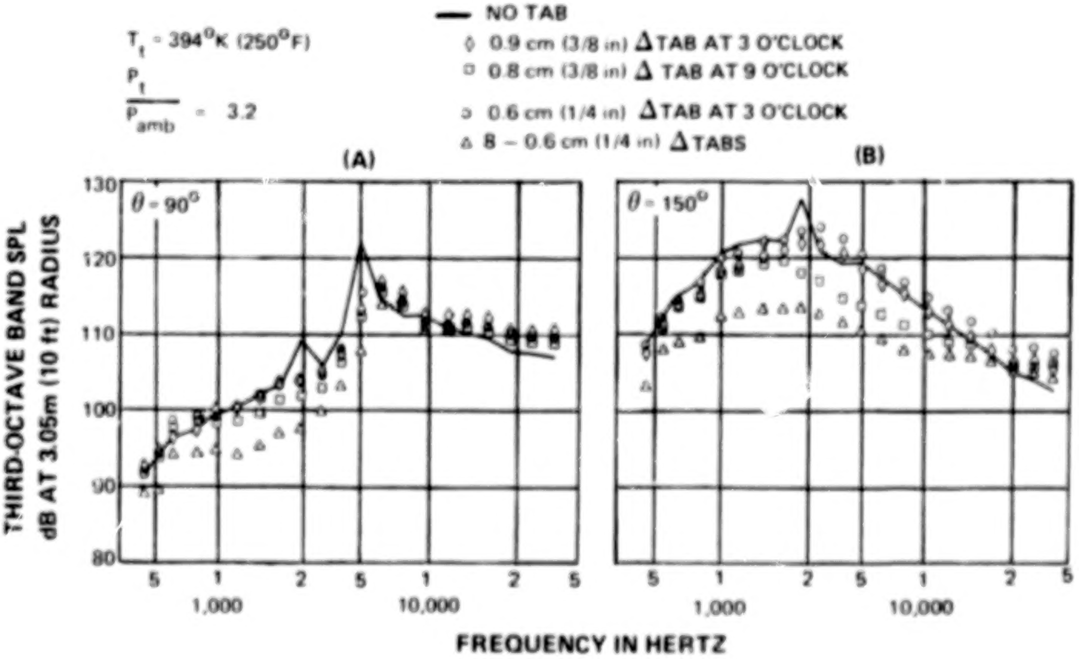

Figure B-6 *SPL Spectra of Lip Modification With Tabs Protruding Into Jet Flow*

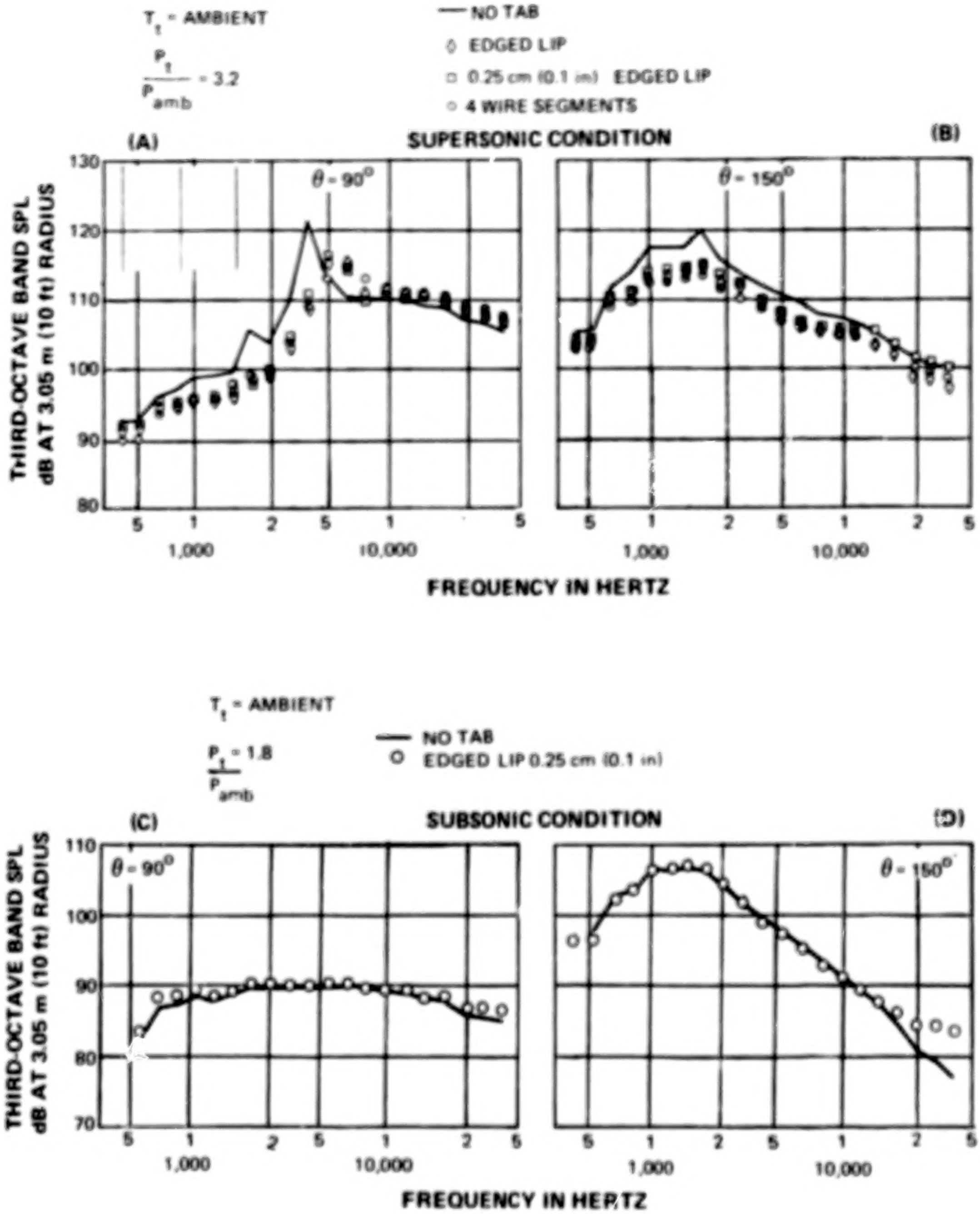

Figure B-7 SPL Spectra of Lip Modification With Tabs Not Protruding Into Jet Flow

The noise spectra of the 0.25 cm edged lip configuration were compared to the data from the configuration without tabs in the subsonic (no screech) condition. As shown in Figure B-7c and d, the 0.25 cm edged lip noise spectra agreed well with the configuration without tabs except at the high frequencies where a slight increase was caused by the generation of aerodynamic noise associated with the lip irregularities. From the results of these studies, a lip modification (0.25 cm edged-lip) of eight small rectangular tabs (designed to not protrude into the flow) placed symmetrically on the nozzle lip shown in Figure B-8 was selected for the test program.

The lip modification used on the reference convergent nozzle was also used on the fan nozzle lip of the three coannular nozzle configurations tested in this program. The effect of the modifications on the noise spectra was similar to the results obtained on the reference convergent nozzle.

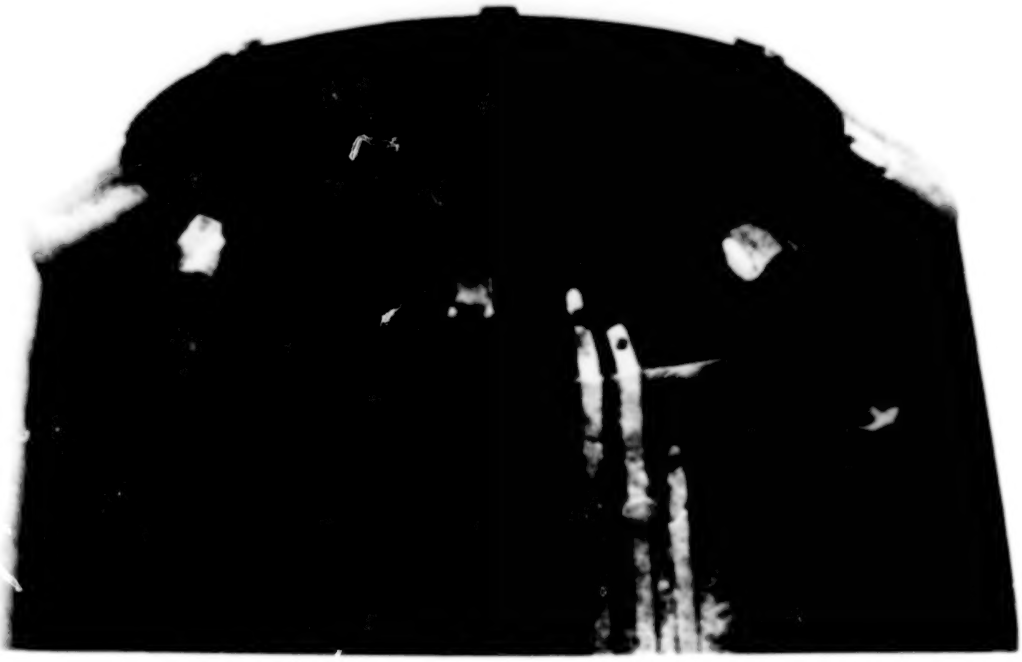

Figure B-8 Nozzle Lip Modification for Shock Screech Tone Elimination

REFERENCES

B-1. Powell, A., "On the Mechanics of Choked Jet Noise," Proc. Physical Society, B, Vol. LXVI, pp. 1039-1056, 1953.

B-2. Lockheed-Georgia Co., "Fifth Oral Briefing for a Supersonic Jet Exhaust Noise Investigation," 17 October 1975.

B-3. Bechert, D., and Pfizenmaier, E., "On the Amplification of Broadband Jet Noise by a Pure Tone Excitation," Journal of Sound and Vibration (1975) 43 (3) 581-587.

B-4. Bradbury, L. J. S., and Khadem, A. H., "The Distortion of a Jet by Tabs," Journal of Fluid Mechanics, Vol. 70, Part 4, pp. 801-803, 1975.

APPENDIX C

THEORETICAL DAY ATMOSPHERIC ABSORPTION CORRECTION

The as-measured data, after cable and microphone response corrections, were transformed to the "theoretical day" by applying the values of atmospheric absorption defined in Reference C-1. This procedure entails adding a ΔSPL as a function of frequency, relative humidity, ambient temperature and microphone distance, to the measured SPL. The ΔSPL corrections represent an estimate of the absolute sound absorption for noise in each of the one-third octave bands. The resulting "theoretical day" data represents the noise that would be measured if no noise were lost by the atmospheric absorption process. Model data presented in this manner can theoretically be scaled to represent the noise of any size engine and extrapolated to any distance. As discussed in Section 4.2, for typical test conditions the corrections at the very high frequencies (i.e., above 40K Hz) are quite large. At 80K Hz under a typical test condition (RH =50% , temp = 28[illegible]°K), nearly 77% of the acoustic energy is attenuated by atmospheric absorption. The corrections defined in Ref. C-1 are in general agreement up to 100K Hz with the results of recent experiments in Ref. C-2, although appreciable deviations have been noted for certain ambient conditions. Therefore, the procedure of Ref. C-1 was used to determine the atmospheric corrections required to correct the data to a "theoretical day".

A typical as-measured noise spectrum for the reference convergent nozzle operating at subsonic conditions is shown in Figure C-1, along with the spectra corrected to a "theoretical day". Also shown is the expected roll-off slope based on the prediction method of Stone[C-5]. Note that the data corrected to "theoretical day" contain an uplift at the very high frequencies. The correction at 80K Hz was approximately 7 dB for this test case. In general, the "theoretical day" noise spectra for most test conditions have an uplift at the high frequencies similar to that shown on Figure C-1. (It should be noted that the as-measured spectra *do not* have an uplift, except at the extreme aft angle (θ_i = 150°) where the large roll-off slope of jet noise is extremely large and the tape recorder dynamic range was exceeded.)

The actual measured electronic floor noise of the measurement system is also shown in Figure C-1 for the system in the identical operating mode used in the sample test case shown. The electronic floor noise was measured with the system amplifiers and/or attenuators at the same settings as used in the specific test, but with the microphones capped thus producing the same system electronic noise as was present during the actual test data recording. It is apparent that the electronic noise was much too low to cause any affect on the measured data at any frequency.

The high frequency noise uplift in the "theoretical day" spectra is also found in model jet data from other nozzle configurations tested in other facilities (e.g., Ref. C-3).

Several experiments were conducted to show that measurement system errors were not responsible for the up-lift phenomenon. The experiments included electronic system response investigation, and tests of microphone size and distance.

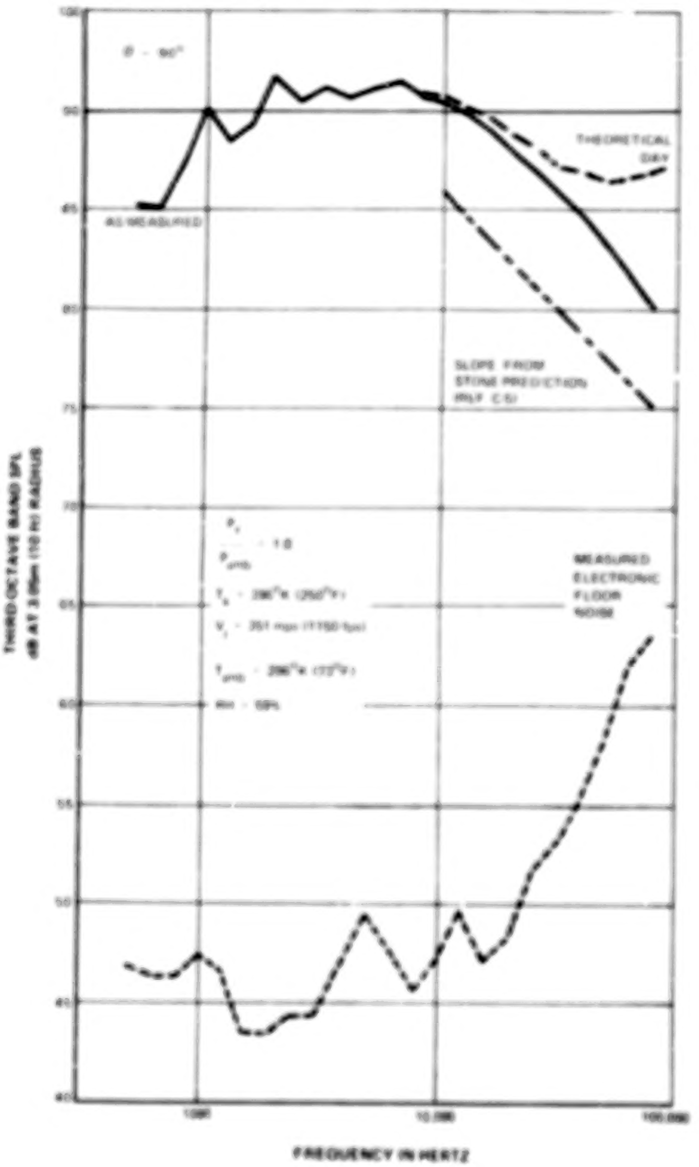

Figure C-1 *Typical Atmospheric Absorption Correction of As-Measured SPL Spectrum to a Theoretical Day*

The microphone system response investigation was conducted by utilizing the recording system used in the test program. The microphone was first removed from the field effect transistor (FET) follower. A 1 volt, 250 Hz sine wave signal was applied through the microphone insert device to establish a reference sound pressure level. Then a broadband white noise signal (equal energy per cycle) was inserted and recorded. The noise signal inserted ranged from 0 to 100K Hz and increased at the rate of 1 dB per one-third octave band. Following the recordings, the tape was analyzed in the same manner as the acoustic data, including application of corrections for system and cable response. Figure C-2 shows the results of the system response investigation.

TABLE OF CONTENTS

Section	Title	Page No.	
1.0	SUMMARY	1	1/B4
2.0	INTRODUCTION	3	1/B6
	2.1 Background	3	1/B6
	2.2 Program Description	4	1/B7
3.0	APPARATUS	6	1/B9
	3.1 Acoustic Wind Tunnel	6	1/B9
	3.1.1 Adapter Section	8	1/B11
	3.1.2 Instrumentation Section	9	1/B12
	3.1.3 Exit Plane Traverse Instrumentation	10	1/B13
	3.1.4 Acoustic Instrumentation	11	1/B14
	3.2 Aerodynamic Wind Tunnel	12	1/C1
	3.3 Nozzle Configuration	14	1/C3
	3.3.1 Reference Convergent Nozzle	14	1/C3
	3.3.2 Coannular Nozzles	15	1/C4
	3.3.3 Ejector	17	1/C6
4.0	DATA	18	1/C7
	4.1 Aerodynamic Data Reduction	20	1/C9
	4.1.1 Thrust Coefficients and Flow Coefficients	26	1/D1
	4.1.2 Surface Static Pressure	27	1/D2
	4.1.3 Exit Profiles and Ejector Inlet Total Pressures	28	1/D3
	4.2 Acoustic Data Reduction	31	1/D6
	4.3 Comparison With Outdoor Results	46	1/E12
	4.4 Coannular Noise Synthesis	51	1/F3
5.0	RESULTS AND DISCUSSION	53	1/F5
	5.1 Discussion of Acoustic Results	53	1/F5
	5.1.1 Acoustic Results	53	1/F5
	5.1.2 Correlation of OASPL Noise Reduction with Relative Velocity Exponents	82	2/A8
	5.1.3 Velocity Profile Correlation	109	2/C7
	5.2 Application of Acoustic Results	113	2/C11
	5.2.1 Comparison of Results with Synthesis	114	2/C12
	5.2.2 Results Scaled to Full Size	120	2/D4
	5.2.3 Application of Results to SCAR Noise Predictions	123	2/D7
	5.3 Aerodynamic Performance	131	2/E1
	5.3.1 Convergent Nozzle	131	2/E1
	5.3.2 Coannular Nozzles	132	2/E2
	5.3.3 Flow Coefficients	136	2/E6
6.0	SUMMARY OF RESULTS	140	2/E10
	6.1 Acoustic Results	140	2/E10
	6.2 Aerodynamic Performance Results	141	2/E11

TABLE OF CONTENTS (Cont'd.)

Section		Title	Page No.	
REFERENCES			143	2/E
APPENDIX A			145	2/F
	Part 1	Model Scale Overall Sound Power Level and Overall Sound Pressure Level Directivity on Theoretical Day	145	2/F
	Part 2	Relative Velocity and Convective Exponents	153	2/G
APPENDIX B		Supersonic Screech Elimination	155	2/G
APPENDIX C		Theoretical Day Atmospheric Absorption Correction	163	2/G
APPENDIX D		Shear Layer Refraction Correction	170	3/A
LIST OF ABBREVIATIONS			180	3/B

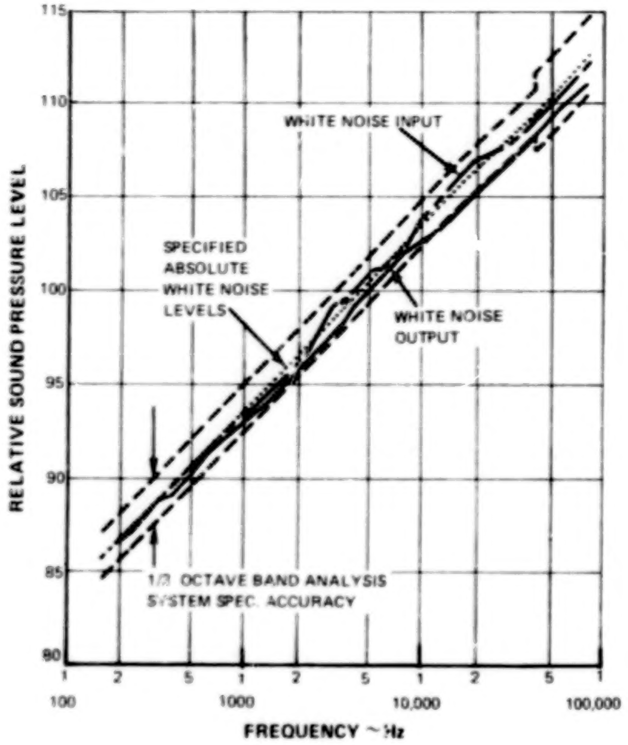

Figure C-2 Microphone System Response Verification

The specified accuracy limit of the one-third octave band analysis system is illustrated in Figure C-2. Deviations between these limits are not meaningful. The specified output of the white noise generator is also illustrated as a straight line. The actual output of the white noise generator is seen to be within ±1 dB of the specified output. The output of the white noise signal, after passing through the entire electronic system, was recorded, analyzed by the one-third octave band analyzer and corrected for cable calibration values. As can be seen, the final white noise output falls within the analyzer accuracy limits for all frequencies. In particular, no up-lift is present at the high frequencies. Based on these results, it can be concluded that the electronic system used to record and analyze the noise measurements in this program was not responsible for the presence of the high frequency up-lift present in some of the data.

Microphone diaphragm frequency response was also investigated as a possible cause for the high frequency up-lift. Although all microphones were calibrated by a procedure traceable to the National Bureau of Standards, as described in Section 4.2, an additional test was done to verify that the microphones were measuring properly.

The B&K #4135 0.006 m (1/4 in) microphones used in the test program are specified to have flat (< ±1 dB) response at normal incidence to above 80K Hz (Ref. C-4). The B&K #4138, 0.003 m (1/8 in.) microphones are specified to have a flat (< ±1 dB) frequency response to above 120K Hz (Ref. C-4).

To determine if the 0.006 m microphones were producing erroneous high frequency levels causing the high frequency up-lift, two 0.003 m microphones were used to measure data simultaneously with the 0.006 m microphones. If the results from the different microphones were similar, the larger microphones could be considered to be functioning properly due to the different frequency response characteristics of the two size microphones used. Thus, two B&K #4138 0.003 m microphones were placed at the 90° and 150° angles 0.05 m (2 in) below the B&K #4135 0.006 m microphones. Results obtained from the 0.006 m and 0.003 m microphones at the 90° angle with the same nozzle operating condition are shown in Figure C-3. The noise levels recorded by the 0.003 m microphone is lower than those of the 0.006 m microphone for all frequencies. The difference of about 1 dB is within the microphone accuracy specification (Ref. C-4). The similarity in spectral shape measured by the two different size microphones excludes the microphone response as being responsible for the high frequency up-lift phenomenon.

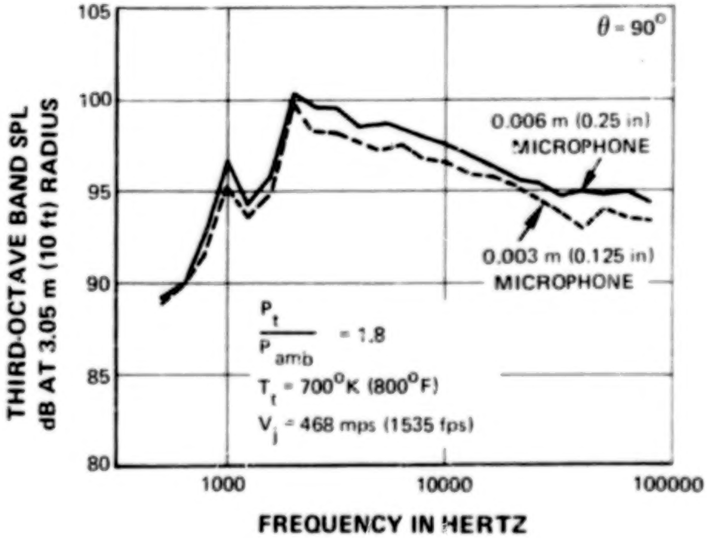

Figure C-3 *Comparison of SPL Spectral Shape Measured by Two Different Size Microphones*

Another test was made to determine if the atmospheric absorption corrections would produce consistent data for varying microphone measuring distances. If the absorption corrections are accurate, the noise measured at any distance (if in the acoustic and geometrical far field) and corrected to theoretical day would exhibit the same spectral shape. A simple spherical divergence correction for distance differences would then produce spectra having the same shape and level.

The effect of microphone distance on the measured data was evaluated by placing the 90° microphone at distances of 0.61 m (2 ft) and 1.22 m (4 ft) away from the nozzle exit. Data at these distances was then compared, after correction for atmospheric absorption. At these relatively close distances (0.61 m and 1.22 m), only the noise at the higher frequencies are considered to be in the geometric and acoustic far field. Thus, only high frequency comparisons can be made. The measurements for each microphone were first corrected for atmospheric absorption, at the appropriate distances, using the corrections as defined in Ref. C-1.

Then, the levels were extrapolated to 3.05 m by the spherical divergence relationship: ΔSPL = 20 Log (R/3.05), where R is the microphone distance. Results of such comparisons are shown in Figures C-4 and C-5 for the 0.61 m and 1.22 m microphone respectively along with the electronic noise spectra of the system which are well below the measured data at all frequencies. The 3.05 m microphone distance noise spectrum represents typical data which show the high frequency uplift. Measurements at the 0.61 m and 1.22 m do not show this uplift phenomenon. From these comparisons, it can be seen that the uplift problem becomes significant as the measuring distance increases. This is not surprising because the atmospheric correction is proportional to the microphone distance. From this simple experiment, it can be concluded that the atmospheric absorption corrections of Ref. C-1 cannot be extended accurately to frequencies above 50K Hz. A final test was conducted to investigate the possibility that the microphone supports might cause a reflection of sound. This was accomplished by covering the 130° microphone support rod and FET follower with sound absorbing material. Results showed no evidence of noise reflection from hardwall surfaces.

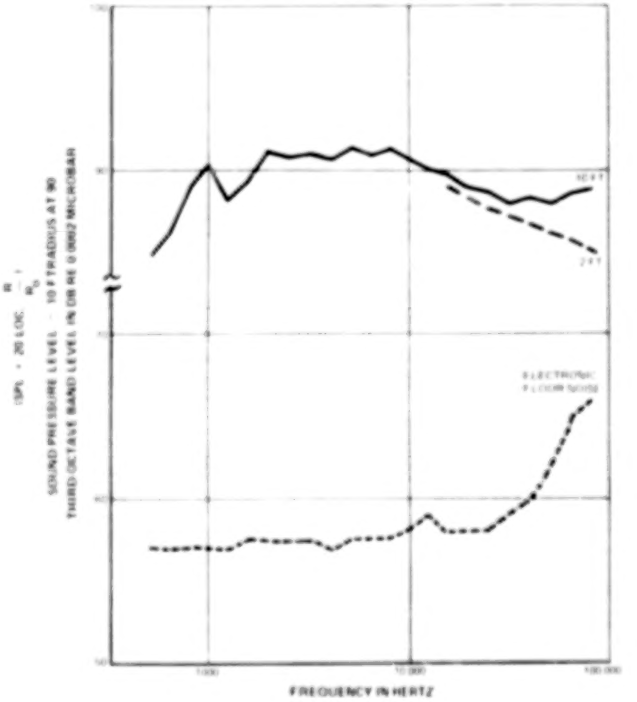

	RUN NO	V_p (fps)	T_p °F	V_1 (fps)	T_1 °F	V_t (fps)
	3864	1159	253	-	-	STATIC
RH = 41%						
$T_{CHAMBER}$ = 72°F						

R_o = 10 FT
R_m = 2 FT

THEORETICAL DAY CORRECTIONS APPLIED
TO MICROPHONE DISTANCE

Figure C-4 *Comparison of SPL Spectral Shape At Microphone Distance of 3.05 M (10 ft) and 0.61 M (2 ft)*

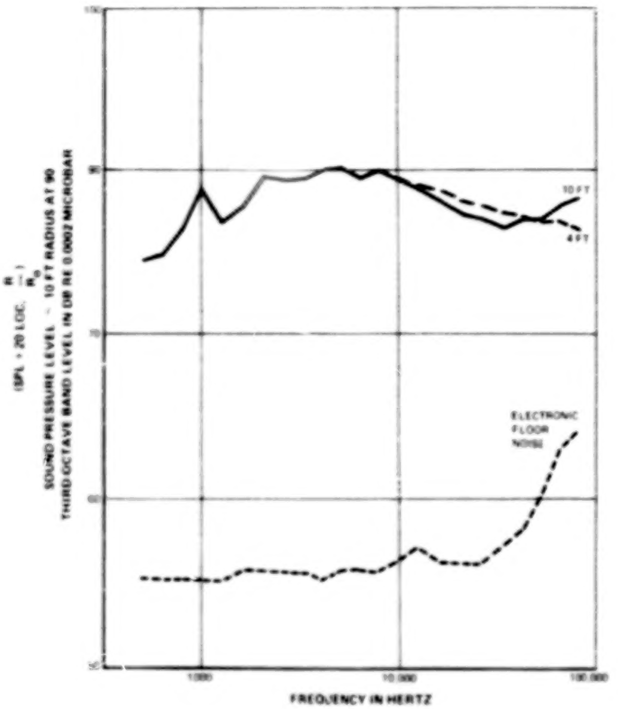

	RUN NO	V_p (fps)	T_p °F	V_s (fps)	T_s °F	V_t (fps)
	3665	1159	253	–	–	STATIC
RH = 25%						
$T_{CHAMBER}$ = 113°F						

R_o = 10FT
R_m = 4FT

THEORETICAL DAY CORRECTIONS APPLIED TO MICROPHONE DISTANCE

Figure C-5 Comparison of SPL Spectral Shape At Microphone Distances of 3.05 M (10 ft) and 1.22 M (4 ft)

The investigations described above appear sufficient to exclude the possibility of system or measurement technique errors as contributing to the high frequency uplift present in some of the "theoretical day" data. If the measured noise is an accurate representation of the no noise existing at the microphone location, then other factors are responsible for the theoretical day uplift problem. One possibility is that the atmospheric absorption corrections determined by the procedure of Ref. 1 are not adequate to describe the acoustic losses present in jet noise tests. A second possibility is that additional noise sources at very high frequencies may be present in small scale model tests.

Based on the results of the experimental investigations into the possible causes of the high frequency uplift present in some of the "theoretical day" data, that the presence of the uplift at angles other than the extreme aft locations is not due to the acoustic measurement system, but is caused by some other factor.

REFERENCES

C-1 Society of Automotive Engineers: Aerospace Recommended Practices ARP 866A, March 15, 1975.

C-2 Bass, W. E., Shields, F. D., "Atmospheric Absorption of High Frequency Noise and Application to Fractional Octave Bands", University of Mississippi, NASA CR-2760, June 1977.

C-3 Heck, P. N., et al: "Acoustic Tests of Duct-Burning Turbofan Jet Noise Simulation", CDR to be released under NAS3-18008.

C-4 Broch, J. T., "The Application of B&K Measuring Systems to Acoustic Noise Measurements", July 1970.

C-5 Stone, J. R.: Interim Prediction Method for Jet Noise, NASA TMX-71618, 1975.

APPENDIX D

SHEAR LAYER REFRACTION CORRECTION

Roy K. Amiet
Senior Research Engineer, Aeroacoustics Group
United Aircraft Research Laboratories
East Hartford, Connecticut

Abstract

The problem of sound refraction by a plane, zero thickness shear layer is treated by combining a previous solution of Ribner and Miles with geometrical acoustics. Analytical expressions are given which allow one to correct far-field measurement angle and acoustic amplitude for the effects of shear layer refraction. The correction is independent of source type and the results represent the sound field one would expect to measure in a flow which has a free stream extending to infinity. Preliminary experimental results are in basic agreement, but further tests are necessary to definitely establish the theory.

List of Symbols

h	Distance of source from shear layer
$\hat{i}, \hat{j}, \hat{k}$	Unit vectors in the x,y,z directions, respectively
M	Tunnel Mach number
P	Pressure
r	Source - microphone distance
x_0	Axial distance from source to point at which sound ray crosses shear layer
y_1	Microphone distance above sound source
z_1	Separation between layers of double shear layer
α	Angle between wave fronts and shear layer; measured just below the shear layer
β	$\sqrt{1-M^2}$
ζ	$\left\|(1-M\cos\alpha)^2 - \cos^2\alpha\right\|^{1/2}$
θ	Angle between shear layer and ray propagation direction above shear layer
θ'	Angle corrected for shear layer effect
θ_0	Value of θ which begins zone of silence
λ	Wavelength
ξ	Parameter defined by Eq. (10a)
Θ	Phase
σ	$\sqrt{x^2+\beta^2(y^2+z^2)}$
ω	Circular frequency

Subscripts

A,B,C,D	Points defined in Fig. 1
i	Incident
m	Measured
r	Reflected

Introduction

In studying the effect of flight speed on a sound source such as a compressor or a jet exhaust, it is necessary to obtain accurate experimental data under controlled conditions. An open-jet anechoic wind tunnel such as those located at United Aircraft Research Laboratories, NASA Langley, NSRDC Carderock, among others, can be used to generate such data. Sound reflection from the walls, which is a problem with closed section tunnels, is eliminated by the use of an anechoic chamber, and the problem of extraneous noise due to flow interaction with microphones is avoided since the microphones are outside the stream. However, the open-jet tunnel does have the disadvantage that the sound produced by the device being tested must pass through the jet shear layer before being sensed by a microphone outside the flow. In crossing the shear layer the sound is refracted, an effect that becomes more important as the Mach number is raised. Also, scattering from the turbulence in the shear layer may occur.

Several previous studies, Refs. (1 through 7) for example, have been conducted on this problem. These, however, generally have considered a specific type of sound source near a shear layer and have calculated a corresponding directivity curve rather than addressing the general problem of correcting any sound source such as a combination of monopoles, dipoles, etc. Reference 8 proceeds along the lines of geometrical acoustics as done here. However, Ref. 8 uses the technique for calculating the directivity pattern produced by a given source in the presence of a shear layer rather than arriving at a method for correcting acoustic tunnel measurements independent of source type. Because the present study corrects both the sound amplitude and the measurement angle, it can be applied to a general source.

Theoretical Development

The modeling of the problem is shown in Fig. 1. The observer is at a distance y_1-h above the shear layer, and the sound source is a distance h below the plane, zero-thickness shear layer. There is no restriction on the size of h. The observer is assumed to be in both the geometrical and acoustic far-field of the source; i.e., the source-observer distance is significantly greater than both the source dimensions and the acoustic wavelength. Both the source and observer are assumed to be in a plane normal to the shear layer and parallel to the flow. The line connecting the source and the observer makes an angle θ_m with the shear layer. The measured angle θ_m goes to zero as the observer moves downstream and to π as the observer moves upstream. The actual path of a sound ray is represented by the line SCO which below the shear layer makes an angle θ' with the shear layer and above the shear layer an angle θ. The change from θ' to θ as the sound passes through the shear layer is a result of refraction by the shear layer. The fluid densities above and below the shear layer are assumed to be the same. (This assumption could be eliminated, but the results would be somewhat more involved.) There is little change in density across the shear layer of the UARL Acoustic Research Tunnel. The Mach number M is assumed uniform below the shear layer and zero above it.

If the shear layer had not been present so that the uniform Mach number M continued out to infinity the sound on reaching the former position of the shear layer would continue to propagate rectilinearly, following the dashed line in Fig. 1 rather than the solid line. Thus, the sound heard at position O in the presence of the shear layer would be heard at position A or B in the absence of the shear layer. If one wishes to correct the data to an equivalent sideline position, the sound would be heard at A in the absence of the shear layer, while if one wanted to correct the data to an equal radial distance from the source, point B would be used.

The method of the derivation is to use geometrical acoustics together with the solution of Ribner for the transmission and reflection of sound by a plane zero-thickness shear layer. The sound measured at the observer point O is traced back by geometrical acoustics to point C+ just above the shear layer. Knowing the amplitude at point C+, Ribner's results are used to cross the shear layer giving the amplitude at point C- just below the shear layer. The amplitude at point A or B that would exist in the absence of the shear layer can then be obtained from the sound level at C- by noting that sound pressure decays inversely as the distance from the source. Thus, the pressure that would exist at point A would be the pressure at point C- times the ratio of distances of the source from points C and A.

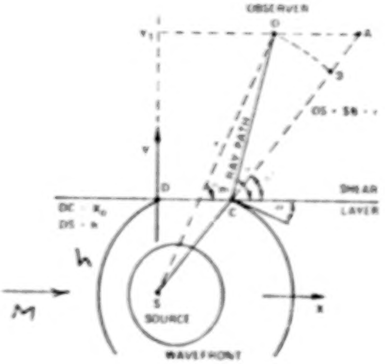

FIGURE 1 ACOUSTIC SOURCE BENEATH PL...
ZERO-THICKNESS SHEAR LAYER

It should be pointed out that it is not necessary for point C to be in the far field of the source. When the sound measured at point O is used to calculate the sound at point C, only the far-field component can be calculated since point O is assumed to be in the far-field. Thus, an actual measurement of the sound at point C might not agree with the value given here unless one were able to separate out the near and far-field parts of the measurement.

The details of the derivation are given in Appendix I. The resulting correction equations are given below.

$$\begin{aligned} \tan\theta' &= \zeta/(\beta^2\cos\theta + M) \\ y_1\cot\theta_m &= h\cot\theta' + (y_1 - h)\cot\theta \end{aligned} \qquad (1a)$$

$$\zeta = \left[(1 - M\cos\theta)^2 - \cos^2\theta\right]^{1/2} \qquad (1b)$$

$$\begin{aligned} \frac{P_A}{P_m} = &\left\{\frac{h}{\zeta^2 y_1}\left[\sin\theta + \left(\frac{y_1}{h} - 1\right)\zeta\right]^{1/2}\left[\sin^3\theta + \left(\frac{y_1}{h} - 1\right)\zeta^3\right]^{1/2}\right\} \\ &\cdot \frac{\zeta}{2\sin^2\theta}\left[\zeta + \sin\theta(1 - M\cos\theta)^2\right] \end{aligned} \qquad (2)$$

$$\begin{aligned} \frac{P_B}{P_m} = &\left\{\frac{h\csc\theta}{r\zeta^2}\left[\sin\theta + \left(\frac{y_1}{h} - 1\right)\zeta\right]^{1/2}\left[\sin^3\theta + \left(\frac{y_1}{h} - 1\right)\zeta^3\right]^{1/2}\right\} \\ &\cdot \frac{1}{2\sin\theta}\left[M^2(1 - M\cos\theta)^2 + (1 - M^2\cos^2\theta)\right]^{1/2}\left[\zeta + \sin\theta(1 - M\cos\theta)^2\right] \end{aligned}$$

$$(3)$$

The first two equations give θ' in terms of θ_m. The angle θ could be eliminated giving a single equation relating θ' to θ_m, but for simplicity of expression θ is left as a parameter here. Equation (2) gives the corrected pressure P_A at an equal sideline distance while Eq. (3) gives the corrected pressure at an equal radial distance from the source. Again, θ appears as a parameter in these equations and is related to θ_m by Eqs. (1).

When the observer is far from the shear layer so that $y_1 >> h$, Eq. (1b) gives $\theta_m = \theta$ and Eq. (1a) becomes

$$\tan\theta' = \zeta_m/(\beta^2\cos\theta_m + M) \qquad y_1 >> h \qquad (4)$$

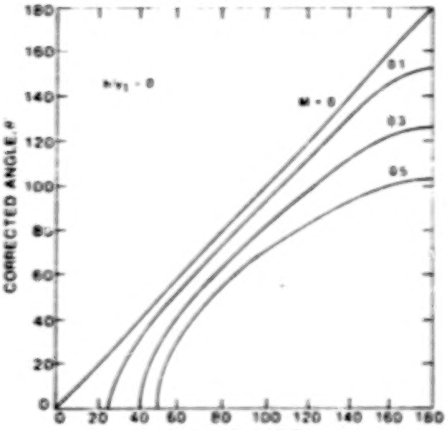

FIGURE 2. CORRECTION OF ANGLE θ_m WITH $h/y_1 = 0$

One of the major simplifying assumptions used in this derivation is that there is only a single layer when in fact the open jet has an upper and a lower shear layer with the sound source in the middle. For the present results to be applicable, the reflection from the lower shear layer should be negligible. The ratio of reflected pressure to incident pressure for the case of a plane wave incident on a plane zero-thickness shear layer was given by Ribner (Ref. 1) as

$$\frac{P_r}{P_i} = \frac{\zeta - \sin\theta(1 - M\cos\theta)^2}{\zeta + \sin\theta(1 - M\cos\theta)^2} \tag{9}$$

This is plotted in Fig. 9 which shows that except for angles near the zone of silence and angles near 180 deg, the amplitude of the reflected wave is small. Thus, if the observer is not near one of these two limits, the lower shear layer would be expected to have little effect.

One additional important assumption was that the thickness of the shear layer could be ignored. Graham and Graham (Ref. 5) made a calculation of the sound transmission through two plane, zero-thickness shear layers a distance z_1 apart. This example should give some idea of the effect of finite thickness on shear layer transmission. Figure 10a shows the problem which consists of two shear layers separated by a distance z_1. The result for the ratio of the amplitude of transmission coefficients (defined as the ratio of transmitted to incident pressure) for a shear layer separation of z_1 to that when $z_1 = 0$ is

$$\left|\frac{T(z_1)}{T(0)}\right| = \left[1 + \frac{(1-\mu_2^2)(\mu_1^2-1)}{(1+\mu_1\mu_2)^2}\sin^2\xi\right]^{-1/2} \tag{10a}$$

$$\mu_1 = \frac{\left[(1+M_1 \sin\alpha)^2 - \sin^2\alpha\right]^{1/2}}{(1+M_1\sin\alpha)^2\cos\alpha}$$

$$\mu_2 = \frac{\left[(1+M\sin\alpha)^2 - \sin^2\alpha\right]^{1/2}(1+M_1\sin\alpha)^2}{\left[(1+M_1\sin\alpha)^2 - \sin^2\alpha\right]^{1/2}(1+M\sin\alpha)^2}$$

$$\xi = 2\pi\frac{z_1}{\lambda}\left[(1+M_1\sin\alpha)^2 - \sin^2\alpha\right]^{1/2}$$

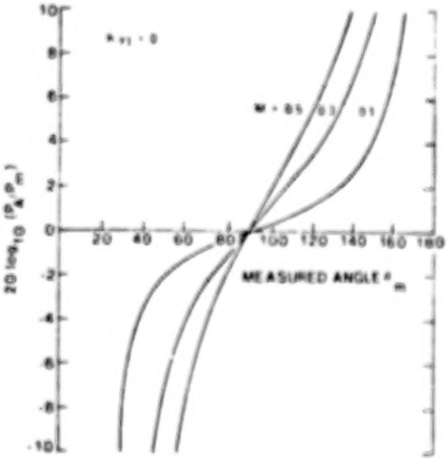

FIGURE 3. CORRECTION OF AMPLITUDE TO EQUAL SIDELINE DISTANCE WITH $h/y_1 = 0$

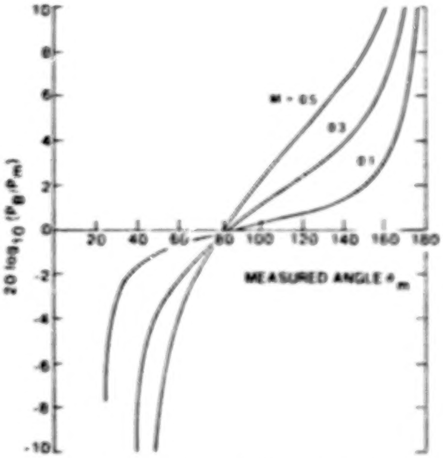

FIGURE 4. CORRECTION OF AMPLITUDE TO EQUAL RADIUS POSITION WITH $h/y_1 = 0$

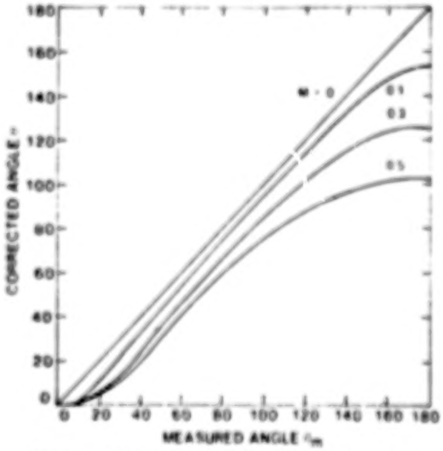

FIGURE 5. CORRECTION OF ANGLE θ_m WITH $h/y_1 = 0.2$

i.e., θ_m replaces θ in Eq. (1a). The terms within the brackets $[\ldots]$ in Eqs. (2) and (3) become unity giving

$$\frac{p_A}{p_m} = \frac{\zeta}{2\sin^2\theta_m}\left[\zeta + \sin\theta_m(1-M\cos\theta_m)^2\right] \qquad (5)$$

$$\frac{p_B}{p_m} = \frac{1}{2\sin\theta_m}\left[\zeta + \sin\theta_m(1-M\cos\theta_m)^2\right] \qquad y_1 \gg h$$

$$\cdot\left[M^2(1-M\cos\theta_m)^2 + 1 - M^2\cos^2\theta_m\right]^{1/2} \qquad (6)$$

It is interesting to compare these results with the results obtained by Gottlieb (Ref. 3) for the directivity of a monopole placed in a stream and extended by Amiet (Ref. 4) to the case of dipole sources. As was done here, Gottlieb assumed a zero-thickness plane shear layer. The distance y_1 was assumed much greater than h. If the directivity pattern given by Gottlieb is corrected in angle and amplitude using Eqs. (4) and (5), one finds that the resulting directivity curve is identical to that produced by a source in a uniform stream with no shear layer. (See the calculation in Appendix II.) In other words, Eqs. (4) through (6) have contained in them the Gottlieb results. The present results are more general, however, in that they don't assume a specific type of sound source, but rather derive a correction valid for any types or combinations of sources. Gottlieb's solution amounts to combining the known directivity of a specific kind of source in a stream together with the correction in angle and in amplitude presented here to give a resulting directivity curve for a monopole in a stream in the presence of a shear layer. Gottlieb did not present the results as a correction in angle and amplitude, however, so it is not possible to use his results for correction of the sound from a general sound source.

An interesting sidelight of this correction is that if the observer point O is on the y axis directly above the source and $y_1 \gg h$, the sound measured by the observer will be just that which would be measured by an observer at the same point and with the same source strength but with no flow. In other words, the sound level produced by the source with the tunnel on should remain unchanged at this particular observer location if the acoustic tunnel is turned off providing that the source strength can be kept fixed during the process. This is not obvious, but it can be shown from Eqs. (4) and (5). In essence it results from the fact that the convective amplification of sound is zero for an observer at 90° to the direction of motion of a source.

In order to apply the results given by Eqs. (1) through (6) it is not necessary for the acoustic wavelength λ or the body size ℓ to be small compared to h. It is only necessary that λ and ℓ be small compared to the source-observer distance OS so that the observer is in the acoustic and geometric far-field of the source. For the particular case of $y_1 \gg h$, it will be noted that Eqs. (4) through (6) are completely independent of h. This was a point noted by Gottlieb to be true so long as the observer is not in the so called "zone of silence".

The zone of silence is the angular region

$$\theta < \theta_0 \qquad (7a)$$

where θ_0 is that particular value of θ for which $\theta' = 0$. From Eq. (1) this gives $\zeta = 0$ or

$$\cos\theta_0 = \frac{1}{1+M} \qquad (7b)$$

Angles θ within the zone of silence will not concern us here since they do not correspond to a real value of θ'. As noted by Gottlieb, acoustic waves propagating to the far field at angles less than θ_0 cannot be matched with acoustic propagating waves beneath the shear layer, but rather are matched with waves which decay exponentially with the distance h.

It should be noted that the corrected angle θ' does not cover the entire range 0 to π when θ_m goes through this range. Rather, θ' ranges from 0 at the zone of silence (given by Eqs. (7)) to a value θ_1' smaller than π when $\theta_m = \theta = \pi$, where from Eq. (1a)

$$\tan\theta_1' = \frac{\sqrt{2M+M^2}}{-1+M+M^2} \qquad (8)$$

Thus, outside the jet stream it is not possible to measure the sound for values of θ' greater than θ_1'. Also, as mentioned below, measurements made near the value $\theta' = \theta_1'$ probably are inaccurate because of reflection from the lower shear layer. This precludes making measurements of the sound radiated forward from the source at small angles to the axis. The sound is reflected from the shear layer and thus is trapped within the jet.

Discussion

Typical results of these equations are plotted in Figs. 2 through 8. Figures 2 through 4 show results obtained from Eqs. (4) through (6) for $y_1 \gg h$. The independent variable in these plots is the measured angle θ_m. Figure 2 gives the corrected angle θ' for several Mach numbers and Figs. 3 and 4 give the dB correction to be added to the measured sound level for equal sideline and equal radius measurements, respectively. Figures 5 through 8 show similar curves for Eqs. (1) through (3). Figures 5 and 6 are for equal sideline measurements and use value $h/y_1 = 0.2$. Figures 7 and 8 are for corrections to equal radius. Since the ratio h/y_1 changes for measurements made on a circular arc, the quantity h/r was kept fixed for the equal radius calculations. The value chosen for Figs. 7 and 8 is h/r = 0.15.

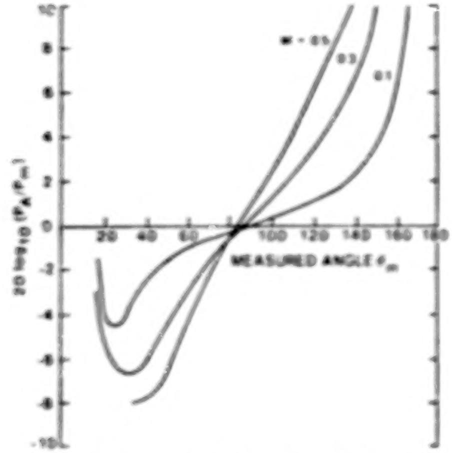

FIGURE 6. CORRECTION OF AMPLITUDE TO EQUAL SIDELINE DISTANCE WITH $h/y_1 = 0.2$

The greatest deviation from unity of this ratio $|T(z_1)/T(0)|$ occurs for those values of z_1/λ such that $\xi = (2n+1)\pi/2 = \xi_n$. Since $\sin \xi_n = 1$, (this of course requires a different value of z_1/λ for each value of θ') Eq. (10a) simplifies to

$$\left| \frac{T(\xi = \pi/2)}{T(\xi = 0)} \right| = \frac{1 + \mu_1 \mu_2}{\mu_1 + \mu_2} \tag{10b}$$

This is plotted in Fig. 10b for a Mach number $M = 0.5$ and $M_1 = 0.25$. There is little effect of finite thickness except near the zone of silence ($\theta' \sim 0$).

Experimental Results

Devising an experiment to measure the refraction effect is complicated by the difficulty of obtaining a source whose directivity in a uniform stream is known. Measuring the directivity of a source in stationary air produces no difficulty, but this directivity would be expected to change in an unknown manner when the source is placed within a stream.

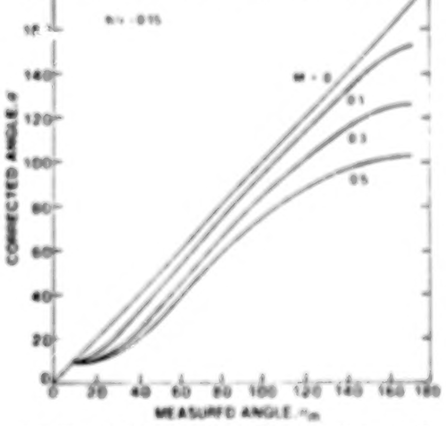

FIGURE 7. CORRECTION OF ANGLE θ_m WITH $h/r = 0.15$

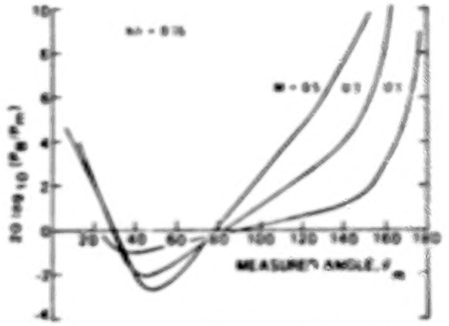

FIGURE 8. CORRECTION OF AMPLITUDE TO EQUAL RADIUS POSITION WITH $h/r = 0.15$

One of the simplest sources is the compact dipole. The directivity of a compact dipole in a stream is known, and so the directivity corrected for the presence of the shear layer can easily be obtained (Ref. 4). This is shown in Fig. 11 for a Mach number of 0.27 along with the directivity of a dipole in stationary flow for comparison. The observer is assumed to be far from the shear layer so that $h/y_1 \ll 1$. Curves for two values of h/λ are also shown, and it will be noted that changing h/λ affects only the sound in the zone of silence.

To obtain an experimental check on these theoretical results, a 1/16" diameter cylindrical rod was placed in the potential core of a 2" diameter free jet. Because of vortex shedding from the rod, a fluctuating dipole with a Strouhal frequency of about 0.2 (based on rod diameter) was produced. Acoustic measurements were taken on a circular arc at a distance of 33" from the rod and are denoted by the circles in Fig. 11. Measurements were taken only in the downstream quadrant because the upstream sound could be partially shielded by the jet nozzle, and because very little difference is expected upstream between directivity of a dipole in stationary air and in a stream. This is evident from the theoretical curve shown in Fig. 11.

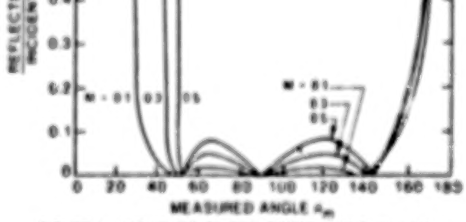

FIGURE 9. AMPLITUDE OF REFLECTED WAVE; $h/y_1 = 0$

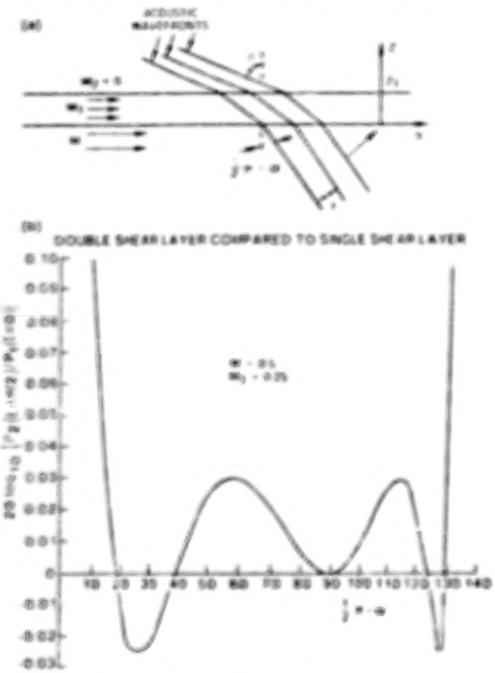

FIGURE 10 EFFECT OF DOUBLE SHEAR LAYER

Since the directivity of a dipole varies rather slowly with measurement angle, the only substantial difference in sound amplitudes between a dipole in stationary air and a dipole in a jet is near the zone of silence, where a rapid dropoff in the sound level is predicted. This dropoff did occur in the measured sound levels at about the proper angle. The sound level was normalized to 1 at $\theta_m = 90$ deg.

Some deviations from the predicted directivity are expected near the zone of silence as mentioned previously. Near the zone of silence, the reflection coefficient of the shear layer becomes important so that the validity of approximating the jet as a single shear layer begins to break down. This may explain the tendency for the measured directivity curve to appear somewhat rippled just before the zone of silence is entered. This tendency was predicted analytically in an unpublished study by Lansing and Brown (Ref. 6) for the case of a source on the centerline of an axisymmetric jet.

There appears to be some uncertainty, e.g., Howe (Ref. 7), as to whether the procedure used here and in Refs. 3 and 4 gives correct results in the zone of silence because of shear layer instabilities. Also, the acoustic prediction for the zone of silence depends strongly on the ratio h/λ. In actuality the shear layer has a finite thickness so that h cannot be defined accurately. Because of these points, it should not be surprising that agreement between experiment and theory is unfavorable in the zone of silence. In this region, however, both theoretical and experimental results have values significantly lower than those of a dipole in stationary air. Any lack of ability to predict the sound level within the zone of silence is not important for purposes of correcting wind tunnel data since measurements made here do not correspond to measurements that could be made in a free stream without a shear layer. That is, for θ in the range $0<\theta<\theta_0$, $\tan\theta'$ as given by Eq. (1a) is imaginary.

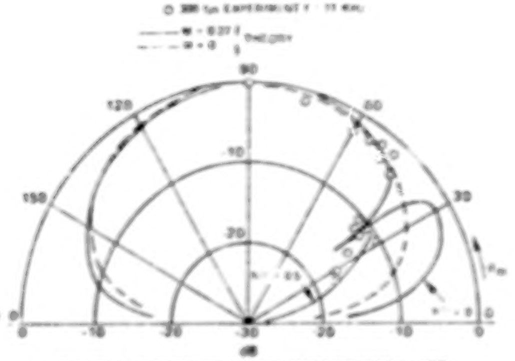

FIGURE 11 DIRECTIVITY OF DIPOLE NEAR SHEAR LAYER THEORY VS EXPERIMENT

Thus, these experimental results give some verification of the theory in that the zone of silence has its onset at about the angle predicted by theory. A better verification could perhaps be obtained by using a more directional source. Some effort has been made along these lines, but significant problems are involved. When a sound source is placed in a stream, one cannot expect that the radiation pattern of the source will remain unchanged even if one has no shear layer. Thus, to have an idea of the amount of shear layer refraction, the source directivity must be measured inside the shear layer and compared to that outside the shear layer.

The measurement inside the shear layer is made more difficult by the fact that the inflow microphone must be in the acoustical and geometrical far-field of the source. This difficulty became more obvious when a small 1/2 inch jet operating supersonically in the screech regime was used as a source. This source produced a narrow-band signal which had a very sharp directivity. However, there was disagreement between the directivities of the inflow and the far-field microphones, even when the acoustic tunnel was not operating (i.e., no shear layer) indicating that the inflow microphone was not in the far-field of the source.

An alternative procedure described below makes use of a source which need not be directional, but which can give verification of the angle correction. A pure tone noise source was placed in the center of the acoustic tunnel. For this purpose a high frequency (25 kHz) dog whistle was used. It was placed behind a 2 inch pipe concentric with the tunnel, the pipe tending to shield the whistle from the effects of the flow. The idea is then to determine the angle of the wavefronts after the sound has passed through the shear layer. This can be done by cross-correlating the output of two microphones. By comparing the cross-correlation with flow to that obtained with no tunnel flow, the shift in phase between the cross-correlation of two adjacent microphones determines the angle of propagation of the far-field wavefront. Given this angle, the point X_0 at which the sound emerged from the shear layer can be calculated. The measured value of θ' is then given as $\tan^{-1}(h/X_0)$. For this particular test the far-field microphones were placed at a distance of $r = 10$ ft. In retrospect, it might have been preferable to make the measurements nearer to the shear layer allowing a better calculation of θ'.

The results of the measurements are shown in Figs. 12. The results are in reasonable agreement with theory, the theory generally underestimating the experimentally measured angle correction.

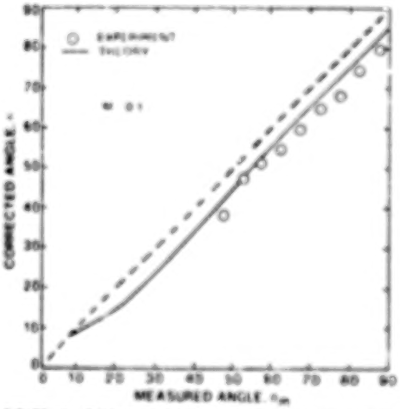

FIGURE 12a COMPARISON OF THEORY WITH EXPERIMENT FOR ANGLE CORRECTION M = 0.1

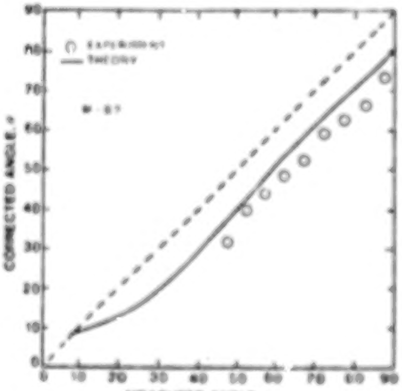

FIGURE 12b COMPARISON OF THEORY WITH EXPERIMENT FOR ANGLE CORRECTION M = 0.2

Conclusions

The dipole produced by a rod in the flow shows the onset of the zone of silence at the angle predicted by theory. The amplitude of the sound outside the zone of silence showed good agreement with theory, but this gives only a weak verification of the theory because of the rather small variation of amplitude with angle; i.e., there were no sharply defined directivity peaks with which one could check the angle and amplitude corrections independently.

As discussed in the text, the use of a source with a sharply defined directivity presented certain difficulties. An alternate procedure of cross-correlating the outputs from nearby microphones to define the wavefront angle gave results for the angle correction which were in reasonable agreement with theory.

Thus, the tests performed gave results which agreed with theory. The author feels, however, that there is further room for experimental verification of various aspects of the theory.

Acknowledgments

The author is grateful for the many helpful discussions with personnel at P&WA and UARL. In particular, discussions with A. A. Peracchio were helpful in formulating the experimental work and the assistance of H. F. Day with the experimental program was appreciated.

References

1. Ribner, H. S.: "Reflection, Transmission and Amplification of Sound by a Moving Medium", JASA, 29, (1957), pp. 435-441.

2. Miles, J. W.: "On the Reflection of Sound at an Interface of Relative Motion", JASA, 29, (1957), pp. 226-228.

3. Gottlieb, P.: "Sound Source Near a Velocity Discontinuity", JASA, 32, (1960), pp. 1117-1122.

4. Amiet, R. K.: "Propagation of Sound Through a Two-Dimensional Shear Layer with Application to Measurements in the Acoustic Research Tunnel", United Aircraft Research Laboratories Report UAR-140, (1972).

5. Graham, E. W. and B. B. Graham: "Effect of a Shear Layer on Plane Waves of Sound in Fluid", JASA, 46, (1969), pp. 169-175.

6. Lansing, D. L. and T. J. Brown: "Refraction of Sound from a Source in a Jet", Memorandum for H. H. Hubbard, NASA Langley Research Center, (Dec. 1970).

7. Howe, M. S.: "Transmission of an Acoustic Pulse Through a Plane Vortex Sheet", J.F.M., 43, (1970), pp. 353-367.

8. Csanady, G. T.: "The Effect of Mean Velocity Variations on Jet Noise", J.F.M., 26, (1966), pp. 183-197.

9. Amiet, R. K.: "Aerodynamic Sound Production and the Method of Matched Asymptotic Expansitions", Ph.D. thesis, United Aircraft Research Laboratories Report UAR-H223, (1969).

10. Paterson, R. W.: "Passage of High Frequency Pure Tones Through a Turbulent Round Jet", United Aircraft Research Laboratories Report UAR-M112, (1973).

Appendix I
Derivation of the Correction Equations

As was mentioned in the text, geometrical acoustics along with the solution of Miles or Ribner will be used to derive the correction relation. The relations between the various angles in Fig. 1 can be derived as follows. (Note that all angles marked in this figure are in the $z = 0$ plane.) The loci of points of equal phase (the wavefronts) of the sound wave are the circles drawn in the figure. These circles propagate outward at the speed of sound and drift downstream at the fluid velocity, the phase of the wavefronts being given by

$$\Theta = t + \frac{Mx - \sigma}{c_0 \beta^2} \tag{A1}$$

where $\sigma = \sqrt{x^2+\beta^2 y^2}$. The angle α is determined by the tangent to the wavefront intersecting the point (x_0, h), and by calculating dy/dx from Eq. (A1), α is found to satisfy the equation

$$\frac{\cos\alpha}{\sin\alpha + M} = \frac{h}{x_0} = \tan\theta' \tag{A2}$$

The relation between α and θ is found by equating the x components of phase velocity across the shear layer. As for the case of a plane wave incident on the shear layer discussed by Ribner (Ref. 1)

$$\frac{1}{\cos\theta} = \frac{1}{\sin\alpha} + M \tag{A3}$$

The last two equations allow the relation between θ and θ' to be written

$$\tan\theta' = \frac{\zeta}{\beta^2\cos\theta + M} = \frac{h}{x_0} \tag{A4}$$

or

$$\cos\theta = \frac{1}{\beta^2}\left[\frac{\cos\theta'}{(1-M^2\sin^2\theta')^{1/2}} - M\right] \tag{A5}$$

Equation (A4) is Eq. (1a) quoted in the text. Equation (1b) relating θ_m to θ and θ' is derived by noting that

$$y_1 \cot\theta_m = x_0 + (y_1 - h)\cot\theta \tag{A6}$$

Using Eq. (A2) gives Eq. (1b).

In order to calculate the corrected amplitude, we must first calculate the amplitude at point C just below the shear layer. To do this, the spreading rate of a ray travelling along CO must be determined.

The rate of spreading in the xy plane is easily determined by calculating $dx_0/d\theta$ from Eq. (A4) giving

$$\frac{dx_0}{d\theta} = \frac{h\sin\theta}{\zeta^3} \quad ? \tag{A7}$$

Figure 13 shows the cross section in the xy plane of a ray tube. The ratio of the lengths $d\ell_2/d\ell_1$ is found to be

$$\frac{d\ell_2}{d\ell_1} = \frac{d\ell_1 + \left[(y_1-h)\csc\theta\right]d\theta}{d\ell_1} = 1 + (y_1-h)\csc^2\theta\,\frac{d\theta}{dx_0}$$

$$= 1 + \left(\frac{y_1}{h} - 1\right)\frac{\zeta^3}{\sin^3\theta} \tag{A8}$$

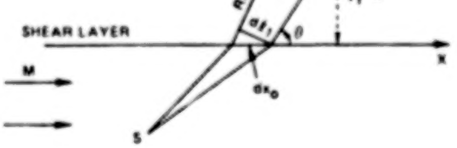

Figure 13. Ray spreading in xy plane.

The spreading of the ray in the perpendicular plane (the plane formed by the line OC and the z axis) must also be determined. To do this, the amount of refraction by the shear layer of a ray propagating out of the xy plane must be determined.

For a plane wave

$$p_i = e^{i(\omega t - \Theta_i)} \tag{A9}$$

incident on the shear layer from below, a transmitted wave

$$p_t = Ae^{i(\omega t - \Theta_t)} \tag{A10}$$

is produced where A is some transmission coefficient (possibly complex) to be described later. The phase expressions θ_i and θ_t must be of a form such that P_t and P_i satisfy the wave equation and the convected wave equation, respectively, and the phases of P_i and P_t must match at the shear layer. The appropriate expressions are

$$\Theta_i = \frac{\omega}{C_0}\Big[x \sin\phi \cos\psi + z \sin\phi \sin\psi + y\sqrt{(1 - M \sin\phi \cos\psi)^2 - \sin^2\phi}\,\Big] \tag{A11}$$

$$\Theta_t = \frac{\omega}{C_0}\Big[x \sin\phi \cos\psi + z \sin\phi \sin\psi + y \cos\phi\Big]$$

These equations were expressed in terms of the angles θ and ψ since these angles are the polar angles of the unit normal to the transmitted wavefronts as shown in Figure 14.

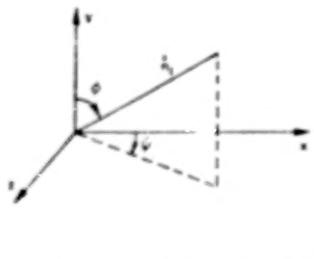

Figure 14. Description of the polar angles θ and ψ.

By calculating $\nabla\Theta/|\nabla\Theta|$ the unit normals to the incident and transmitted waves are

$$\hat{n}_i\,(1 - M \sin\phi \cos\psi) = \hat{i} \sin\phi \cos\psi + \hat{k} \sin\phi \sin\psi + \hat{j}\sqrt{(1 - M \sin\phi \cos\psi)^2 - \sin^2\phi} \tag{A12a}$$

$$\hat{n}_t = \hat{i} \sin\phi \cos\psi + \hat{j} \cos\phi + \hat{k} \sin\phi \sin\psi \tag{A12b}$$

In the actual case the wavefronts are circular rather than plane and are given by Eq. (A1). By calculating the gradient of Eq. A1 the unit normal to the actual wavefront is

$$\frac{\nabla\Theta}{|\nabla\Theta|} = \frac{\hat{i}(x - M\sigma) + \hat{j}\beta^2 y + \hat{k}\beta^2 z}{\sigma - Mx} \tag{A13}$$

By comparison with Eq. (12a), the angle of propagation of the transmitted wave can be related to the position (x_0, h, z) at which the ray crosses the shear layer. Thus,

$$\frac{\sin\phi \cos\psi}{1 - M \sin\phi \cos\psi} = \frac{x_0 - M\sigma}{\sigma - Mx_0} \tag{A14a}$$

$$\frac{\sin\phi \sin\psi}{1 - M \sin\phi \cos\psi} = \frac{\beta^2 z}{\sigma - Mx_0} \tag{A14b}$$

For the $z = 0$ plane $\psi = 0$, $\phi = \frac{\pi}{2} - \theta$ and Eq. (A14a) becomes equivalent to Eq. (1a). Equation (A14b) is the equation of interest at present. By taking the derivative of z with respect to ψ, for small ψ we find

$$\left(\frac{dz}{d\psi}\right)_{\psi=0} = \frac{\sin\phi}{1 - M\sin\phi}\,\frac{1}{\beta^2}\left(\sqrt{\beta^2 + x_0^2/h^2} - Mx_0/h\right) = \frac{h\cos\theta}{\zeta} \tag{A15}$$

where Eq. (A4) was used to evaluate x_0/h.

Rather than using the polar angle ψ as measured in the x-z plane, we wish to use the angle ψ' which is measured in the plane perpendicular to the xy plane and along the ray OC as shown in Figure 15.

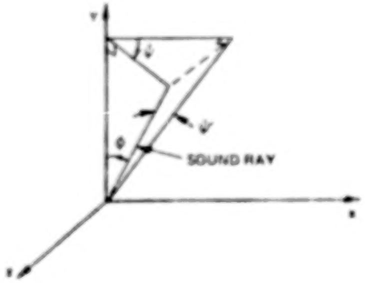

Figure 15. Relation of angle ψ' to ψ.

The relation between ψ and ψ' is

$$\sin\psi' = \sin\psi\left[\cos^2\psi + \cot^2\phi\right]^{-1/2} \tag{A16}$$

which becomes for small ψ

$$\psi' \approx \psi \sin\phi \tag{A17}$$

Thus, Eq. (A15) becomes

$$\left(\frac{dz}{d\psi'}\right)_{\psi'=0} = h/\zeta \tag{A18}$$

Figure 16 shows the ray spreading in the plane produced by the z axis and the sound ray.

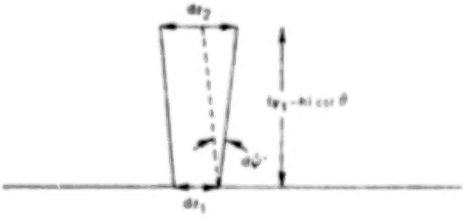

Figure 16. Ray divergence in plane perpendicular to xy plane.

The ratio of the two lengths dz_1 and dz_2 is

$$\frac{dz_2}{dz_1} = \frac{dz_1 + (y_1 - h)\csc\theta\, d\psi'}{dz_1} \tag{A19}$$

$$= 1 + \left(\frac{y_1}{h} - 1\right)\zeta \csc\theta$$

The product of the two length ratios given by Eqs. (A8) and (A19) gives the ratio of ray tube cross sectional area for a point in the far field to that for a point just above the shear layer. In order to conserve acoustical energy in the ray tube, the acoustical pressure should behave inversely with the square root of the ray tube cross sectional area. Thus,

$$\frac{P_{C+}}{P_m} = \sqrt{\frac{dz_2}{dz_1}\frac{dl_2}{dl_1}} \tag{A20}$$

$$= \left[1 + \left(\frac{y_1}{h} - 1\right)\zeta\csc\theta\right]^{1/2}\left[1 + \left(\frac{y_1}{h} - 1\right)\zeta^3\csc^3\theta\right]^{1/2}$$

For the case of a plane wave incident on the shear layer, the ratio of the transmitted pressure to the incident pressure was found by Ribner to be

$$\frac{P_{C-}}{P_{C+}} = \frac{1}{2\zeta}\left[\zeta + \sin\theta(1 - M\cos\theta)^2\right] \tag{A21}$$

Using this expression along with Eq. (A20) then allows P_{C-} to be calculated in terms of the measured pressure P_m.

Since the pressure decays as r^{-1} in the far field, knowing P_{C-} allows us to calculate the pressure P_B in Fig. 1. Thus,

$$\frac{P_B}{P_{C-}} = \frac{\sqrt{h^2 + x_0^2}}{r} = \frac{h}{r}\csc\theta' \tag{A22}$$

$$= \frac{h}{r\zeta}\left[M^2(1 - M\cos\theta)^2 + 1 - M^2\cos^2\theta\right]^{1/2}$$

Combining Eqs. (A20) and (A22) then gives Eq. (3) for P_B.

For correction to equal sideline positions rather than equal radius, the ratio of P_A to P_{C-} is

$$\frac{P_A}{P_{C-}} = \frac{h}{y_1} \tag{A23}$$

Combining this with Eqs. (A20) and (A21) gives Eq. (2).

Appendix II
Relation to the Solution of Gottlieb

Gottlieb has found the directivity to be expected from a monopole sound source placed beneath the shear layer to be

$$P_m \propto \frac{2\sin\theta_m(1 - M\cos\theta_m)}{\sin\theta_m(1 - M\cos\theta_m)^2 + \zeta_m} \tag{A24}$$

$$\cos\theta_m \le \frac{1}{1 + M} \qquad y_1 >> h$$

This relation assumes the observer is in the far-field at a constant radial distance from the source. The angle θ_m is restricted to lie outside the zone of silence. Let us apply the appropriate correction equations (Eqs. (4) and (6) assuming $y_1 << h$) to determine if the correct directivity for a monopole in a stream in the absence of the shear layer can be calculated from Gottlieb's solution.

Equation (6) when combined with Eq. (A24) gives the corrected pressure P_B in terms of the measured angle θ_m as

$$P_B \propto (1 - M\cos\theta_m)\left[M^2(1 - M\cos\theta_m)^2 + 1 - M^2\cos^2\theta_m\right]^{1/2} \tag{A25}$$

From Eq. (4) one can show that

$$\cos\theta' = \frac{\beta^2\cos\theta_m + M}{\left[M^2(1 - M\cos\theta_m)^2 + 1 - M^2\cos^2\theta_m\right]^{1/2}} \tag{A26}$$

$$y_1 >> h$$

giving

$$P_B \propto \frac{1}{\cos\theta'}(\beta^2\cos\theta_m + M)(1 - M\cos\theta_m) \tag{A27}$$

Finally, using Eq. (A5) gives the result (since $\theta_m = \theta$ here)

$$P_B \propto \frac{1}{\beta^2\sigma'}\left(1 - \frac{Mx'}{\sigma'}\right) \tag{A28}$$

where $x' = r\cos\theta'$

$y' = r\sin\theta'$

$\sigma' = \sqrt{x'^2 + \beta^2 y'^2} = r\sqrt{1 - M^2\sin^2\theta'}$

Now Eq. (A28) (except for constant factors such as monopole strength which were omitted from Eq. (A24)) is the far-field solution for a monopole in a stream (see Eq. (1.33) of Ref. 9 for example). Thus, the solution procedure used by Gottlieb has inherent in it the same assumptions such as geometrical acoustics used here. The main difference is that Gottlieb's procedure gives directivity predictions for each of the source types (monopole, dipole, etc.) whereas the present procedure gives a method for correcting the data independent of the source type.

LIST OF ABBREVIATIONS

NOMENCLATURE (The following symbols are used throughout the report unless otherwise defined in the text.)

A – Area
ΔA_i – Surface of Spherical Segment Associated With i^{th} microphone
C – Speed of Sound
C_D – Flow Coefficient (Actual Weight Flow/Ideal Weight Flow)
C_F – Thrust Coefficient (Actual Thrust/Ideal Thrust)
d – Diameter of Jet
F – Thrust
f – Frequency
L – Length
M – Mach Number
n – Relative Velocity Exponent
OASPL – Overall Sound Pressure Level – dB re 20×10^{-6} Newtons/m^2
P – Pressure
$\overline{p_i^2}$ – Mean Square Sound Pressure
PNL – Perceived Noise Level
PWL – Power Level – dB re 10^{-12} Watts
$\mathscr{R}$ – Gas Constant
r – Radius
Ref – Reference
RH – Relative Humidity
SPL – Sound Power Level – dB re 20×10^{-6} Newtons/m^2
SSPL – Sum of Sound Pressure Level (500 Hz – 80 K Hz)
TSPL – Total Sound Pressure Level (100 Hz – 80 K Hz)
V – Jet Velocity (Ideally Expanded to Ambient Conditions)
V_{rel} – Relative Jet Velocity, $V_j - V_\infty$
V_{to} – Tunnel Induced Velocity (Static Condition)
V_∞ – Tunnel Flow Velocity
W – Acoustic Power
W_t, W_i – Air Flow Rate, Measured ideal
X – Position of pressure orifice relative to leading edge of ejector (station 52.54)
γ – Specific Heat Ratio
Δ – Difference In Noise or Thrust Levels
θ' – Angle After Shear Layer Refraction Correction
θ_m – Measured Angle from Inlet Centerline
θ_R – Noise Emission
ρ – Density
ϕ_V – Velocity Parameter

LIST OF ABBREVIATIONS (Cont'd.)

SUBSCRIPTS (The subscripts are used in either lower case or upper case form.)

a – Ambient
ejec – Ejector
eq – Equivalent
f – Fan
i – Ideal
j – Jet
m – Mixed
max – Maximum
o – Atmospheric Condition
p – Primary
Per – Perimeter
ref – Reference
s – Static
t – Total
∞ – Tunnel Stream

1. Report No. **NASA CR-3018**	2. Government Accession No.	3. Recipient's Catalog No.

4. Title and Subtitle **FLIGHT EFFECTS ON THE AERODYNAMIC AND ACOUSTIC CHARACTERISTICS OF INVERTED PROFILE COANNULAR NOZZLES**	5. Report Date August 1978 6. Performing Organization Code
7. Author(s) **Hilary Kozlowski and Allan B. Packman**	8. Performing Organization Report No. **PWA-5501** 10. Work Unit No.
9. Performing Organization Name and Address **Pratt & Whitney Aircraft Group** **United Technologies Corporation** **East Hartford, Connecticut 06108**	11. Contract or Grant No. **NAS3-17866** 13. Type of Report and Period Covered **Contractor Report**
12. Sponsoring Agency Name and Address **National Aeronautics and Space Administration** **Washington, D.C. 20546**	14. Sponsoring Agency Code

15. Supplementary Notes

Final report. Project Manager, Orlando A. Gutierrez, V/STOL and Noise Division, NASA Lewis Research Center, Cleveland, Ohio 44135.

16. Abstract

The effect of forward flight on the jet noise of coannular exhaust nozzles, suitable for Variable Stream Control Engines (VSCE), was investigated in a series of wind tunnel tests. Scale models, having a total area equivalent to a 0.057-m diameter convergent nozzle, simulated coannular nozzles with and without ejectors. The ratio of fan-to-primary area was varied from 0.75 to 1.2. The external velocity was varied from 0 to 129 mps. During the acoustic tests, which provided far field data, the velocity of the fan stream was varied from 240 to 630 mps and temperature from 394 to 700 K. The primary stream properties were maintained constant at 300 mps and 394 K. A total of 230 acoustic data points was obtained. Force measurement tests using an unheated air supply covered the same range of tunnel speeds and nozzle pressure ratios on each of the nozzle configurations. A total of 80 points was taken. These data are all presented in the companion Comprehensive Data Report, NASA CR-134189. The coannular nozzle OASPL and PNL noise reductions observed statically relative to synthesized values were basically retained under simulated flight conditions. The effect of fan to primary stream area ratio on flight effects was minor. Attempts were made to correlate ΔOASPL reductions in flight with simple relative velocity exponents. Also, a promising prediction procedure based on separate analysis of pre-merged, post-merged and shock noise sources was exercised. At take-off speed, the peak jet noise for a VSCE was estimated to be over 6 PNdB lower than the static noise level. High static thrust coefficients were obtained for the basic coannular nozzles, with a decay of 0.75 percent at take-off speeds.

17. Key Words (Suggested by Author(s)) **Supersonic Cruise Airplane Research (SCAR) Program; Wind tunnel aero/acoustic experimental data; VSCE exhaust nozzles; Coannular jet noise**	18. Distribution Statement **Unclassified - unlimited** **STAR Category 71**

19. Security Classif. (of this report)	20. Security Classif. (of this page)	21. No. of Pages	22. Price*
Unclassified	**Unclassified**	**195**	**A09**

* For sale by the National Technical Information Service, Springfield, Virginia 22161

90

50

END

DEC 18 1978